Wind Tunnel Tests and Fluid Dynamics Analyses of Wake Flows Near Blunt and Streamlined Bodies Models at high Reynolds numbers

by

Manuel FLORES SALINAS

MANUSCRIPT-BASED THESIS PRESENTED TO ÉCOLE DE TECHNOLOGIE SUPÉRIEURE IN PARTIAL FULFILLMENT OF THE REQUIREMENTS FOR THE DEGREE OF DOCTOR OF PHILOSOPHY
Ph.D.

MONTREAL, JULY 30, 2023

ÉCOLE DE TECHNOLOGIE SUPÉRIEURE
UNIVERSITÉ DU QUÉBEC

BOARD OF EXAMINERS

THIS THESIS HAS BEEN EVALUATED

BY THE FOLLOWING BOARD OF EXAMINERS

Mrs. Ruxandra Mihaela Botez, Thesis Supervisor
Department of System Engineering, École de technologie supérieure

Mr. Guy Gauthier, Thesis Co-supervisor
Department of System Engineering, École de technologie supérieure

Mr. Thien-My Dao, President of the Board of Examiners
Department of Mechanical Engineering, École de technologie supérieure

Mr. Tony Wong, Member of the jury
Department of System Engineering, École de technologie supérieure

Mr. Rosario Pecora, External Evaluator
Department of Industrial Engineering, University of Naples Federico II

THIS THESIS WAS PRESENTED AND DEFENDED

IN THE PRESENCE OF A BOARD OF EXAMINERS AND PUBLIC

ON JULY 19, 2023

AT ÉCOLE DE TECHNOLOGIE SUPÉRIEURE

ACKNOWLEDGMENTS

First, I would like to thank very much to both my Ph.D. Thesis advisors, Professors Ruxandra Mihaela Botez and Guy Gauthier for their time. I am grateful for all the guidance and support they have given me.

The perfect introduction to multidisciplinary morphing wing research was the CRIAQ MDO 505 project, where I have learned a lot and worked with the best Master's and PhD students from the LARCASE laboratory all working now in academic and industrial environments as Lecturers or researchers: Joel, Andreaa, Oliviu, Mehdi, Olivier, Francois and Yvan.

I was fortunate to work also with other motivated students and team colleagues during my research years at the Subsonic Price-Païdoussis wind tunnel facility. To name a few: Jimmy, Adrien, Thomas, Nicolas, Jeremy, Mohammed, Rachid, Alexandre, Larry, Guillaume, Florian, Alexandre, Olivier, Francois, Luc-Olivier and David.

I am particularly grateful to formet Ph.D. students and now graduated students, Dr. Abdallah Ben Mosbah and Mohammad Tavallaeinejad for working with me on a very interesting research in the fields of neural networks and inverted-foils dynamics.

Since my Master's studies, Professor Botez has set a very good example, with her commitment and dedication to her research, and gave me the opportunity to work on high-caliber research projects, such as the ones presented in this PhD thesis. I have also to thank to Emeritus Professor Michael Païdoussis for all his time, energy and patience in commenting my work on the inverted-foils research. I sincerely thank Oscar Carranza for introducing me to subsonic wind tunnel testing.

Lastly, a heartfelt thanks to my whole family, specially to my mother Aurora , my father Manuel, my uncle Gustavo, my sister Silvia and my nephew Valentino for their continuous encouragements and support.

Essais en soufflerie et analyses de la dynamique des fluides du sillage à proximité d’un corps non profilé et profilé à des écoulements à grand nombre de Reynolds

Manuel FLORES SALINAS

RÉSUMÉ

Cette thèse présente trois travaux de recherche qui se résument comme suit.
Premièrement, une nouvelle méthodologie est proposée pour mesurer et analyser les caractéristiques du fluide à proximité d’un corps non-profilé sans introduire des capteurs dans le champ d'écoulement, car ils modifieraient le comportement de l'écoulement. Cette méthodologie analyse la région du sillage du “système de surveillance au sol” (radar) et évalue l'intensité de la turbulence, les coefficients de traînée, les coefficients de la pression de surface et la séparation de la couche limite. Les résultats numériques ont montré un détachement périodique de l’écoulement à la surface du radar, une séparation de la couche limite, des niveaux élevés de la turbulence et une augmentation de la traînée.
Des plaques flexibles, serrées à une extrémité et soumises à un fluide s'écoulant axialement, produisent des oscillations à grande amplitude. La motivation pour des recherches sur la dynamique des plaques flexibles est due à leur potentiel pour récupérer de l’énergie de l’environnement. Il a été constaté expérimentalement que pour les plaques de rapport de dimensions AR < 1, il y a un équilibre statique stable jusqu’à l’apparition d’un flambage soudain. Pour les plaques AR ≥ 1, il y a des oscillations qui apparaissent. À des vitesses d'écoulement plus grandes, les plaques ont des régimes d’oscillations variées et à des vitesses critiques, les plaques ont un régime d’oscillation périodique à une grande amplitude, produisant une grande quantité d’énergie. Les expériences ont été réalisées dans notre soufflerie subsonique Price-Païdoussis à l'ÉTS. Les résultats numériques ont été validés avec des résultats expérimentaux, tels que les rapports AR, la fréquence et le régime d’oscillations, les nombres de Strouhal et de Reynolds, les amplitudes d’oscillation et les forces produites par les plaques.
Le rôle des opérations des systèmes aériens sans pilote (UAS) a augmenté ces dernières années. De nouvelles connaissances multidisciplinaires sont présentées pour la conception, l'optimisation aérodynamique et la validation d'un prototype d'aile adaptative. Les recherches effectuées sur le système aérien sans pilote UAS-S45 se sont concentrées sur le remplacement de l'aile rigide par un système d'aile adaptatif capable de modifier activement la forme de l'aile. Les résultats expérimentaux et simulés ont montré une faible production de traînée et un rapport portance/traînée élevé du prototype d'aile adaptative qui se traduit par une réduction de la consommation de carburant et une augmentation de l'autonomie de vol en croisière et donc par une amélioration du climat.

Mots-clés: Aile déformable, turbulence, réduction de traînée, corps non-profilé, plaque, récupération de l’énergie de l’environnement, validation du modèle numérique

Wind Tunnel Tests and Fluid Dynamics Analyses of Wake Flows Near Blunt and Streamlined Bodies Models at high Reynolds numbers

Manuel FLORES SALINAS

ABSTRACT

This PhD thesis presents three different research accomplishments, as summarized below.
Firstly, a new methodology is proposed to measure and analyze the flow characteristics near blunt bodies without introducing physical probes into the flow-field, which would alter the flow behavior. This methodology analyses the wake region of a “Ground Surveillance System” (Radar), with the aim to evaluate the turbulence intensity, drag coefficients, pressure distribution coefficients, and boundary layer separation. The numerical results obtained on the radar’s wake region showed periodic vortex shedding, boundary layer separation, high levels of turbulence, and induced drag; the nature of the adverse pressure gradient and the high turbulence intensity values at the radar surface needed a mechanism to reduce flow fluctuations and to allow the boundary layer increase.

Foils subjected to a fluid flowing axially from the free end towards the clamped-end, known as “inverted-foil” configurations, have been observed experimentally for large-amplitude flapping beyond a critical flow velocity. The motivation for further research on the dynamics of inverted-foils is due to its presence in nature and engineering. It was found from experimental results that, for foils with aspect ratio AR<1, the undeflected static equilibrium was stable prior to a sudden bifurcation. For foils with AR≥1, however, the undeflected stable static equilibrium was subjected to a slow bifurcation, associated with its buckling. Higher flow velocities generated a flapping motion around the deflected static equilibrium. At higher flow velocities, flapping motions are symmetric around the undeflected static equilibrium. Experiments with foils in a reverse axial flow were conducted in our Price-Païdoussis subsonic wind tunnel at ÉTS. Numerical results were validated with experimental results for parameters, such as the foils lengths (aspect ratios), flapping frequency and regime, Strouhal and Reynolds numbers, flapping amplitudes and forces for energy harvesting purposes.

The role of Unmanned Aerial System (UAS) operations has increased in recent years. A new multidisciplinary methodology is presented for the design, aerodynamic optimization, and model validation of an adaptive wing prototype. The research performed on the UAS-S45 focused on replacing the conventional rigid wing with an adaptive wing system capable of actively changing the wing's shape. The experimental and simulated results have shown a low drag production and a high lift-to-drag ratio of the adaptive wing prototype that translates into a reduction in fuel consumption and an increase in cruising flight range and therefore into climate improvement.

Keywords: Adaptive wing, transition, turbulence, drag reduction, blunt body, inverted foil, energy harvesting, CFD, model validation

TABLE OF CONTENTS

LIST OF TABLES

Page

LIST OF FIGURES

Page

LIST OF ABBREVIATIONS

AIAA	American Institute of Aeronautics and Astronautics
ASHRAE	Refrigerating and Air-Conditioning Engineers
ASME	American society of mechanical engineers
CEA	Centroids of Equal Areas
CFD	Computational Fluid Dynamics
CIRA	Italian Center for Aerospace Research
CRIAQ	Consortium for Research and Innovation in Aerospace in Quebec
ÉTS	École de technologie supérieure
LARCASE	Laboratory of Research in Active Controls, Avionics and AeroServoElasticity
MDO	Multidisciplinary Design Optimization
NACA	National Advisory Committee for Aeronautics
NRC-IAR	National Research Council - Institute for Aerospace Research
NSERC	Natural Sciences and Engineering Research Council of Canada
SMA	Smart Material Actuators
UAS	Unmanned Aerial System

LIST OF SYMBOLS

A	Foil amplitude of oscillation (peak-to-peak)
AOA	Angle of attack
AR	Aspect ratio
B	Deflection rigidity of the foil
C_l	Lift coefficient
C_d	Drag coefficient
d	Dimensionless amplitude of oscillation
E	Young modulus
f	Frequency of the vortex shedding (Hz)
F_x, F_y, M_x, M_y	Forces and moments measured by the aerodynamic scale (N, Nm)
Kb	Deflection rigidity and fluid inertia ratio
L, H, h	Foil dimension length, height, thickness (m)
LE,TE	Leading edge and trailing edge
$\overline{p}$	Extracted power (mW)
P_t	Total pressure
P_s	Static pressure
q_c	Dynamic pressure
Re	Reynolds number
St	Strouhal number
U	Flow speed (m/s)
ν	Poisson's ratio
μ	Mass fluid-to-foil ratio
ν	Kinematic viscosity of air at 22˚C
ρ_f	Fluid density of air at 22˚C
ρ_s	Solid density
ρ_m	Polycarbonate material density (Foils tested)

INTRODUCTION

The importance of drag reduction was first identified in the late 1930s, and since then, drag is the aerodynamic design main parameter. Changes in the drag coefficient can be critical for the specified payload that an aircraft or a drone can carry on certain distance, thus affecting the economic performance of aeronautical companies. Environmental concerns, fuel costs and aviation regulations contribute to the aerospace industry’s progress towards more efficient aircraft development. The American “Continuous Lower Energy, Emissions and Noise” CLEEN (FAA, 2001), the Canadian “Low Emission Aviation Program” LEAP (NRC 2022) and the European “Clean Sky Joint Undertaking” CSJU (CSJU, 2014) are governmental programs, that were created to address the efficiency of the aircraft problem and to increase awareness on future environmental challenges and catalyze aeronautical innovation. These initiatives aim to reduce CO2 emissions by 50%, NOx emissions by at least 60% and perceptible noise by 50% by 2050 through the development of new aircraft and engine technologies.

Since 2021, The National Research Council of Canada's (NRC) Low‑Emission Aviation program will contribute to the Canadian aviation sector's decarbonization transition by developing fast, market‑ready, sustainable solutions. These solutions will be found through a collaborative ecosystem that will stimulate the green aviation industry’s transition by use of Green Technologies Aircraft policies and regulations. Therefore the development optimization and integration of low‑carbon technologies will be done safely into aviation applications.

Through the public and private partnership and via a cost-sharing approach, the international aviation industries will accelerate aircraft development and integration with the aim to achieve a net reduction in climate impact (Rutherford *et al.*, 2009). A crucial study by the International Air Transport Association (IATA) estimated that promoting laminar flow on an aircraft’s wing would reduce fuel consumption by 10-15% (IATA, 2009) while a study conducted by NASA estimated a fuel reduction of 25% (Collier, 2008). Boeing studied new concepts to improve laminar flow that could save over 100,000 liters fuel/year (Boeing, 2014). New design technologies, and regulations are being explored to meet these low emissions programs.

In this PhD thesis, two solutions to obtain low induced drag by use of technologies that promote laminar flows. The numerical and experimental analyses of a drag-reduction-device for a FLIR Ground System, and of an adaptive wing prototype for an Unmanned Aerial System UAS-S45 from Hydra Technologies are presented in details, in Chapters 3 and 4, respectively.

It is possible to harvest small amounts of dissipating energy, and use it as available electrical energy. New technologies in "energy harvesting" are attracting high attention from various international organizations, such as the World Health Organization in their 2030 Agenda for Sustainable Development, held in 2015, which main goal is to ensure access to affordable, reliable, sustainable and modern energy for United Nations (UN) countries. To the best of our knowledge, the term “energy harvesting” has been used for photovoltaics cells in the late 1980s. Since the 2000s, various energy harvesting technologies were mentioned. The overall range of energy harvesting technologies targets electromagnetic waves, heat, and vibrations from the ambient environment. Energy harvesting technologies should “Extract” the ambient energy and convert it into renewable electric energy, and “used” it to power small devices.

As mentioned previously, the overall motivation for this PhD thesis is to investigate new technologies to reduce fossil energy consumption. In Chapter 5, the dynamics of inverted-foils is analyzed as an efficient energy harvesting system. This method of renewable energy production requires fluid kinetic energy to be transferred to the foil (as “strain energy”), and then this strain energy to be converted into electrical energy.

CHAPITRE 1

PROBLEM STATEMENT, RESEARCH OBJECTIVES, CONTRIBUTIONS AND THESIS ORGANIZATION

1.1 Problem statement

The first problem statement of this thesis regards drag reduction systems on aircraft structures. The significant increased interest among major aircraft corporations, that include Boeing, Airbus and Embraer in the research and development of new technologies for optimized fuel consumption on long range aircraft and modern unmanned aerial systems (UAS) cannot go unnoticed. An adaptive wing system could offer a technological solution that would allow airliners and UAS manufacturers to obtain the desired efficiencies and performances. The ability to increase the extent of laminar flow over the wing surface for all flight conditions that occur during a typical flight, could lead to significant reductions in drag, and thus in fuel consumption.

In the context of structures subjected to variable flow conditions, a drag reduction system that extends the laminar flow region, would lead to major reductions, and thus improvements in terms of stress loading, vibrations, material fatigue, and overall drag. The research on technologies for drag reduction was performed within the frame of two projects and their corresponding articles. Firstly a project on drag optimization, and consequently on fuel reduction for the UAS-S45 manufactured by the aerospace company Hydra Technologies entitled “New Validation Methodology of an Adaptive Wing for UAS-S45 for Fuel Reduction and Climate Improvement”. Secondly, a project on drag reduction in turbulent flows on a full size and operational Air and Ground Surveillance Radar manufactured by FLIR Systems entitled “New Numerical and Measurements Flow Analyses near Radars”.

The second problem statement in this thesis refers to the current knowledge on inverted-foils dynamics, and to their capabilities for energy production. The oscillations, vibrations and flutter of slender bodies (such as “foils”) in a conventional-foil configuration have been studied in academia during many years; an excellent book written by Professor Païdoussis (Païdoussis, 1980) provides theoretical predictions and experimental observations of the critical flow velocity in terms of foil thickness and length sizes. The first theoretically studies on linear stability of slender bodies were attributed to C. Q. Guo and Michael P. Païdoussis (2000).

Finally, reduction of energy consumption is one of the main goals in modern times. The energy produced by a foil in an inverted-foil configuration from an ambient environmental wind conditions, is many times greater than a conventional-foil configuration in the same wind conditions. A self-induced oscillating inverted-foil can be a new technology to produce renewable electrical energy, from ambient wing conditions, in remote areas; which is the conclusion of the study conducted in the article entitle "Experimental wind-tunnel study of the dynamics of inverted foils for energy harvesting".

1.2 LARCASE infrastructure used for the research

1.2.1 UAS-S45 from Hydra Technologies

The Unmanned Aerial System UAS-S45 is manufactured by Hydra Technologies. The S45 incorporates a monoplane design with twin tail booms. The airframe is made of lightweight materials, such as carbon fiber, S-glass, and Kevlar. The main dimensions of the fuselage are: wingspan equal to 6.11 m; length from the frontal rotor to the rear rotor equal to 1.93 m; and tail span equal to 1.36 m. Its length from the frontal rotor to the tail is equal to 3.094 m, and its wing surface is equal to 2.72 m². It is composed of many new materials, such as aluminum, titanium, and a composite material (carbon fiber, S-glass, and Kevlar). This UAS is very light for its class and can transport large payloads, with the following characteristics: the operating empty weight (OEW) is 55 Kg; the maximum takeoff weight (MTOW) is 69.4 Kg; the maximum landing weight is 66.50 Kg; and its maximum payload, which is its carrying capacity, is 3.89 Kg. The UAS-S45 thrust power is provided by twin-cylinder engines of 80 cc with a fuel capacity of 31 L. What makes it different from the other aerial vehicles is: i) its autonomy of 12h, ii) its maximal operating altitude of 20 000 ft, iii) its operational range of 120 Km, and iv) its cruising speed of 50 knots (25.72 m/s). The S45's main characteristics are indicated in Figure 1.1, which has numbers corresponding to the propulsion system (1–4), the two Pitot tubes (12,13), and the 10 control surfaces (5–11,14–16).

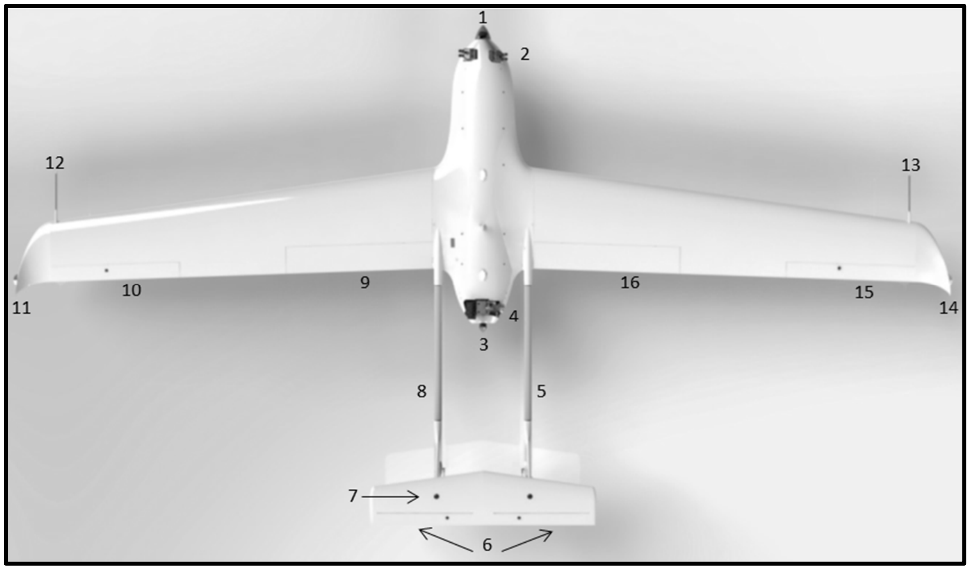

Figure 1. 1 The aerodynamic and propulsion components of the UAS-S45

This state-of-art research equipment was obtained by Professor Ruxandra Botez with funds from the Canada Foundation for Innovation (CFI) and Ministère du Développement Économique, Innovation et Exportation (MDEIE). The UAV-S45 by Hydra Technologies are used in the Canada Research Chair (CRC) in technologies for aircraft modeling and simulation projects. One of the axes of the CRC is to design "New Modeling and Simulation methodologies for aircraft and helicopter flight dynamics and control. Using flight test data, many non-linear optimization algorithms are developed to identify and validate aircraft and helicopters". In this thesis, an adaptive wing was developed for this UAS-S45.

1.2.2 FLIR Ground Surveillance System Radar

The ground surveillance system (radar) was specifically designed to detect and track personnel and vehicles within a 20-km range. It provides a fast 90-degrees coverage by incorporating the next generation track and scan capabilities within an entire area covered twice per second. When deployed on a pan/tilt device, the FLIR radar can provide 360-degrees coverage. The full size radar model tested at the LARCASE wind tunnel has a height of 0.37 m and a length of 0.75 m. The FLIR radar positioned in our Price-Païdoussis Wind Tunnel test section is illustrated in Figure 1.2.

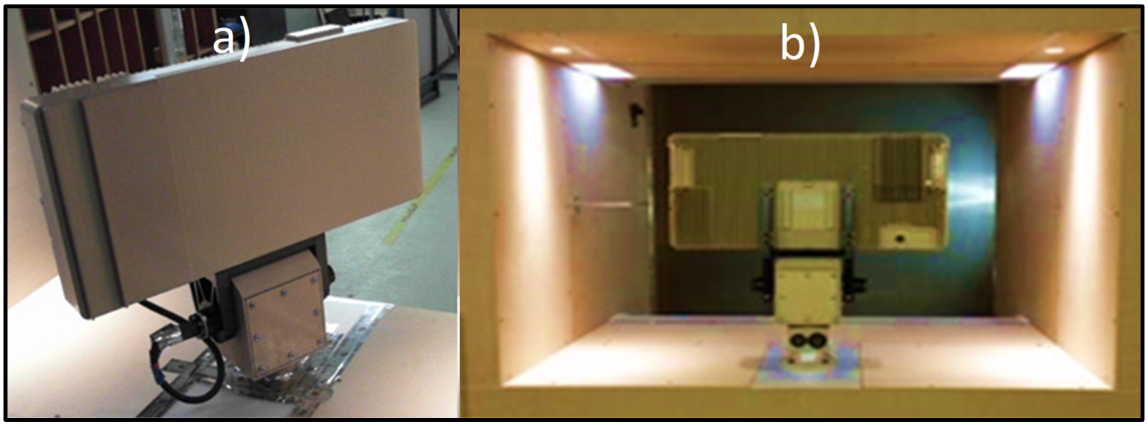

Figure 1. 2 FLIR ground radar a) front and b) rear images of the full-size radar

1.2.3 Inverted-foil Scale

For the study and analysis of foils in their inverted-foil configuration, a novel design was developed in-house of an aerodynamic scale for measuring forces and moments, along the three axes oriented parallel and perpendicular to the foil's surface and parallel to the foil's height. The components of this aerodynamic scale are illustrated in Figure 1.3. The novel clamping screw mechanism uses 27 flat-head screws and two symmetrical NACA 0012 airfoils to support the inverted foil at its trailing edge. The chord length of the airfoil was 100 mm and the spanwise length 610 mm. Metal and plastic foils were tested in the wind tunnel.

Brass foils were found to give asymmetric oscillations and undergo permanent deformation. Zinc foils were found to have a high material damping and could not flap at all. Stainless steel and Propylene foils had other problems while Polycarbonate foils were found to behave much better, and they were selected for manufacturing and experimental validation. Table 1.1 shows the properties and dimensions of the foils analyzed and experimentally tested for this research.

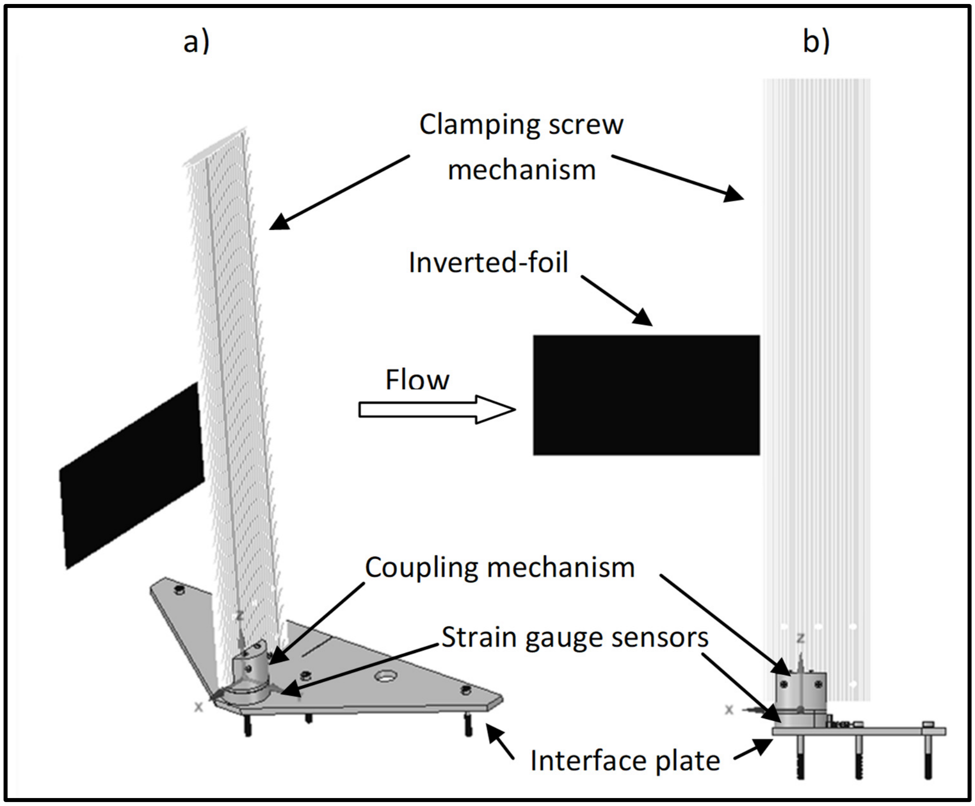

Figure 1. 3 Inverted foil aerodynamic scale: (a) side view; (b) right view

Table 1. 1 Properties of the foils tested in the Price-Païdoussis wind tunnel.

Foil properties	
Material	Polycarbonate
Young’s Modulus E	2.38 GPa
Poisson ratio v	0.38

Foil density ρ_m	1200 Kg m^{-3}
Foil aspect ratio (Length x Height x Thickness)	AR=0.50 (150 x 75 x 1.02) 10^{-3} m
Foil aspect ratio (Length x Height x Thickness)	AR=0.75 (150 x 112.5 x 1.02) 10^{-3} m
Foil aspect ratio (Length x Height x Thickness)	AR=1 (150 x 150 x 1.02) 10^{-3} m
Foil aspect ratio (Length x Height x Thickness)	AR=2 (150 x 300 x 1.02) 10^{-3} m
Foil properties (continued)	
Foil aspect ratio (Length x Height x Thickness)	AR=3 (150 x 450 x 1.02) 10^{-3} m
Foil aspect ratio (Length x Height x Thickness)	AR=4 (150 x 600 x 1.02) 10^{-3} m
Air density ρ_{air}	1.225 Kg m^{-3}
Mass ratio μ (ρ_{air} Length) / (ρ_m Thickness)	$\mu = 0.15$ 1.225 x 150 / (1200 x 1.02)

1.3 Research Objectives

The purpose of this thesis is to numerically and experimentally investigate streamlined, blunt, and oscillating (flapping) bodies, and to develop: i) New methodologies for drag reduction coefficients of blunt and streamlined bodies; and ii) Analysis of flexible foils for energy harvesting purposes, with the aim to broaden our understanding of the dynamical behavior of self-induced periodic oscillations of foils subjected to an axial flow.

These objectives refer to the understanding and achievement of drag reduction systems for streamlined (UAS-S45 wing) bodies and blunt (FLIR Ground Surveillance System) by:

1. Designing, fabricating and experimentally testing an adaptive wing prototype for the S45, while taking into account the shape optimization of its controlled surfaces.
2. Developing a novel validation methodology for high resolution three-dimensional CFD models for the UAS-S45 adaptive wing with wind tunnel data, using Area Metric and Adjusted R^2 metrics.

3. Designing a new methodology for numerical and experimental analyses of blunt radars bodies in turbulent flows with quantitative metrics to measure flow analysis improvements and drag reduction.
4. Analyzing a drag reduction system for blunt radar bodies in turbulent flows.
5. Developing a novel validation methodology for high resolution three-dimensional CFD models for blunt radars bodies with wind tunnel data, using Area Metric and Adjusted R^2 metrics.

Other objectives refer to the analysis of inverted-foils dynamics for energy production by:
6. Investigating the effects of foil length and height (aspect ratio), flapping frequency, flapping regime, Strouhal number, Reynolds number and its peak-to-peak amplitude.
7. Designing a new type of aerodynamic scale for experimental measurements of the forces acting on inverted foils for a better understanding of inverted-foil dynamics for energy harvesting purposes and power generation.

It is important to mention that all theoretical and numerical analyses were experimentally validated using the Price-Païdoussis Wind Tunnel.

1.4 Contributions and Originality

The originality of this PhD thesis is based on three major contributions, which are: a novel method for model validation, an adaptive wing aero-structural shape optimization, and an experimental analysis of the dynamics of inverted-foils for energy harvesting. These contributions can be referred in the following ways:
(1) Design of a novel method for the analysis and validation of three-dimensions CFD model, using uncertainty analysis and a new metric for engineering applications “Area Metric”. This method was useful for validation of the FLIR Ground Surveillance System and UVS-S45 numerical models.

(2) The design, aero-structural shape optimization and in-house manufacturing of an adaptive wing prototype for UAS-S45, that can reduce drag production, thus fuel consumption and climate change impact.

(3) Developing a new method to experimentally investigate the effects of aspect ratio, mass, amplitude and frequency on the dynamics of inverted-foils in a cantilevered configuration. Inverted-foils subjected to a steady uniform flow are recently studied since 2016.

(4) Design and in-house manufacturing of a new aerodynamic scale system for flexible foils, which allow to measure, in real time, forces and moments, without interfering with the fluid flow.

(5) It was shown that flexible foils, in an inverted configuration, produce sufficient flapping forces to harvest energy from the ambient moving airflow, which can be converted in renewable electrical energy.

1.5 Organization of the thesis

This thesis consists of six chapters, including the introduction and literature review of the research, as described in Chapter 1 and Chapter 2 respectively.

1.5.1 First journal paper

In Chapter 3, an experimental and numerical investigation of the flow near a blunt radar body has been conducted. The main goal of this research was the development of a new methodology to analyze flows, and to measure their flow characteristics. A series of experiments were performed on the blunt body (ground surveillance radar) in a subsonic wind tunnel. Forces and moments were measured as functions of wind speeds and angular positions by use of an aerodynamic scale, designed and built in-house. A Computational Fluid Dynamics three-dimensional model was employed to analyze the wake region of the ground surveillance radar. A turbulence reduction system was proposed and analyzed.

1.5.2 Second journal paper

In Chapter 4, a new methodology is presented for the design, aerodynamic optimization, and model validation of an adaptive wing prototype. The optimization framework is applied for the design, finite element analysis, and numerical model validation. A computational fluid dynamics (CFD) model of the adaptive wing and its surrounding flow was developed and its results were validated with experimental data, and expressed in terms of lift, drag, and lift-to-drag ratio. A new genetic algorithm strategy was chosen to find the optimized airfoil shapes for the UAS-S45 adaptive wing prototype's upper surface. The reliability of the proposed methodology was investigated through the design, manufacture, and testing of a wing prototype proposed for the S45. The simulated and experimental results have shown a low drag production and a high lift-to-drag ratio of the adaptive wing prototype that further conducted to a reduction in fuel consumption and an increase in cruising flight range.

1.5.3 Third journal paper

In Chapter 5, a novel methodology is used to analyse the oscillations of foils of a wide range of aspect ratios, $0.5 \leq AR \leq 4$, and Reynolds numbers, $10^4 \leq Re \leq 10^5$, for energy harvesting purposes. These foils were fixed at their trailing edge, and their dynamical behavior was captured as the wind speed was varied. The foil response was then analyzed as a function of velocity, Reynolds number, oscillation amplitude and frequency. Additionally, the forces and moments acting on the foils were measured by utilizing an aerodynamic scale, designed and built in-house. An empirical power generation equation was derived to determine the foil characteristics for maximum energy harvesting production.

The Section Discussion and Conclusions discuss the findings of this thesis, the Section Recommendations outlines suggestions for future research and Annex A and B elaborate on the subjects of Vortex Shedding Interference and Inverted-foil research preparation respectively.

CHAPITRE 2

LITERATURE REVIEW

The literature review presented in Chapter 2 is encompassing the studies on blunt, streamlined and oscillating bodies subjected to a fluid flow. This review is presented as follows: Review on adaptive wings studies for drag reduction in Section 2.1; Investigation of foils subjected to flow for energy harvesting in Section 2.2; Validation process of numerical models in Section 2.3; and subsonic wind tunnels review in Section 2.4.

2.1 Adaptive Wing Studies

Engineers and researchers have started to integrate various disciplines in the aircraft design process. The strong coupling between aerodynamics and structures has motivated aircraft designers to apply new optimization methodologies to aero-structural challenges to reduce fuel consumption and maximize flight time. Previous research has focused on minimizing the total drag and maximizing the aircraft range without simultaneously optimizing the wing shape. In order to improve aircraft aerodynamic efficiency, researchers have investigated wing configurations, for which aero-structural optimization was performed to find their optimal shapes (Suzuki *et al*, 1993). Aircraft manufacturers commonly use various analysis techniques to predict aerodynamic loads, which are of major importance for wing design. Recent environmental concerns motivate researchers to reduce fuel consumption through morphing and adaptive wing systems. The application of optimization methodologies present many challenges, as it involves a large number of parameters and constraints to be considered. These parameters and constraints are related to different disciplines, including Structure, Aerodynamics, Stability, Control, and Propulsion.

A large amount of references on morphing and adaptive wing structures are described in literature and their word is mostly based on materials and morphing mechanisms. Some of these references classified morphing wings based on their geometrical changes or actuation concepts, while other references focused on new technologies and applications. The references documented in this section show the progress on morphing and adaptive wings made so far. The main morphing and adaptive wing concepts described in literature are summarized by their dates of tests, since 2003, in Table 2.1.

Table 2. 1 Main morphing and adaptive wing concepts described in literature since 2003

Project name	**Wing concept**	**Tests performed**	**Year of test**	**References**
SMA reconfigurable airfoil	Variable camber	Wind tunnel	2003	Strelec J.K., Lagoudas D.C. *et al.* 2003.
Virginia Polytechnic Institute Telescoping wing	Variable span	Flight and wind tunnel	2004	Mason W., Robertshaw H., *et al.* 2004.
Morphing inflatable wing	Variable camber, twist	Flight and wind tunnel	2005	Simpson A., Coulombe N., *et al.* 2005.
Lockheed Martin Z wing	Folding wing	Wind tunnel	2006	Min Z., Kien V.K., *et al.* 2010.
NextGen aeronautics bat wing	Variable sweep	Wind tunnel	2006	Bowman J., Sanders B., *et al.* 2007.
CRIAQ 7.1 Adaptive wing with SMA torsion actuators –ÉTS, Montreal Polytechnique, Bombardier Aerospace, Thales Canada, IAR-NRC	Variable camber	Wind tunnel	2009	Popov A.V., *et al.* 2010. Popov A.V., *et al.* 2008 Grigorie L.T., *et al.* 2012 Grigorie L.T., *et al.* 2012
Multi segmented folding wing	Folding wing	Wind tunnel	2012	Wang I., Gibbs S.C., *et al.* 2012.
Compliant adaptive leading edge	Variable camber	Wind tunnel	2014	Tong X., Ge W., *et al.* 2014.
Variable span morphing wing	Variable span	Wind tunnel	2015	Woods B.K., Friswell M.I. 2015.
Spanwise trailing edge	Variable camber	Wind tunnel	2015	Pankonien A.M., Inman D.J. 2015.
CRIAQ MDO505 ÉTS, Montreal Polytechnique and Italian partners Alenia, CIRA and University of Naples – Frederico II	Variable wing camber, morphing aileron	Wind tunnel	2015	Koreanschi A., Gabor O.S., *et al.* 2017. Kammegne M.J., Botez M.R., *et al.* 2016. Gabor O.S., *et al.* 2016. Koreanschi A., *et al.* 2016.
Biohybrid morphing wing with finger-like motion	Twist,camber variation	Flight	2019	Chang E., Matloff L.Y. *et al.* 2020.
Morphing wing airborne wind energy (AWE) project - ETH Zurich	Variable camber	Wind tunnel	2019	Fasel U., Keidel D., *et al.* 2019.
Fuel reduction adaptive wing for UAS-S45 project – ÉTS	Variable camber with adaptive LE	Wind tunnel	2022	Salinas M.F., Botez R.M., Gauthier G. 2023.

The following review section is intended to present morphing and adaptive wing concepts based on the variation and change at the airfoil and wing-structure-levels. Structural and aerodynamics airfoil shape modifications can be obtained by camber (Section 2.1.1), thickness (Section 2.1.2), and length (Section 2.1.3) variations.

2.1.1 Wing Camber Variation

An adaptive camber can improve aerial vehicle aerodynamics properties. The variation of the camber shape can be performed locally or globally, on the wing structure. This type of wing variation can have adaptive surfaces that produces high-lift configuration, and when combine with other control surfaces, such as slats and flaps; the wing can generate maximum lift coefficients. A variable camber wing is intended to promote laminar flow, thus reduce drag on the wings surface. Additionally, an adaptive leading-edge coupled in an adaptive wing with a variable camber can increase lift coefficients in various flight conditions significantly. Pecora *et al.* in 2021 studied the design phase, as well as the experimental testing and fabrication of a smart-leading-edge device of one of the major aircraft manufacturer Airbus. The Airbus project focused on the structural challenge, design and manufacturing of high-lift mechanical systems. First, a new wing concept was designed manufactured and experimentally tested in two-dimensional flow. The experimental observations indicated high degrees of stiffness of the smart-leading-edge morphing wing structure, to support aerodynamic loads and the desired morphing shapes. Subsequently, a full-size wing prototype was tested in a larger wind tunnel test section for three-dimension flow conditions; the wing performed as predicted by the numerical model, at various flow conditions. The good agreement of the experimental results and simulations indicated a feasible design method. In the next phase of the project, it will include the integration of electro-thermal ice protection inside the leading edge structure.

A variable camber wing with an adaptive leading-edge can produce chord-wise and span-wise variations, with a simple actuation mechanism inside the wing structure. Aerodynamic and structural optimization techniques on adaptive wings should always try to be complementary to the control-surfaces, flaps and ailerons functions. An innovative variation of a classical variable camber concept is the “fingers-like” designs presented by multiples organizations. The German aerospace research center (DLR) and Airbus demonstrated the feasibility of this newly designs. DLR with the “fingers” design and Airbus with the “belt-rib” design, are structurally, a series of ribs-structures segments, with a two-degree of motion allowing changing on the whole wing-box structure. One main challenge with adaptive and morphing wing concepts, it is the skin material degrees of freedom. The skin of morphing and adaptive wings must be flexible in the morphing direction but stiff in other directions to withstand the aerodynamic loads and maintain the airfoil shape. Covering the finger-like structure, the skin has to adapt onto the flexible ribs and deforms without creating undesired multi-axis shape changes and wrinkling. Elastomeric skins with biaxial strain rates and pre-stretch ratios, and precise stiffness properties with accurate stress relaxations factor is used for morphing wing skin needing two morphing degrees of freedom to withstand and maintain the airfoil shapes. The actuation system for multi-segments systems can be simple but repetitive, as a single servo-motor per segment is necessary, and multiples servo-motors need to be connected to a multi-channel controller card, to actuate the segments in parallels without any time-lag in between the segments, which will produce unwanted wing shapes. Another solution is to use transmission belts to cluster the rib-segments and reduce the number of the actuators or servo-motors significantly (Safla *et al.*, 2010).

2.1.2 Wing Thicknesses Variation

Another type of variation of the wing-box structure it’s the “thicknesses variation” which may produce the drag-coefficient to be reduced. This wing variation has also an impact in pushing-back or retarding the laminar-to-turbulent transition to the trailing-edge of the wing surface and increasing the laminar flow. The shape of the wing-box surface is changed by using an actuation system composed of brushless motors (certified and suitable for hazardous environment.) inside the wing. The motor coupled with rods or shafts rotates producing a change in the thicknesses of the wing. The position of the rods or shafts can vary between 20-60 percent of the chord length, and their final positions are found by analysis their optimized control position. Additionally, Smart Material Alloys (SMA) can be used for their shape memory effect capable of sustaining when subject to a temperature or magnetic field gradient. The SMA can be used as an actuation system, by changing its length, as long as the thermal or magnetic stimulus is active. It was observed that a SMA open-loop control methods exhibited higher accuracy on the airfoil shapes and was more accurate in terms of aerodynamic results. Numerical studies and wind tunnel tests of a SMA morphing wing project CRIAQ 7.1 aiming to delay laminar-to-turbulence transition was presented by Coutu et al., 2010 and Grigory et al., 2011a.

2.1.3 Wing Length Variation

Wing length variation, span-wise, can change drastically an aerial vehicle operational objectives and light efficiency. Shorten wings aircraft can go fast with a higher maneuverability, but lack aerodynamic and fuel efficiency. A longer wing length can be very fuel efficient, but operates low cruising speeds. The design and development of wings with length-variation capabilities aim to change the wing's aspect ratio while able to support the changing structural wing loads. A variable span-wise wing has advantages over other adaptive or morphing wings configuration. The wing only needs variable spars, span-wise, that can be actuated while supporting the excess loads. This concept wing has been designed particularly for UAS types of aircrafts;

A telescoping wing, based on the BAE Systems HERTI (High Endurance Rapid Technology Insertion) unmanned aerial vehicle developed by the British company BAE Systems. This morphing wing can continuously change the wing span by having an inner wing that slides in and out of the outer wing. The structural solution adapted to achieve the variable span capability consists of a hollow outer wing structure and reinforced ribs structures, allowing the movable inner wing segments to slide span-wise. Parameters location and dimensions such as rib and stringer spacing and skin thicknesses have to be carefully calculated. In-flight tests showed that the morphing system could double its span length, while maintaining a constant chord, with a minimum of out-of-plane deflection. Elelwi M., Schiavoni F. *et al.*, (2021), Elelwi M., Calvet T. *et al.*,(2021), Elelwi M., Kuitche M.A. *et al.*, (2020) presented numerical results of the "Topology Optimisation of the Morphing Variable Span" project showing that a variable-span wing can improve various flight missions up to 46.89% compared to the original wing and its structure can be optimized for weight-saving purposes, and reduce, up to 15.3% from the original wings weight. Experimental results for in-flight tests showed a 5% reduction in drag and a 17% increase in flight range (Ajaj, Friswell *et al.* 2014).

Twisting the wing and inducing an optimum angle can increased the lift-coefficient, improve control of the wings and enhance overall flight performance. This type of wing shape change may be seen as the oldest form of morphing. It began in 1899, with The Wright brothers and an authority on aviation Octave Chanute that will employed the wing-twist technique on a flexible wing, which would provide roll control for their first airplane. From their bicycle shop in 1896, to their long distance and controlled flight, the Wright brothers understood that for solving complex problems, they need critical thinking and innovative solutions. Until 1899, all flight machines could only go straight at a fixed altitude. The first known morphing wing by twisting or as they called it "wing warping", by a series of pulley systems, could make the biplane climb, dive and make the plane swing left to right, by changing the bank angle. Major lift distribution along the span of the wing will improve flight performance, however higher speeds will produce stresses, loads and elastic instabilities (flutter) that only modern materials, with high stiffness and strength properties, can handle Safla et *al.*, (2010).

2.1.4 CRIAQ and MDO505 Research Projects

Since the early 2006, morphing wings were studied at our Laboratory of Applied Research in Active Controls, Avionics and AeroServoElasticity (LARCASE) at the ÉTS. The two major projects funded by the Consortium of Research and Innovation in Aerospace in Quebec (CRIAQ) were successfully completed, achieving the specified objectives for each project. The two projects, CRIAQ 7.1 and CRIAQ MDO 505, were carried out in collaboration with Bombardier, Thales, NRC-IAR and École Polytechnique in Canada (Popov *et al.*, 2008, 2010, Grigorie *et al.*, 2012, 2015, Gabor *et al.*, 2016, Koreanschi *et al.*, 2016, Botez *et al.*, 2021). The first project, took place between 2006 and 2009, named CRIAQ 7.1 for Consortium of Research and Innovation in Aerospace in Quebec, was carried out with the cooperation of universities, industrial partners and research institutes, to design, manufacture a morphing prototype wing and experimental testing at National research center of Canada (NRC-IAR), and finally publish the research results in high impact Journal. This project had to study and analyze Smart Material Actuators (SMA), as an actuation system for morphing wings. The main objective of the project was to improve and control the laminarity of the flow over a morphing wing, in order to obtain high drag reductions. The resulting deformation made it possible to delay the flow transition on the wing. An ideal rectangular wing was used, and therefore no existing structural constraints for a real wing were considered. This concept was experimentally validated in the NRC-IAR subsonic 2 m by 3 m wind tunnel.

The CRIAQ MDO 505 project took place between 2012 and 2015; the project main objective was to design, optimized airfoil shapes, test and validate a Bombardier Regional wing structure with a rigid aileron and with an adaptive aileron, which was able to delay the flow transition at the upper surface of the wing. The CRIAQ MDO-505 morphing wing was equipped with four actuators (designed and manufactured in-house) able to change the composite-material skin shape. The morphing wing and the morphing aileron were able to reproduce the optimized shapes and reduced drag production (Tchatchueng Kammegne, *et al.*, 2016, Sugar Gabor *et al.*, 2016 and Koreanschi *et al.*, 2016).

The studies published on adaptive wing technologies were not investigated in an experimental setup fuel reduction by means wing shape variations. Experimental tests were performed in the Price-Païdoussis wind tunnel for various flight conditions. The research performed on adaptive wing for the S45 has been published in the following paper:

1. Salinas M.F., Botez R.M., Gauthier G. (2023). New Validation Methodology of an Adaptive Wing for UAV S45 for Fuel Reduction and Climate Improvement. Applied Sciences.13(3): 1799.

All the work done in the above mentioned article, including performing calculations and analysis, conducting experiments, and writing, was done by myself, under the guidance of my supervisors, Professors Ruxandra Botez and Guy Gauthier.

2.2 Foil Subjected to a Fluid Flow

In generic terms, the challenges of inverted-foils fall into the broad field of Fluid-Structure Interactions (FSI). FSI describes diverse situations where solid structures are in contact with fluid flow, with often intriguing and interesting behavior occurring as a result of these interactions. Some cases can have complex interactions, such as self-excited oscillations (flutter) on an aircraft's wing; free vibrations of pipes-conveying-fluid (pumps or vacuums machines interaction with a fluids, such as water or air); loads and temperature variations on pressure-driven systems (rocket, space shuttle or jet engines) or high-tension cables covered on ice oscillating at specific flow velocities (Shelley & Zhang 2001, Païdoussis, 2016).The dynamics of the inverted-foil problem is often too difficult to be fully described using interpretation on kinetic energy and mass with Newton and Hamilton equations of motion. A multi-disciplinary investigation involving empiricism, experience, numerical simulation, experiments and analogy to simpler problems is often necessary. There exist many cases for which a general theory for foils can be established under a set of reasonable assumptions, and from which analytical or semi-analytical conclusions can be derived. Slender structures subjected to axial flow may be studied using these general theories.

Slender structures can be defined as pipes, cylinders, plates, foils and shells. Slender body dynamics is a vast topic in science and has been of continuous interest to researchers. These studies may be classified into three types of configuration, based on the fixation of the foil. We have limited the type of FSI system considered in this literature review, as follows: Firstly, the slender body was considered to be thin, flexible, easily bent, and of finite length. Secondly, vibrations, oscillations and flutter of the body can be expected at subsonic flow velocities. Thirdly, the slender body was only clamped (fixed) at one edge; all other edges were free to move in the flow. Lastly, the incoming air flow was assumed to be steady, uniform and laminar, and it passed over all surfaces of the slender body. Review of the three types of configurations of foil interacting with airflow was mentioned by Kim *et al.*, 2013.

2.2.1 Cantilevered Configuration

The first configuration is considered when there is a single clamped side, and the rest of the slender body is parallel to the flow, also known as a cantilevered configuration. A cantilever configuration is a rigid structural element that extends horizontally and is supported at one end. One of the most studied cases of a cantilevered configuration is that of a fixed wing aircraft and the aerodynamic forces acting on its structure. The wing is attached to the fuselage at its root, while the rest of the wing is free to interact with the incoming flow. This configuration can produce bending, twisting and vibrations on the wings that can lead to structural failures. When a critical high flow velocity occurs, the wing structural dynamics becomes unstable, with increasing vibrations and self-oscillations; this type of aero-elastic oscillation instability is referred to as “flutter instability” in the scientific literature. Some very large structures exposed to changing flow conditions, such as bridges, buildings, and exterior equipment, can behave as “blunt-bodies”, thus accelerating the turbulent flow transition on their surfaces, which can provoke early boundary layer separation and produce vortex shedding and turbulence flows (Sader *et al.* 2016).

2.2.2 Conventional-foil Configuration

The second configuration, referred as “conventional-foil”, defines a foil fixed by its leading edge by means of a “fixation” or “support” clamped to it, with the other side (trailing edge) is free to move within the incoming flow (Figure 2.1). An everyday example of this phenomenon is the flags waving motion, produced by the wind breeze. Historically, the term ”foil” is frequently used to refer to a structure with perfect flexibility; when the bending stiffness of the material is considered for a study, then "plate" is the correct terminology. We will use the term “foil” in the rest of this thesis to describe the flexible body structures tested in this research. A foil, in a conventional-foil configuration, can be positioned in three ways: vertical, horizontal or "hanging" configuration, with reference to the incoming flow *U*. The geometrical characteristics of a rectangular foil are the length *L*, width *H* and thickness *h* as shown in Figure 2.1. The other physical parameters of the foil are: the material density, Young's modulus, Poisson ratio and bending stiffness. In a "hanging" configuration, gravity plays an important role in the foil dynamics; while in the “vertical” and “horizontal” configurations, the effects of gravity are neglected (Guo & Païdoussis, 2000).

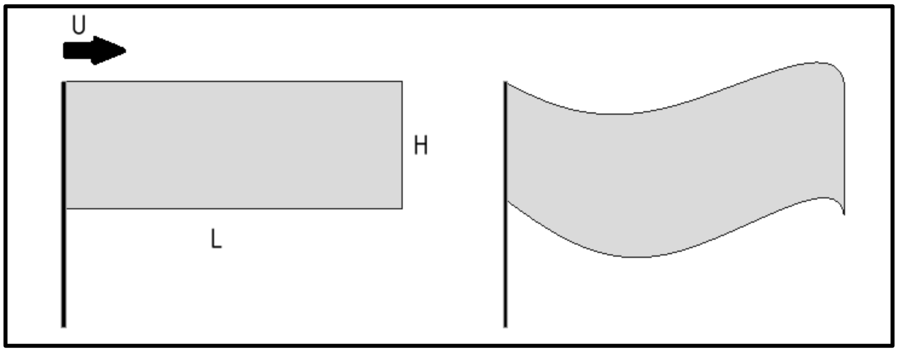

Figure 2. 1 Conventional-foil configuration of a flexible foil in an axial flow *U* at (a) Original position and (b) Deformed position

One important observation on foil flutter was the correlation between system stability and the evolution of its wake vortices. It has been observed that flutter occurred in an abrupt manner for foils fixed at their leading edges. Once the flow velocity has reached a critical point, vibrations occurred at the surfaces of the foils, followed by large amplitude deflections. When the foil was already oscillating and the flow velocity was gradually reduced, the foil has returned to rest at another, usually higher flow velocity. This hysteresis phenomenon was part of the foil dynamics and no existing theory or model was able of predicting it. A particular aspect of slender body dynamics models is the assumption of a two-dimensional flow behavior that neglects edge-effects, vortices' shedding and other effects of three-dimensional flows that have not been sufficiently understood.

The flutter of a flexible plate immersed in an axial flow is an example of flow-induced vibrations. This instability can be experienced in everyday life when one observes a foil flapping in the wind. Because this phenomenon appears in many applications (paper manufacturing industry, airfoil flutter, human snoring), a literature review was performed (Huang, 1995, Sane, 2003). This instability can be regarded as an interaction between fluid forces and elasticity and the system can be studied by restricting the analysis to one-dimensional flutter modes.

2.2.3 Inverted-foil Configuration

The third type of configuration for a slender body interacting with fluid is referred to as the "inverted-foil", which is the focus of this thesis. The physical parameters of an "inverted-foil" subjected to a moving fluid are represented in Figure 2.2, where a foil is clamped at the trailing edge (TE), while its leading edge (LE) is free to move in the y axis. The 2D representation shows the length *L* and height *H* of the foil, as well as its only degree of freedom, in the *y* axis, allowed in this research.

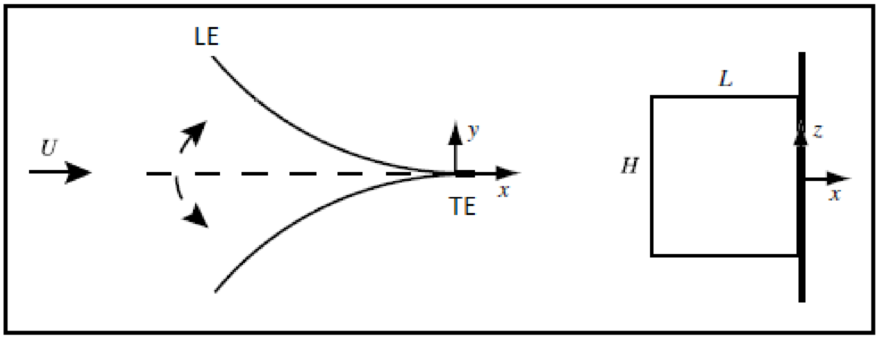

Figure 2. 2 Physical parameters of an inverted-foil configuration

For a comprehensive review of the subject, the reader is referred to the book “Fluid-Structure Interactions: Slender structures and axial flow” written by Michael P. Païdoussis (2016). The following section reviews in details the literature on “inverted-foil” configuration.

2.2.4 Inverted-foil Configuration Studies

The first studies of Guo and Païdoussis (2000), they have worked on rectangular plates and foils dynamics with various flow regimes and boundary conditions (clamped and free leading-edge), in inviscid, incompressible two-dimensional (2D) flow. They found that free foils and inverted-foils oscillate at a critical flow velocity which is inversely proportional to the fluid-to-foil mass ratio defined as $\mu = \rho_{\text{fluid}}/\rho_{\text{foil}}$ proposed by Kim *et al.* (2013), Sader *et al.* (2016b), Gurugubelli & Jaiman (2015), and Goza *et al.* (2018). Kim *et al.* (2013) explored the dynamics of inverted foils in an open-loop wind tunnel at high Reynolds numbers $\text{Re} = UL/\nu_f \approx 10^4 - 10^5$, where ν_f is the kinematic viscosity of the fluid. Theses researches observed three consecutive modes: i) stretched-straight mode, ii) the flapping mode and iii) the fully deflected mode, as the flow velocity in the test-section was increased. In comparison to a conventional-foil configuration, which undergoes flapping beyond a critical flow velocity, the inverted-foil performs flapping only within a finite range of flow velocities, somewhat similarly to Vortex Induced Vibration (VIV) of a spring-supported cylinder in cross-flow. It was also found that the inverted foil displays “flapping” amplitude (peak-to-peak) up to 80% of the foils length, which is larger than conventional-foil amplitude.

Goza et *al.* (2018) showed that large-amplitude flapping arises even for low Re < 50, but the mechanism of instability is not a vortex induced vibration. Gurgubelli and Jaiman (2019) have found that the aspect ratio of the foil (0.25 ≤ AR ≤ 2) has a minor impact on the large-amplitude flapping. Finally, they attributed the periodic flapping motion to an interaction between the unsteady shedding of leading-edge vortices and the structural dynamics of the flexible foil; the trailing-edge vortices were found to have an marginal impact on the flapping. Sader et *al.* (2016a) combined the results of numerical models experimental measurement to understand inverted-foils flapping. They concluded that the large-amplitude flapping motion of an inverted-foil is a vortex induced vibration, in contrast to the flapping of a conventional-foil, which is a self-excited oscillation. For Sader, flapping occurred for i) Strouhal numbers (St) values in the range of 0.1 and 0.2, which are independent of the Reynolds number, and ii) above a minimum amplitude oscillation, accompanied by flow separation and periodic vortex shedding. The Strouhal number was calculated by measuring the foils peak-to-peak amplitude, as observed in experiments.

In a 2016 study by Sader *et al*., it was found that two key parameters of the dynamics of inverted-foil are the foil's length L and height H. For foils, with L at least 10 times the dimension of H, they found that foils do not flap, but they go from straight mode (a) to fully-deflected mode (f), as shown in Figure 2.3. Tavallaeinejad & Païdoussis, 2020, 2021 have identified additional dynamical regimes as functions of flow velocity and foils aspect ratio. For sufficiently large aspect ratio, as shown in Figure 2.3, the foil undergoes (a) straight, (b) buckled, (c) small-amplitude asymmetric flapping, (d) large-amplitude flapping, (e) aperiodic or chaotic flapping, and (f) fully deflected regimes.

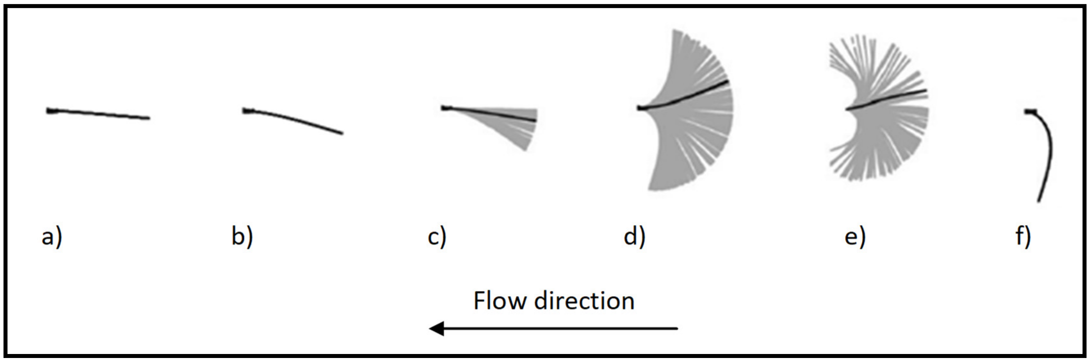

Figure 2. 3 Experimental measurement of a foil clamped at the trailing edge (inverted foil configuration) in axial flow. The direction of the flow is from right to left, as shown by the arrow. The foil is in black color and its recorded path is in gray color. The foil dynamics shows the followings modes: (a) straight, (b) buckled, (c) small-amplitude asymmetric flapping, (d) large-amplitude flapping, (e) aperiodic or chaotic flapping and (f) fully deflected state. Data collected and image produced in Matlab software version (R2016a)

In recent studies by Tavallaeinejad and Païdoussis *et al.* (2020, 2021, 2022), it was found that an inverted-foil configuration exhibits a “stable no-deflection” equilibrium at low flow speeds. As the flow speed gradually increases, this equilibrium regime conducts leading edge LE (tip of the foil) vibrations, and, if the speed is increased further, it provokes large-amplitude oscillations comparable in size to the foil's length. As the flow speed is increased even further, the oscillations cease abruptly, resulting in a stable deflected equilibrium of the foil, as shown in Figure 2.3.

For this thesis, experiments with cantilevered flexible plates in reverse axial flow were conducted in the Price-Païdoussis subsonic wind tunnel at ÉTS to understand the effects of different system parameters on the stability and dynamics of inverted-foils. The experimental observations were compared with simulation models. Four research studies co-authored on inverted-foils dynamics, two conferences (1,2) and two journal papers (3,4) has been published in peer review journals, as follows:

1. Tavallaeinejad, M., M. F. Salinas, A. R. Abdelbaki, M. Legrand, R. M. Botez, M. P. Paidoussis. (2019). "An experimental investigation of the dynamics of an inverted flap with a rigid splitter plate." IUTAM Symposium on Fluid-Structure Interaction.

2. Tavallaeinejad, M., M. P. Paidoussis, M. F. Salinas, M. Legrand, M. Khein, R. M. Botez. (2020). "Why inverted foils flap: An experimental study." Second International Symposium on Flutter and its Application (ISFA2020).
3. Tavallaeinejad, M., Païdoussis, M P., Flores Salinas, M., Legrand, M., Kheiri, M., Botez, R. (2020). Flapping of heavy inverted foils: A fluid-elastic instability. *Journal of Fluid Mechanics*, 904, p.R5.
4. Tavallaeinejad, M., Salinas, M.F., Païdoussis, M.P., Legrand, M. Kheiri, M., Botez, R.M. (2021). Dynamics of inverted foils: Experiments and comparison with theory. *Journal of Fluids and Structures*.Vol.101, 103199.

These articles include an experimental investigation to understand the fascinating behavior of inverted-foils dynamics. In this thesis, the experimental investigations on inverted-foils were validated by expanding the understanding of their flapping motions, and their potential for energy production.
ANNEX A (p.181) presents supplementary observation on the influence of vortex shedding on foils flapping.

2.2.5 Energy Harvesting Studies

Studies on foils with a fixed trailing edge and a free leading edge, referred to as an inverted foil were proposed in the previous section 2.2.1. Experimental observations on inverted-foil, both in wind and water tunnels have shown foils amplitudes approximately twice than those of conventional-foil configurations. The energy harvesting was highly improved by the use of inverted-foils and ambient wind as a source of energy production. The strain energy generated by an inverted foil is at least twice higher than that achieved for a conventional-foil (Gurugubelli and Jaiman, 2015). Shoele and Mittal (2016) did an important observation on electrical-power-coefficient for the inverted-foil manufactured with piezoelectric materials, which can produce energy many times higher than for the corresponding conventional-foil. Renewable energy production that can function for extended periods of time and reduce the need of batteries is of major concern in the modern world. The concept of power harnessing works towards developing self-powered devices that can capture strain energy from oscillating foils and convert it into electrical energy (Orrego *et al.* 2017, Cossé 2014). A flexible foil submerged in a fluid flow can experience a self-induced periodical oscillation at various flow velocities. The foils oscillation is of interest not only due to its occurrence in nature, but also because of the fact that the fluid–structures interactions can generate high quantities of clean renewable energy even using relatively small-sized foils (Fan *et al*. 2019, Yu et *al.*, 2019).

Renewable power generation technologies are providing new power sources, as mentioned by Jacobson (2009), Zhu (2011) and Liu *et al*. (2016). They also stated that flow-induced oscillations for energy harvesting are the new state-of-the-art technology for generating renewable electrical power for small-scaled applications. For Dunnmon *et al.* (2011), harvesting energy with inverted-foils could give free electrical power to wireless sensor which likely requires maintenance-free operations for decades due to access costs. In recent observations, variations of the wind flow speeds will influence the flapping performance of specific inverted-foil sizes, and consequently the power output. Therefore, in future research, it is necessary to study the use of an array of inverted-foils, with various AR sizes, and their effects on the energy harvesting performance.

As stated earlier, the overall motivation of this PhD research thesis is to investigate the dynamics of inverted-foils as an efficient energy harvesting solution. The flow-induced flapping of flexible foils is proposed as a new approach for harvesting energy. This method of renewable energy production requires fluid kinetic energy to be transferred to the foil (strain energy), and then the strain energy is converted into energy. The energy generated by an oscillating foil can be determined using the empirical equation $\overline{P} = A\, St^3$ described by Micheson *et al*. (2008), which shows that the power $\overline{P}$ is proportional to the amplitude A and the cube of the Strouhal number *St*.

Experimental tests were performed in the Price-Païdoussis wind tunnel with multiples foils sizes. The methodologies and results of the research performed on inverted-foils dynamics are under revision in an article in the Aeronautical Journal:

1. Salinas, M.F., Botez, R.M., Tavallaeinejad, M., Païdoussis, M.P. 2023. Experimental wind-tunnel study of the dynamics of inverted foils for energy harvesting. *Aeronautical Journal*, under revision.

All the work done in this thesis as well as in the above papers, including calculations and analysis, experimental testing and writing, was done by myself, under the guidance of my thesis supervisors, Professors Ruxandra Botez and Guy Gauthier. The revision and remarks by Emeritus Professor Michael P. Païdoussis on the inverted-foils articles were extremely valuables.

ANNEX B (p.189) presents the experiment setup for energy harvesting with inverted-foils.

2.3 Model Validation Process Review

The simulation of 3D modeled bodies is becoming standard in the fields of Aerospace, Automobile and Civil engineering as means to design products. By definition, 3D prediction models cannot reproduce or predict the experimental observations accurately. Uncertainty, as defined by the American Institute of Aeronautics and Astronautics (AIAA) is a potential deficiency in any phase of modeling and simulation that is due to the lack of knowledge. Simulation uncertainties are due to erroneous modeling of boundary conditions or imprecise turbulence characterisation in the vicinity of the body; and discrepancies can exist between numerical models and experimental data, thus a verification and validation procedure must be a research requirement to quantify these uncertainties.

2.3.1 Uncertainty Measurements

Numerical computational fluid dynamics (CFD) models are computer programs applied to flows with restricted boundary conditions, and designed to solve numerically integrated fluid equations. The calibration and validation of CFD models are extremely difficult, and most CFD models can solved laminar flows, but are limited to specific turbulence flow conditions. In 1986, The American Society of Mechanical Engineers (ASME) Journal of Fluids Engineering was published a recommendation stating the need for quantification of numerical accuracy. Other journals (AIAA and MDPI) have issued similar statements. These statements lead to research on the best method to determine numerical uncertainty. In 1998, the AIAA Journal published the "Guide for the Verification and Validation of Computational Fluid Dynamics Simulations". This document was one of the first guidelines for verification and validation assessment on numerical models. This AIAA models guideline defines several terms, such as uncertainty, errors and predictions. The “uncertainty” is defined as a potential deficiency in any phase of the modeling process due to incomplete knowledge, and the “error” is defined as a recognizable deficiency in the simulation, not due to lack of knowledge, but caused by other limitations. These two terms are linked to the accuracy of the models, which the guideline defines four predominate sources: i) insufficient spatial discretization convergence, ii) insufficient temporal discretization convergence, iii) lack of iterative convergence, and iv) program inherent limitation.

The AIAA guidelines emphasize that systematically refining the grid size and time step would solve most of the models uncertainty and error deficiencies. In 2008, the ASME Journal of Fluids Engineering published a "Procedure for Estimating and Reporting of Uncertainty Due to Discretization in CFD Applications". The ASME published several guides applied to Finite Element Analysis (FEA) and CFD in 2006 and 2009 respectively. These guides constitute a working tool in which advice and best practices are offered. The Verification and Validation (V-V) approach described in the ASME V-V 10(2009) document is based on the following items: (i) Verification of programming errors and numerical calculations must precede the validation. (ii) Validation is specific to the chosen digital model and the intended use of it. The validation of a complex system must be done hierarchically and from its simplest to its most complex form. (iii) The experimental and simulation results must take into account the uncertainties to be able to assess their probabilities. The ASME does not use of any particular metric; but the main characteristics of metrics to be chosen are the following: (i) The metric should express a quantitative measure of the difference between the simulated and experimental values. The metric must also be objective, in the sense that the results must not depend on the engineer who conducts the analysis. (ii) The metric should be able to capture the differences between simulation and observations across all statistical distributions, which means that the shape of the distribution must be taken into consideration in the measurements. (iii) Model acceptance criteria must be independent of the results obtained by the metric used. (iv) Uncertainties in both the simulation and observations must be taken into account. (v) The metric must be able to quantify the agreement of observations with respect to a simulation both at the local and global level of a system.

2.3.2 Verification Process

Many journals in mechanical and aerospace engineering have published articles on this subject, but the ASME method has been adopted by many researchers and provides a detailed approach on CFD verifications process. The method published in the ASME Journal of Fluids Engineering was used for evaluating the CFD models in Chapters 3 and 4 of this Thesis. The Fluids Engineering Division of ASME has worked on the detection, estimation and control of numerical uncertainties and errors in simulation models. The “Verification” is the process of determining if a computational model accurately represents the underlying mathematical model, and its solution is subdivided into two major components: (i) code verification seek to remove programming and logic errors in the computer programs, and makes sure that the mathematical models are working as defined, and (ii) calculation verification estimates the numerical errors dues to discretization approximations, and makes sure the accuracy of the discrete solutions. The numerical simulation was solved in this Thesis and the numerical results were compared to experimental data for validation.

2.3.3 Validation Process

The validation process had the unique objective of assessing the predictive capability of the numerical simulation. This assessment can only be made with experimental data obtained following the principles, guidelines and best practices defined by the work and observations of Rae (1966), Bradshaw (1984), Mehta (1979) and Pope (1978), which are the standard in the field of subsonic wind tunnel testing.

A "Validation" metric is the term used for evaluation of numerical model results with experimental data. Validation metrics can have binary or a probability output, in which the output should be a quantitative assessment of the agreement between the experiment and simulation. This quantification also included an estimate of the variability in the agreement and a confidence statement about the variability, which includes a relative error (%) and a confidence level (%) between the experiment and simulations for a determined range of values. The ASME Verification and Validation (V-V10) guidelines provided a useful validation approach when experimental values and simulation data were available.

The Area Metric method (Wang, 2018) allows the comparison of the whole set of predicted data with experimental observations. The Area Metric has numerous advantages compared to others validation methods, such as hypothesis tests, Bayes factor and linear regression, because its results do not depend on whom conducts the analysis or on the assumptions made since this method relies only on the data distribution shape. It produces a quantitative measure of the discrepancy between the numerical predictions and the experimental data, for which this method is considered objective and robust, and it enables to obtain a graphical representation of this discrepancy in the same physical units as the experimental data. The metric measures the differences between the model results and simulation uncertainties while considering the experimental uncertainties (ASME, 2016). The conclusion given by the Area Metric method does not depend on how a researcher is conducting the analysis or on the assumptions of the researcher had in the beginning of the design of the model. The measure of the mismatch *d*(*P,O*) is calculated using equation (2.1) on the whole set of data available, where *P(x)* are the predictions values and *O(X)* are the observed values obtained during wind tunnel tests. This area metric is evaluated with the Cumulative Distribution Function (*CDF*) of the experimental data and that of the model data. Both *CFD*s are step functions (Chatenet *et al.* 2016).

$$d(P,O) = \int_{-\infty}^{\infty} |P(x) - O(x)| \, dx \tag{2.1}$$

2.3.4 Experimental Process for Subsonic Wind Tunnel

Wind tunnel tests provide precise flow conditions allowing qualification, analysis, measurement and characterization of empirical and theoretical research. While flow conditions can be maintained, wind tunnel experiments have some drawbacks, primarily those associated with turbulence flow intensities levels, the scale and size of the models, the blockage effects corrections and the boundary layer thickness. Many factors can be consider in wind tunnel testing procedures, but Barlow, Rai, and Pope (1999) experimentally observed two main source of inaccuracy for subsonic flows. i) Blockage and wall-interference represent the confinement of the flow around the body, combined with the flow interaction inside the wind tunnel boundary (closed walls), that modifies the flow field. Different techniques are available to explain the wind tunnel data corrections of these flow effects. However, whenever possible, model scaling is done in order to obtain a blockage area ratio smaller than 10% to minimize the results uncertainties (ASME V-V10). Although reduced scale models are preferred to minimize blockage and interference effects their use can lead to inaccurate measurements. The aerodynamic loads on a surface body can be strongly dependent on viscous effects in the shear layers turbulence and also, wake and flow-separation regions. A simulation would require matching the air parameters, such as density (ρ), viscosity (μ) and wind speed *U*. ii) The Reynolds numbers combines the air properties with the scale model geometry in order to obtain the aerodynamics performance of the full size body. In the case of a half-scale model (model of size equal to 50% of the full scale body to be tested), the wind speed must be doubled to match the Reynolds number (the wind tunnel tests speed musts be twice the speed flow). In some cases, this fact can be accomplished, but many wind tunnels cannot reach the required speeds when reduced-scale models are used (Mehta, Bradshaw, 1979).

2.4 Subsonic Wind Tunnels

Several well-known works in the field of wind tunnel tests served as references for this thesis. Given the research topic studied in this thesis, the author focuses on the scientific literature on subsonic wind tunnels, and then the emphasis is placed on the characterization of the Price-Païdoussis wind tunnel and its intrinsic characteristics.

2.4.1 History of Subsonic Wind Tunnels

A British scientist John Smeaton used a sophisticated method to perform aerodynamic testes, shown in Figure 2.4. It used a rotating arm installed inside a building to minimize variations in the air properties, which allowed tests repeatability. In his 1759 article entitled "An Experimental Enquiry Concerning the Natural Powers of Water and Wind to Turn Mills and Other Machines Depending on Circular Motion", Smeaton developed the bases of the Smeaton coefficient k, as presented in the equation $L = kV^2AC_l$ (Smeaton, 1759). Smeaton coefficient represented the ratio between the lift force L and the product between the wing area A the flow speed V^2 and the lift coefficient C_l. The Smeaton coefficient accuracy was later improved, by the Wright brothers. In recent CFD analysis, the lift coefficient is normalized by the dynamic pressure instead of using the Smeaton coefficient.

The first wind tunnel in USA was built by Albert J. Wells, shown in Figure 2.5 on April 29 in 1896, in the laboratories of the Massachusetts Institute of Technology (MIT). Wells had used the university's ventilation system, a vertical pipe of 5 feet of length and another horizontal pipe of 13 feet of length. At the exit of his wind tunnel, Wells placed an aerodynamic balance which allowed him to measure the vertical and horizontal forces on the models. At the distance of 500 miles from Cambridge, Massachusetts and almost 50 years later, in the laboratories of the National Advisory Committee for Aeronautics (NACA) in the state of Virginia in the USA, the two engineers David J. Biermann and Lindsey I. Turner Jr have developed a 16-ft wind tunnel, capable of reaching speeds equal to 80% of the speed of sound (Mach 0.8).

The Wright Brothers have obtained the largest aerodynamic database in the world. The wind tunnel developed by them is shown in Figure 2.6; this open-circuit wind tunnel had a single speed developed by its axial fan and motor. The fan was placed at the entrance of the wind tunnel, very close to its test chamber, and produced a variable flow with swirls due to the fan blades. The brothers have developed two aerodynamic scales and more than a 100 reduced-scale wing models. The experimental results were obtained by the measurement of forces variation on the aerodynamic scale. The Wright brothers measured the lift and drag forces of their models at various angles of attack.

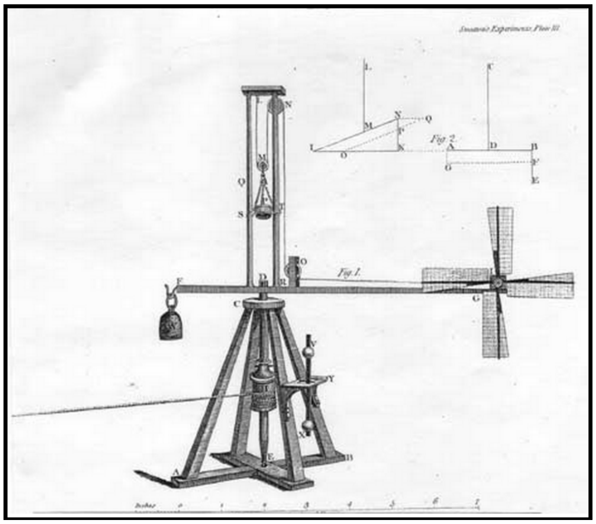

Figure 2. 4 John Smeaton wind tunnel from
Lee, James Lawrence, (2001)

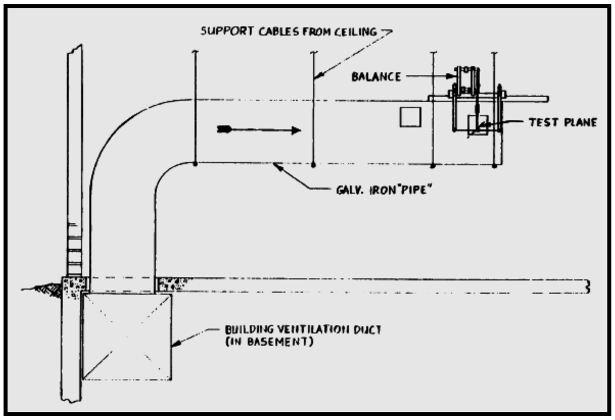

Figure 2. 5 Albert J. Wells wind tunnel from
Lee, James Lawrence, (2001)

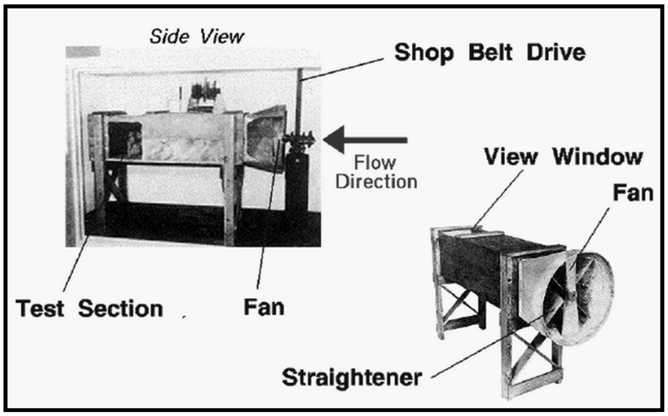

Figure 2. 6 Wright bothers wind tunnel illustration
from Wind Tunnels of NASA (Baals Donald, 1981)

2.4.2 Calibration of Subsonic Wind Tunnels

The characteristic most often observed and measured in wind tunnels concerns the motion of fluid particles over a given period of time. The flow speed depends on the design and construction of the wind tunnel. According to Lindgren and Johanson (2002), a large variation in the average speed inside the test chamber indicates that the axial or centrifugal fan does not have the right size, because of the fact that the pressure produced by the blades is low or the fan does not operate in optimal speeds ranges. If the test chamber and converging nozzle are not installed at the minimum distance recommended by Mehta and

Bradshaw (1979), the rectifier filters cannot perform their functions of reducing transverse and longitudinal uniformities of the flow inside the test chamber. The turbulence rate inside the test chamber is another important characteristic to measure and reduce as much as possible. The upstream section of the test chamber called “convergent nozzle” must respect its manufacturing geometry, as shown by Mehta and Bradshaw (1979), and Rae and Pope (1999). The cross-sectional area of the test chamber should be between 6 times and 9 times the cross-sectional area of the converging nozzle.

Studies on separation bubbles and their effects on the boundary layer were carried out at very low turbulence rate and various speeds; wind tunnel tests on reduced scaled wing models at Mach number lower than 0.3 have a turbulence rate below 1% and an average speed variation of 3%, relative to the maximum wind tunnel velocity.

The calibration of a wind tunnel consists in measuring and quantifying the flow variations in the vicinity of a reduced scaled model representing a wing airfoil or an aircraft. The physical quantities that can be monitored in the test chamber are the speed, static and dynamic pressures, related by Bernoulli's theorem. The temperature, humidity and density of the fluid are monitored during testing, however in most installations where wind tunnels are located, temperature and humidity variations are minimal. Low-speed wind tunnels ($M < 0.3$) assume that the flow inside the wind tunnel remains incompressible under the force generated by the centrifugal fan; the mass conservation (air) is constant throughout the volume of the test chamber where the incoming flow is equal to the outgoing flow, which implies that the density of the fluid is considered to be constant.

Measuring the fluid speed distribution inside the wind tunnel could take a high amount of time that would require measuring the speed at each section. This operation would not comply with the specifications required by the The American Society of Heating, Refrigerating and Air-Conditioning Engineers (ASHRAE) methodologies (2001). The ASHRAE standards emphasize that the ducts must be analyzed according to one of two approaches depending on their shapes. The “Log Tchebycheff” method is applied mainly for rectangular volumes, while the “Centroids of Equal Areas” (CEA) method is applied for spherical volumes. The test chamber is defined as the component of the wind tunnel (duct) through which the flow interacts with the model or the airfoil. The CEA approach applies only to ducts with a circular or elliptical cross-sectional area.

The “Log Tchebycheff” is a method through which local speed variations are obtained using a Pitot tube and a minimum of control points. "Log Tchebycheff" is part of the ASHRAE methods included in the section on Standard Methods for Laboratory of Air-Flow Measurement (ASHRAE Standard 41.2, 1987) and since 2008 is an ISO standard (ISO 3966:2008). The "Log Tchebycheff" method recommends dividing the volume to be analyzed (in the case of a wind tunnel, this volume is the test chamber) into surfaces perpendicular to the flow and then each surface is squared in a finite number of points. Each grid point has its coordinates (*x, y, z*) in which the static and dynamic pressures are measured and the flow speed U can determined by use of the air density ρ and the difference between the total pressure P_t and the static pressure P_s, as shown in the equation 2.2.

$$P_t - P_s = q_c = \frac{1}{2}\rho U^2 \tag{2.2}$$

The increase in computational power and experimental approaches contributed to the understanding and solving of many complex engineering problems in various disciplines and fields. Fluid and solid interactions is one of these fields, in which aeroelastic instabilities (such as flutter, divergence), laminar-to-turbulent transition, vortex shedding, turbulent flows and others are studied.

In this thesis, the author wishes to reduce the state-of-the-art gap between fluid dynamics and solid interaction in three investigations related to blunt and streamlined bodies subjected to a steady axial flow at high Reynolds numbers. All these three investigations are published in three journal papers.

The first investigation, presented in Chapter 3, analyzes the turbulent flow at the wake region near blunt bodies (ground surveillance system). The second investigation, presented in Chapter 4, analyzes the aerodynamic characteristics of a streamlined body (wing) with

adaptive shape capabilities to reduce drag production. Both investigations were realized using both Computational Fluid Dynamics (CFD) and Wind Tunnel Testing approaches.
The third investigation, presented in Chapter 5, concerned a "reduction of research gap" and "application oriented" study of renewable energy harvesting production with flexible foils. For this reason, the authors conducted an experimental analysis on the global dynamics of foils, that generated continuous and large-amplitude oscillations at various Reynolds numbers. Numerical analysis was also conducted in collaboration with co-authors of this investigation.

The literature review presented in section 2.3 Model Validation Process and section 2.4 Subsonic Wind Tunnels were applied by the author in the following 5 articles journal (1-5) and conferences (6-7):

1. **Salinas M.F**., Botez R.M., Gauthier G. (2023). New Validation Methodology of an Adaptive Wing for UAV S45 for Fuel Reduction and Climate Improvement. Applied Sciences. Jan 30; 13(3): 1799.
2. **Salinas M.F**., Botez R.M., Gauthier G. (2021). New numerical and measurements flow analyses near radars. Applied Mechanics. 2(2):303-30.
3. **Salinas, M.F**., Botez, R.M., Tavallaeinejad, M., Païdoussis, M.P. Experimental wind-tunnel study of the dynamics of inverted foils for energy harvesting. Aeronautical Journal (1st review).
4. Tavallaeinejad, M., Païdoussis, M**. M.F. Salinas**, Legrand, M., Kheiri, M., & Botez, R. (2020). Flapping of heavy inverted foils: A fluid-elastic instability. Journal of Fluid Mechanics. 904, R5.
5. Tavallaeinejad, M., **Salinas, M.F**., Païdoussis, M.P., Legrand, M. Kheiri, M. and Botez, R.M. (2021).Dynamics of inverted flags: Experiments and comparison with theory. Journal of Fluids Structures. Vol.101, 103199.

6. Tavallaeinejad, M., **M.F. Salinas**, A.R. Abdelbaki, M. Legrand, R.M. Botez, and M. P. Païdoussis. (2019). An experimental investigation of the dynamics of an inverted flap with a rigid splitter plate. (IUTAM Symposium on Fluid-Structure Interaction).

7. Tavallaeinejad, M., M.P. Paidoussis, **M.F. Salinas**, M. Legrand, M. Khein, and R.M. Botez. (2020). Why inverted foils flap: An experimental study. (Mcgill Symposium on Flutter).

CHAPITRE 3

NEW NUMERICAL AND MEASUREMENTS FLOW ANALYSES NEAR GROUND SURVEILLANCE SYSTEMS

Manuel Flores Salinas, Ruxandra Mihaela Botez and Guy Gauthier

Department of Systems Engineering, École de Technologie Supérieure,
1100 rue Notre-Dame West, Montreal, Québec, Canada H3C 1K3

Paper published in MDPI Applied Mechanics Journal, May 2021

Résumé

Une étude expérimentale et numérique de l'écoulement près d'un corps non profilé a été menée. La plupart des méthodes expérimentales utilisent la visualisation de l'écoulement et l'introduction de sondes (capteurs) dans le champ d'écoulement. L'objectif principal de cette recherche a été le développement d'une nouvelle méthodologie pour analyser les écoulements et la mesure des caractéristiques des écoulements sans tenir compte des effets de distorsion des sondes de mesures. Une série d'expériences a été réalisée sur un radar de surveillance au sol dans la soufflerie subsonique Price-Païdoussis. Les forces et les moments ont été mesurés en fonction des vitesses des vents et des positions angulaires à l'aide d'une échelle aérodynamique à six composantes. Un modèle en trois dimensions, à l'aide des calculs de dynamique des fluides, a été utilisé pour analyser la région de sillage du radar de surveillance au sol. Un système de réduction de la turbulence a été proposé et analysé dans cette recherche. L'utilisation du système de réduction de la turbulence proposé s'est avérée être un moyen efficace de réduction de l'intensité de l'écoulement turbulent de 50 %, les coefficients de traînée de 9,6 % et le retard du point de transition de l'écoulement de 7,6 positions.

Abstract

An experimental and numerical investigation of the flow near a blunt body has been conducted in this study. Most experimental methods of flow studies use flow visualization and probes introduction into the flow field. The main goal of this research was the development of a new methodology to analyze flows, and to measure flow characteristics without taking into account the distorting effects of measuring probes. A series of experiments were performed on a ground surveillance radar in the Price-Païdoussis subsonic wind tunnel. Forces and moments were measured as functions of wind speeds and angular positions by the use of a six-component aerodynamic scale. A Computational Fluid Dynamics three-dimensional model was employed to analyze the wake region of the ground surveillance radar. A turbulence reduction system was proposed and analyzed in this research. The use of the proposed turbulence reduction system was found to be an effective way to reduce turbulent flow intensity by 50%, drag coefficients by 9.6%, and delay the flow transition point by 7.6 times.

3.1 Introduction

Blunt body flow analyses are very important in Engineering. Most bodies and structures do not present a streamlined shape; for this reason, an accurate analysis of wake regions would lead to a major understanding of turbulence flows and turbulence reduction mechanisms (Lee et al., 2011). Blunt bodies in turbulent flow conditions can lead to material fatigue and damage, and therefore, to increased drag and energy consumption. There are few studies, both in theoretical and in experimental research related to methods of studying flow behaviors in the presence of blunt bodies (Degani et al., 1998),(Brahimi & Paraschivoiu, 1995). A methodology to measure and analyze the flow characteristics near a full-size “Ground Surveillance Radar” without introducing probes into the flow field, that would affect its structure, to the best of our knowledge, has not been described in the literature. The proposed methodology employs a quantitative approach (Mason & Beebe, 1978) to analyze the wake region to evaluate the turbulence intensity, drag coefficient, pressure distribution coefficient, and boundary separation of a flow near a blunt body. A procedure to quantitatively validate numerical models using experimental data from wind tunnel tests, including an analysis of a proposed “turbulence reduction system” is also part of this research.

The experimental tests were performed for the ground surveillance radar in the Price-Païdoussis subsonic wind tunnel at our Research Laboratory in Active Controls, Avionics and Aeroservoelasticity LARCASE. The LARCASE laboratory is one of the few multidisciplinary aerospace research laboratories in Canada that has four pieces of state-of-the-art research equipment, such as a Cessna Citation X Business Aircraft Research Flight Simulator, a Bombardier series regional jet CRJ-700 Research Flight Simulator, an Autonomous Aerial System UAS-S4 from Hydra Technologies and a Subsonic Wind Tunnel Price-Païdoussis. At the LARCASE, new methodologies in the aeronautical industry have been developed in the areas of actuated morphing wings and wing-tip systems (Grigorie, Botez & Popov, 2015), (Gabor et al.,2016), (Koreanschi, Gabor & Botez, 2016) upper surface optimization of wing shapes for unmanned aerial systems (Gabor, Koreanschi & Botez, 2013),(Gabor et al., 2016), (Tchatchueng et al.,2016), (Gabor et al., 2014) and Computational Fluid Dynamics models validations with experimental results from subsonic wind tunnel tests (Koreanschi, Gabor & Botez, 2016), (Gabor, Koreanschi & Botez, 2016).

3.2 Literature review

3.2.1 Wake Characteristics of Blunt Bodies

The boundary layer at the blunt body surface can be described in terms of flow separation, shear layers, vortex shedding, flow recirculation, and vortex formation, which may lead to a high surface drag coefficient. The reason is that the sharp edges of blunt bodies accelerate a transition to turbulent flow and a flow separation dominated by vortices and eddies

(Rebuffet, 1996),(Duell & George, 1993). The “ground surveillance radar” in this study had the same characteristics as a blunt body while the wake region had a turbulent flow behavior. The “ground surveillance radar” will be shortened by “radar” in the following sections. Figure 3.1 illustrates the flow behavior at the wake on a blunt body (radar), as explained in experimental research papers done on blunt bodies. On the left side of Figure 3.1, the radar model is visualized, while on its right side, the flow starts to separate, and then reattach on the radar upper surface, but the viscous forces and shear layers are not strong enough (Roshko, 1954),(Menter & Kuntz, 2004). The detached shear layer path was indicated by number **1**. At the wake region, a closed boundary would form; the length and width increase as the recirculation regions indicated by number **2**, and the separation regions indicated by number **3** grow at the rear of the blunt body.

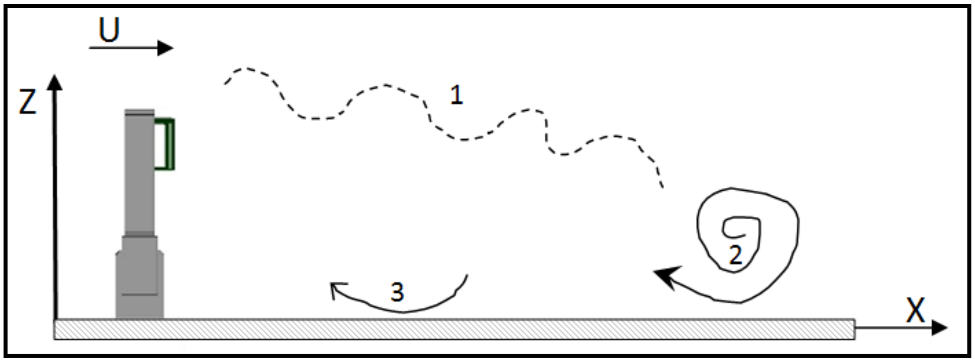

Figure 3. 1 Flow behavior at the wake on a blunt body, a figure designed by the author

3.2.2 Turbulence Model

Most common flows encountered in nature and industrial applications are three-dimensional, and they are turbulent. There are the Reynolds-Averaged Navier-Stokes (RANS) one-equation turbulence models, such as the Spalart-Allmaras model, that are useful in wings and wing tip CFD simulations (Cestino et al., 2019), and two-equation models such as k-ε models and k-ω models. In the next section, only the k-ε turbulence model will be used. The k-ε

turbulence model predicts the flow behavior by solving the RANS equations where k is the turbulence kinetic energy and ε represents the rate of dissipation of turbulence kinetic energy; it is also a suitable model for solving external flow problems with complex geometries where the wall function and y+ values have to be carefully considered for each type of simulation (Kalitzin et al., 2005), (Durbin, 1995). Solving at the flow smallest scales, near the wall region, as well as at the flow largest scales, has led to the development of hybrid models, which combine the best properties of RANS with those of Large Eddie Simulation (LES). One of these hybrid techniques is the Detached Eddy Simulation (DES) model, where the regions close to the walls are solved using a RANS model, while the rest of the flow is solved with an LES approach (Frunzulica, Dumitrescu & Dumitrache, 2013), (Frohlich & von Terzi, 2008).

The choice of a hybrid model was the best option to solve the flow model of the radar in this paper, because of the fact that important pressure gradients, eddies, and vortices were expected.

3.2.3 Model Validation

According to the ASME's guide (ASME, 2016), uncertainties should be taken into account during the validation process of a numerical model. To validate a model, a specific metric is not imposed by ASME, but this metric should "be equal to zero" when the data is identical to the experimental results.

The "Area Metric" method allows the comparison of simulation results with experimental data. Moreover, this metric meets all the ASME's requirements including the uncertainties modeling. This method has an important advantage with respect to classical methods for being able to evaluate and subsequently refuse or accept the proposed model (Ferson, Oberkampf & Ginzburg, 2008), (Brahimi, Allet & Paraschivoiu, 1995). This method is robust, as it provides quantitative measures of differences between the predicted and experimental data, and enables a graphical representation of these differences in the same physical units as for experimental data (Romeo et al., 2012), (Correa et al., 2015). The measurement of the error $d(P,O)$ is evaluated using Equation (1) on the entire range of the distributed data, where *P(x)* are the predicted values and *O(X)* are the observed values obtained during wind tunnel tests. This method is applied using the Cumulative Distribution Function (CDF) of experimental and numerical model data. Both CDFs are step functions and the variable A represents the difference between the model and the experimental test data.

$$A = d(P, O) = \int_{-\infty}^{\infty} |P(x) - O(x)|\, dx \tag{3.1}$$

3.2.4 Vortex Detection

A vortex detection technique would greatly improve the results obtained in our research. There are a few vortex techniques developed in the last years, but the classical and more used vortex techniques are Q-criterion, Delta-criterion, and Lambda2-criterion (Dubief & Delcayre, 2000). The vortex detection technique Lambda2 (suggested by the reviewers) is used mainly for body shapes where multiples vortices are presented. The radar body is a symmetric blunt body with one main vortex created by the boundary layer at its upper surface. We have consulted the suggested articles, as well as other articles in which various vortex techniques were used, and we found that the Q-criterion applies to the shape of the radar, and to the subsonic flow velocity in this study, and is less time consuming than the Lambda2 criterion.

Largely steady or recirculation vortices at the wake region can orientate the flow in different directions and change the pressure distribution around the blunt body surface. Unsteady vortices can store energy and dissipate it in the wake flow, thus increasing the induced drag of the blunt body. Besides using the flow variables, such as velocity, pressure, and vorticity, it is challenging to analyze vortices at the surface and the wake region of a blunt body. From the classical vortex detection techniques (Dubief & Delcayre, 2000), (Jeong & Hussain, 1995) studied in the literature, the Q-Criterion (Hunt, Wray & Moin, 1988)) was found to be well suited to accurately identify vortex location, strength, and behavior in the flow field encountered in the radars wake region. The Q-Criterion vortex representation technique shows the variation of the rotational and deformation components of a fluid element in the flow field.

Equation (2) was programmed in the CFD model, in which W is the vorticity magnitude and S is the rate of strain.

$$Q = \frac{1}{2}(W^2 - S^2) \tag{3.2}$$

The vortex detection technique Q-Criterion shows the local balance between the shear strain rate and the rotation rate or vorticity magnitude near the wake region of the radar. The Q-Criterion allows separating the region of the location where the strength of rotation overcomes the strain rate of a flow field. The threshold applied to the Q-Criterion plays an important role in detecting the outer shell of the vortex, as well as the strength of the vortices. The threshold values for Q-Criterion $10^1 < Q \leq 10^6$ were chosen to account for the highest velocity of the flow inside the wind tunnel (15 m/s), the large size of the radar, and the fully turbulent flow at the wake region.

The vortices made up sheering motion, as well as their inviscid part cannot be captured using the Q-criterion. Most of the classical vortex detection techniques are limited to the narrow core region of vortices and are not applied outside it. Classical vortex criteria are tools to capture the topological structures of the flow rather than to extract and quantify values of individual vortices (Mariotti, Buresti & Salvetti, 2019), (Rochio et al., 2020). We are presenting results obtained using the Q-criterion for the original radar without a turbulence reduction system and for the radar with a turbulence reduction system.

3.2.5 Wind Tunnel

There are two main factors to be considered in a wind tunnel test procedure for blunt bodies; the “blockage constraint” of a closed test section and the Reynolds number. Different techniques and methods were established to measure, and thus to reduce the impact of blockage constraint on experimental data. It was found that the blockage area ratio should be 10% to remove wall interference and to calculate the wind tunnel empirical factor ω needed to remove the blockage constraint from aerodynamic coefficients. The Reynolds number plays an important role in experimental testing because of the fact that flow separation and turbulence are often dependent on the Reynolds number (Maskell, 1968).

3.3 Research Objectives

The research objectives are:

1. The design of a new methodology for numerical and experimental analysis of turbulent flows.
2. The quantitative metrics consideration to measure flow analysis improvements.
3. The analysis of a “turbulence reduction system” for blunt bodies.

3.4 Apparatus and Instrumentation

The Applied Research Laboratory in Active Controls, Avionics, and Aeroservoelasticity LARCASE team obtained the Subsonic Wind Tunnel Price-Païdoussis for numerical model validation and testing in the Aerospace field. The details of this Blow-Down Subsonic Wind Tunnel, the aerodynamic scale, as well as the instrumentation used in this research are described in this section.

The Price-Païdoussis Open Return Subsonic Wind Tunnel shown in Figure 3.2 is a research apparatus for the validation of Computational Fluid Dynamics (CFD) models of various geometrical shapes and dimensions. The wind tunnel consists of a centrifugal fan, a diffusing and settling chamber, a contraction section, and a test chamber or test section, as shown in detail in Figure 3.3. The air supply enters the wind tunnel by two inlets located on opposite sides of the centrifugal fan. The engine and the centrifugal fan are protected from dust particles inside a closed area.

Figure 3. 2 Price-Païdoussis Blow Down Subsonic Wind Tunnel

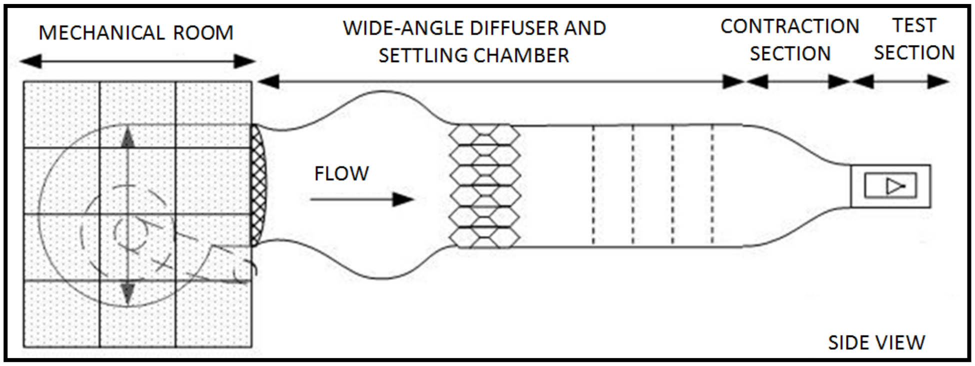

Figure 3. 3 Price-Païdoussis Wind Tunnel schematic designed by authors

An important step to perform before experimental tests is the "calibration phase", in which the flow conditions inside the test chamber are obtained. The main parameters to characterize the flow during a wind tunnel test are: (1) the total, static and dynamic pressures; (2) the temperature variation during the test; (3) the controlled flow speeds, and finally the Reynolds number. The internal filters shown in Figure 3.3 are dissipating the flow turbulence, and the laminar flow enters the contraction section where the flow speed increases. The large test chamber for full-scale models has a height, width, and length of 1.5 × 2 × 4 m, respectively, a maximum speed given by Mach number M = 0.05, and a maximum Reynolds number of $1x10^5$.

The "aerodynamic scale" was designed and built in-house. It has three strain gages that convert force into 'electrical resistance', which can be used to measure forces and moments values in all three coordinates. The output signal from strain gages is amplified and filtered, and the overall noise is minimized. The LARCASE aerodynamic scale can measure *Fx* and *Fy* forces up to 2500 N with an accuracy of ½ N and can support full-scale models with an *Fz* of up to 6250 N with an accuracy of ¾ N. The maximum values of *Mx*, *My,* and *Mz* moments are 400 Nm with an accuracy of 1/20 Nm. The radar was fixed to a pan/tilt device by use of eight screws, which lead to a ground clearance of 0.38 m and 360° operational range. The scale can measure three forces (lift, drag, and side) and three moments (pitch, roll, and yaw) and it was mounted between the pan/tilt device and a high-grade steel tripod screwed to the floor. The pan/tilt device allows the variation of the yaw angle within ±0.01°. Two circular aluminum plates were used as interfaces and manufactured for this study. They were rigidly coupled to align the pan/tilt device, the aerodynamic scale, and the tripod. The pan/tilt device is a cube with a constant surface area on its front, back, and both sides (FLIR, 2021).

The temperature and pressure readings are important for calculating the air density and flow speed during wind tunnel tests. The sensor used in the wind tunnel for measuring the temperature is a thermocouple type K with its accuracy of ±0.5 per degree Celsius. The Pitot tube inside the test section measures the flow static and the total pressures. The holes on the Pitot tube surface that are perpendicular to the speed direction are used for static pressure measurements, and the hole at the tip of this tube is used for total pressure measurements (Martin, 1990). A multifunction data acquisition system USB-6210 from National Instruments (NI) was chosen to convert the analog signals of the aerodynamic scale into digital during the wind tunnel tests, and further to save them for their post-processing. The USB-6210 allows measurements of up to 16 analog inputs and does not require external power for its functioning. It reduces all input signals to a single USB cable, and can thus send the data from the force sensors to a remote PC. A custom interface was designed to acquire, visualize, and save data for post-processing. A video film was also recorded during the wind tunnel tests by use of the camera installed inside the test section. The aerodynamic data saved for each wind tunnel test were later imported in MATLAB 9.0 (2016b) for their analysis in the research post-processing phase. Each wind tunnel test was done at a sampling rate of 1000 Hz for pressure and temperature sensors, and 10,000 Hz for force and moment sensors.

3.5 Experimental Approach

For each wind tunnel test performed for this research, the authors measured and recorded the values of forces, moments, shedding frequencies, pressure, and velocity variations at the wake region of the radar. Before performing experimental tests, a structural analysis was done to evaluate the stress distribution on the radar at the flow speed of 15 m/s. The photograph of the radar tested at the LARCASE wind tunnel is illustrated in Figure 3.4. The dimensions of the radar are the following: the height H = 0.37 m, the length L = 0.75 m, and the thickness h = 0.16 m. The projected frontal area of the radar is $A_m = 0.278\ m^2$ with an aspect ratio AR = H/L = 0.49. Experimental tests were conducted at the Price–Païdoussis subsonic wind tunnel in its 1.5 m × 2.0 m × 4.0 m test section with a frontal surface area $A_{wt} = 3.0\ m^2$. The positions of the yaw angle were denoted by γ as they measured the angles in degrees between the airflow direction and the frontal area of the radar. The angles are positive in are oriented in the clockwise direction. An angle $\gamma = 0°$ indicates that the radar maximum surface A_m is perpendicular to the flow, and an angle $\gamma = 90°$ indicates that the radar maximum surface rotates towards the right side wall of the test section while the radar's smaller surface (side of the radar) is perpendicular to the airflow direction.

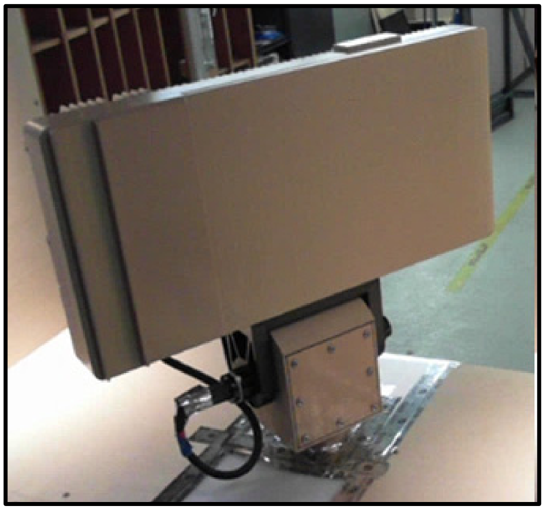

Figure 3. 4 Front and rear images
of the full-size radar

The radar was located at the center of the test section, where the blockage ratio $\frac{A_m}{A_{wt}}$ is equal to $\frac{0.278}{3.0} = 9.27\%$ for $\gamma = 0°$.

3.5.1 Empirical Equations

The flow speed U was determined by using the air density ρ and the difference between the total pressure P_t and the static pressure P_s, as shown in the Bernoulli equation (Barlow, Rae & Pope, 1999).

$$P_t - P_s = q_c = \frac{1}{2} \rho U^2 \tag{3.3}$$

The Reynolds number Re_H was calculated using the wind tunnel speed U, the radar height H, and the constant air kinematic viscosity $\vartheta(T)$ at $T = 22°$:

$$\mathrm{Re_H} = \frac{UH}{\vartheta(\mathrm{T})} \tag{3.4}$$

The drag coefficient C_d is a non-dimensional form of the drag force F_d acting on the radar body and in the flow opposite direction. Equation (3.5) of the drag coefficient is given next:

$$\mathrm{C_d} = \frac{2F_d}{\rho(\mathrm{T})U^2A_m} \tag{3.5}$$

As the flow acts on the radar in the wind tunnel test section, a constraint occurs in the flow at the wake region. Equation (3.6) proposed and verified experimentally by Garner and Maskell captures the blockage effects on bluff bodies. To determine the aerodynamic coefficients C without taking into account the constraints of the wind tunnel test section walls, the values of the uncorrected aerodynamic coefficients (Garner et al., 1966) C_u, the blockage ratio $\frac{A_m}{A_{wt}}$ and the empirical value ω need to be calculated. Therefore C is obtained using the next equation:

$$C = \omega\, C_u \left(\frac{A_m}{A_{wt}}\right) \tag{3.6}$$

The blockage factor for blunt-body (Garner et al., 1966) ω is an empirical value describing the effects of the rigid walls, and those of the blunt body stopping the flow lateral displacement. The ω value is calculated based on the pressure coefficient C_p as follows:

$$\omega = \frac{1}{(1 - C_p)^2 - 1} \tag{3.7}$$

The pressure coefficient C_p is a non-dimensional ratio between the local static pressure differences and the dynamic pressure of the incoming flow. The local static pressure P_i is evaluated at various locations in the test section. The pressure coefficient C_p measures the local static pressure relative to the freestream static pressure P_s and the freestream dynamic pressure q_c. The pressure distribution is therefore calculated with the following equation:

$$\mathrm{C_p} = \frac{P_i - P_s}{q_c} \tag{3.8}$$

The dynamic pressure increase at the wake region produces a local reduction of the static pressure; therefore, the correction C presented in Equation (6) is applied to the aerodynamic coefficients C_u. The corrected C values are given by the following equation:

$$C = 0.942\ \mathrm{C_u} \tag{3.9}$$

The turbulence intensity *I* is the ratio between the velocity variation in the flow local components u_x, u_y, and u_z and the free stream velocity *U* inside the wind tunnel test section. The turbulence intensity values *I* were calculated with the following equation:

$$I = \frac{(u_x + u_y + u_z)^2}{U^2} \tag{3.10}$$

The Strouhal number (*St*) is the most important parameter associated with periodic vortex shedding, flow oscillations, and turbulence kinetic energy production at the wake region for blunt bodies (Eisenhohr & Eckelmann, 1989). At $St \geq 0.3$, the flow is fully turbulent and dominated by periodic vortices shedding. For an intermediate range of Strouhal number $0.2 \leq St \geq 0.3$, oscillations and periodic motions appear, and a turbulent wake forms behind the blunt body. At low Strouhal numbers ($St \leq 0.2$), the oscillations and vortices are dissipated by the moving fluid. *St* is defined by the vortex shedding frequency *f*, the length *H*, and the free stream flow velocity *U*. The *St* value is calculated with the following equation:

$$St = \frac{fH}{U} \tag{3.11}$$

3.5.2 Experimental Data

The experimental data were collected in real-time as the radar changes its angular position. The unfiltered drag forces obtained for three flow velocities are presented in Figure 3.5. The drag force has a maximum value at $\gamma = 0°$, and has its minimum value at $\gamma = 90°$. It can be mentioned that as the cross-section surface of the radar decreases with the angular position γ, the drag force exerted on the radar body decreases independently of the flow speed. Figure 3.5 also shows the blunt body symmetry between its front and rear sides, as well as between its left and right sides.

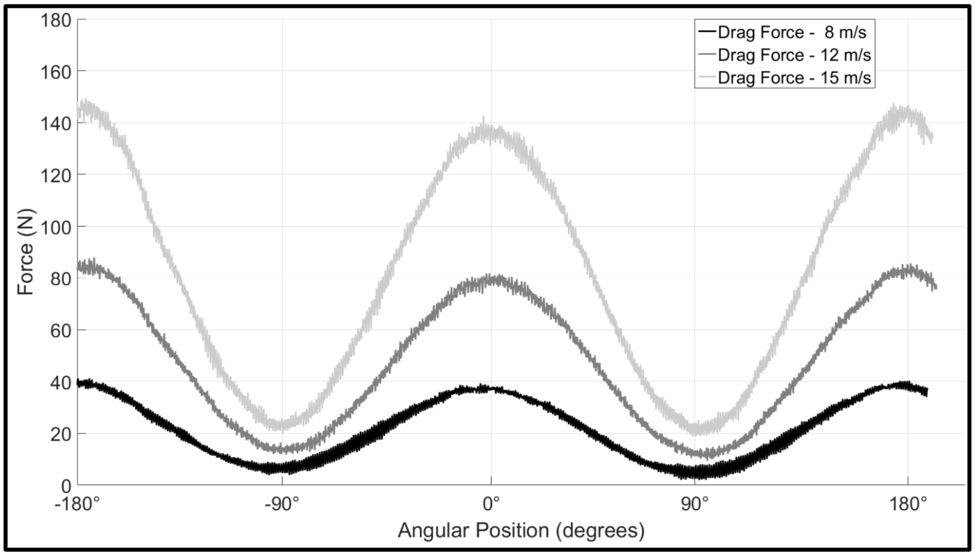

Figure 3. 5 Experimental drag forces at various angular positions

For blunt bodies, the drag coefficient is independent of the Reynolds number because of the fact that in a turbulent flow regime, the wake region is dominated by sharp edges and blunt body shapes. The drag coefficient values variations were obtained using Equations (3.5) and (3.9) and they are presented in Figure 3.6. The experimental drag coefficient values were found to be close for each angular position, which meant that they were independent of the Reynolds number. Their non-dependence on the Reynolds number allowed the design and analysis of a system able to decrease the drag force for any flow speed encountered by the radar.

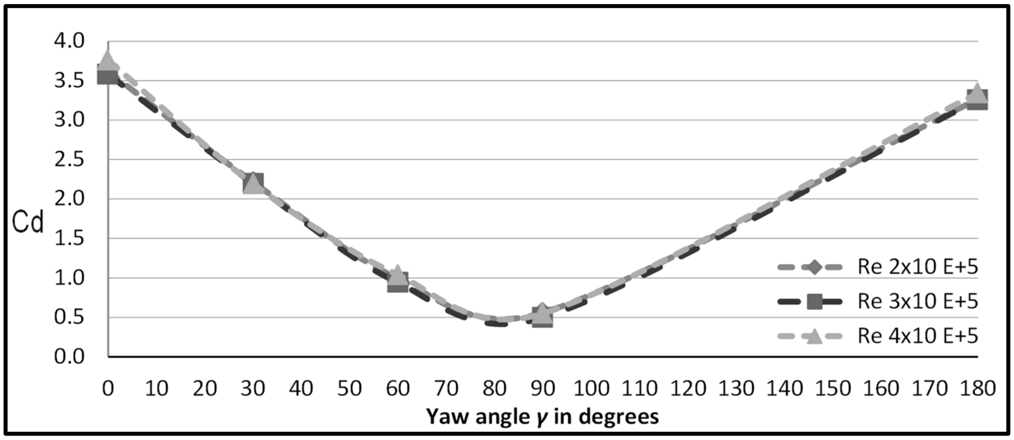

Figure 3. 6 Experimental drag coefficients versus yaw angle and Reynolds numbers

Periodic oscillations are present in the streamwise loads for the three flow regimes tested during the wind tunnel test of the radar. The experimental load *Fx* is characterized by a periodic motion, associated with oscillations in the wake region and provoked by the constant boundary layer separation at the upper surface of the radar, and by changes in the velocity of the flow field. Figure 3.7 presents the drag coefficient of the force *Fx* variation with time at the angular position $\gamma = 0°$ collected for 10 s and for three flow velocities: 8, 12, and 15 m/s.

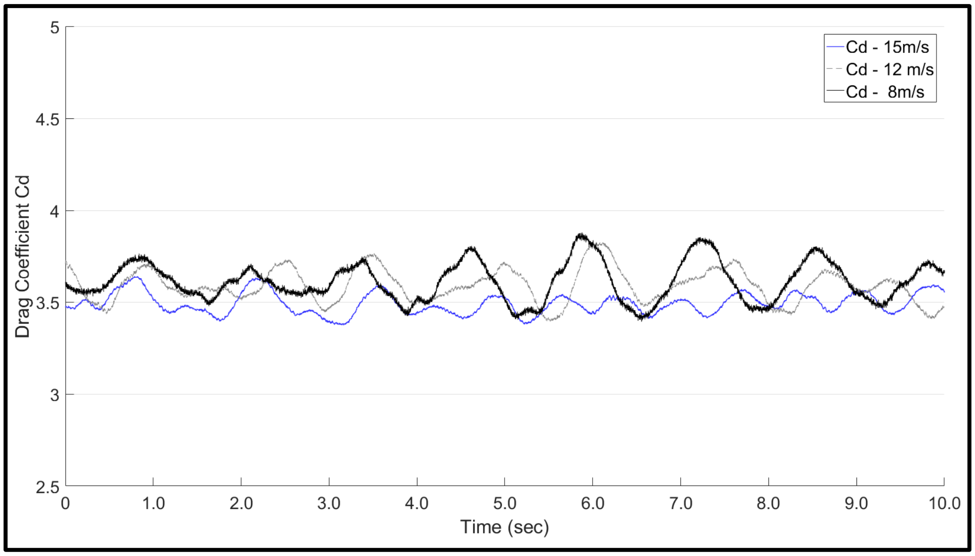

Figure 3. 7 Time history of drag coefficients for angular position 0°

The Strouhal number (*St*) describes turbulent periodic flow characteristics of blunt bodies. The oscillations for the drag forces are composed of a spectrum of frequencies. To find the frequency distribution for each flow velocity, the drag coefficients values shown in Figure 3.7 are decomposed in discrete frequencies as seen in Figure 3.8, where the power spectrum for each drag coefficient is traced versus frequency. The fundamental frequency presented in the flow at a velocity of 8 m/s is 7.89 Hz; at a velocity of 12 m/s is 11.53 Hz and at a velocity of 15 m/s is 14.77 Hz. Using the dimensionless Strouhal number defined in Equation (3.11), the radar's dimension normal to the flow direction H = 0.37 m and the fundamental frequencies for each wind tunnel test, the *St* number representing the vortex shedding on the radar blunt structure had three values $St_{8\mathrm{m/s}} = 0.365$; $St_{12\mathrm{m/s}} = 0.356$ and $St_{15\mathrm{m/s}} = 0.364$. As a Strouhal number $St \geq 0.3$, we can conclude that the wake region of the radar is turbulent and unsteady while flow separation and vortices shedding downstream occur.

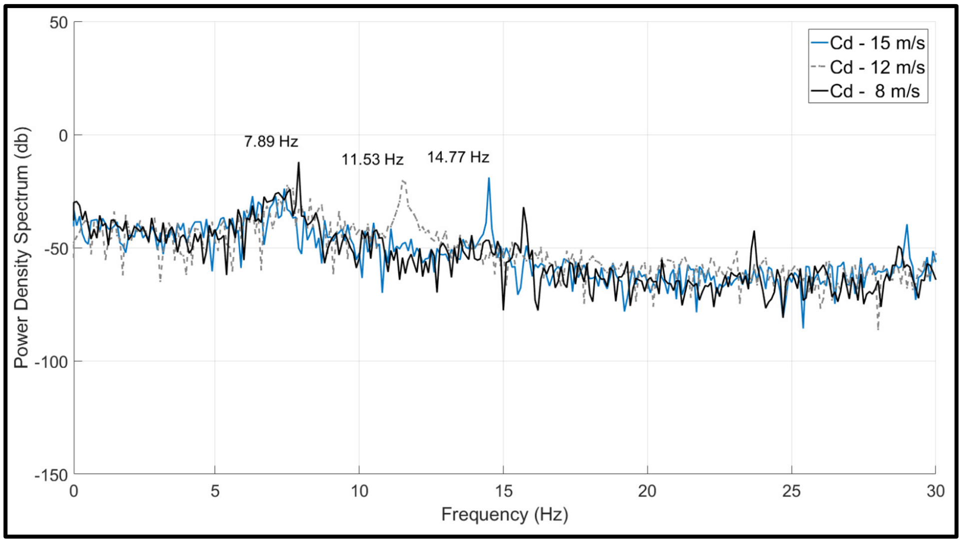

Figure 3. 8 Power spectrum frequencies on the radar drag coefficients

3.6 Numerical Approach

The full-scale radar, the Price–Païdoussis subsonic wind tunnel, and the flow around the radar were all modeled, meshed, and solved using ANSYS Fluent. This section shows in detail the numerical approach needed to obtain the radar aerodynamics coefficients; also, it shows the verification and validation process following the ASME guidelines.

3.6.1 CFD Models Design and Grid Domain

The physical dimensions and shapes of the test section and the radar were used to design a numerical representation of these two models. The aerodynamic scale measures the forces and moments at the base of the radar system; therefore, the moments are calculated at the same location as the forces. The meshing process includes the next steps: (a) the design of an initial mesh, followed by an evaluation of its quality, and by specifications of its boundary conditions; (b) the improvement and repairing of the mesh discontinuities and space between its cells; (c) the generation of the volume mesh using Triangle and Quad elements and refining of the mesh density close to its boundary layer; (d) the exportation of the final mesh to a neutral format. Two meshes were designed separately and then merged into a single mesh for its use in the Finite Element Analysis and Computational Fluid Dynamics solvers. The CAD of the original radar has been prepared for meshing by eliminating small details on the radar's surface. The y+ value was an important parameter for mesh-size calculation in the near-the-surface-mesh design with a growth rate of 20% for the next mesh layers. The radar mesh at its surface was composed of 130,580 unstructured mesh elements; 97% of these elements were modeled by triangular prisms. The radar face and rear meshes can be seen in Figure 3.9.

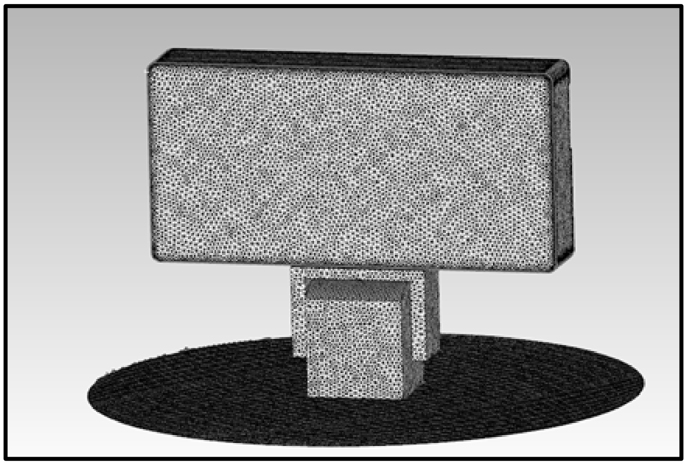

Figure 3. 9 Mesh resolution of the radar model

A mesh with a higher resolution was designed around the radar to accurately capture the turbulent wake at the rear of the radar. The 3D mesh was called '*InnerFluid*', and it was composed of 2,583,142 prisms and tetra unstructured mesh elements. To ensure an accurate simulation of the boundary layer flow near the model, 15 prism layers were used with the $y+$ calculated value as the first mesh size. The grid independence tests were performed with coarse, medium, and fine meshes; the forces and moments were not dependent on the mesh resolution (Katz & Sankaran, 2011), (Bradshaw, 1997).

The numerical model of the radar was constrained by four wall regions and two pressure regions (inlet and outlet) to simulate the flow conditions during wind tunnel tests. The flow direction, the radar position inside the test section, and the reference axis are shown in Figure 3.10.

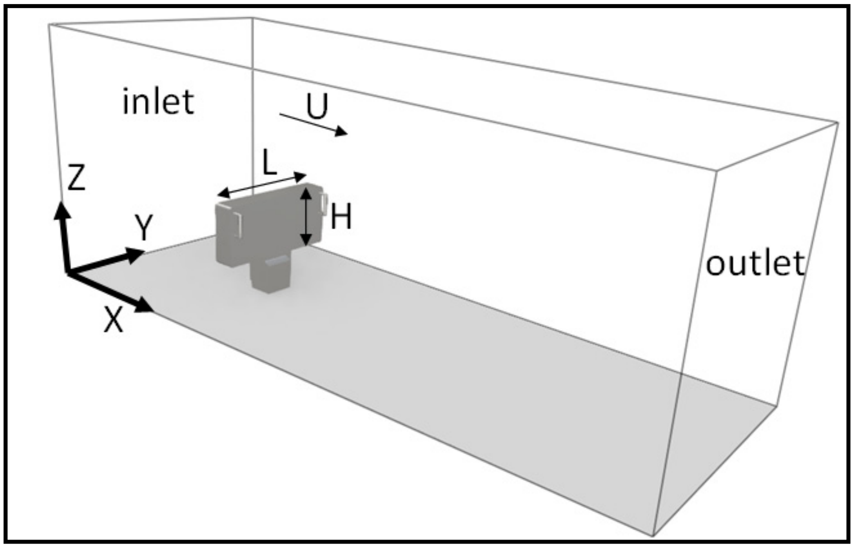

Figure 3. 10 Representation of the radar inside the wind tunnel test section for the numerical CFD model

3.6.2 Boundary Layer Region Thickness

Speed gradients are important for enclosed domains, such as wind tunnels, where the mesh resolution and number of inflation layers are critical (Spalart, 2000),(Menter, 2009). The flow mesh inside the wind tunnel section was called ‘Inner_Fluid’ in the CFD software. An accurate mesh size and number of layers at the boundary layer near the four walls of the test section were needed to accurately simulate and describe the flow behavior in this region.

The resolution and size of the mesh (cells heights forming the mesh) and the number of cells-layers at the boundary layer were important for the turbulence model to accurately find the speed profile and further to predict the flow behavior. The CFD model allows modifying the mesh resolution and size, as well as the height of each cell by use of a non-dimensional distance $y+$. To accurately simulate a CFD model, the $y+$ distance must be calculated as a function of the (1) turbulence model, (2) Reynolds number defined by the experimental tests of the radar, and (3) flow behavior at the wake. In this study, the k-ε turbulence model was chosen to be used with $Re > 10^5$ and a wake region experiencing flow separation, recirculation, and vortices (Kroll et al., 2002), (Jameson et al., 1998).

The turbulence model k-ε recommends $y+ = 300$ to define the boundary conditions at the wall. Since it is difficult to gauge the near-wall resolution requirements for the size of the radar, the $y+$ value was estimated inside the wind tunnel test section by use of a semi-empirical equation provided by ANSYS Fluent documentation (Fluent, 2021).

For this study, it was important to calculate the height of the boundary layer inside the wind tunnel test section for the same flow conditions as the ones of the wind tunnel tests. The density was set to $\rho(22°C) = 1.196$ Kg/m^3 and the dynamic viscosity was set to $\mu(22°C) = 1.822 \times 10^{-5}$ $Pa{*}s$. The Reynolds number was calculated with Equation (3.5) for 15 m/s at the location of the radar $L = 5$ m, thus $Re_L = 5 \times 10^6$ was obtained.

The turbulence thickness δ at the location L was calculated with Equation (3.12):

$$\delta = \frac{0.382\,L}{{Re_L}^{0.2}} \tag{3.12}$$

The turbulence thicknesses δ at the locations L = 2 m and L = 5 m were $\delta_{L=2} = 4 \times 10^{-2}$ m and $\delta_{L=5} = 9 \times 10^{-2}$ m. The skin friction coefficient for a turbulent flow C_{ft} was calculated with Equation (3.13), thus $C_{ft} = 2.7 \times 10^{-3}$ for $Re_L = 5 \times 10^6$.

$$C_{ft} = \frac{0.0583}{{Re_L}^{0.2}} \tag{3.13}$$

The wall shear stress $\tau_w = 0.36$ Pa was calculated with Equation (3.14).

$$\tau_w = C_{ft} 0.5\,\rho U^2 \tag{3.14}$$

The frictional velocity U_τ = 0.55 m/s was obtained by use of Equation (3.15).

$$U_\tau = \sqrt{\frac{\tau_w}{\rho}} \tag{3.15}$$

The estimated boundary layer thickness at the radar position had a height $\delta = 4 \times 10^{-2}$ m. Therefore 15 mesh layers were installed at the boundary layer region to ensure accurate grid inflation on the whole mesh. The total height $\delta = 4 \times 10^{-2}$ m of the boundary layer divided by 15 mesh gave the value $y = 2.7 \times 10^{-3}$ m for each mesh layer by use of Equation (3.16).

$$y = \frac{4 \times 10^{-2}}{15} \tag{3.16}$$

Then, Equation (3.17) was used to find y^+ for a cell height of $y = 2.7 \times 10^{-3}$ m.

$$y^+ = \frac{\rho\, U_\tau}{\mu} y = 96 \tag{3.17}$$

Therefore, $y^+ = 96$ for the radar's wake region.

3.6.3 CFD Model Simulation Characteristics

The flow around the radar changes over time from laminar to turbulent flow with its recirculation and vortices emerging in the wake region; as a result, the CFD model of the radar was solved using a transient flow simulation. The solver was designed to simulate with a high degree of accuracy the wind tunnel tests performed on the radar. In this paper, the pressure-based method was used as it was mainly developed for incompressible low Reynolds number applications (Mach numbers below 0.3); in fact, the Pressure-Implicit with Splitting of Operators algorithm was used as a pressure-velocity calculation procedure for solving the Navier–Stokes equations. A *k*-*ε* model coupled with the Detached Eddy Simulation (DES) and a wall function with the above-calculated value of $y+$ were chosen for the flow analysis. The inlet *x*-velocity was set to its desired speed during the wind tunnel tests (8 m/s, 12 m/s, and 15 m/s). During these tests, the speed variation across the empty test section was 1% while the turbulence intensity was 0.3%; these values were used in the turbulence model. The outlet gauge pressure was set to atmospheric pressure as the outlet pressure of the wind tunnel. The radar transient simulations were calculated for more than 22,500 iterations for each case (1 case is considered for 1 flow speed and 1 angular position of the radar). To have information on the flow time variation, the simulation step time was set to a value of 10^{-4} s. The simulation time converged to an accurate solution after 2000 time steps, which corresponded to a total time of $2000 * 1 \times 10^{-4} = 0.2$ s. The Residual Convergence criteria were set to a value equal to 1×10^{-5}, to obtain accurate forces and moments values.

3.6.4 CFD Validation

This sub-section provides the validation requirements of the ASME guidelines described in Section 2.3. In total, 15 test cases were performed during wind tunnel tests, in which three forces *(Fx, Fy, Fz*) and three moments (*Mx, My, Mz*) were measured by our in-house aerodynamic scale. The radar and aerodynamic scale were mechanically connected by a non-permanent joint consisting of a bolt flange and 4 bolts (each bolt of a diameter of 10 mm). This joint has not allowed any motion in the *Fz* direction and has not allowed any *Mz* moment between the radar and the aerodynamic scale. The values measured by the aerodynamic scale were found to be very low, *Fz* = 0.002 N and *Mz* = 0.001 Nm. These *Fz* and *Mz* values were observed during experimental tests for safety reasons, to ensure that the radar and aerodynamic scale were fixed together. These values were not calculated by use of CFD as they were very low and have not provided any information on the interaction between the radar and the flow. The *Fx, Fy, Mx,* and *My* values were calculated by CFD as they were the most important loads in this research.

3.6.4.1 Linear Regression Method

Linear Regression analysis is a statistical process that allows for an estimation of the order of difference between the model's predicted values and its experimental values. The correlation magnitude between the experimental values and the predicted values can be quantified by calculating the Adjusted R^2 (R-squared) of the model. This value denoted the proportion of the variance in the experimental data that is predicted by the model data. An Adjusted R^2 of 1 indicates that the model predicts very well all experimental data, but practically models are never perfect, therefore an Adjusted R^2 has any value between 0 and less than 1. The Adjusted R^2 values were 0.9986 for *Fx,* and 0.9945 for *Fy,* therefore the prediction for *Fx* was 99.86% and for *Fy* 99.45%. The moments *Mx* and *My* have an Adjusted R^2 of 98.29% and 98.26% respectively, which suggested a very good agreement between the experimental data and the simulated data.

3.6.4.2 Area Metric Method

The Area Metric method (Chatenet et al., 2016) is part of the validation process required by the ASME guidelines when numerical models are used. This second type of validation measures the agreement between the simulated data and the experimental data by calculating the mismatch of the surface area between the two sets of data. The fact that this method allows validating a model when only a few experimental values can be measured is an advantage over other available validation methods. All experimental values were compared with the simulation values using the Area Metric method, as shown in Figure 3.11. This method measured a maximum difference of 2.34 N between the predicted *Fx* forces and the observed *Fx* forces. The Area Metric method, in a similar way, provided differences for *Fy, Mx*, and *My* which were respectively 3.43 N, 1.21 Nm, and 4.15 Nm, as shown in Figures 3.12, 3.13, and 3.14, respectively.

In conclusion, drag forces *Fx* were predicted very well with an accuracy of 99.86% (Linear Regression), and with a small mismatch of 2.34 N using the Area Metric Method.

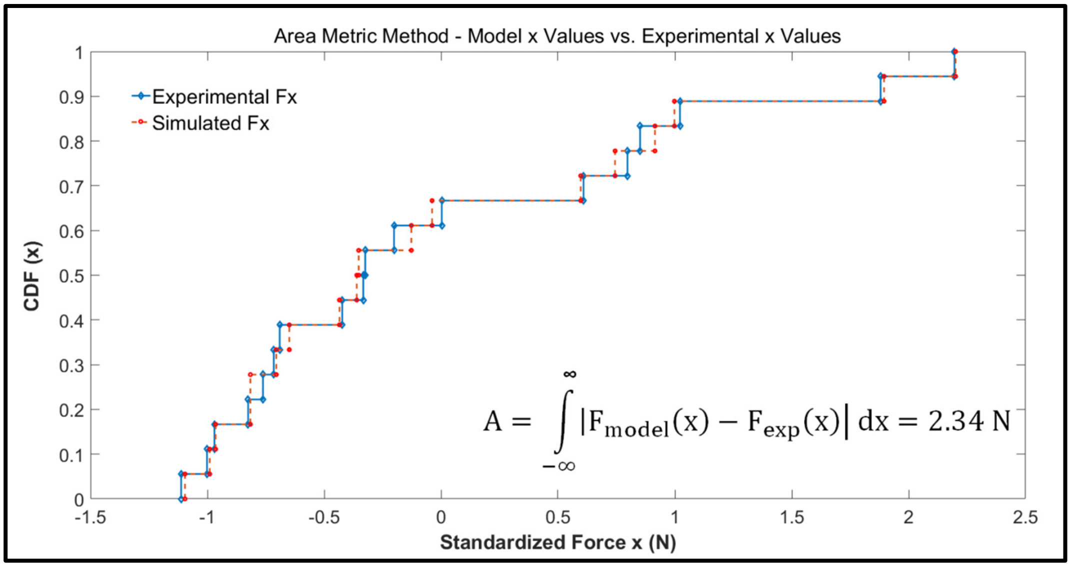

Figure 3. 11 Area Metric results for *Fx*

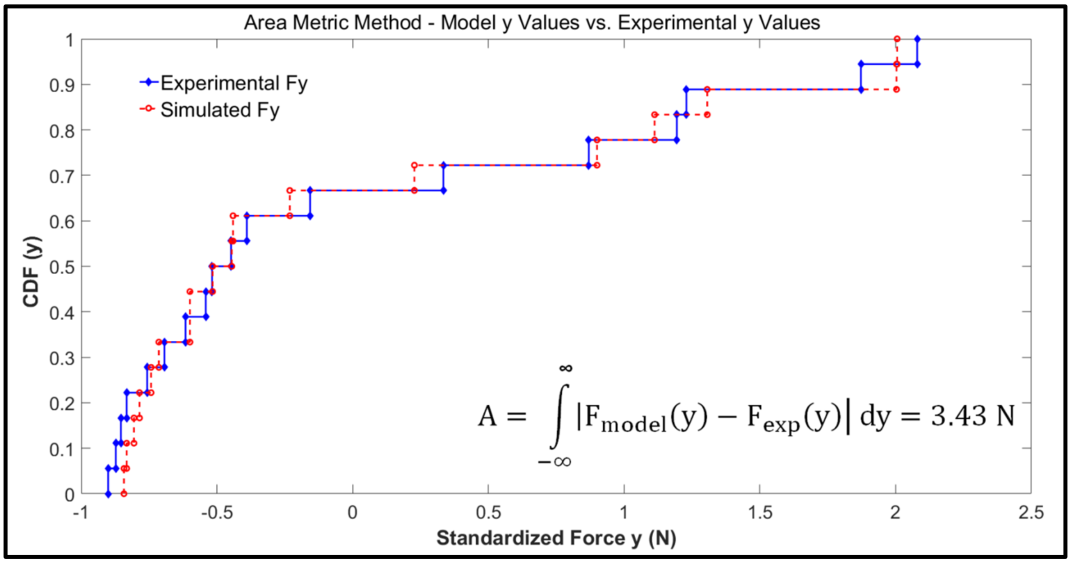

Figure 3. 12 Area Metric results for *Fy*

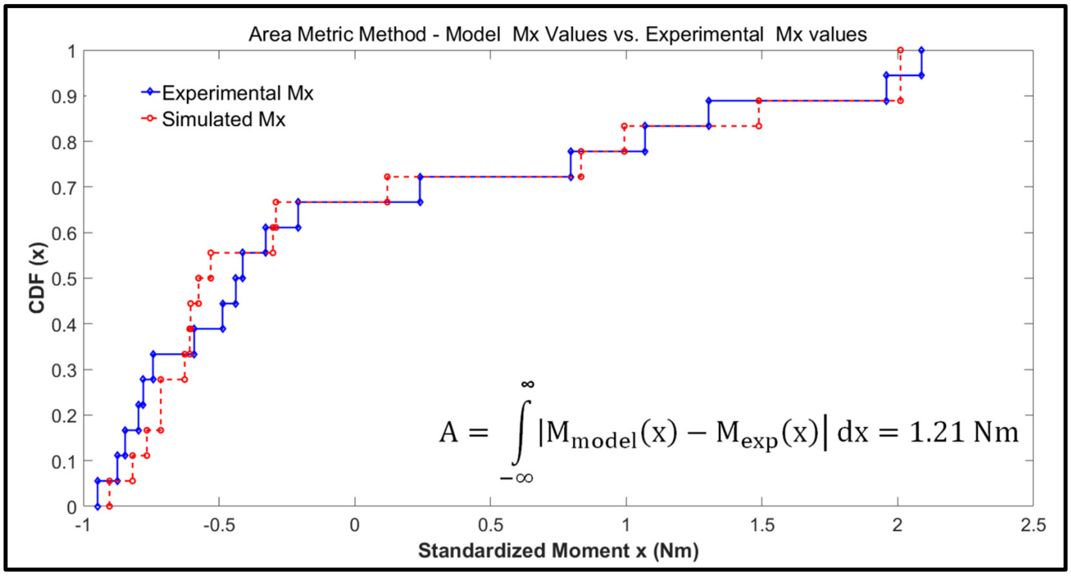

Figure 3. 13 Area Metric results for *Mx*

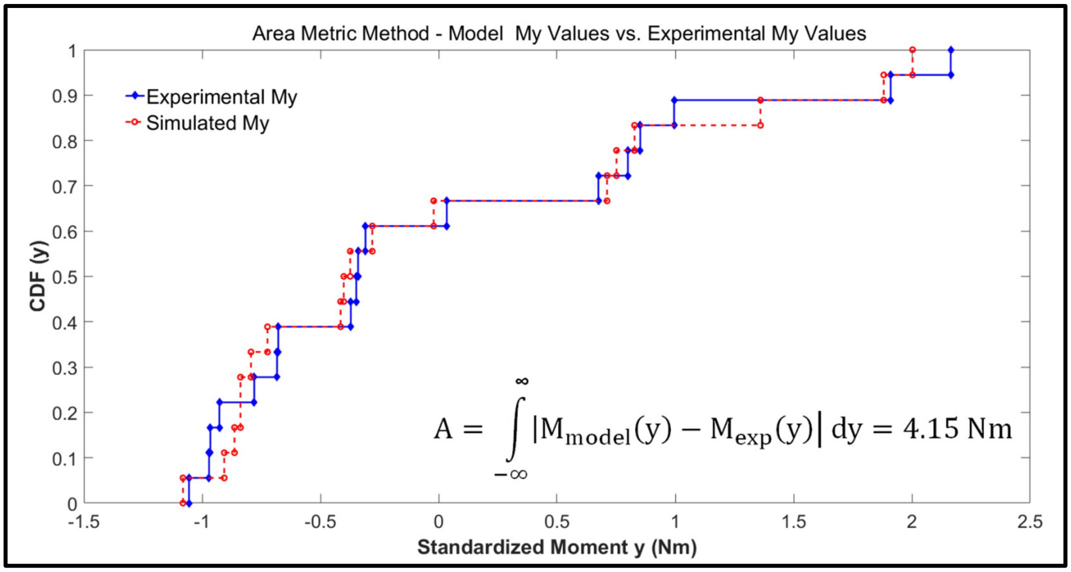

Figure 3. 14 Area Metric results for *My*

3.7 Flow Analysis and Discussion

Literature review suggests that the flow behavior near blunts bodies have distinctive and recognized features contrasting those of streamlined bodies. Following flow disturbance on the blunt body, its motion can either continue developing its turbulent behavior at the wake or it can be damped by means of a turbulence reduction system. The CFD results have allowed analyzing the boundary layer behavior and unsteady wake flow region of the original radar and the radar with the turbulence reduction system. Figure 3.15 shows the main locations affecting flow behavior, the initial contact of the fluid with the upper surface of the radar, denoted by position 2, was called "leading edge" and the final contact point, denoted by position 4, was called "trailing edge". The radar surface where most turbulence fluctuations occurred was called "upper surface" and represented by position 3. The "front region" and "rear region" are denoted by positions 1 and 5, respectively.

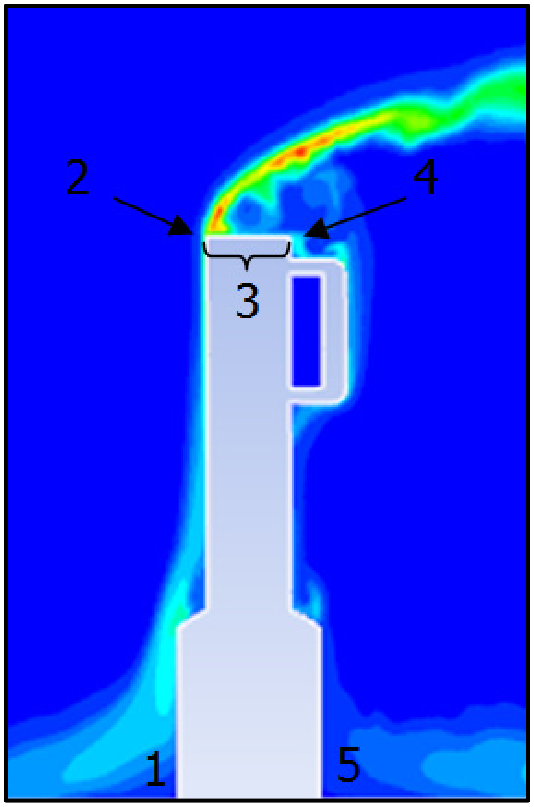

Figure 3. 15 Flow interaction locations
on the radar surface

3.7.1 Original Radar Flow Analysis

The validated CFD model gave new insights to study the fluid in contact with the radar surface from its boundary layer separation to vortex formation and turbulent transition. This section describes the transitional state where a laminar flow interacts with a blunt body by provoking boundary layer separation, vortex formation, and flow instabilities. When the flow approached the radar blunt body, there was an increase in dynamic pressure at its upper surface and a sudden decrease in static pressure at the “front region” and at the “rear region”. The rapid increase in dynamic pressure at the upper surface of the radar produced a vacuum in the wake region shown in Figure 3.16 in blue color. As the flow moved forward, the main recirculation region started to form with a high rotation dynamic energy shown by red, yellow, and green colors. The fluid at the front and the rear of the radar moved slowly with respect to the rest of the flow by provoking the boundary layer to separate abruptly at the “leading edge”. The high flow velocity and dynamic pressure at the upper surface increased the turbulent energy in the wake region.

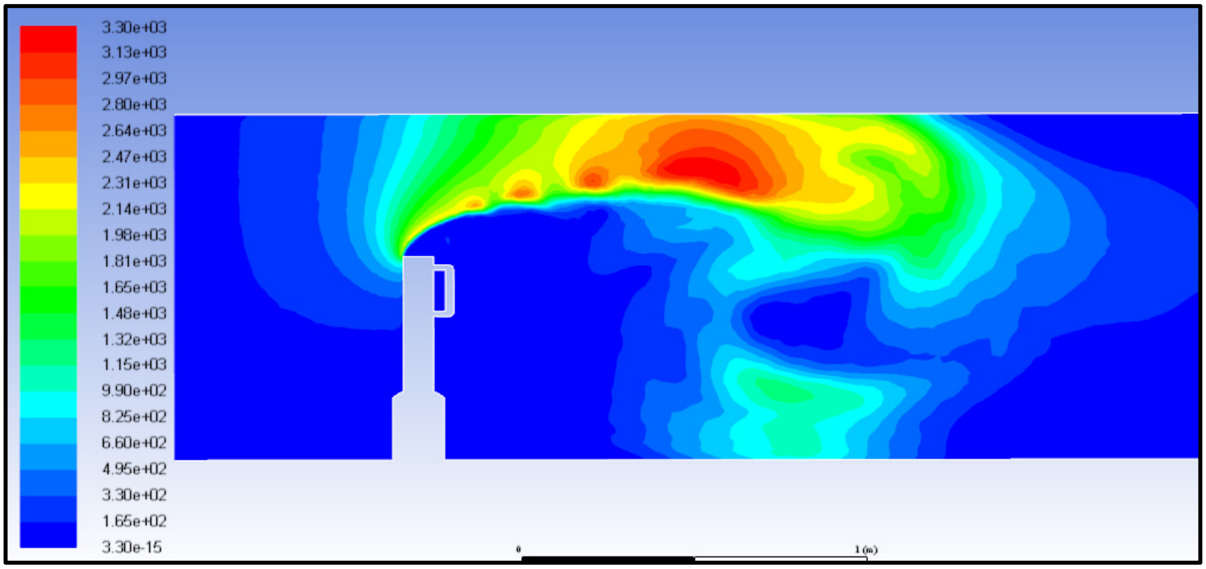

Figure 3. 16 Simulation results of dynamic pressure at the wake region

It is known that the flow surrounding a blunt body is mainly formed by pressure drag, and a small fraction of it is due to friction drag. The flow structure seen in Figure 3.17 contains the major components of a turbulent flow calculated with fluctuations of the mean flow speed, as described by the turbulence intensity *I* in Equation (3.10). In Figure 3.17, at position **1**, the flow separates from the radar surface, and the flow transitions to its turbulent state with its intensity close to 20.6%. At position **2**, the separated shear layer gain momentum, and small irregular eddies appear with a high-intensity ratio *I* = 29.4%, as seen at position **5**. High intensities regions are representing velocities fluctuations and vortices. The flow tries to reattach to the radar's upper surface and also to its rear handles as shown at position **3**. The main recirculation region is formed at a distance of 1 m from the radar location. The high velocities gradients at the wake and close to the upper wall (of the test section) are shown in green and yellow colors with their intensities ranging from 10% to 20% at position **4**. At the main recirculation region, the high kinetic energy generates a vortex with a high turbulence intensity ranging from 10% to 29.4%, as shown at position **5**. It is known that multiples recirculation regions occur on blunt bodies inside wall-bounded flows, as shown at position **6**.

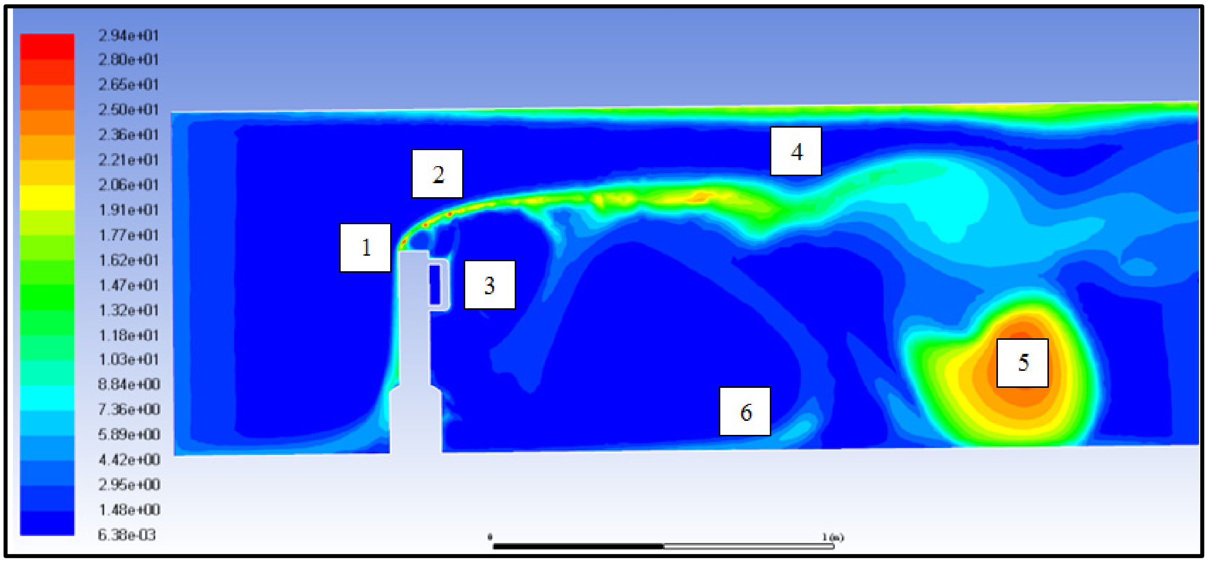

Figure 3. 17 Simulation results of turbulence intensity *I* at the wake region

Immediately after contact with the blunt body, the fluid had changed to a fully turbulent flow. Figure 3.18 shows the streamlined directions and magnitudes of the fluid dynamic pressure field in the wake of the radar body. Initially, the flow separates abruptly at the "leading edge" of the radar due to a high range of dynamic pressures shown by cyan, yellow and orange colors in Figure 3.18; these high-pressure fields prevented the boundary layers to re-attach to the "upper surface" and thus, to produce two recirculation regions; the first recirculation region, shown by number **3**, was attached at the rear of the radar surface, with the same diameter as the height "*H*" of the radar. The angular kinetic energy was not higher compared to that of the rest of the fluid in the wake region, but the local rotation was oriented in the opposite direction of the incoming flow (counter-clockwise rotation). The second recirculation region, shown by number **4**, had a diameter three times higher than the height of the radar "*H*", it was located at two lengths "*H*" from the rear of the radar, had high clockwise rotational direction and up to five times (2866/573 = 5 times) the dynamic pressure higher compared to the dynamic pressure of the rest of the flow. The pressure distribution at the front and back of the radar's base produced two separation bubbles identified by number **1** at the "front region" and by number **2** at the "rear region". The dynamic pressures, in these regions, were low and close to the stagnation pressure and local flows were moving in the clockwise direction.

The impact of the accelerated fluid on the surface of the radar has increased the turbulence production in the wake region; this flow transition to a turbulent regime can be observed and analyzed at the "upper surface" of the radar body. The original shape of the "upper surface" of the radar did not dissipate well the energy produced by the impact of the fluid with a blunt body into the fluid "kinetic energy", therefore it created fluctuating instabilities and increased turbulence production.

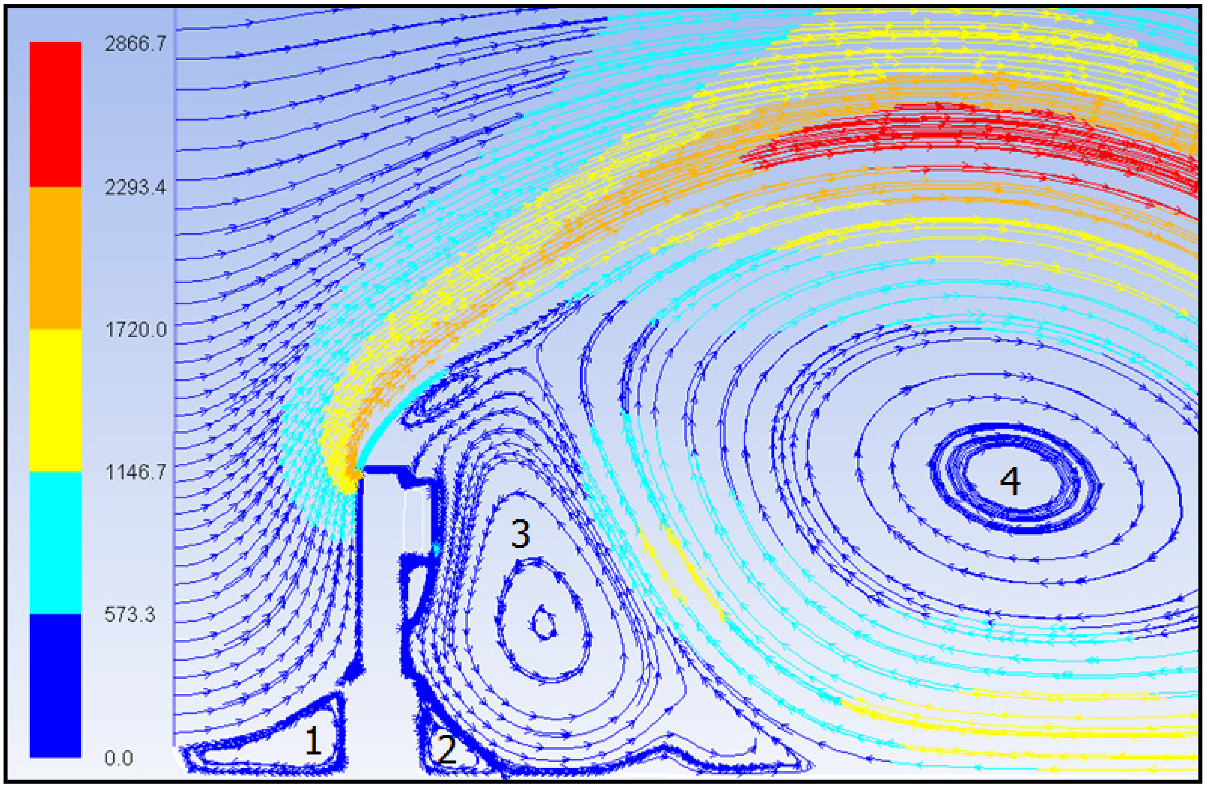

Figure 3. 18 Streamlines simulation of the dynamic pressure (Pa) for the original radar

Figure 3.19 shows the isosurfaces obtained using the Q-Criterion applied to the velocity flow of 15 m/s. The isovalues presented in Figure 3.19a–f show the longitudinal vortices variation in time at the wake region of the radar without a turbulence reduction system. The dominant vortices are emphasized and clearly predicted from the beginning of the simulation. The topology of the turbulent flow field at the wake region is well solved and visualized. A vortex structure is present at the upper surface and the base of the radar body. This vortex structure persists and gains in strength at the upper surface of the radar, and is developed into the main structure at the wake region. The boundary layer over the upper surface of the radar is believed to be responsible for the vortex growth and its intensity gain. It can therefore be concluded that there are no additional main vortex structures in the wake

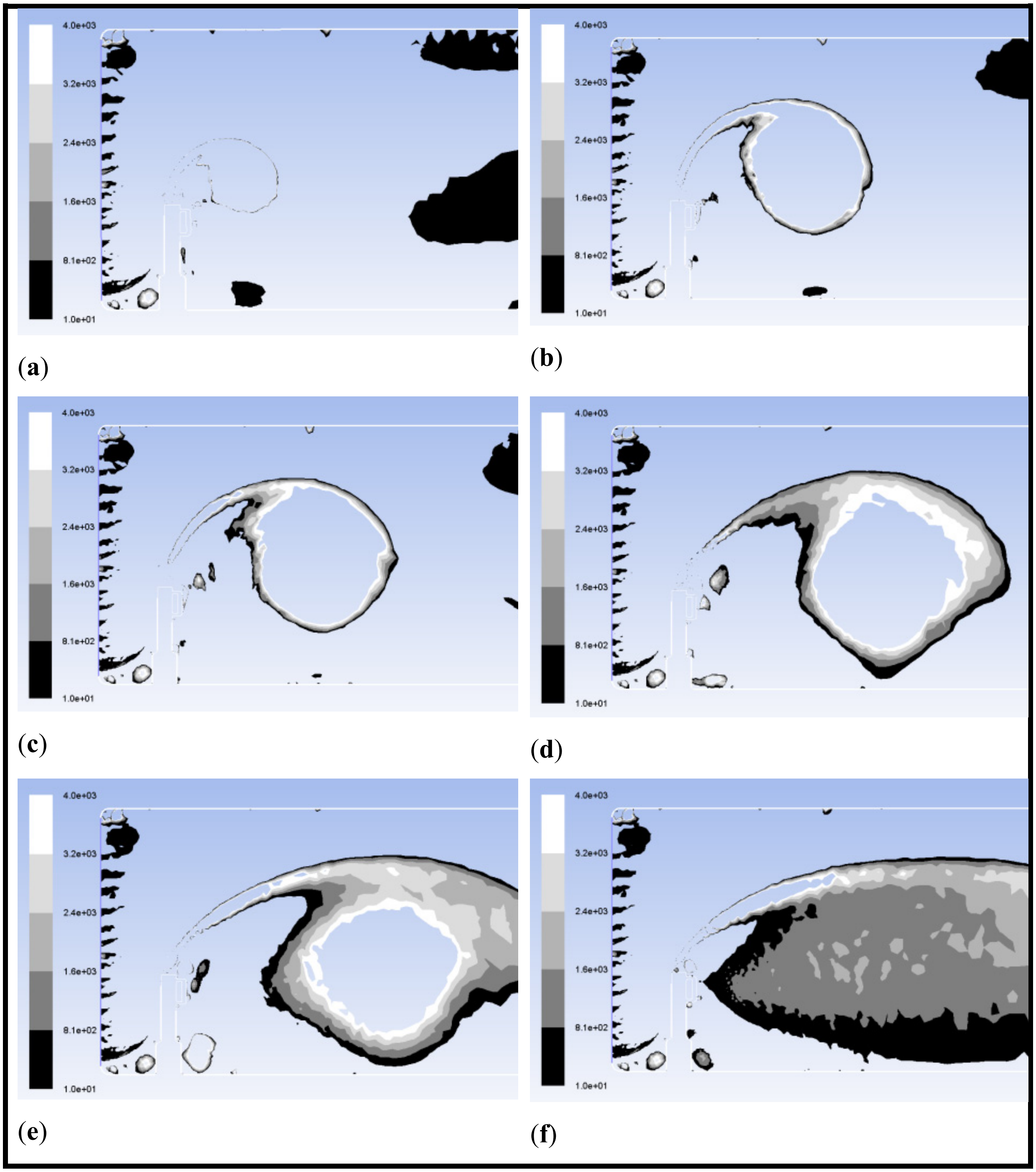

(a) (b) (c) (d) (e) (f)

Figure 3. 19 In plane Q-Criterion simulation results of vortices variation with time (a) to (f) on the original radar body for Q = $[10^1 - 10^6]$

3.7.2 Radar Mounted with a Turbulence Reduction System Flow Analysis

In this section, the wake region of the radar mounted with a proposed turbulence reduction system was analyzed. The radar surface denoted by "upper surface" in Figure 3.15 by number **3** is the location where the turbulence reduction system was installed; in this location, the dynamic pressure was higher, flow separation was important and eddies started to occur.

Figure 3.20 shows the original radar geometry (**a**) equipped with the proposed turbulence reduction system (**b**); The sharp edge was changed to a streamlined edge, as shown by number **1**; at the upper rear surface of the radar, a turbulence reduction system was positioned, as shown by number **2**. The system had a length of 0.50 m and was inclined with an angle of 25° at the top of the radar. The turbulence reducing system could have a high impact on the reduction of abrupt pressure gradients at the surface of the radar, and an important decrease in vortices formation downstream the wake region. The size and location of the turbulence reduction system did not affect the weight or the operating behavior of the radar.

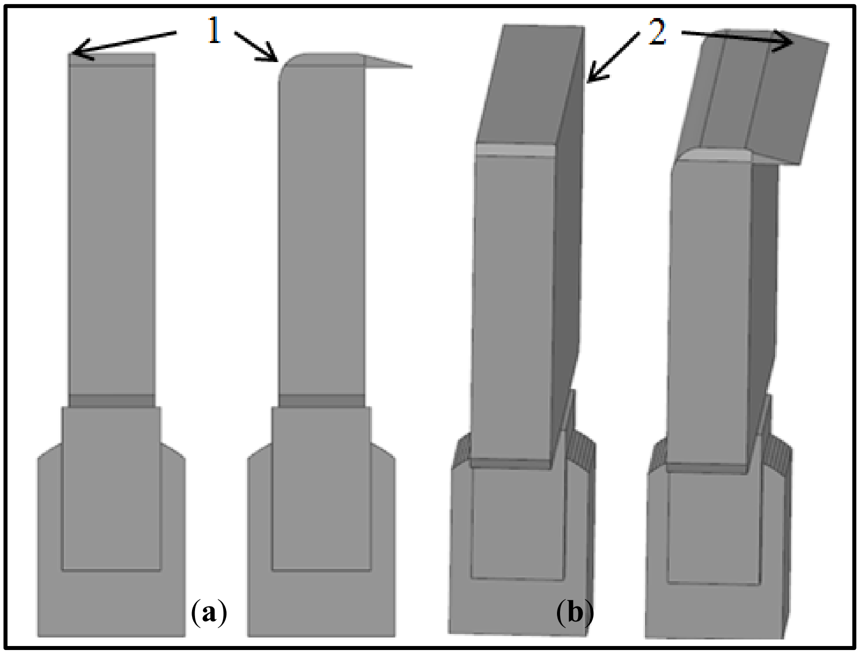

Figure 3. 20 Original radar versus modified radar geometry with turbulence reduction system (a) side view and (b) upper view

The optimization of the curvature of the front upper surface of the radar referred to in our article by "leading edge" was considered. The optimized radius of the leading edge should be calculated by considering a compromise between the CFD simulation models (using the same metrics presented in this paper to evaluate the turbulence reduction system) and the manufacturing tolerances needed for the prototype. It is well-known that in the field of experimental testing, the numerical model predictions have to take into account the fabrication (machining) limitations (tolerances) of a prototype.

The "leading edge" optimization shape algorithm has to take into account the fabrication limitations variables (constraints) to produce a viable solution. The development of a prototype with the proposed "turbulence reduction system" and with an "optimized leading edge shape" is part of future research.

It is important in this section to find a way to compare the performance of the turbulence reduction system on the original radar shape. Figures 3.21 and 3.23 present the results in a quantitative form, while Figures 3.20 and 3.22 presented the results in a qualitative form. Figure 3.21 shows the streamline dynamic pressures on the radar body mounted with the turbulence reduction system, which gradually increases from low-pressure regions visualized in blue color to higher pressure regions shown in orange and red colors. The four recirculation regions shown in Figure 3.18 are also presented in Figure 3.21. The main recirculation region indicated by number **4** in Figure 3.21 has reduced in size to a diameter of 1.4 times the height "*H*" of the radar. The secondary recirculation region indicated by the number **3** reduced in size to 0.3 times the height "*H*" and the two separation bubbles indicated by numbers **1** and **2** were reduced in size significantly.

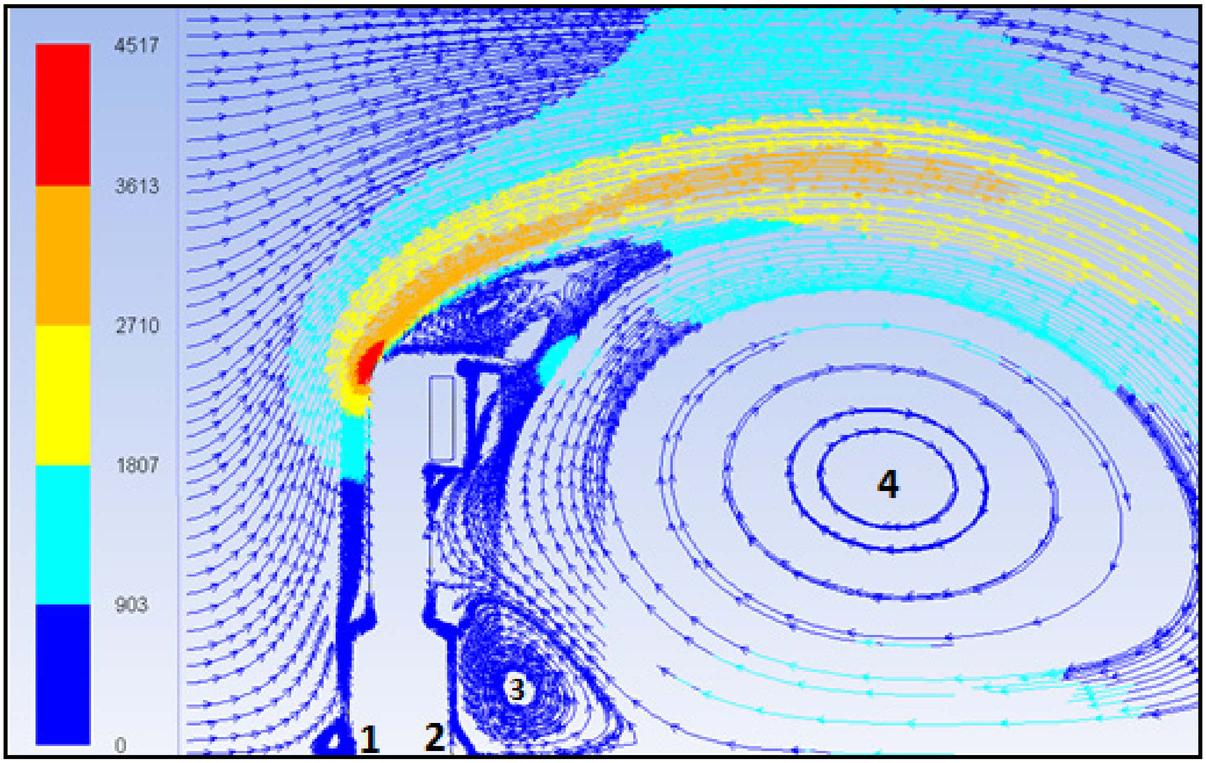

Figure 3. 21 Streamlines simulation of the dynamic pressure (Pa) for the radar with turbulence reduction system.

The local turbulence intensity data in five locations inside the wake region of the original radar, and of the radar with the turbulence reducing system can be seen in Figure 3.22. These five locations behind the radar body and along the *z*-axis (vertical plane) were chosen because of the high-pressure gradients and important recirculation regions obtained numerically, and are also shown in Figure 3.18 and Figure 3.22. The five locations described the flow behavior at the radar rear (x = 0 m), at 0.2 m from the radar rear (x = 0.2 m), at 0.4 m from the radar rear (x = 0.4 m), at 0.7 m from the radar rear (x = 0.7 m) and at 1.2 m from the radar rear (x = 1.2 m) were calculated. The normalized values between 0 and 1 of the turbulence intensity I were calculated at five downstream locations for the two radar models. The original radar model was represented by a "solid" line and the radar with the turbulence reduction system was shown by a "circle dash" line. A significant decrease in flow turbulence was found for the radar with a turbulence reduction system at each of the five wake locations. In Figure 3.22, abrupt changes in turbulence intensities seen by "peaks" in the solid lines (original radar) for all locations were considerably reduced due to a gradual evolution of the turbulent flow behavior downstream the wake, which is shown by the "circle dash" lines (radar with the turbulence reduction system). The wake regions with the highest improvement in flow conditions were located above the "upper surface" of the radar, where the turbulence reduction system was installed. These locations above the radar, at heights between $z = 0.6$ m and $z = 1.2$ m, presented a turbulence intensity reduced by half ($u^2/U^2 = 0.5$).

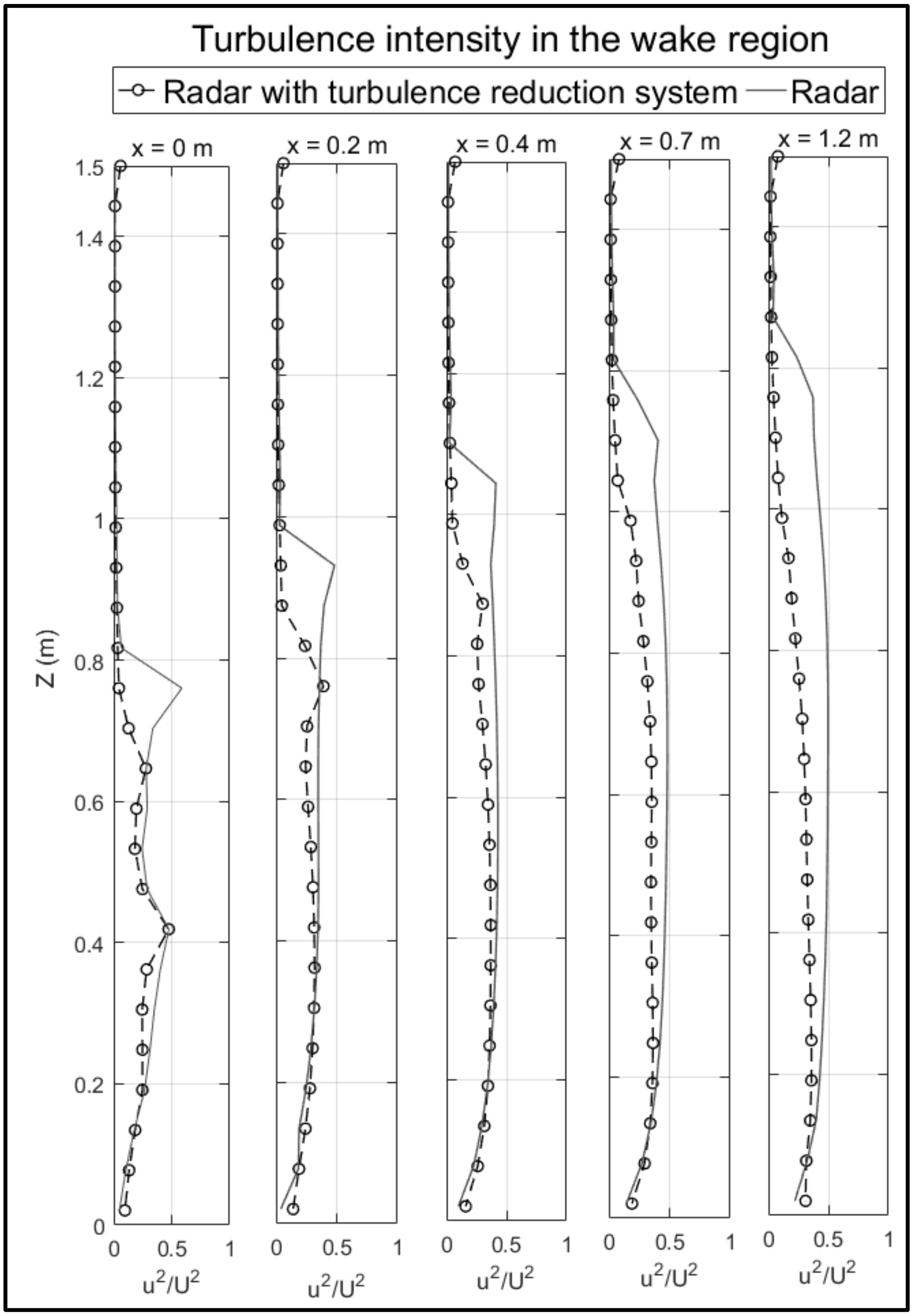

Figure 3. 22 Turbulence intensity at five wake locations of the original radar and the radar with the turbulence reduction system

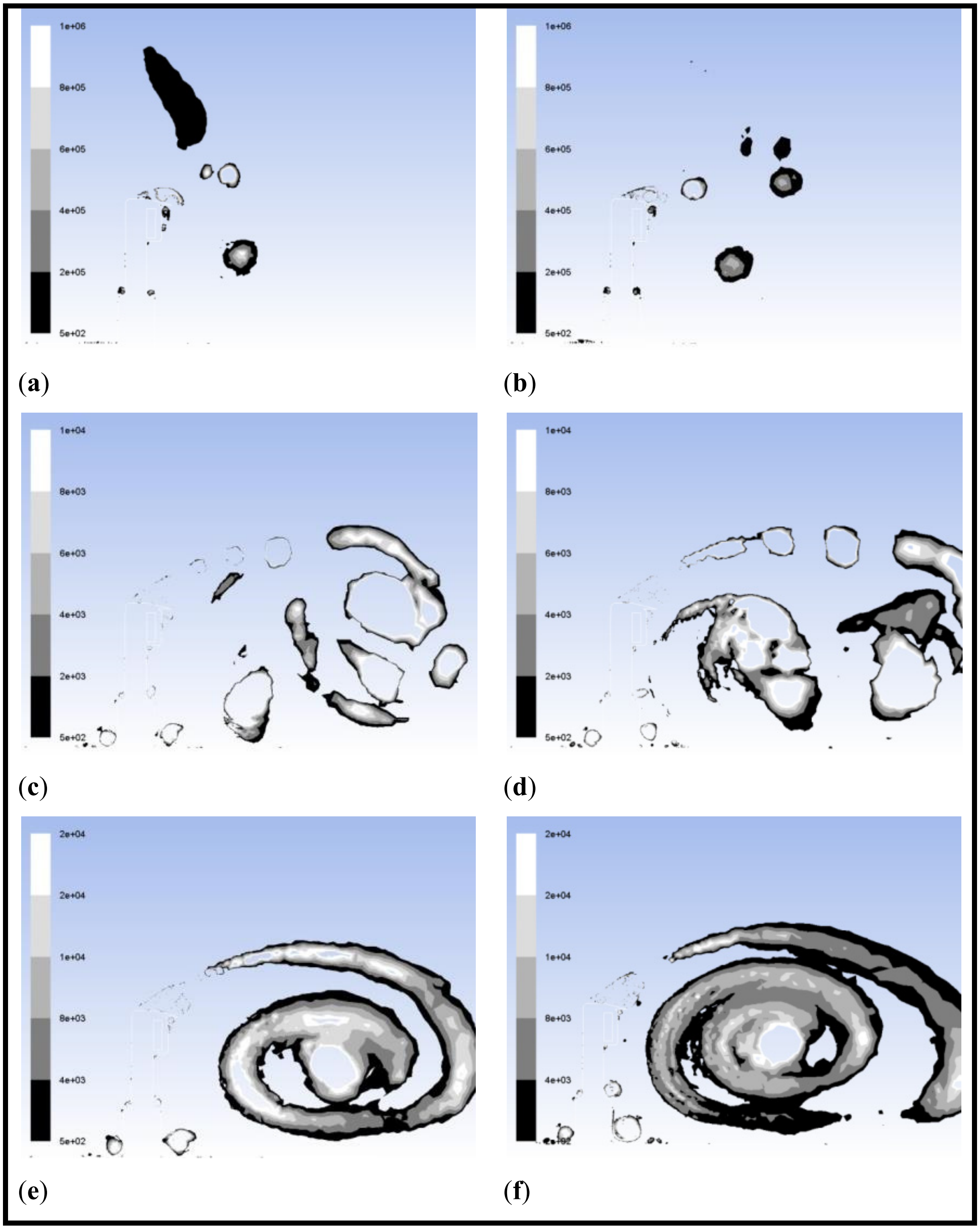

Figure 3. 23 In plane Q-Criterion simulation of vortices variation with time (a) to (f) of the flow near the radar with a turbulence reduction system for Q = $[10^1 - 10^6]$

The Q-Criterion separates very well the regions where the flow rotations are high. The Q threshold identifies the longitudinal vortices and allows one to find the main vortex structure in the wake region. The chosen upper and lower Q limits do not have any effects on the location or size of the detected vortex. The vortex structure shown in Figure 3.23 grows in size and strength as it spans downstream the radar body. The isovalues shown in Figure 3.23a–f show the longitudinal vortices variation in time and it can be noted that the vortex radius is higher when a turbulence reduction system is not installed on the radar. In the case of the radar with turbulence reduction system, the main vortex had moved closer to the reduced scale radar body. The boundary layer over the upper surface of the radar is still originated from the main vortex, but its kinetic energy is smaller than the kinetic energy needed for the vortex growth.

3.7.3 Metrics for Turbulent Flows

The flow differences in the wake regions of the original radar (**a**) and of the radar with the turbulence reduction system (**b**) were shown in Figure 3.24. The high-pressure gradients, the short transition length, the boundary layer separation, and the fully turbulent behavior at the time when the flow contacts the radar body can be seen in Figure 3.24(**a**) indicated by number **1**. The proposed turbulence reduction system had a streamlined shape with a pre-determined flap that allowed the reduction of flow fluctuations and vortex shedding production. The improved flow behavior had also a positive impact on the turbulence intensity, the pressure distribution coefficient, the transition point, and the drag coefficient of the original radar shape. The number **2** indicated in Figure 3.24(**b**) presents the improved wake region of the radar with the turbulence reduction system.

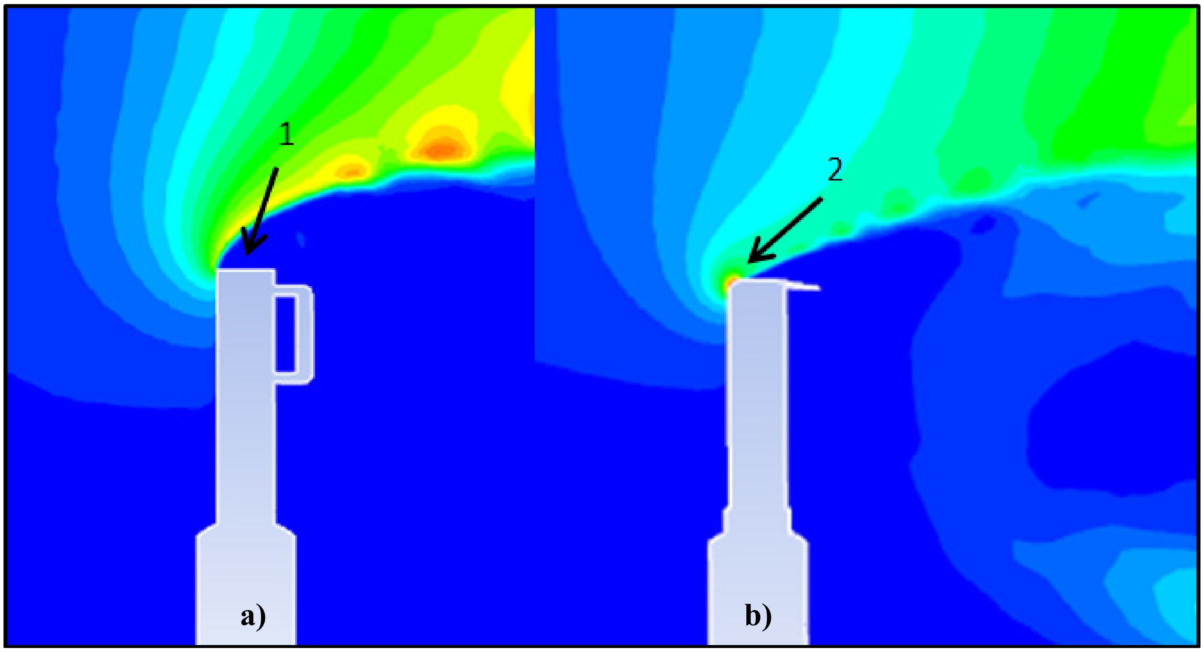

Figure 3. 24 Pressure gradients simulation on the original radar (a) and for the radar with turbulence reduction system (b)

The turbulence intensity *I* expressed in Equation (3.10) was one of the parameters used to measure the performance of the turbulence reduction system. Figure 3.25 shows the turbulence variation at the surface of the radar called the “upper surface”. At the initial point of contact location 0% at the surface of the radar, the turbulence intensity has increased to 15%, compared to the laminar incoming flow with lower turbulence intensity ($I = 0.1\%$). For the first half of location 0% to 50%, it can be seen that the turbulence intensity values fluctuations range from 0.15 = 15% and 0.20 = 20%. At the second half of location 50% to location 100%, the numerical model predicts higher values of turbulence, up to 0.50 = 50%, the boundary layer can no longer reattach to the surface of the radar and the flow becomes fully separated, as seen on Figure 3.25.

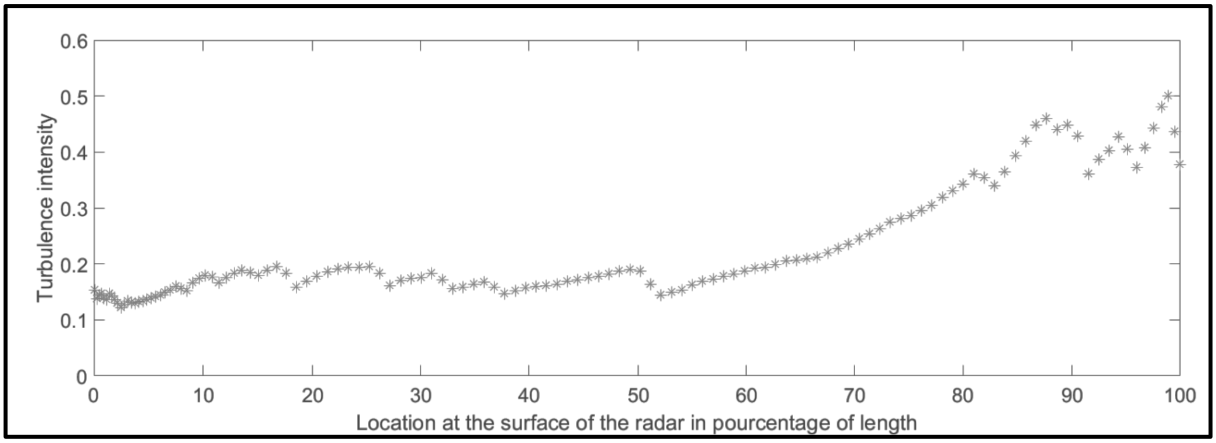

Figure 3. 25 Turbulence intensity at the upper surface of the radar with turbulence reduction system

Figure 3.26(**a**) shows the transition point on the original radar model, as another metric parameter needed to measure the improvement of the flow at the wake region. The boundary layer separates at the location 6.5% from the leading edge of the radar, shown by number **1**. After this point, a flow in the opposite direction to the free stream creates a recirculation region, which keeps the boundary layer from reattaching to the surface. The turbulence reduction system allows the boundary layer to remain attached to the surface at a longer distance. The turbulence transition point had been delayed to the location 50% = 0.50, as shown in Figure 3.26(**b**) by number **2**. The improvement of the transition point has been also shown in the numerical data presented in Figure 3.25. It has been observed that the transition point has been delayed by $\frac{50\%}{6.5\%}$ = 7.6 times with the aid of the turbulence reduction system. After the location 50% = 0.50, the turbulence increased abruptly with high-intensity values, which indicates a fully detached turbulence flow.

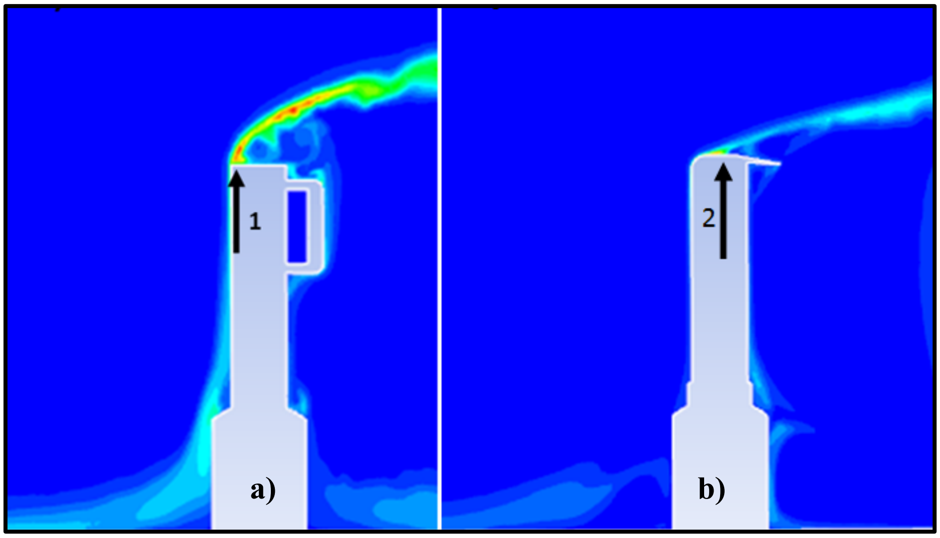

Figure 3. 26 Transition point location simulation on (a) the original radar versus (b) the radar with turbulence reduction system

The pressure coefficient C_p contributed to the evaluation of the turbulence reduction system. The dimensionless values of C_p, as expressed in Equation (3.8), can be used to determine the maximum flow speed locations and magnitudes of adverse pressure gradients, which are associated with regions of flow transition and boundary layer separation. The numerical data of pressure distributions at the surface of the original radar and the surface of the radar with the turbulence reduction system are presented in Figure 3.27. The pressure distribution changes abruptly from high static pressure to a low static pressure due to the radar blunt shape while the C_p varies on a short distance because of the fact that the boundary layer could not develop gradually at the surface of the original radar, as indicated by the data shown in the “solid” line on Figure 3.27 by number **1**. The “circle dash” lines on Figure 3.27 present pressure coefficients variation on the radar upper surface, that were obtained from the CFD model of the radar mounted with the turbulence reduction system.

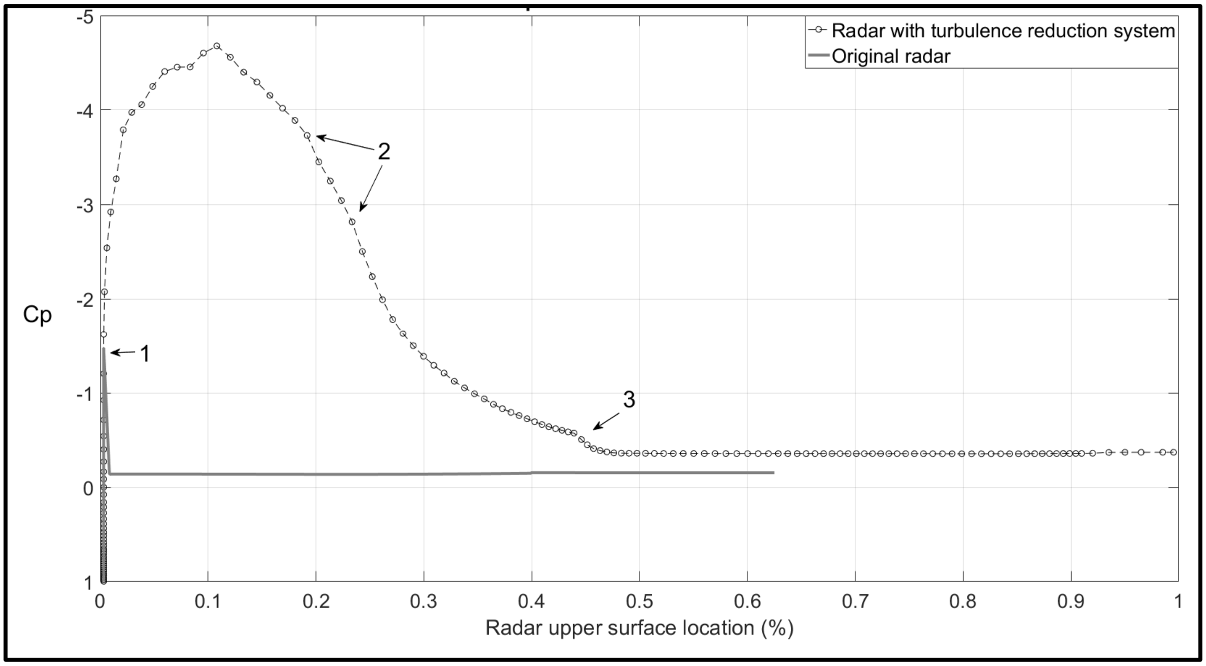

Figure 3. 27 Pressure coefficients on the upper surface of the radar

A pressure gradient $C_p = -4.67$ that acts as a "suction force" of the boundary layer on the radar's upper surface was found at the location 10.2%. This location of minimum C_p also indicates the beginning of the "pressure recovery" region. After this C_p value, the adverse pressure gradients keep increasing at the surface of the radar, but the high values of the local static pressure kept the boundary layer from its reattaching, as indicated by number **2** in Figure 3.27. The time when the boundary layer separated, and when the flow was unsteady and fully turbulent at the surface of the radar was indicated by number **3**. Downstream this transition point, from location 45.5% to the trailing edge of the radar (location at 100%), the pressure coefficient was constant, $C_p = -0.3$, the boundary layer thickness was very small, the local flow was moving slowly and the turbulence intensity values were the highest.

In this section, the drag coefficient was used to measure the drag force reduction of the radar body. The flow around a blunt body separates early, resulting in adverse pressure gradients at its surface by increasing the boundary layer separation and the contribution of pressure drag or "form drag" to the total drag of the body. However, the magnitude of the pressure drag can be reduced by improving the flow conditions at the wake region and by delaying flow separation. To evaluate the turbulence reduction system in terms of drag reduction, we had to use the experimental data collected for the original radar body, as presented in Figure 3.6. The angular position of zero degrees for the radar body and a flow Reynolds number of 4×10^5 was chosen because of the fact that these conditions are the most demanding and challenging operating conditions for the radar presented in this study. The drag coefficient for the original radar was $C_d = 3.51$ while $C_d = 3.17$ for the radar mounted with the turbulence reduction system.

The high effectiveness of the turbulence reduction system led to the turbulence intensity reduction at the surface of the radar, the flow transition delay, while the transition point moved downstream the surface of the radar and increased the boundary layer "suction force"; thus, major positive impacts were observed in the "form drag" produced by the blunt body. It is concluded that the turbulence reduction system has decreased the drag coefficient of the original radar by a percentage of $\frac{(3.17-3.51)}{3.51} = -9.67\%$.

3.8 Conclusions

The new methodology proposed in this paper allowed a detailed investigation of the wake region of the original radar body and the radar body with a turbulence reduction system. The numerical results obtained on the original radar's wake region showed periodic vortex shedding, boundary layer separation, high levels of turbulence, and induced drag; The nature of the adverse pressure gradient and high turbulence intensity values at the radar surface needed a mechanism to reduce flow fluctuation and to allow the boundary layer to increase.

This study showed also the results of the Price-Païdoussis wind tunnel experiments for a large "ground surveillance radar". The wind tunnel test data completed, and thus validated the numerical results obtained for the Strouhal number, Reynolds number, and drag coefficients values. Spectral analysis was also performed on the experimental data. The forces and moments data showed high dependency on the angular position of the radar and low dependency on the wind tunnel flow speed. Vortex shedding tended to occur at any angular position at different shedding frequencies. Based on experimental values, one shedding frequency and one high drag coefficient were obtained at Reynolds number 4×10^5 and when the radar was perpendicular to the flow. It was decided to measure the performance of the proposed "turbulence reduction system" for the same flow conditions.

The flow pattern at the wake region was identified in the absence of distorting effects of direct measurements using probes and visualization methods, such as "white smoke" and "tufts" attached to a wing model surface. It was demonstrated that a turbulence reduction system mounted on the radar surface can improve its behavior at all flow conditions. The CFD model was an important tool to understand and analyze the flow around the radar because of the fact that it indicated the regions where flow separated and then reattached; in these regions of stagnation and recirculation, eddies and vortices were formed. Using the CFD model data, a turbulence reduction system with an optimized upper profile and a streamlined flap surface was proposed.

Based on the CFD model results, it was concluded that the adverse pressure gradients have significantly decreased at the upper surface of the radar with its turbulence reduction system mounted. The proposed system strongly influenced the unsteady flow fluctuations and vortex shedding as the large turbulent motions were suppressed in the wake region. The numerical results showed an important reduction of the turbulence intensity as well as a growth in the boundary layer region compared to that of the original radar configuration. The pressure distribution developed by the proposed system helped the boundary layer to reattach to it. The turbulence reduction system produced a reduced recirculation region at the rear of the radar's surface, due to a better control of the incoming flow.

As future work, the authors believe that the methodology proposed in this research will be useful to study and quantify unsteady flow regimes where experimental measurements of the flow are limited or difficult to obtain. A very good experiment would be able to describe and analyze the flow near a self-oscillating flexible membrane placed in a laminar flow; the proposed new method for flow analysis could evaluate if the vortices generated at the wake are contributing to the flapping oscillation of the membrane.

It would be also interesting to design an adaptive turbulence reduction system that will use a brushless motor to change its upper surface position. The research will also include a CFD analysis to measure the reduction of the drag coefficient, the flow transition delay, and the turbulence intensity reduction for different radar upper surface shapes and angle of attack.

Acknowledgments: This research was performed in the frame of the Canada Research Chair in Aircraft Modeling and Simulation Technologies. The authors would like to express their thanks to Michael Païdoussis and Stuart Price for the donation of the Price-Païdoussis Open Return Subsonic Wind Tunnel at the LARCASE research laboratory at École de technologie supérieure. Many thanks are dues also to NSERC and to FLIR Systems team, as part of this research was done using the NSERC Engage program. The authors would also like to thank LARCASE's Oscar Carranza for the design and manufacturing of the large test section needed to accomplish this project.

CHAPITRE 4

NEW VALIDATION METHODOLOGY OF AN ADAPTIVE WING FOR UAV-S45 FOR FUEL REDUCTION AND CLIMATE IMPROVEMENT

Manuel Flores Salinas, Ruxandra Mihaela Botez and Guy Gauthier

Department of Systems Engineering, École de Technologie Supérieure,
1100 rue Notre-Dame West, Montreal, Québec, Canada H3C 1K3

Paper published in MDPI Applied Mechanics Journal, January 2023

Résumé

Une nouvelle méthodologie multidisciplinaire est présentée dans cet article pour la conception, l'optimisation aérodynamique et la validation d'un prototype d'aile déformable. Le cadre d'optimisation intègre la conception, l'analyse par éléments finis et la validation du modèle. Un modèle numérique en dynamique des fluides de l'aile déformable et de l'écoulement a été développé et validé avec des mesures des charges obtenues expérimentalement, telles que la portance, la traînée et le rapport portance/traînée. Une nouvelle stratégie d'algorithme génétique a été choisie pour trouver les formes de profil optimisées sur l’extrados de l’aile. La fiabilité de la méthodologie proposée a été étudiée à travers la conception, la fabrication et des essais en soufflerie du prototype de l’aile déformable proposée pour l'UAV-S45. Les résultats de simulation et expérimentaux ont montré une faible production de la traînée et un rapport portance/traînée élevé, qui se traduit par une réduction de la consommation de carburant, une augmentation de l'autonomie de vol en régime de croisière et ainsi une protection du climat.

Abstract

New knowledge in multidisciplinary methodology is presented in this article for the design, aerodynamic optimization, and model validation of an adaptive wing prototype. The optimization framework integrates the design, the finite element analysis, and the model validation. A computational fluid dynamics model of the adaptive wing and the flow in its vicinity was developed and validated with experimental metrics, such as the lift, the drag, and the lift-to-drag ratio. A new genetic algorithm strategy was chosen to find the optimized airfoil shapes for the prototype's upper surface. The reliability of the proposed methodology was investigated through the design, manufacture, and testing of a wing prototype proposed for the UAV S45. The experimental and simulated results have shown a low drag production and a high lift-to-drag ratio of the adaptive wing prototype that will translate into a reduction in fuel consumption and an increase in cruising flight range and therefore into climate improvement.

4.1 Introduction and Literature Survey

Aerodynamics and structures have motivated aircraft designers to apply new methodologies for reducing fuel consumption and increasing the cruising flight time of unmanned aerial vehicles (UAVs). To improve wing efficiency, researchers have investigated lifting surface optimal configurations by performing aero-structural optimization (Ameduri & Concilio, 2020). The aircraft structure was designed to give optimum cruise performance while withstanding the critical loads corresponding to other flight conditions. These studies in aerodynamic analysis have shown that wing optimization should be considered as early as possible in the UAV design process to optimize the overall performance (Giuliani et al., 2022). It is expected that adaptive wing technologies will become essential in the future of UAV design due to the development of improved aeroelastic concepts in UAV structures and the introduction of new materials with high strength and a high stiffness-to-weight ratio, such as polymer materials (Pecora, 2021). These adaptive wing structures and new materials pose a considerable modelling challenge as they involve highly coupled and nonlinear interactions between the aerodynamic and the structural dynamics (Dimino, Lecce & Pecora, 2017).

4.1.1 Wing Design Methodologies

The high level of interaction between the rigid-body dynamics and the structural dynamics poses a significant challenge to a successful actuation of wing system design. Aircraft structures must sustain significant loading variations when flying through turbulence and must suppress catastrophic aeroelastic phenomena such as flutter. One of the earliest works in the field of wing design was performed by Suzuki (Suzuki, 1993), who minimized wing structural weight by designing the structure and the control system simultaneously. An aeroservoelastic design framework was also presented by Haghighat *et al.* (2012), who considered the interactions between the aircraft structure and the control system. The structural and the control optimization were performed separately. The same authors also considered maneuver load inaccuracies and their effects on optimum design.

In a traditional design process, the aircraft configuration is first designed, followed by the control system design; this prevents the flight control system from affecting the aircraft configuration (Arena, Concilio & Pecora, 2019). It has been shown that by designing the aircraft configuration and the actuation control system (for the adaptive wing) concurrently these two design optimizations can improve aircraft performance (Gundlach, 2012).

A variety of modeling and simulation methods to implement and solve the wing optimization problems are available in the literature. These methods can be classified according to their level of fidelity or the degree to which a model or a simulation reproduces the state and behavior of a real-world object (Sadraey, 2012). For aerodynamic analysis, the fidelity levels result from different simplification degrees applied to the Navier–Stokes (NS) equations, from the Reynolds-averaged Navier–Stokes (RANS) down to the potential flow theory methods, such as the vortex lattice method (VLM) and the lifting line theory (LLT) (Lee, Segupta & Araghizadeh, 2022).

4.1.2 Adaptive Wing

The ability of a wing to change its shape during flight has been a significant area of interest over the years for both researchers and aircraft designers. Moreover, the adaptive wing can be used to further optimize an aircraft's flight throughout all phases of its typical flight mission by providing significant drag reduction during the climb, descent, and cruise regimes. Flight tests have demonstrated that a 20% reduction in the overall drag of an aircraft leads to an 18% reduction in fuel consumption (Valasek, 2012). The design of the active aeroelastic wing was based on modifying the wing of an existing aircraft in order to make it lighter and more flexible, thereby increasing the aircraft's dynamic performance.

In 1980, with developments in morphing aircraft already a goal for both academia and major aeronautics companies, Boeing modified an existing military aircraft with an adaptive wing structure able to alter its curvature during flight, thereby optimizing its aerodynamic performance for various flight conditions (Liebeck, 2004). The Adaptive Wing project, carried out by EADS (European Aeronautic Defense and Space Company), Airbus, Daimler, and DLR (German Aerospace Center) (Monner et al., 2000), developed a compliant wing structure that could redistribute external aerodynamic forces so that it could be morphed in predetermined areas while remaining rigid to deformation in other areas. In 2001, researchers from NASA Dryden Flight Research Center conducted several flight tests on a UAV equipped with inflatable wings, whose curvature could be modified by adjusting the pressure input.

Other efforts in adaptive wing design have resulted in a variety of morphing concepts, as reviewed by Sofla et *al.*, (2010) who combined conventional flap devices with morphing technologies and presented promising aerodynamic gains. Since the early 2000s, adaptive wings have been studied at our Laboratory of Applied Research in Active Controls, Avionics and AeroServoElasticity (LARCASE) at the École de technologie supérieure (ÉTS). The team has studied adaptive wing technologies in two large-scale projects of the Consortium of Research and Innovation in Aerospace in Quebec (CRIAQ). Each of these projects has led to the design and manufacturing of prototypes and their experimental wind tunnel tests. Both projects, called CRIAQ 7.1 and CRIAQ MDO 505, were led at ETS in collaboration with Bombardier, Thales, NRC-IAR, and École Polytechnique in Canada. In the CRIAQ 7.1 project (Popov & Botez, 2008), (Grigorie, Botez & Labib, 2008), (Grigorie & Botez, 2014), the deformation of the upper surface of a morphing wing was conducted using "Smart Material Actuators" (SMA) to improve and control the laminarity of the flow past a morphing wing in order to obtain drag reductions of up to 40%. The resulting deformation made it possible to delay the flow transition on the wing. The CRIAQ MDO 505 project (Botez et al., 2021), (Gabor et al., 2016), (Tchatchueng Kammegne, et al., 2016) was to design and validate a morphing wing with a morphing aileron capable of delaying the flow transition at the upper surface of the wing. The prototype was equipped with four electrical actuators to change its upper surface shape. This concept was experimentally validated in the NRC-IAR wind tunnel.

In this article, we developed a multidisciplinary methodology that can consider the interactions between structures, actuators, and aerodynamics. This methodology is capable of finding the geometry of an airfoil and its internal structure, which allows its shape to be changed for aerodynamic performance maximization. This research covers the study of a new adaptive wing prototype for the UAV S45 Balaam. The main objective of this adaptive wing is to promote large laminar regions on its surface, thereby reducing drag over the cruising flight phase. A prototype wing with an adaptive leading edge and upper surface was developed for this study. The flow response at the surface of the prototype wing was measured with an aerodynamic scale. The adaptive wing prototype was manufactured in-house using polymer, wood, and aluminum structures and rapid manufacturing techniques. The position of the leading edge and the upper wing surface were simulated in order to generate airfoils. An optimizer (a genetic algorithm) coupled with an airfoil analysis solver (XFoil) was used to determine the aerodynamic coefficients (C_L, C_D) and then to evaluate the fitness function 'lift to drag ratio' of the generated airfoils. The validation data for the CFD model were obtained during wind tunnel tests performed at the Research Laboratory in Active Controls, Avionics and Aeroservoelasticity (LARCASE) at ETS University.

4.2 Research Objectives

The objectives for this methodology are:

1. The design and fabrication of an adaptive wing prototype for the S45. The wing prototype shape was optimized while acting on its controlled surfaces.
2. The generation and evaluation of the optimized airfoil shapes of the wing's upper surface in terms of the aerodynamic coefficients (C_L, C_D) and fitness function 'lift to drag ratio'.
3. The validation of the adaptive wing with the area metric and adjusted R² methods.

4.3 Wind Tunnel Instrumentation and UAV S45

The Open Return Subsonic Wind Tunnel, the unmanned aerial vehicle, and the aerodynamic balance, as well as the instruments used during wind tunnel tests, are described in this section. The LARCASE laboratory at ETS owns the Price–Païdoussis Twelve-Meter Open Return Subsonic Wind Tunnel, shown in Figure 4.1. This research apparatus, which is used to test wings and diverse types of prototypes, makes it possible to safely perform studies at various flow conditions.

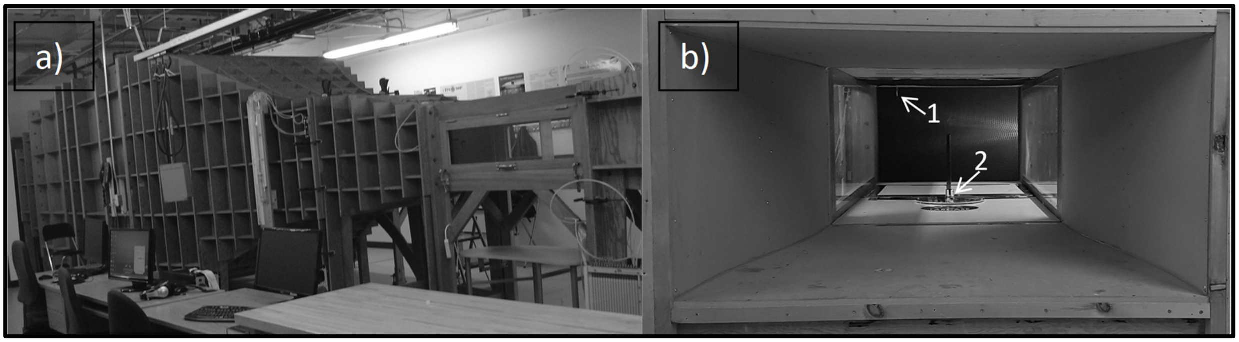

Figure 4. 1 a) The Price–Païdoussis Open Return Subsonic Wind Tunnel. b) Pitot tube location (1) and aerodynamic scale location (2)

The LARCASE wind tunnel consists of a centrifugal fan, a diffusing section, a settling chamber, a contraction section, and a working section. The airflow can develop a maximum speed of 0.18 Mach thanks to the engine and the double impeller centrifugal fan. The two inlets at the opposite side of the rotor allow the air supply to increase the pressure flow, and the 24 small propellers inside each inlet allow the fan to turn at a much higher speed than fans with large blades. The engine and the centrifugal fan are located inside the soundproof mechanical room that protects the wind tunnel from dust particles. The working section is the most critical part of a wind tunnel as that is where the effects of the flow of the wing prototypes are measured. An important step before testing is the calibration of the test chamber that contains the studied model so that the flow conditions inside it can be monitored (Salinas, Botez & Gauthier, 2021). The main parameters to describe the flow in a wind tunnel are the total pressure, the static pressure, the dynamic pressure, the temperature, the flow speeds, and the Reynolds number (Mehta & Bradshaw, 1979). These flow conditions can be monitored from the instruments inside the test section. The diffusing section consists of a wide angle diffuser, a large settling chamber, a contraction section, and a test section. The flow goes through a series of five filters; the first is a honeycomb-shaped filter, and the other four are nylon square-shaped filters positioned 0.5 m from each other, as shown in Figure 4.2. The settling section makes it possible to straighten and to reduce the turbulence in the flow to a turbulence intensity value of 1%.

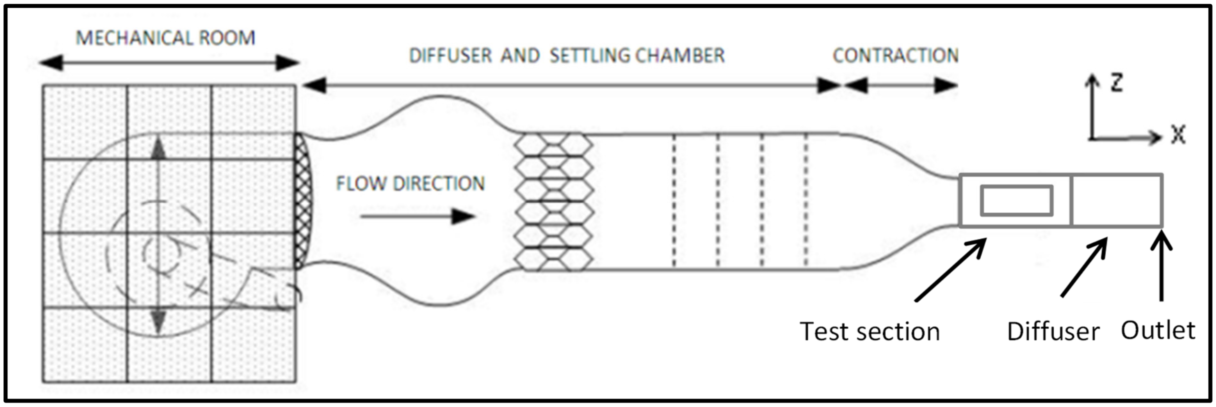

Figure 4. 2 The wind tunnel sections with coordinates

Figure 4.3 shows the different dimensions of the wind tunnel sections. Figure 4.4 shows the design of the wind tunnel sections with the ANSYS ICEM CFD software. Figure 4.4 shows (a) the settling chamber section, (b) the inlet location, (c) the inner fluid where the wind model is located, (d) the test section and diffuser, and (e) the outlet section.

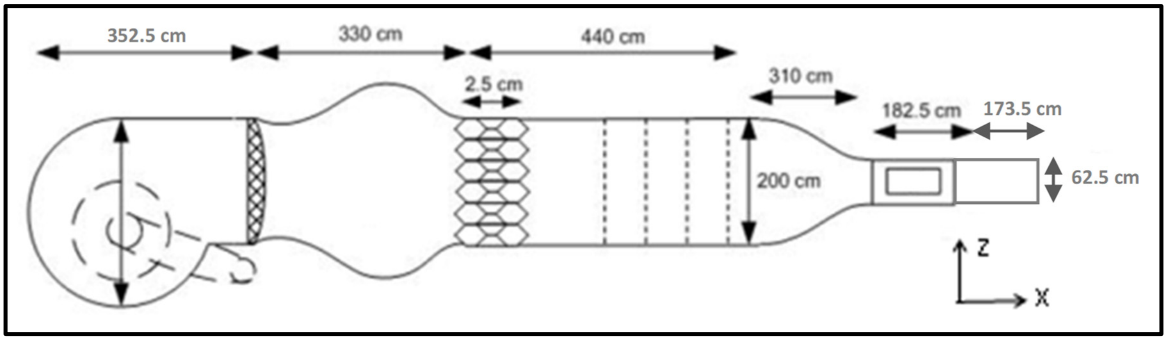

Figure 4. 3 The wind tunnel dimensions in cm

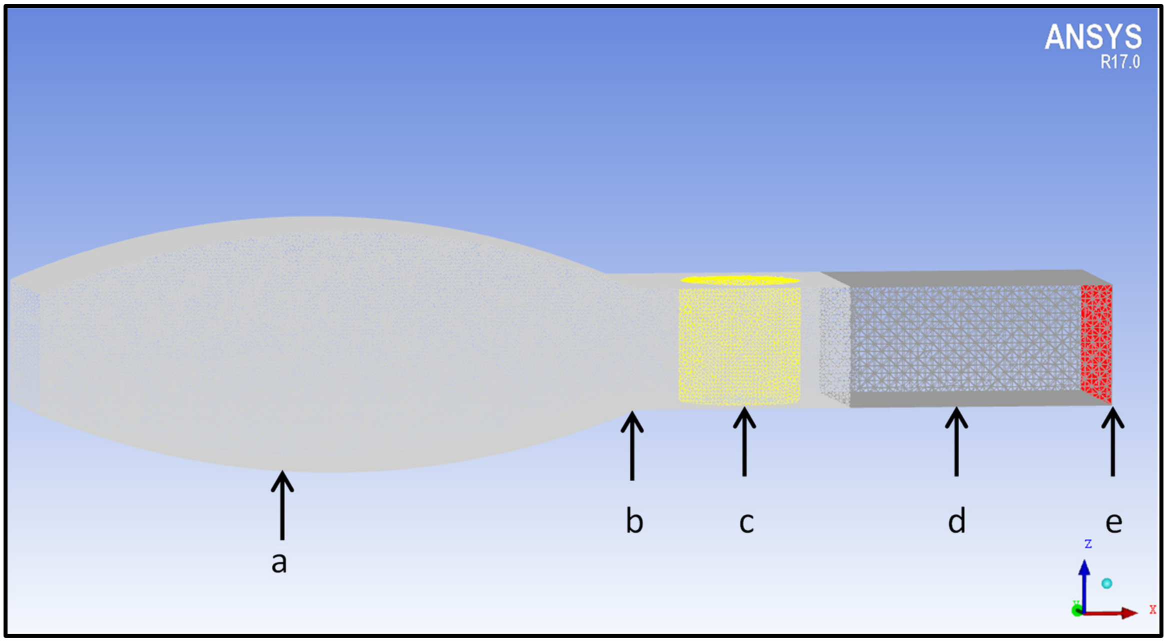

Figure 4. 4 Geometries of the wind tunnel sections in 3D with coordinates: (a) the settling chamber section, (b) the inlet location, (c) the inner fluid where the wind model is located, (d) the test section and diffuser, and (e) the outlet section

The S45 is an unmanned aerial vehicle (UAV) manufactured by Hydra Technologies, a company based in Mexico. It serves in Mexico as a surveillance platform for the military, law enforcement, and police agencies. The UAV S45 incorporates a monoplane design with twin tail booms. The airframe is made of lightweight materials, such as carbon fiber, S-glass, and Kevlar. The UAV S45 has the following dimensions: wingspan: 6.11 m; half wingspan: 2.70 m; length from the frontal rotor to the rear rotor: 1.93 m; and tail span: 1.36 m. Its length from the frontal rotor to the tail is 3.094 m, and its wing surface is 2.72 m². The UAV's materials are aluminum, titanium, and a composite material (carbon fiber, S-glass, and Kevlar), and its weights are as follows: the operating empty weight (OEW) is 55 Kg; the maximum takeoff weight (MTOW) is 69.4 Kg; the maximum landing weight is 66.50 Kg; and its maximum payload, which is its carrying capacity, is 3.89 Kg. The engines are twin-cylinder of 80 cc with a fuel capacity of 31 L. The main flight specifications of the UAV S45 are its autonomy of 12h, its maximal operating altitude of 20 000 ft, its operation range of 120 Km, and its cruising speed of 50kt (25.72 m/s). The UAV S45's main characteristics are indicated in Figure 4.5, which has numbers corresponding to the propulsion system (1–4), the two Pitot tubes (12,13), and the 10 control surfaces (5–11,14–16).

The Pitot tube measures the static pressure and the total pressure of the flow. The fluid speed U can be determined by using the air density ρ and the difference between the total pressure P_t and the static pressure P_s, as defined in detail in Section 5.4.

Temperature and humidity readings are important for calculating the air density and its flow rates during experimental testing. The sensor used for measuring the temperature is a thermocouple type-K wire with an accuracy of ±1 per degree Celsius. The humidity sensor has an accuracy of ±2% at 25 °C. A multifunction data acquisition system from National Instruments (USB-6210) was used to convert the physical forces into digital values that can be interpreted and thus used by the software. The signal measurements were acquired from the aerodynamic balance in order to obtain the signals (Fx, Fy) for the lift and drag force values, respectively, of the adaptive wing prototype.

The measurements of two accelerometer and four actuators signals were performed by a controller installed inside the wing prototype. A custom interface was created to acquire, visualize, and save the aerodynamic balance and the controller data during the wind tunnel tests. The recorded data were imported into the MATLAB software for analysis during the post-processing phase of the project.

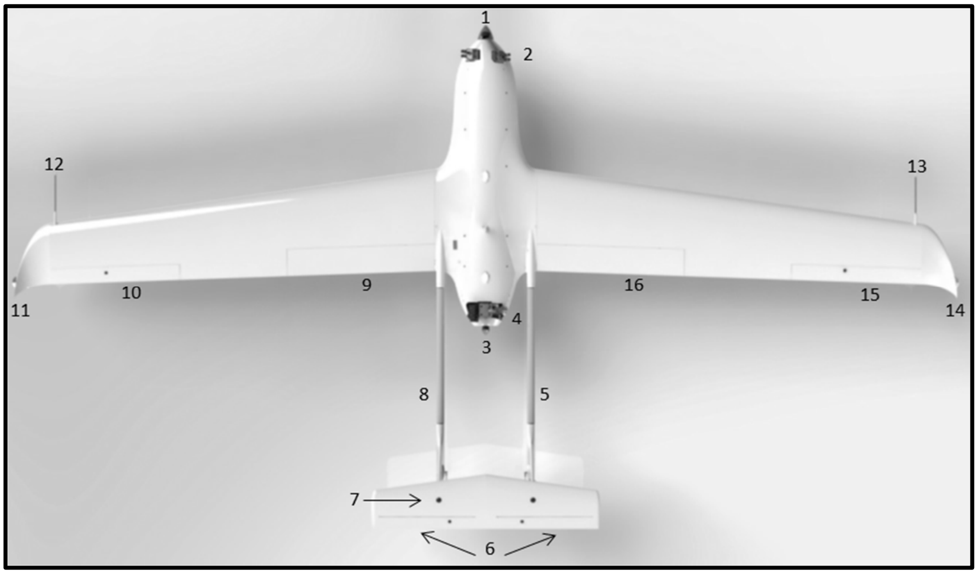

Figure 4. 5 The aerodynamic and propulsion components of the UAV S45

4.4 Multidisciplinary Design, Analysis, and Optimization of an Adaptive Wing

The aerodynamic characteristics of the under-actuated airfoil (wing without actuators) are determined by evaluating the aerodynamics coefficients C_l, C_d and the lift-to-drag ratio, which are also the same parameters used to measure the performance of the new shapes produced by the actuators inside the wing. The airfoil shape configurations are determined through the activation of the actuators and by considering the effects of the actuators and aerodynamic forces acting on the wing's skin simultaneously. The shape of the initial airfoil is defined through a set of parameters determined in the design and manufacturing phases. The configuration and structural properties of the prototype wing's inner structure and the size of the actuators were used to generate a finite element model; in this way, the upper surface of the FE model fit with the desired initial airfoil shape.

The values characterizing the structural properties are directly modified in the finite element FE model, thus allowing the structural and geometrical parameters to be changed simultaneously.

The ability to improve the wing aerodynamic coefficients with internal actuators, and for that system to withstand the aerodynamic forces, is dependent on the size, weight, location, and properties of the wing structure. Additionally, it is necessary to design an underlying structure with reduced stiffness to achieve the needed deformations. This reduced stiffness, however, increases the probability of a structure being influenced by aero-elastic effects (such as flutter).

These challenges drive the need for a multidisciplinary optimization method designed from the early phases of the project, namely preliminary analysis and concept development. The methodology presented in Figure 4.6 will be followed in this study.

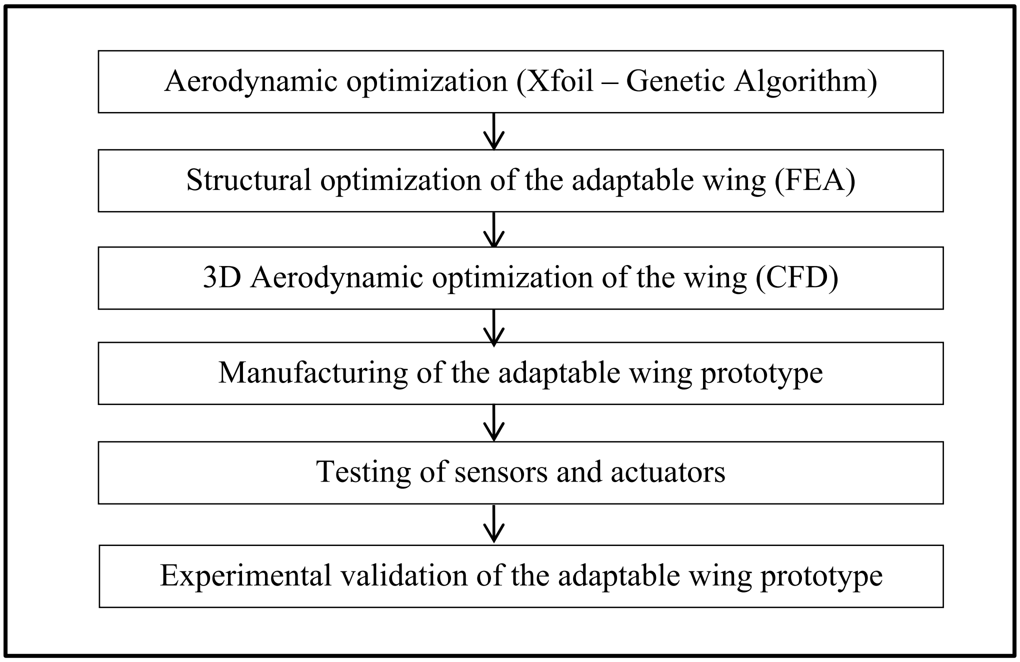

Figure 4. 6 The methodology for the study of an adaptive wing

The optimization method consists in the coupling of XFoil with the genetic algorithm (GA). The GA routine determines the best spline curve shape passing through the beginning, the middle, and the end of the airfoil geometry. Thus, the coordinates of this spline correspond to the new airfoil shape. These coordinate files (.dat file) are introduced in XFoil to perform the aerodynamic analysis. The optimization method evaluated all of the optimized shapes possible, with a ±5 mm vertical displacement of the actuators. The optimization method can find the optimal shape with the corresponding actuators' displacements; the optimal shape corresponded to the optimal C_p curve where the transition point was pushed toward the direction of the trailing edge. Delaying or holding back the laminar-to-turbulence flow process has an important impact in drag reduction.

This optimization method allows the real structural deformation shape to be compared with the predicted one given by the GA. When the best shape has been defined, the new airfoil coordinates are tested in XFoil to determine whether the aerodynamic coefficients are better, equal, or worse. The optimization method gives the maximal displacement of the actuators as well as the shape coordinates of the new optimized airfoils.

4.4.1 Aerodynamic Constraints

The formulation of the aerodynamic constraints for new airfoils is based on the flight conditions. In this paper, only the cruise flight phase of the UAV S45 will be covered. It is assumed that during the cruise flight trajectory the distributions of the lift and drag forces along the wingspan cannot exceed the limitations of the structural loads. The design optimization procedure implicitly defines the following requirements:

1. The under-actuated airfoil shape will achieve the same lift and drag coefficients as the reference wing requirements;
2. The angle of attack will remain constant throughout the cruise flight phase;
3. The C_l and C_d improvement (variations) will be achieved through the adaptive system-controlled variation of the airfoil shape;
4. Constraints ensure that the airfoil shape remains within the structural and geometrical limitations of the wing prototype. For instance, the wing prototype will have a minimal and maximal allowed vertical displacement (A_{min}, A_{max}) of ±5 mm;

5. Based on the fitness function definition $f = C_L/C_D$, an airfoil can subsequently be optimized to maximize this objective, and only the best aerodynamically, high-performing new airfoil shapes are experimentally tested in the Price–Païdoussis wind tunnel.

The proposed approach developed at LARCASE to design an adaptive wing considers the interactions between aerodynamics, structures, and control. This multidisciplinary approach is used throughout the design and manufacturing optimization phases of the prototype.
The approach outlined in Figure 4.7 allows the wing prototype to be designed and optimized with the aerodynamics requirements specific to the S45 cruise flight phase. From these data, the airfoil aerodynamic coefficients are calculated and used as inputs by the subsequent aero-structural optimization to determine the geometrical and structural properties of the airfoil. The key feature of our approach is that the new airfoil shapes are determined by the aero-structural optimization, the structural constraints of the actuators, and the material properties.

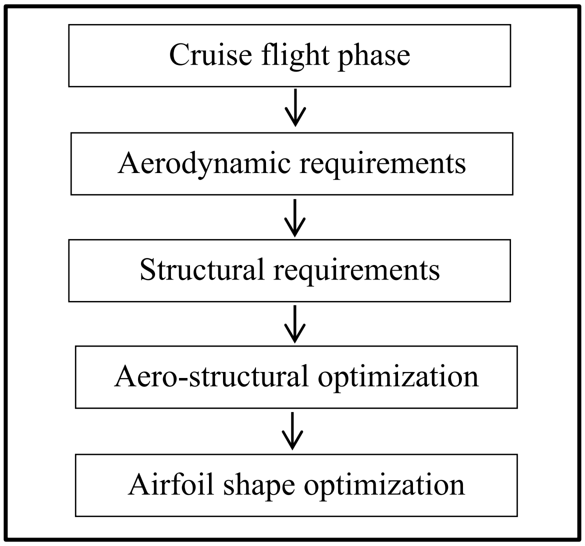

Figure 4. 7 Adaptive wing multidisciplinary optimization methodology

4.4.2 Adaptive Wing Aero-Structural Analysis

A static aero-elastic analysis was performed to obtain the aerodynamic and structural data of the studied model. The structural data include the displacements, stresses, strains, and overall weight. Among the aerodynamic outputs, those of primary interest are the lift and drag coefficients, noted as C_l , C_d, respectively, and the pressure coefficient C_p at the wing upper surface. For the structural solution, the ANSYS software with a nonlinear solver was used.
Design and manufacturing solutions seek to reduce the dynamic aero-elasticity effects. The wing prototype materials are chosen to have high stiffness properties, which is a solution to reduce the occurrence of dynamic instabilities and to delay the occurrence of possible flutter-related phenomena.

4.4.3 Adaptive Wing Actuation Design

The key aspect of the proposed method is that it takes advantage of the interaction between the aerodynamic loads and the structural design of the internal actuators to improve the airfoil's performance. This section describes the wing structure, the actuators, and the finite element modeling. An adaptive wing was designed to be small and compact so that it could be installed inside the UAV S45 wing; it achieves the required deformations via its distributed hinge-less structure. The compression forces and twisting motions are supported by a redesigned wing box, which allows the decoupling of aerodynamic loads in the spanwise and chordwise directions. This adaptive wing model is designed using a structure composed of segments of different thicknesses connected to its rear spar. When bent under the actuators' force, the space between the plate in the middle and the actuators on the upper surface is filled with polymer foam and honeycomb structures with a high stiffness-to-weight ratio. The compression modulus and dynamic fatigue are properties that assess the foam's ability to support external weight and to retain its reference shape. For instance, when the leading and trailing edge are moving in the downwards direction the bottom half of the material covering the plates will be compressed, while the upper half will be elongated.

These two actions lead to an increase in concavity for the inner part and an increase in convexity for the upper part, and thus to an equivalent increase in camber.

Figure 4.8 shows the FEA of the angular position variation on the leading edge and trailing edge produced by the actuation system. Both the leading and the trailing edge surfaces must be able to move up to 30˚ in the upward and downward positions. Figure 4.9 shows the FEA results measured in terms of stress (in MPa) on the actuation system "arm" and "fixation" at different angular positions of the airfoil leading edge and trailing edge. This evaluation was necessary to validate that the actuation system can displace/move the leading edge and the trailing edge when the airflow is moving at a speed of 30.1 m/s on the prototype surface. Figure 4.10 shows the bench test validation of the FEA results for the angular position displacements of the leading edge and trailing edge. This bench test also allowed the validation of the script code written by the main author, and it was used to control the leading edge and trailing edge positions with a feedback signal from the accelerometer inside the wing prototype.

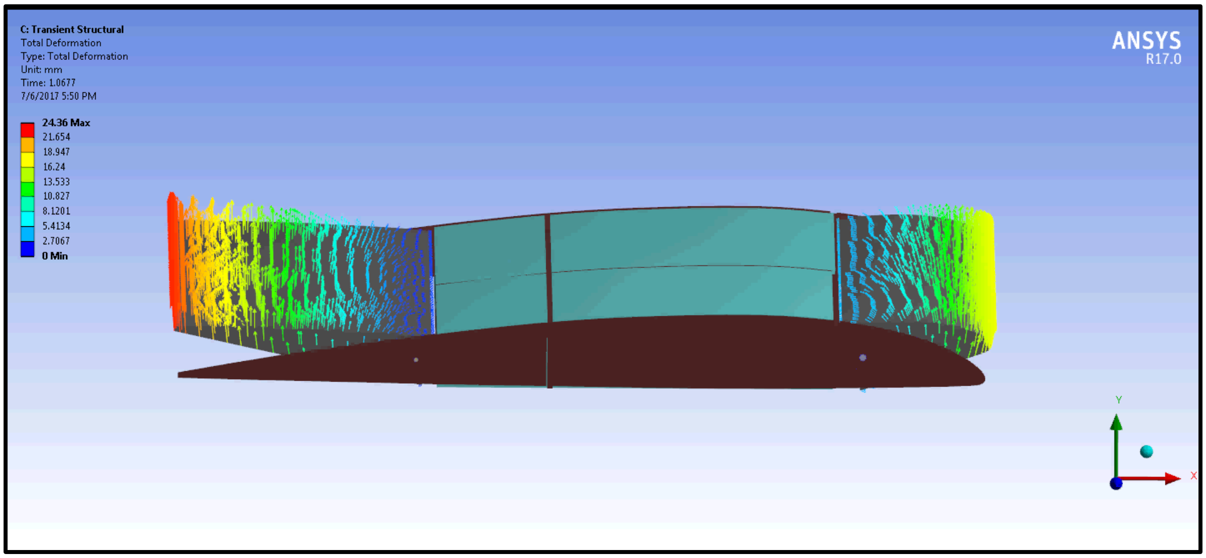

Figure 4. 8 Leading edge and trailing edge angular position variation produced by the actuation system

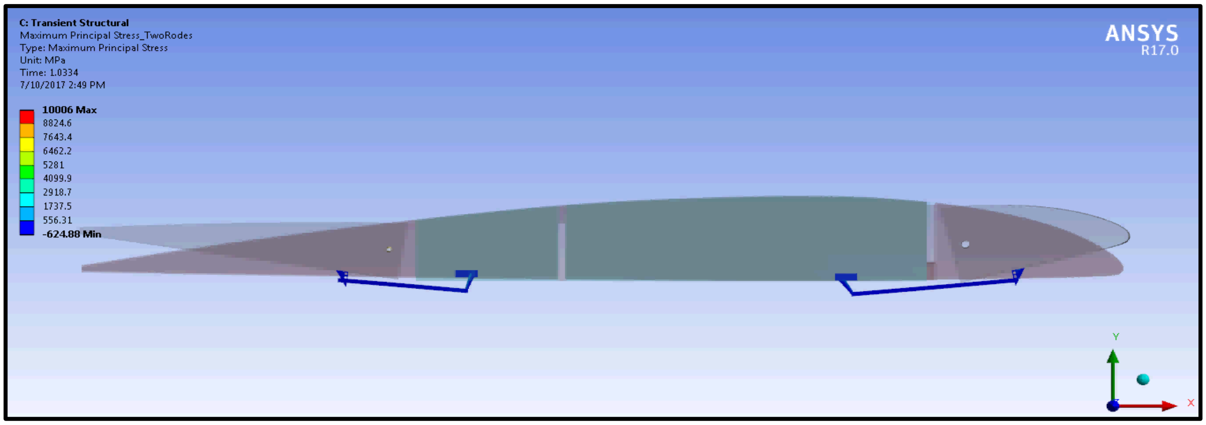

Figure 4. 9 FEA results on the actuation system

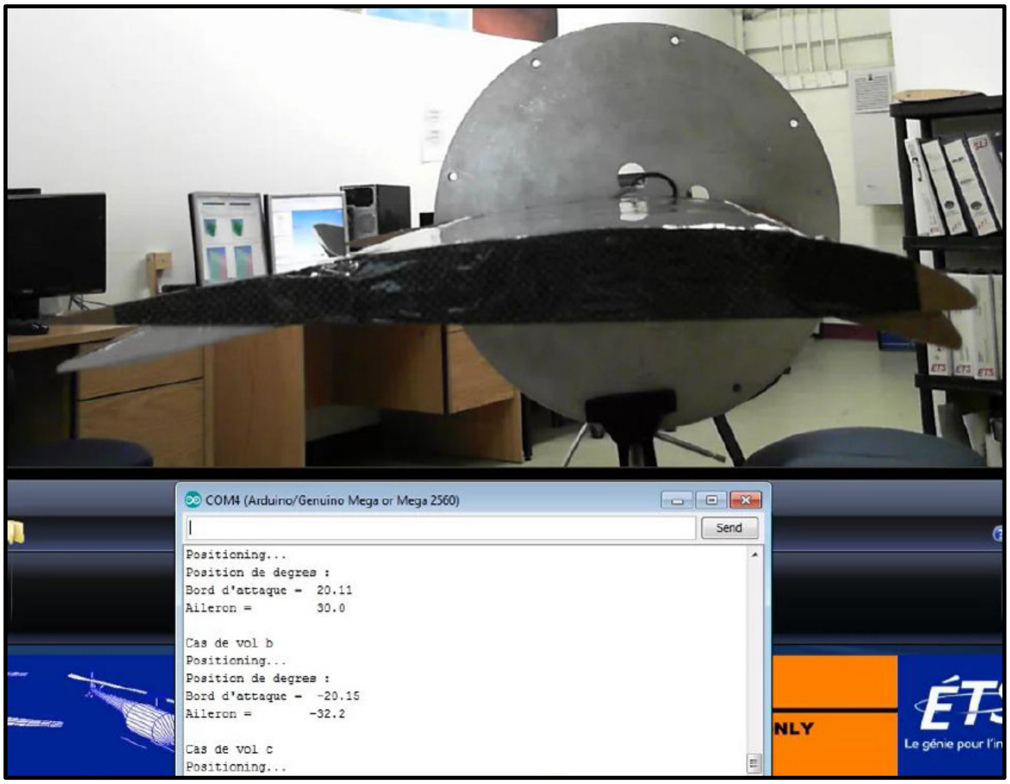

```
Positioning...
Position de degres :
Bord d'attaque -  20.11
Aileron =         30.0

Cas de vol b
Positioning...
Position de degres :
Bord d'attaque -  -20.15
Aileron =        -32.2

Cas de vol c
Positioning...
```

Figure 4. 10 Bench tests of the wing prototype for the FEA results validation

The UAV wing prototype's actuation is achieved by four servo motor drives that change the wing shape with the structural stresses applied to its polymer skin. The advantages of this skin are the stiffness and the nonlinearity of the material behavior with respect to the stress–strain and to the actuation level-produced force relationships. These actuator motions were modeled in a 3D CAD that considers the results of the structural finite element analyses found with ANSYS FEA software. The following section describes the definition of the goals of the optimizer and the results of the optimization.

4.4.4 Airfoil Shape Optimization

A genetic algorithm (GA) was used for the generation of new airfoil shapes, starting from their reference shape. This type of algorithm is used in computing to find true or approximate solutions to optimization and search problems and is inspired by the evolutionary principles of biology. The global functioning of genetic algorithms (GA) follows five distinct steps (Katoch, Chauhan & Kumar, 2021). In the first step, the initial population needs to be created in order to reduce the calculation time. Each individual of this population is a potential solution to the problem. In the second step, the individuals are evaluated in order to create the next generation. The evaluation function is user-defined as the users determine which individuals are selected. In the third step, new individuals are created. Once the best individuals are selected, the new ones are created by “mutation” or “crossover”. In the fourth step, the new individuals are added to the population, while the N best individuals of this population are selected. Finally, the fifth step consists of iterating the previous steps until the best solution is found. The evaluation function that defines the evolution of the population is the “fitness function”. The GA follows the Darwinian evolution principle via genetic selection and gives valid shapes for almost any combination of parameters characterizing the (i) camber, (ii) location, and (iii) maximum thickness of the airfoils. Certain combinations will be excluded; for instance, high curvature combined with a strong trailing edge deflection can result in undesired airfoil shapes.

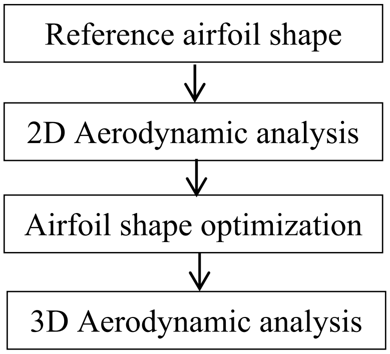

Figure 4. 11 The adaptive airfoil shape optimization methodology

The optimization method used on the S45 airfoil is presented in Figure 4.11. This method is focused on optimizing the upper surface part located between 30% and 67% of the chord. This area was chosen because both the leading edge and the flap zone must not be deformed. A MATLAB script was developed in-house to perform the airfoil optimization by using the class/shape transformation (CST) method to parameterize the airfoil, the Artificial bee colony algorithm (ABC) to optimize the shape of the airfoil, and the numerical 2D XFoil solver to run the aerodynamics calculations. Another script was used to run the calculations with the PSO and ABC algorithms and thus to allow the results given by each algorithm to be compared. The optimization method was based on the previous work performed by Koreanschi et al. (2016) and Gabor, et al.(2016).
The optimization is applied to the airfoil between 30% and 67% of its chord and is limited to ±5 mm of displacement in the direction normal to the airfoil. This study has also been conducted in previous projects at our LARCASE laboratory, where we measured the flow transition point “displacement” in wind tunnel tests with the use of very sensitive pressure sensors (Kulite XCQ_062), which were able to detect the Tollmien–Schlichting frequencies (Project CRIAQ MDO 505).

A new numerical technique was developed at the LARCASE by Popov et al., (2008) ; it allows the detection of the transition point location using the pressure distribution at the upper surface of the wing (Cp values); the first derivative of the Cp versus the chord variation curve shows the laminar-to-turbulence transition point location using an inflection point in the Cp curve.

In our work, the Kulite sensor could not be installed on the wing prototype because it required the drilling of holes on the prototype skin, and the thickness of the skin (of the prototype) was too thin to keep the Kulite sensors "flush mounted", meaning straight and perpendicular to the skin surface.

The Cp variation with the chord was solved with the XFoil software, and the first derivative of the Cp curves was obtained using MATLAB. Figure 4.12 shows the final particle swarm optimized (PSO) airfoil, which has a transition point delayed to 0.3% of the chord.

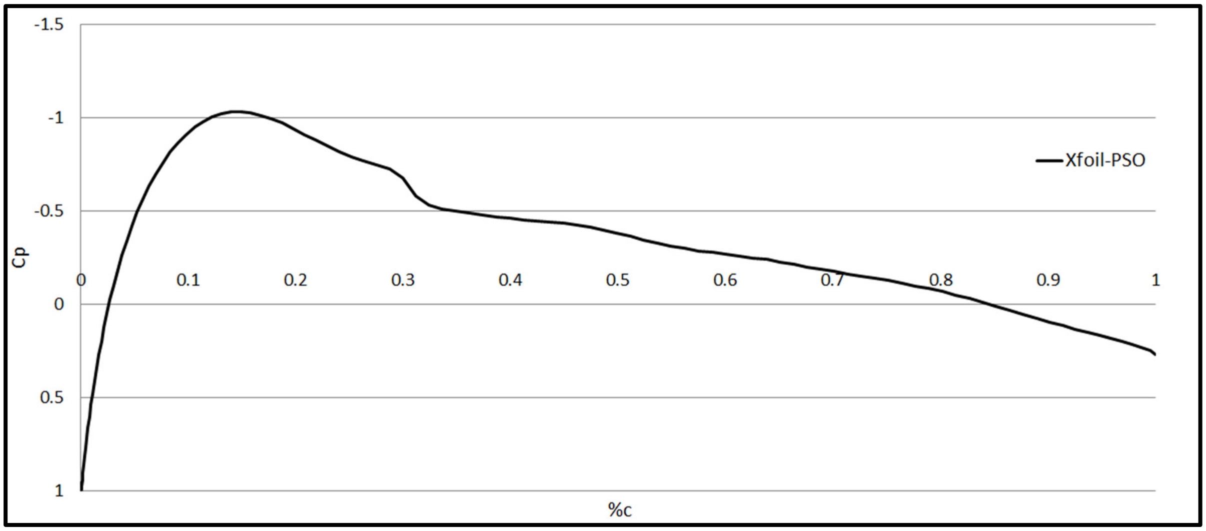

Figure 4. 12 Pressure distribution (Cp) of the optimized airfoil PSO for AOA = 3 for a flow speed of 30.1 m/s

Figure 4.13 shows the Cp derivative of a non-optimized (reference) airfoil, with an inflection point located at 0.27% of the chord and the optimized PSO airfoil, with an inflection point delayed to 0.3% of the chord.

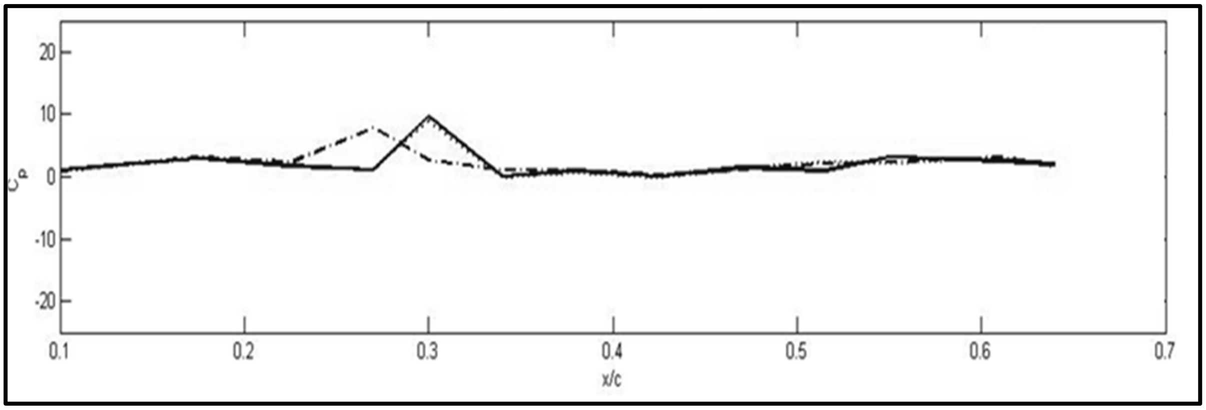

Figure 4. 13 First derivative of the pressure distribution (Cp) of the original (not-optimized) airfoil (short dash line) and the optimized PSO airfoil (solid line)

The airfoil shape was optimized for angles of attack between 0 and 5 degrees. The parameters used in these algorithms are the size of the colony, the maximum number of iterations, and the number of variables, with the number of iterations fixed at 500.
The aerodynamics conditions are fixed for each airfoil optimization at the cruise altitude of the UAV S45 (2000 ft) and a flight speed of 30.10 m/s. The objective of the optimization is to maximize the fitness function $f = C_L/C_D$, expressed as the lift/drag coefficients ratio, which can be used as an efficiency or a performance factor of the airfoil shapes.

Once the optimization has been performed by each algorithm for each angle of attack between 0 and 5 degrees, it is possible to compare their results. The C_L/C_D are analyzed and compared in Figure 4.14, where we can observe that the optimized airfoils have improved efficiency for the angle of attack (AOA) between 2° and 4°. The C_L/C_D values for the AoA = 3˚ were improved by 21% and 26% with the ABC (long dash line) and the PSO (short dash line) algorithms, respectively, when compared to the reference airfoil shape (solid line).

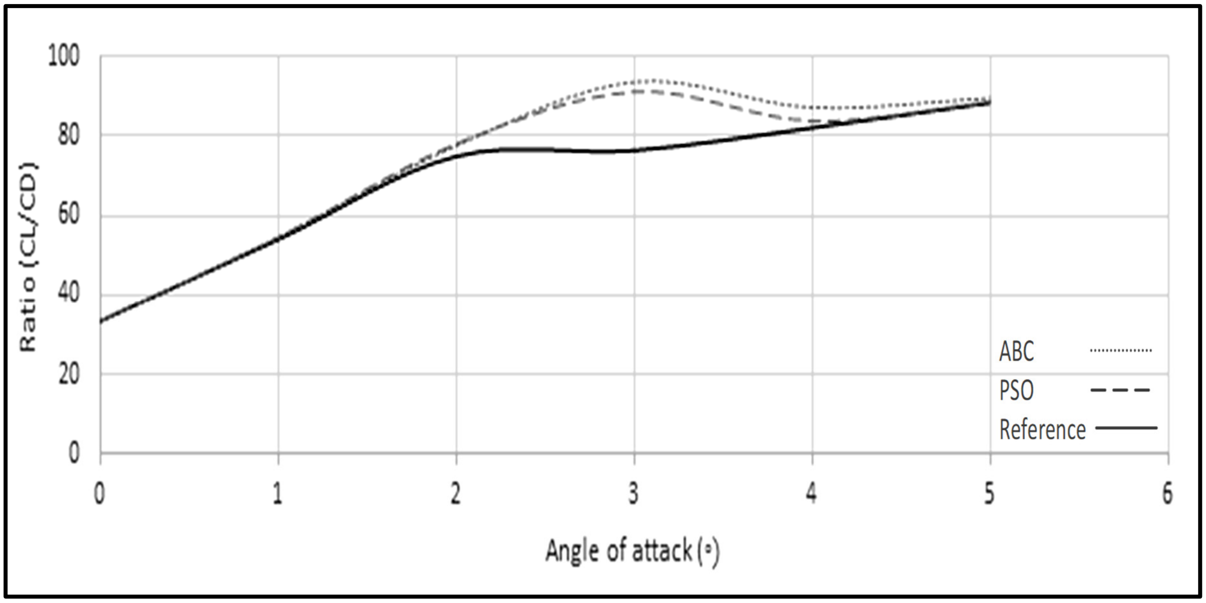

Figure 4. 14 Results of the ABC and PSO optimized airfoils versus original UAV S45 airfoil

The aerodynamic shape optimization method described in Section 5.5, coupled with the aero-structural analysis method presented in Section 5.5.2, together with the airfoil parameterization in Section 5.5.4, allows for aero-structural optimized airfoil shapes with increased performance.

4.5 Adaptive Wing Design and Manufacturing

4.5.1 Adaptive Wing Design

This section describes the design of the adaptive wing on which the surfaces controlled by the actuators are to be installed. The most effective way to alleviate the associated problems with controlled or actuated surfaces is to design the stiffest possible wing box structure, without exceeding the wing weight limitation. The main parameters, such as airfoil section, wing planform area *S*, wing chord length *c*, wingspan *b*, aspect ratio *A*, and thickness-to-chord ratio *t/c*, have to be found at the early stages of the aircraft design. For the design of the prototype, the basic wing parameters were defined by the original S45 wing structure, as shown in Figure 4.15.

The wing box design depends on the location and material properties of the spars, ribs, and skin. The prototype wing box should have reinforced spars to support the actuators’ push and pull forces. As a single spar cannot sustain the prototype structural stress, another spar was added to the wing box. Wing design approaches indicate that for a two-spar wing, the front spar should be located at between 12 and 17% of the chord if the rear spar is located at between 55 and 60% of the chord (Roskam, 2005). The main reason for these spar locations is to support the pressure distribution and improve the aero-elastic characteristics of the wing prototype.

As described in Section 5.5, we need to install four actuators to change the airfoil shape. These actuators need support arms to apply their forces to the control surfaces. Therefore, two support ribs for the actuation are needed. In addition, three more ribs are needed to stiffen the front and rear spar relative distortions and to prevent skin buckling, which could lead to an increase in the critical stress threshold of the skin material.

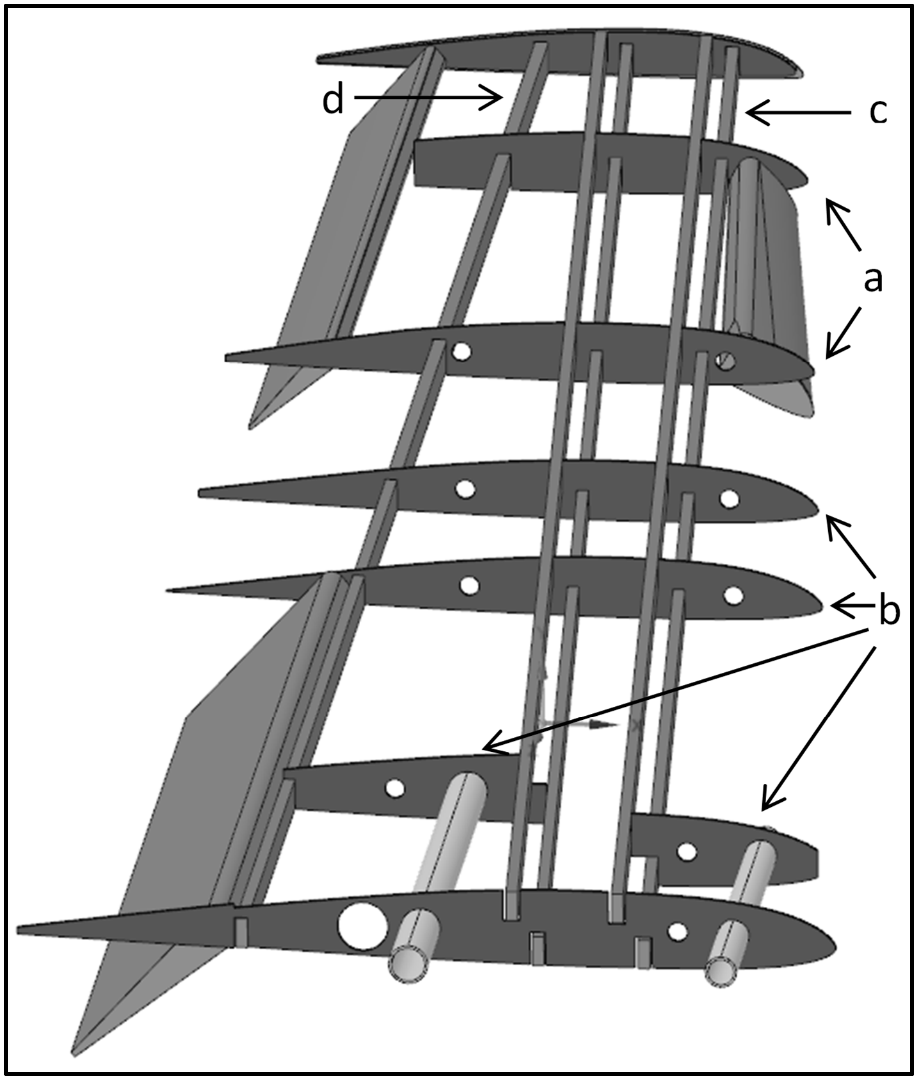

Figure 4. 15 Adaptive wing prototype based on the S45 structure, spanwise view: (a) two actuators support ribs, (b) three skin support ribs, (c) front spar, and (d) rear spar

4.5.2 Adaptive Wing Structural Analysis (FEA)

The structural modeling of the prototype wing is accomplished by using the finite element method (FEM) and ANSYS software. This section describes the selection of the element types, the FEM solid modeling, the part connection, the mesh generation, and the boundary conditions. The most commonly used element type in aerospace is two-dimensional (2D), as the industry is mostly dealing with thin-walled structures. Almost every main structural part can be modeled using this type of element. One-dimensional-type elements on the other hand also have applications for connecting beam-like structures (Raymer, 2012), (Communier et al., 2015). Two-dimensional-type elements are generally chosen for the design of thin-walled structures such as the polymer skin for the wing considered here. The thicknesses of the other parts in the wing box could also be reduced and modeled with 1D-type elements, but for the spars, it was determined that they be modeled using 2D-type elements to obtain more accurate results in the bending responses. The last sets of structural parts are the ribs, which are used to increase the torsional stiffness of the wing structure and to stabilize the skin panels. The resultant stress levels on the ribs, except for the concentrated stresses around the fasteners, are assumed to be very low compared to the stresses on the spars and the skin (Concilio et al., 2022). Hence, 1D-type elements were assigned to the ribs.

The modeling of the structural parts was conducted by generating surfaces. First, the geometrical model of the composite skin was generated. Second, the surfaces representing the wing box were generated. Third, the ribs were generated in three sections by location. The first section was located at the leading edge section up to the location of the first spar. The second section was located in between the two spars. The last portion starts at the second spar and continues until the trailing edge.

The spar and rib surfaces can be meshed using a meshing technique called ‘Iso-Meshing’, whereas complex surfaces such as the skin and the wing box can be meshed using the ‘Paver Meshing’ method (Lo & Lee, 1998), (Grisval & Liauzrun, 1999). The Iso-Meshing method creates elements that have the same angles between edges, but Paver Meshing only keeps the global element edge length defined for the meshing approximately the same, and then, it creates non-symmetrical elements.

There were two sets of connections for the wing. The first one was the connection between the spars and the skin, and the second one was the connection between the ribs and the skin. All the necessary edges for the defined connection sets have been associated with the related surface. The resulting geometry is shown in Figure 4.16.

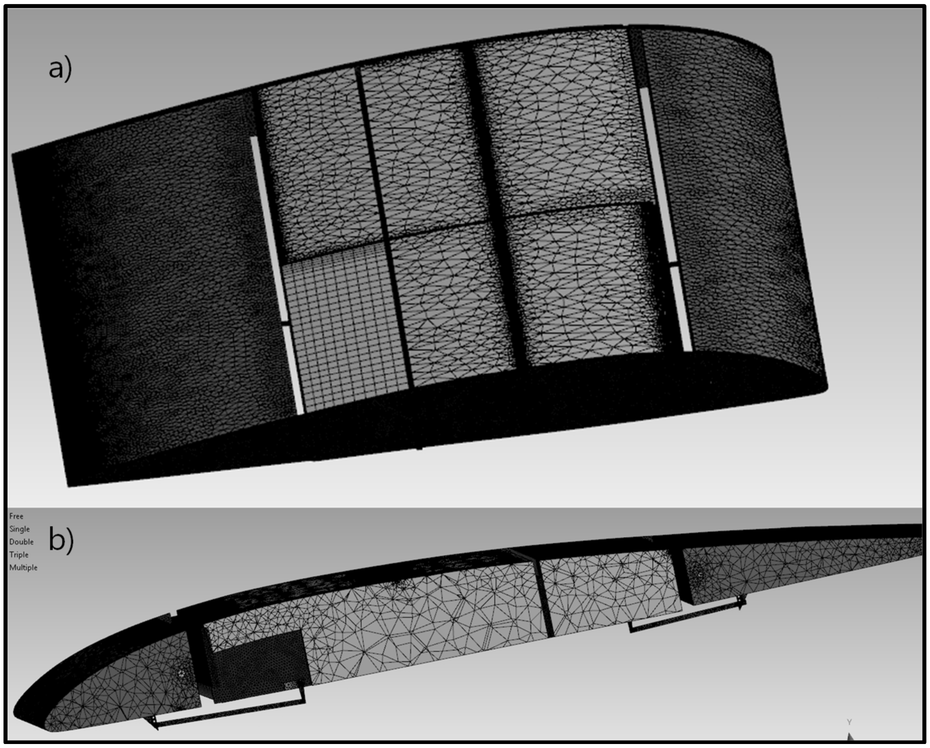

Figure 4. 16 Mesh generation of the adaptive wing:
(**a**) top view and (**b**) isometric view

The purpose of the FE model property updating is to integrate the components of a structure model and their properties. A wing mesh model becomes a structure composed of spars, ribs, and skin, which has specific mechanical properties, material properties, and other information, in addition to the geometrical information. Shape optimization is solved at each iteration. The mesh and the FE model are updated at the same time in the process of the optimization iterations, causing a new round of meshing and physical property loading.

The FE methodology presented in this section allows (i) the generation of the FE model through a CATIA design template. The template interface can achieve rapid model modifications and improvements. (ii) It allows the mesh segmentation of the spars, ribs, and skin, which are divided and meshed separately inside the FE model. (iii) The FE properties and model analysis are loaded on the wing structure after iteration.

The FE model developed in this section was manufactured in-house and is presented in Section 4.5.3.

4.5.3 Adaptive Wing In-House Manufacturing

The new wing design must replace the actual rigid wing of the UAV S45; therefore, the new design must have the same span length, a tip chord length of 0.40 m, a base chord length of 0.65 m, and an approximate weight without any instruments of 4.5 kg. The design of the adaptive wing structure has the same internal structure as a rigid wing in the sense that it consists mostly of spar and rib structures. The difference between a rigid wing and an adaptive wing structure is the configuration of the wing box structure to support the actuators.

Rigid wing structures rely on ribs to support the skin and maintain their airfoil shape. In the case of the proposed adaptive wing prototype, the rib structures have to change forms, allowing additional shape variations. These ribs are also intended to support the chordwise bending moments occurring through the pressure differential between the upper and lower surfaces. Furthermore, the ribs provide the sliding mechanism that allows the leading and trailing edge structures to change their shape, as shown in Figure 4.17. The additional torsional loads are supported by spars located as specified in Section 4.5.1.

To manufacture an adaptive wing prototype with improved performances compared to those of the original S45 wing, it is necessary to consider not only the flight phase conditions of the UAV, as presented earlier, but also the additional loads of the actuators. The fabrication of the wing parts requires CAD files and a program supported by Windows operating systems, as well as scripting capabilities. The ANSYS software package allows the CAD design to be exported into files of a format (Step files) that can be used by the FEA and CFD programs. The manufacturing of the adaptive wing was carried out in several stages.

As the scope of this thesis is the design and fabrication of a prototype, further descriptions are given below.

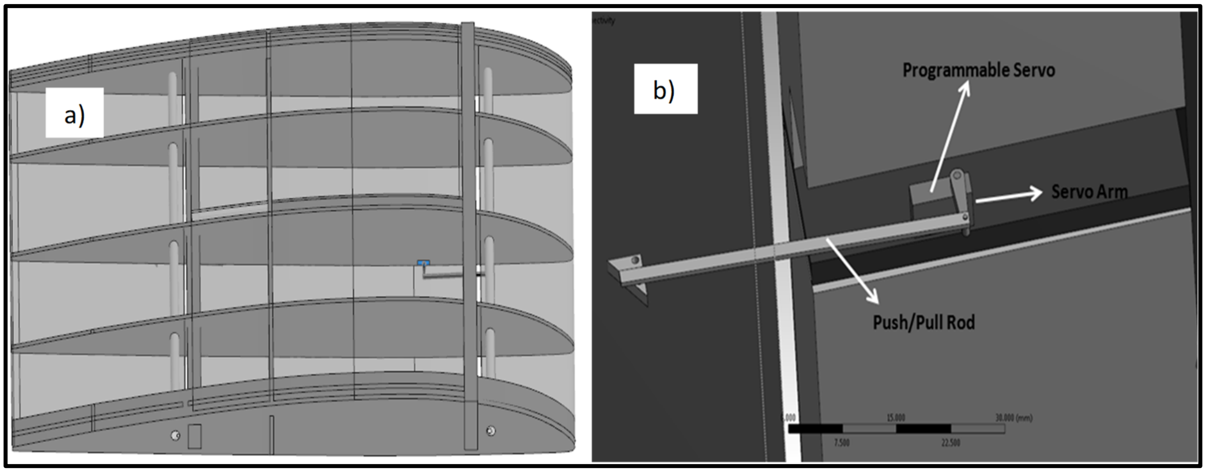

Figure 4. 17 a) Top view of the leading edge adaptive wing prototype; b) actuator design is composed of a servo motor and a push/pull rod

The flexible upper surface or skin used on an adaptive wing prototype must support the surface pressures resulting from the flow over the wing while allowing a controlled wing shape change. Compensation for the additional loads is included in the design of the adaptive wing structure. To obtain the desired optimized shapes, the polymer skin material is incorporated in the design and fabrication of the adaptive wing to allow for a precise and smooth transition during the shape changes. The skin material must have the required structural properties for the flight conditions of the UAV S45 and be able to sustain the original rigidity while allowing a quick transition and a very good recovery force, as the skin must return to its original shape when the adaptive wing system is not functioning. A material with increased modulus and toughness is desired so that the transfer of the surface pressure can proceed with minimal skin deflection. In order for the polymer skin to be stretched to a new configuration, while activated, a specific polymer material with a well-suited modulus value is needed.

Other factors for the selection of the wing skin material are the yield and ultimate strengths, thermal resistance, stiffness, and density. Moreover, the manufacturability, cost, and availability are important factors. Finally, polycarbonate polymer was chosen for the prototype upper surface (skin). The material properties (Bendler, 1999) and dimensions are shown in Table 4.1. The mass ratio is calculated with the equation shown in the last row. A more detailed equation for the mass ratio (*μ)* is shown here: μ = Density fluid × foil length/Density foil × foil thickness = 1.225 * 150 mm/1200 * 1.02 mm = 0.15

Table 4. 1 Polycarbonate polymer properties of the prototype skin

Skin Properties	
Material	Polycarbonate polymer
Young’s Modulus E	2.38 GPa
Poisson ratio v	0.38
Density ρm	1200 kg/m^3
Mass ratio μ	μ = 1.225 * 150/1200 * 1.02 = 0.15

The optimal design of the wing structure involved restrictions for the actuators and a skin support mechanism. These restrictions included the need to house the actuation components within the rib structures to ensure no interference with the skin support structure designed to slide on the rib surface, as shown in Figure 4.18.

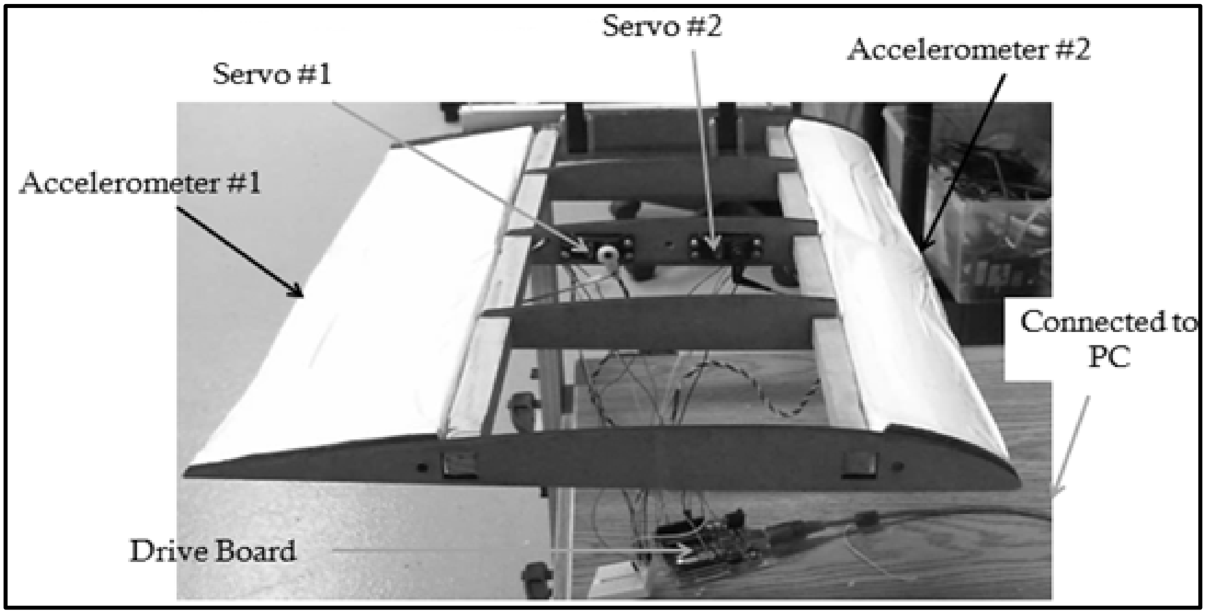

Figure 4. 18 Adaptive wing prototype instrumentation and sensors

Attaching the skin to the upper wing surface can result in a torsional strength increase for a wing. In the case of this adaptive wing structure, since the skin will change between the rigid and the elastic state, the inner and lower wing structure was sized to compensate for losses in its torsional strength. The manufacturing of the adaptive wing prototype was achieved with a safety factor of 2.0, which is a recommendation by Mehta et al., (1979) for wind tunnel testing. The images of the prototype inside the Price–Païdoussis wind tunnel are given in Figure 4.19.

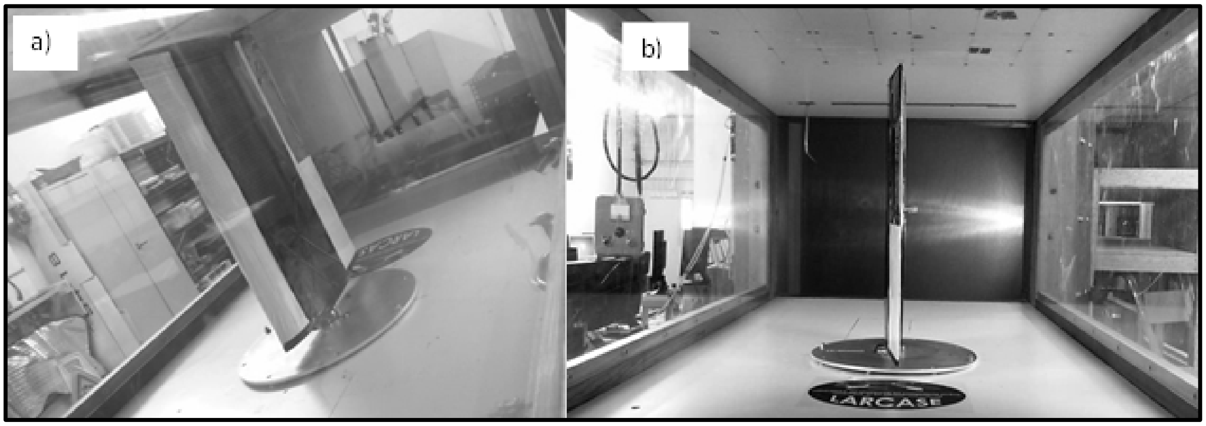

Figure 4. 19 Adaptive wing prototype experimental tests: **a**) side view and **b**) back view

4.5.4 Dimensional Analysis with Buckingham's Theorem

The “dimensional analysis method” solved with the aid of “Buckingham's theorem” can be a very powerful tool for understanding complex wind tunnel tests (Mendez & Ordonez, 2005), (Cheng et al., 2004). Buckingham's theorem is used to analyse the relationships and interactions between the fluid flow and the wing prototype during wind tunnel tests. The physical unit of mass (Kg), the time (s), the length (m), and the temperature (K) are represented by the independent variables M, T, L, and Θ, respectively.

Table 4. 2 Variables for the analysis of the adaptive wing

Variables for the Analysis on the Adaptive Wing Prototype	**Dimensions**
(I) Input variables representing the fluid in the wind tunnel	
(1) Density (ρ)	ML^{-3}
(2) Fluid velocity (U)	LT^{-1}
(3) Dynamics viscosity of the fluid (μ)	$ML^{-1}\ T^{-1}$
(4) Temperature of the fluid (t)	Θ
(5) Static pressure of the fluid (P_s)	$M\ L^{-1}\ T^{-2}$
(6) Dynamic pressure of the fluid (P_d)	$M\ L^{-1}\ T^{-2}$
(7) Total pressure of the fluid (P_t)	$M\ L^{-1}\ T^{-2}$
(II) Input variables representing the adaptive wing prototype	
(1) Wing chord (c)	
(2) Angular displacement of the leading edge	L
(LeadingEdge)	non-dimensional
(3) Angular displacement of the trailing edge	non-dimensional
(TrailingEdge)	non-dimensional
(4) Angle of attack of the wing (AOA)	
(III) Output variables representing the wind tunnel results	
(1) Lift force	MLT^{-2}
(2) Drag force	MLT^{-2}

The forces (lift and drag) are determined by the relationships between the 11 input variables, 7 of them defining the fluid, and 4 of them defining the adaptive wing model, as shown in Table 4.2.

The Bernoulli Equation (4.1) allows the expressing of the subsonic fluid velocities (U) with three pressure variables (static, dynamic, and total pressure) and one fluid density (ρ) variable. The three pressure variables can be reduced and their effects expressed by the variable U magnitude.

$$U = \sqrt{\frac{2(P_{dym})}{\rho}} \text{ where } P_{dym} = (P_T - P_s) \tag{4.1}$$

The fluid temperature (T) affects the dynamic viscosity (μ) and the density (ρ) values of the air during wind tunnel tests. The value of the temperature variable (t) is used to define the density and the dynamic viscosity of the air at which the tests will be conducted; therefore, the variable (T) can be reduced in this analysis. The four variables (P_T, P_{dym}, P_s, T) can be excluded from the list of 11 input variables, as their effects are expressed as independent variables (U, ρ). The aerodynamic forces (drag and lift) can be expressed as a function of seven independent input variables, as shown in Equation (4.2).

$$\text{Force (Lift, Drag)} = \text{f}\,\{\rho\ , U\ , \mu\ , c, \text{LeadingEdge}, \text{TrailingEdge}, \text{AOA}\} \tag{4.2}$$

To find the relationships between these seven variables and their effects on the drag and lift forces considered as output (Table 4.3), we have to use the Buckingham theorem in Equation (4.2).

Table 4. 3 Variables for the lift and drag analysis

Variables Specified for the Analysis of the Adaptive Wing Prototype	**Dimensions**
(I) Input variables representing the fluid in the wind tunnel	
(1) Density (ρ)	
(2) Fluid velocity (U)	ML^{-3}
(3) Dynamics viscosity of the fluid (μ)	LT^{-1}
(4) Wing chord (c)	$ML^{-1}\,T^{-1}$
(5) Angular displacement of the leading edge	L
(LeadingEdge)	non-dimensional
(6) Angular displacement of the trailing edge	non-dimensional
(TrailingEdge)	non-dimensional
(7) Angle Of Attack of the wing (AOA)	
(II) Output variables representing the wind tunnel results	
(1) Lift force	MLT^{-2}
(2) Drag force	MLT^{-2}

We can observe in Table 4.3 that all seven input variables and the two output variables can be defined by these three M, L, T physical dimensions. The theorem makes it possible to find the number of π terms (symbolized by the Greek letter π_1, π_2, etc.) needed to define the relationships between the input and output variables, which in this case are the drag and lift forces. The first step of the theorem is to remove the number of dimensional parameters from the input and output variables. The non-dimensional input or output variables are excluded in the analysis. For the lift force analysis, there are only four input variables and one output variable. The removal of the physical dimensions from the variables gives a minimum of two π terms for the lift force, as shown in Equation (4.3):

$$\text{4 input variables} + \text{1 output variable} - \text{3 physical dimensions} = 2\ \pi \text{ terms} \qquad (4.3)$$

Next, we separate the dimensional independent input variables and the input variables containing all three physical dimensions (M,L,T), as shown in Table 4.4.

Table 4. 4 Independent, dependent, and output variables of lift

Independent Variable Dimensions		**Dependent Variable Dimensions and Output Variable of Lift**	
Density (ρ)	ML^{-3}	Dynamics viscosity (μ)	$ML^{-1}T^{-1}$
Fluid velocity (U)	LT^{-1}	Lift force (F)	MLT^{-2}
Wing chord (c)	L		

The independent variables of the physical dimensions are matched to reduce the lift force (F) physical dimensions; therefore, the first term found is shown in Table 4.5.

Table 4. 5 Dimensional analysis first term found

Reduction with the variable: ρ	$\frac{(F)}{(\rho)} = \frac{MLT^{-2}}{ML^{-3}} = \frac{LT^{-2}}{L^{-3}}$
Reduction with the variable: U^2	$\frac{(F)}{(\rho)(U^2)} = \frac{LT^{-2}}{T^{-2}L^2L^{-3}} = \frac{L}{L^{-1}}$

Reduction with the variable: c^2	$\frac{(F)}{(\rho)(U^2)(L^2)} = \frac{L}{L\,L\,L^{-1}} = non\ dimensional$
First π term result:	$\pi_1 = \frac{F}{\rho\ v^2\ l^2}$

Only using the independent variables of the physical dimensions to match and reduce the dynamic viscosity (μ) physical dimensions, the second term is found and shown in Table 4.6.

Table 4. 6 Dimensional analysis second term found

Reduction with the variable: ρ	$\frac{(\mu)}{(\rho)} = \frac{ML^{-1}T^{-2}}{ML^{-3}} = \frac{T^{-1}}{L^{-2}}$
Reduction with the variable: *U*	$\frac{(\mu)}{(\rho)(U)} = \frac{T^{-1}}{L^{-2}\,L\,T^{-1}} = \frac{1}{L^{-1}}$
Reduction with the variable: c	$\frac{(\mu)}{(\rho)(v)(l)} = \frac{1}{L^{-1}L} = non\ dimensionnel$
Second π term result:	$\frac{1}{\pi_2} = \frac{\mu}{\rho\,v\,l} \rightarrow \pi_2 = \frac{\rho\,v\,l}{\mu}$

The first term π_1 is associated with the force produced by the wing surface versus the dynamic characteristics of the fluid. This dimensional term is associated with the lift coefficient C_l.

The second term π_2 is the ratio between the fluid inertial forces and the viscous forces inside the fluid. This term is associated with the Reynolds number (Re), and it is essential in wind tunnel testing because it allows the comparison of the fluid flow conditions between the full-scaled wings and the scaled-down models. The Buckingham theorem allows the finding of the relationship between the two π terms, which are thus proportional between the coefficients of the forces of lift and drag and the Reynolds number. The relationship is shown in Equation (4.4), where $\emptyset$ is the angle of the leading edge and the trailing edge.

$$\frac{F}{\rho\ v^2\ l^2} = \emptyset\,(\frac{\rho\, v\, l}{\mu}) \tag{4.4}$$

4.5.5 Dynamic Similitude with the Reynolds Number

The flow conditions for a prototype wing ($wing_{prot}$) and the UAV S45 original wing ($wing_{ref}$) can be reproduced if all the relevant parameters have the same values. The Reynolds numbers of the prototype and the original wing have to be equal to reproduce the aerodynamics forces and pressure coefficients during wind tunnel testing.

$$wing_{prot}\left\{\frac{\rho\, v\, l}{\mu}\right\} = wing_{ref}\left\{\frac{\rho\, v\, l}{\mu}\right\} \tag{4.5}$$

The $wing_{ref}$ has a chord length of 0.52 m and a cruising speed of 25.72 m/s.
The $wing_{prot}$ built in-house has a chord length of 0.445 m, which is smaller than $wing_{ref}$ due to the test section size and the maximum size of a model for wind tunnel tests, to reduce the "blockage effect", as described by Mehta et al., (1979).
Solving the dynamic similitude Equation (4.5) gives a flow velocity for the wind tunnel tests of 30.10 m/s, as shown in Equations (4.6) and (4.7).

$$v_{prototype} * 0{,}445\, m \;=\; 25.72\frac{m}{s} *\; 0{,}52\, m \tag{4.6}$$

$$v_{prototype} = 30{,}10\frac{m}{s} \tag{4.7}$$

For the CFD simulations, the flow speed will be set precisely at 30.10 m/s. The wind tunnel test flow speed will be set at 30.1 m/s. The flow speed was measured with a pressure sensor connected to a Pitot tube with a sensor accuracy of ±0.05 m/s.

4.6 Adaptive Wing CFD Model

In this section, a simulation model must be designed and meshed for CFD calculations. The first step consists of the design of the geometry of the adaptive wing prototype in Figure 4.20 and that of the wind tunnel, as shown in Figure 4.3 in CATIA V5. The second consists of the geometries meshing using structured and unstructured mesh sizes on the model's surface, and the last step is the use of CFD solver to find the lift and drag forces (Liauzum, 2010). A robust mesh model of the adaptive wing prototype was designed using an ANSYS ICEM mesh generator. The mesh volume of these two objects consists of a finite number of polygons composed of triangle and quad elements. Quad polygons have a better topology (how the polygons are connected to the flow around them) and a better resolution of the flow boundary conditions.

For a wind tunnel CFD model, there are five boundary conditions that must be specified during the mesh design, and as well as in the CFD Solver: (i) the "inlet boundary condition", which is the surface where the flow is initiated, mainly when the flow speed in one of the axes (x, y, z) is specified; (ii) the "outlet boundary condition", which is the region where the flow attains a fully developed state and where no change in velocity or direction occurs far from the model disturbances; (iii) the "wall boundary condition", which defines the appropriate flow condition near the walls (inside the wind tunnel test chamber and at the surface of the model); (iv) the "Constant pressure boundary conditions", which are used when the inlet pressure is known and when the outlet pressure can be determined; in an open circuit wind tunnel, the outlet pressure is the atmospheric pressure; and (v) the "symmetric boundary condition", which is calculated when the same physical conditions exist on two sides of a model.

The designed CADs (step files) of the adaptive wing prototype and of the wind tunnel were imported to the ANSYS ICEM meshing software. The meshing process includes the (i) design of an initial mesh, followed by an evaluation of its quality and the boundary conditions specifications; (ii) the improvement and repairing of the mesh holes, discontinuities, and space between its cells; (iii) the generation of the volume mesh using triangle and quad elements and the refining of the mesh density close to its boundary layer; and (iv) the exportation of the final mesh to the CFD solver.

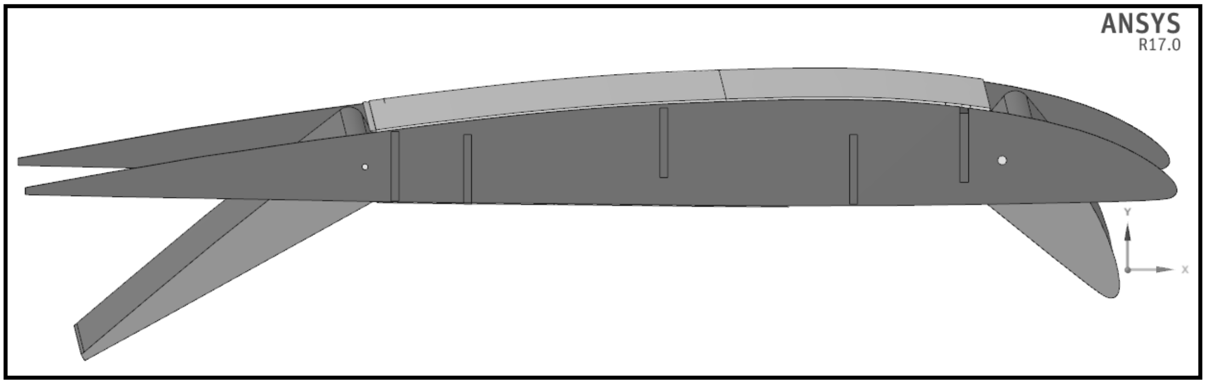

Figure 4. 20 CFD model of the adaptive wing prototype

A mesh with an optimum grid resolution had to be refined along the model's surface. The fluid at the wing model surface, named "Inner_fluid", and the flow inside the wind tunnel have to be simulated together. The generated grids have coarse regions, and it was achieved using the octree method with "Tetra Cell". It was re-meshed using the Delaunay refinement mesh technique. The octree method allows the design of regular internal mesh geometry and does not require an initial mesh to be implemented. The Delaunay technique allows for a smoother mesh and a better accuracy in representing complex shapes.

A "grid sensitivity" study was conducted to determine the mesh density required to produce final results of acceptable fidelity. Grids of varying resolution were tested using the flight test number 22 (leading edge at −5° and trailing edge at −10°), the angle of attack of 3°, and the Reynolds number of 5.89×10^5, corresponding to a flow velocity of $U = 30.10$ m/s. The wall parameter $y^+ < 1$ was maintained regardless of the tested grid (Katz & Sankaran, 2011). The variations of C_l, C_d and C_l/C_d are shown in Table 7. It can be observed that the results change significantly for the first three grid resolutions (Grid 1, 2, and 3); after the fourth and fifth grid resolutions (Grid 4 and 5), the mesh density does not significantly affect the results of the aerodynamics coefficients.

There is a 1% error between the grid 4 and 5 results and a mesh size reduction of 1.266 million cells for grid 4, compared to the grid 5 density. Based on the Table 7 results, the grid 4 density will be used for all the adaptive wing simulations.

Figure 4.21 shows only the mesh volumes of the adaptive wing model. The main motivation for determining these grid sensitivity results is to reduce the computational time while obtaining accurate results.

Table 4. 7 Grid sensitivity results

Grid Density	**Quantity of Cells**	C_l	C_d	C_l/C_d
1	900 542	0.02489	0.00920	2.70
2	1 325 584	0.02435	0.008665	2.81
3	1 854 000	0.02313	0.007896	2.92
4	2 258 477	0.022869	0.007584	3.02
5	3 524 648	0.022855	0.007545	3.03

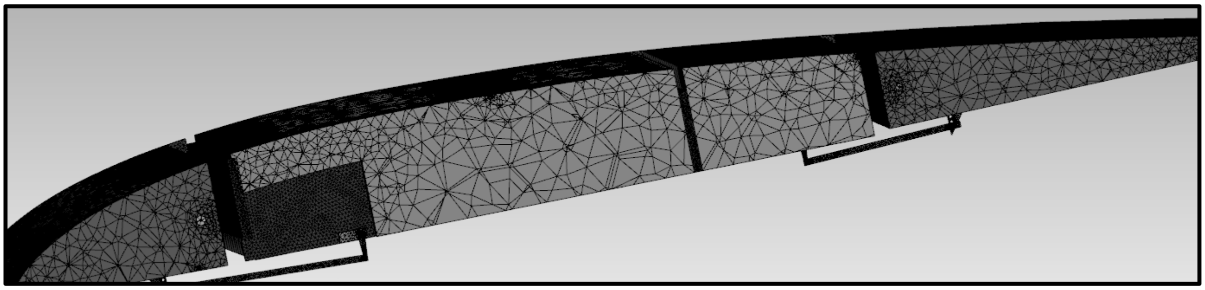

Figure 4. 21 Mesh of the adaptive wing model

The boundary conditions are required in CFD simulations to solve the differential equations for the fluid volume. An inlet surface allows the air mass to flow into the domain of the test velocity of 30.10 m/s, while a pressure outlet surface allows the air mass to flow out of this domain. Slip walls were imposed on the sides of the far field to improve the solution convergence, and a no-slip wall was enforced at the surface of the wing model to obtain a fluid velocity at its surface equal to zero. The simulation implicit solver had a time step size of 0.001 s, which was considered necessary for numerical stability, for which 400 total time steps were conducted to a converged solution at the residual target of 1×10^{-5} for all the flow and turbulence variables.

The CFD Fluent software was used to solve the adaptive wing model mesh, as described previously. The data obtained experimentally were compared with the "steady state" analysis results (simulations), but the errors and uncertainties were beyond the 10% validation metric limit, which will be explained in detail in Section 4.8.

A rigid wind model, with no moving parts, in a laminar flow regime can be accurately predicted by the steady state Navier–Stokes equations by assuming, at simulation convergence, that the local speeds do not vary with time. In the case of an adaptable wing, the simulations have to be solved in a transient state analysis. A transient state allows for an accurate representation of flow behavior. The flow turbulence intensity was kept at 1% and therefore at the same turbulence levels as in the Price–Païdoussis wind tunnel tests. Selecting an accurate turbulence model for an accurate representation of wall-bounded flow, mild to important flow separation and recirculation, and flow transition is a challenging aspect in CFD simulations. The presence of a wing prototype with actuated/controlled leading edge and trailing edge surfaces generates additional turbulence characteristics to the flow regime in the test section.

Four RANS models were tested with the CFD solver: Spalart–Allmaras (SA), K-epsilon (K-ε), K-Omega (K-ω), and the shear stress transport (SST). The Spalart–Allmaras model is a single-equation model involving wall-bounded flows and a low Reynolds number (Spalart, 2000). The SA model produced an absolute error of 20% compared to the experimental loads. The K-epsilon two-transport equation model solves for kinetic energy k and dissipation ε, where dissipation is the rate at which the velocity fluctuations dissipate (Durbin, 1995). It uses coefficients that are found empirically, and it was found that the K-epsilon model is accurate for unsteady flow regimes. The absolute errors with the experimental loads were within the 10% validation limit. The K-Omega is a two-variables model, used to obtain the kinetic energy k and frequency ω. This model allows for a more accurate near-wall treatment and demonstrates superior performance for wall-bounded and low Reynolds number flows and for predicting transition (Lauder, 1995). The absolute errors between the experimental and the simulated loads were within the 10% validation limits. The shear stress transport (SST) model is a variant of the standard K–Omega model; it combines the original Wilcox k-Omega model for use near walls and the standard K-epsilon on the regions far from the walls (Menter, 2009), (Jameson, Martinelli & Pierce, 1998). This model has been proven to offer high accuracy on the boundary layer regions, but it does not converge to a solution quickly. Therefore, the initial conditions of the simulation were solved with the K-Omega model to improve the conversion rate. The absolute errors between the experimental and the simulated loads were below the 5% validation limits. The adaptive wing model was simulated with the SST model.

4.7 Experimental Data and Model Validation

The CFD models do not always reproduce data accurately, and there are many sources of errors in the simulation results. Due to these errors, model verification and validation is a research requirement to obtain accurate simulations with quantified uncertainties (Oberkampf & Trucano, 2002), (Huvelin et al., 2019). The 2012 ASME committee provides a useful validation approach for cases when experimental data are available. Even though no specific metric is imposed, the guide recommends using a single metric to better quantify the difference between the simulation and the experimental data. The metric must measure the difference between the experimental outcomes and the simulation outcomes; it should be equal to zero if the outcomes are identical, and it should provide a coherent numerical value expressing the model's accuracy and adequacy. The area metric method proposed by Ferson et al. (2008) allows the comparison of the simulation results with the experimental data.

Table 4.8 presents the S45 wing parameters and flow conditions allowing the calculation of the aerodynamics coefficients of the lift and drag and the lift-to-drag ratio. Consequently, it would be possible to compare the S45 performances with the wing prototype experimental data.

Table 4. 8 Aerodynamic parameters of the S45 reference wing

Flow Conditions	
Velocity Flow (m/s)	30.1
Density air (kg/m³)	1.225
Temperature (˚C)	22
Wing structure	
Wingspan (m)	0.495
Wing chord (m)	0.455
Wing surface (m²)	0.2252
Experimental data	
Lift force (N) =	1.942
Drag force (N) =	0.644
C_l =	0.022869
C_d =	0.007584
$\frac{L}{D}$ =	3.02

The 29 wind tunnel tests results (lift and drag forces) are presented in Table 4.9, and they show a very good agreement with the simulation values. The wind tunnel tests are sorted by the angular position of the adaptive leading edge. In total, 29 wind tunnel tests were performed, and the two forces of lift and drag were measured by the aerodynamic scale.

Table 4. 9 Experimental and simulated data of the adaptive wing prototype

	Adaptive Wing Surfaces		**Experimental**		**Simulation**	
Test	**Leading Edge (Degrees)**	**Trailing Edge (Degrees)**	**Wind Tunnel**		**CFD Model**	
			L_{exp} (N)	**D_{exp} (N)**	**L_{sim} (N)**	**D_{sim} (N)**
1	0	0	1.942	−0.644	1.5885	−0.6457
2	−5	0	1.839	−0.67	1.4504	−0.6637
3	−10	0	1.676	−0.736	1.3584	−0.6817
4	−15	0	1.484	−0.84	1.2723	−0.8780
5	−20	0	1.359	−0.865	1.1917	−0.8960
6	5	0	2.011	−0.618	1.7083	−0.5690
7	10	0	2.197	−0.678	1.8239	−0.5510
8	15	0	2.254	−0.713	1.9474	−0.7460
9	20	0	2.26	−0.729	2.0792	−0.7750
10	0	-5	2.293	−0.701	2.0833	−0.4341
11	0	-10	2.769	−0.759	2.5740	−0.5186
12	0	-15	3.506	−0.908	3.0948	−0.6004
13	0	-20	4.199	−1.046	3.6680	−0.6780

14	0	-25	4.784	−1.135	4.3163	−0.7687
15	0	-30	5.502	−1.295	5.0620	−0.8469
16	0	5	2.029	−0.604	0.9018	−0.2779
17	0	10	1.142	−0.549	0.3660	−0.1897
18	0	15	0.216	−0.45	−0.2298	−0.1040
19	0	20	−0.532	−0.404	−0.9080	−0.0286
20	0	25	−1.222	−0.296	−1.6913	0.0501
21	0	30	−1.811	−0.243	−2.6020	0.1420
22	−5	−10	1.43	−0.988	2.0148	−0.6457
23	−10	−15	2.971	−1.165	3.1309	−0.4750
24	−15	−20	4.182	−1.306	4.2898	−0.9360
25	−20	−30	4.987	−1.131	5.2796	−0.9540
26	5	10	2.441	−0.734	2.5712	−0.5455
27	10	15	1.051	−0.486	1.1005	−0.6457
28	15	20	−0.201	−0.468	−0.2096	−0.6637
29	20	30	−0.724	−0.349	−0.7706	−0.6817

4.7.1 Residual Analysis of the Lift and Drag Forces

The observed and predicted lift and drag quantities were very close, as shown in the residual errors in Table 4.10. As mentioned in the ASME validation guidelines, a simulated CFD model should be able to predict up to 85% of the experimental output, with less than 5% error (Holger & Munk, 1998). This means that for this project with 29 simulation and wind tunnel tests (Table 4.9), the validation guidelines require (29*85% = 24.6) that at least 24 simulations results have 5% or less difference (error) with the experimental data.

The residuals of the lift and drag forces are defined as the differences between the observed values during the wind tunnel tests and the estimated values by the CFD simulation. Mathematically, the residual r of a specific value is the difference between the observed response value y and the predicted response value ŷ. The residuals should be scattered randomly and centered on zero throughout the range of the fitted values. The non-random pattern in the residuals indicates a calibration error or a bias during the experimental tests or an inadequate model. The Fluent simulation accurately captures the interaction of the adaptive wing model with the fluid, as shown in the values of the residuals in Table 4.10.

The residuals for the lift and drag forces appear to be random and distributed above and below the 0 error values, respectively. The differences between the experimental and the predicted values are independent and normally distributed, following a normal law with a mean value equal to zero and a very low variance. The residual values were calculated from the values shown in Table 4.10. The sum of the residuals shows that they are symmetric around the “zero” value.

Table 4. 10 Residual of the experimental and simulated lift and drag forces

Test	**Residual Lift (N)**	**Residual Drag (N)**
1	0.35	0.00
2	0.39	−0.01
3	0.32	−0.05
4	0.21	0.04
5	0.17	0.03
6	0.30	−0.05
7	0.37	−0.13
8	0.31	0.03
9	0.18	0.05

10	0.21	−0.27
11	0.20	−0.24
12	0.41	−0.31
13	0.53	−0.37
14	0.47	−0.37
15	0.44	−0.45
16	1.13	−0.33
17	0.78	−0.36
18	0.45	−0.35
19	0.38	−0.38
20	0.47	−0.35
21	0.79	−0.39
22	−0.58	−0.34
23	−0.16	−0.69
24	−0.11	−0.37
25	−0.29	−0.18
26	−0.13	−0.19
27	−0.05	0.16
28	0.01	0.20
29	0.05	0.33

4.7.2 Validation Method Durbin–Watson Test and Adjusted R^2

Figure 4.22 shows a quartile graph in which the drag residuals follow a line (at 45 degrees), indicating that its “different” values are distributed according to a normal law. The Durbin–Watson test predicts whether there is correlation in the order of appearance of the residuals for the drag force; given that the probability is 0.016% and less than 0.05%, there is evidence of correlation at a confidence level of 95%. We can reject the H_0 hypothesis (H_0 = there is no correlation between the residual drag values). The data show in Figure 4.23 show that the residuals for the lift force follow a normal distribution, and the histogram graph indicates a leftward bias.

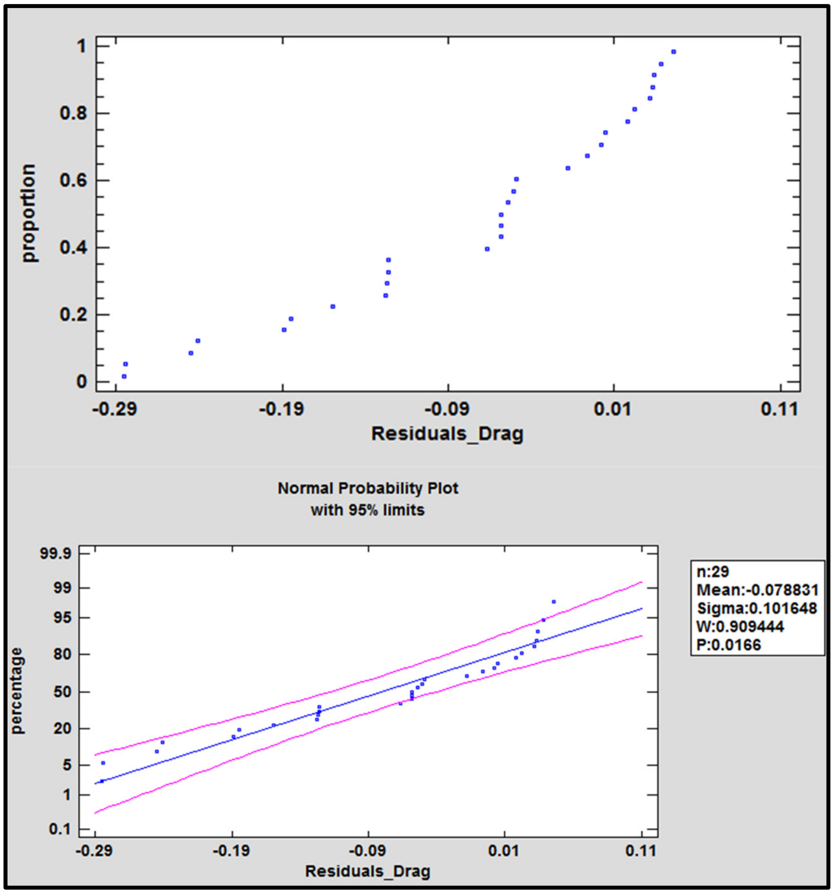

Figure 4. 22 Analysis of the drag forces' residual values between the wind tunnel and model data

Linear regression analysis with adjusted R^2 is a statistical process that focuses on the relationships between sets of variables; in this case, the regression analysis allows for an estimation of the difference between the model's predicted values and the experimental values. The predicted and observed data are numerically sorted from small to large; the model data are placed on the x-axis and the observed data on the y-axis (Rawlings, Pantual & Dickey,1998), (Devore, 1982). A line with a 45° slope is added to the plot where the dispersed data are shown. This line represents the ideal outcome where all the predicted values are 100% identical to the observed values. The magnitude of the correlation between the response and the predicted values can be quantified by calculating the adjusted R^2 (R-squared) of the model. This value denotes the proportion of the variance in the experimental data, which is predicted by the model data. An adjusted R^2 of 1 indicates that the model predicts all the experimental data perfectly, but in the real world, the models are never perfect, and the adjusted R^2 values may take any value from 0 to less than 1.

This method shows in Figure 4.24 that the model predicted the lift and drag forces values within the 95% bounds for the linear regression method. The adjusted R^2 values are 0.9986 for the lift and 0.9945 for the drag forces, thus indicating that the predictions of the variance for the lift force are 99.86% and 99.45% for the drag force, as accounted for by the model predictions and as seen in Figures 4.22 and 4.23, respectively.

To validate a statistical hypothesis on a group of data, if we set H_0 as the observed values and the simulated values from the same population, it is possible to assess at a confidence level of 95% whether this hypothesis is rejected or accepted. The weakness of this type of validation is that it is qualitative and not quantitative. This type of validation is mostly used to reject a model rather than to validate it at a high level of confidence (Liu et al., 2011).

The adjusted R^2 for the drag forces are strong and indicate that 87.24% of the experimental data can be explained by the model. The Durbin–Watson test makes it possible to check the correlation between the observed drag values and the simulated drag values. In this case, the test has a *p*-value much lower than its 0.05% threshold, which indicates a strong correlation. This hypothesis test does not reject H_0; so, the model is adequate for estimating drag forces. The adjusted R^2 for the lift forces indicates that the model represents 97.27% of the observed data. For the lift forces, the hypothesis test shows that there is a strong correlation between both results values, while the hypothesis H_0 cannot be rejected with a confidence level of 95%.

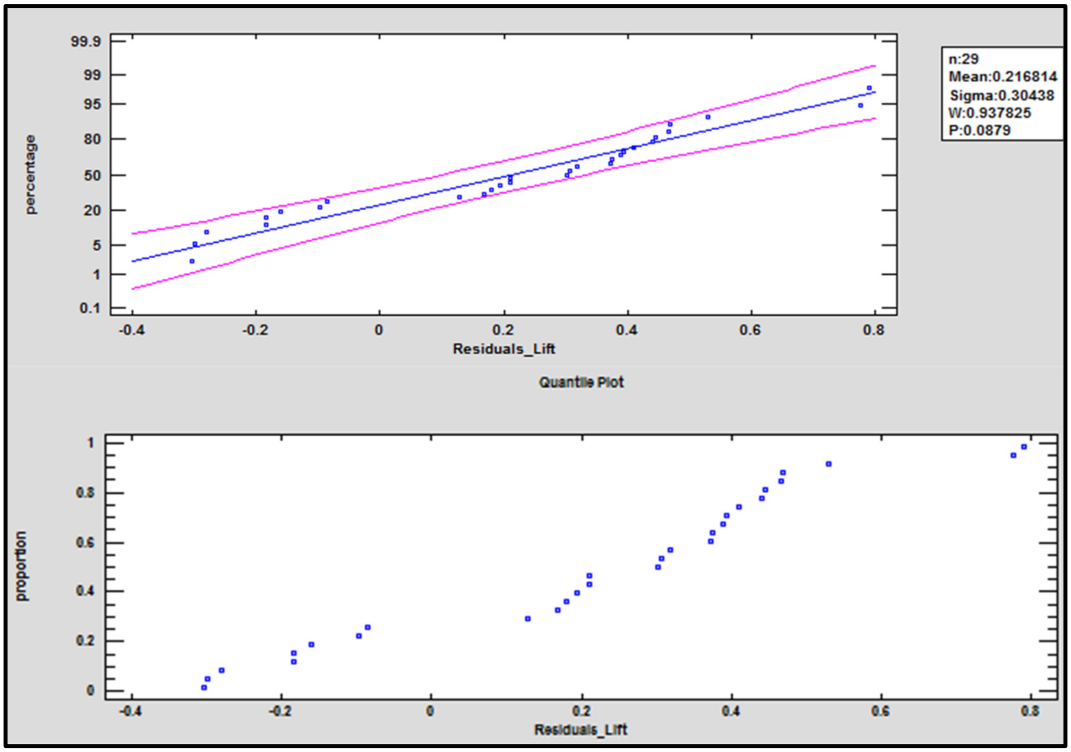

Figure 4. 23 Analysis of the lift forces' residual values between the wind tunnel and model data

The validation tests were conclusive, thus indicating that the CFD model can simulate lift and drag forces at a 95% confidence level. The drag force residuals appear to have an autocorrelation, possibly due to the non-linearity of the range of observed values. These experimental values have an uncertainty of ±0.04N, estimated at a confidence level of 95%. The simulation model of the adaptive wing prototype was validated by the Durbin–Watson and adjusted R^2 tests, and it can be used to obtain accurate aerodynamics lift and drag forces.

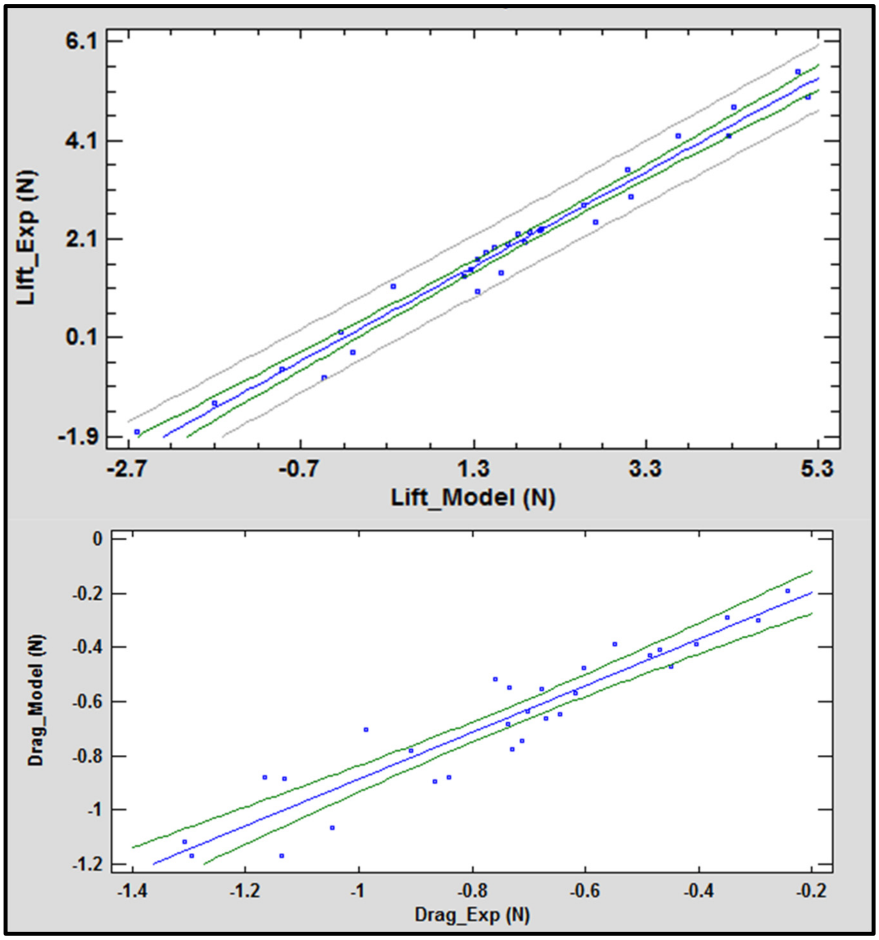

Figure 4. 24 Analysis of the lift and drag data with the adjusted R^2 validation method

4.7.3 Validation Method of the Area Metric for the Drag and Lift Forces

The area metric is the method recommended by ASME in their validation guidelines as being well-suited for the experimental research (Chatenet et al., 2016), (Wang et al., 2018). This method does conclude that a model is accepted or rejected, and it also allows the model validation to be quantified. The area metric method uses the cumulative probability of the observed data and the simulated values and calculates the integral (using the trapezium method) obtained for the surface of the observed values and the simulated values. The difference in the surfaces (between the curves) gives the value of the quantified metric in the same units as the analyzed data.

Comparing the curves obtained from the physical experiments with those given by the mathematical models is an important technique used by researchers to determine whether a model adequately represents the physical phenomena. This method allows the validation of a simulation model when only a limited number of experimental values can be measured, which is an advantage over the other validation methods.

Due to its quantitative measure of the discrepancy between all the data available (predicted data and observed data), the area metric offers an important advantage compared to classical validation methods; it is considered objective and robust (Wang et al., 2018) in producing a graphical representation of the discrepancy in the same physical units as the experimental data, and this makes it possible to evaluate the differences across the full range of prediction results while considering simulation uncertainties.

The area metric is calculated with the cumulative distribution function (CDF) of the experimental data and that of the model data. Both CDFs are step functions. Figures 4.25 and 4.26 illustrate the mismatch between the prediction distribution (shown in the "red" line) and the experimental data (shown in the "blue" line), with the area metric shown as the grey shaded area. This metric response has a value of 0.056N for the drag force. With the area metric, it is possible to check the adequacy of the model locally (on a specific point of the experimental test) or globally, by evaluating the difference value of 1.44N, for the lift forces.

The model validation process was conducted using three methods recommended by the ASME. The residuals, the adjusted R^2, and the area metric validation methods agree that the CFD model accurately estimates the lift and drag forces of the adaptive leading edge wing prototype. The model gave a 98% prediction rate, which is above the prediction rate of 85% recommended by ASME.

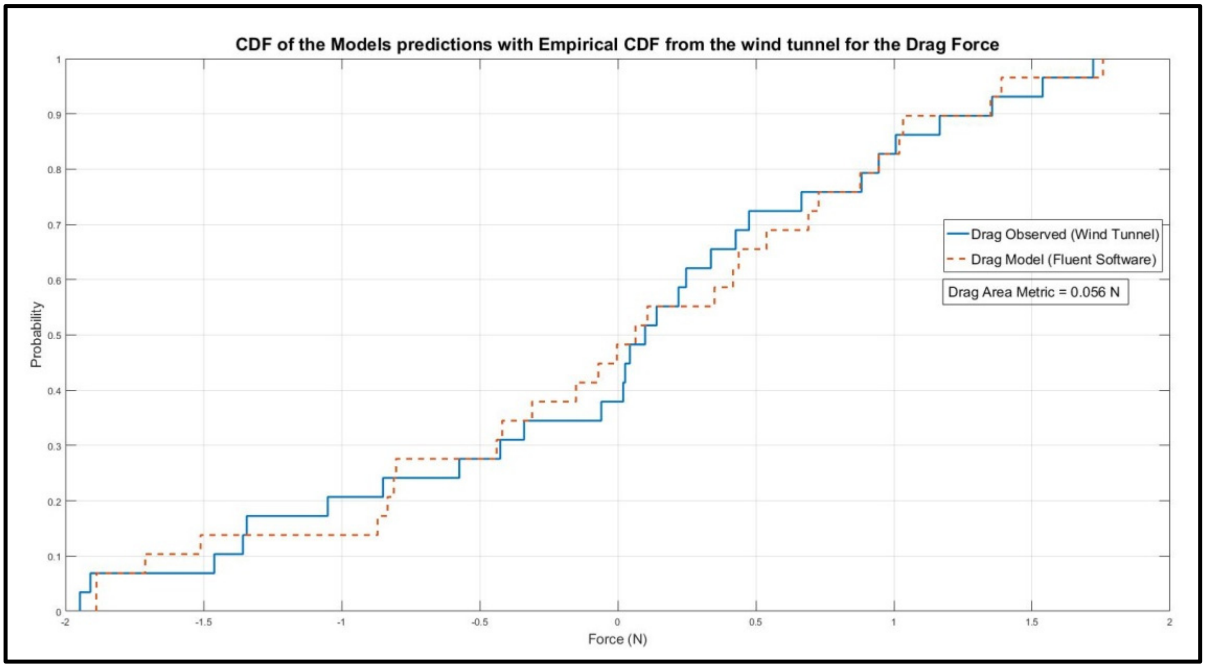

Figure 4. 25 Area metric results for drag forces

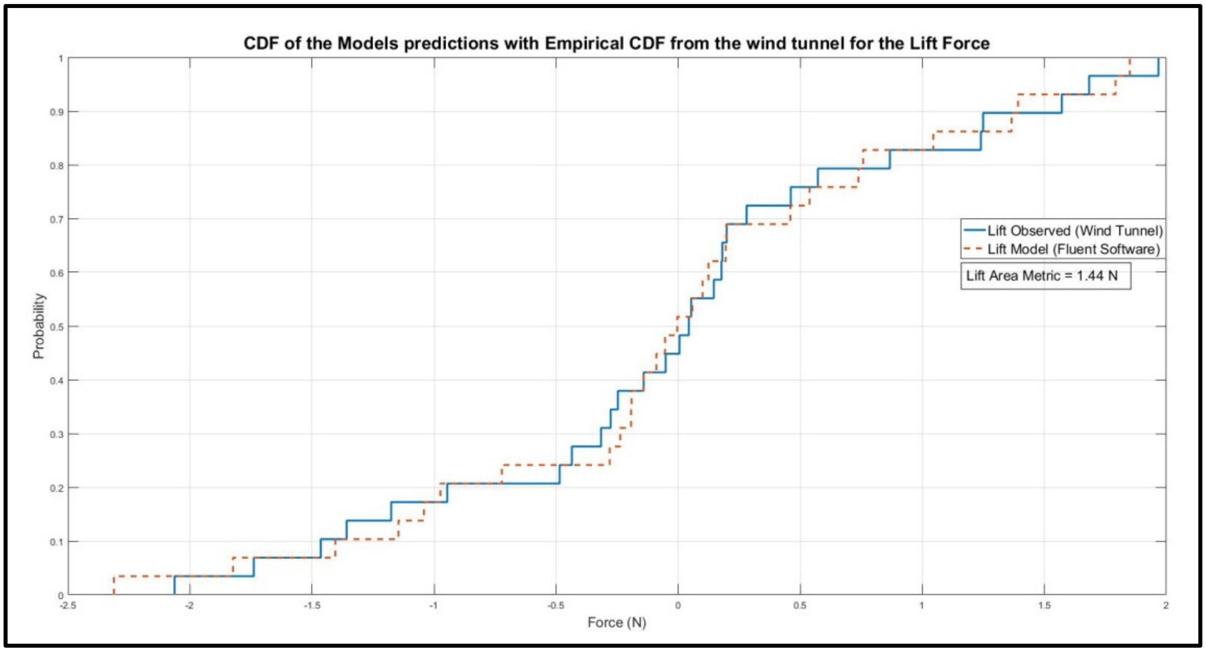

Figure 4. 26 Area metric results for lift forces

4.8 Conclusions

The study of the current "state of the art" of adaptive wings systems capable of improving the overall performance at subsonic speeds of UAVs was investigated as part of the literature review of this paper. It is thought by the authors that the present validation methodology on adaptive UAV wings will further improve the knowledge in this field. In this paper, a new validation methodology was developed to improve UAV aerodynamic performance during the cruise flight, by means of the model design, fabrication, simulation, and model validation of an adaptive wing prototype for the UAV S45. An adaptive wing was designed and validated using the proposed multidisciplinary methodology to find its optimized wing shapes that are able to improve the lift and drag performance during cruising phase. The main objective of this article was to develop a validation framework for an adaptive wing.

Aircraft design disciplines, airfoil shape optimization, computational simulations, and wind tunnel tests were integrated into this framework. The CFD models allowed us to obtain the aerodynamic performances of the wing equipped with an adaptive leading edge and trailing edge.

The verification and validation of the CFD model with an accurate mesh grid and the area metric method were successfully performed. The simulation results obtained, with the specific flow conditions defined in the wind tunnel tests, accurately agree with the experimental studies.

The authors have used the term “New knowledge” in the abstract as we believe that the MDO methodology and the CFD model validation presented in this study both correspond to “a novel research outcome” on improving the performance of adaptive wings.

The results of the adaptive wing system can be seen in Figure 4.27, where the lift-to-drag ratios can increase compared to the S45 original wing shape value of $L/D = 3$. The wind tunnel results show the efficiency of the adaptive wing prototype in producing less drag and more lift, resulting in higher L/D values, depending on the configuration of the actuators. This prototype wing can produce an important lift-to-drag ratio without extra fuel consumption from the UAV's engine. The L/D = 7.5 for test #21 is at the maximum displacement of the actuators but within the safety structural parameters of the prototype.

The low drag production and high lift-to-drag ratio (efficiency factor) of the adaptive wing will translate into a reduction in fuel consumption and an increase in the S45 effective range. Adaptive wing systems for UAVs are a promising technology and have become a major solution for multipurpose flight operations because they allow the aerodynamic potential of UAVs to be optimized by adapting the wing to several flight conditions, and they also result in climate improvement by fuel consumption minimization.

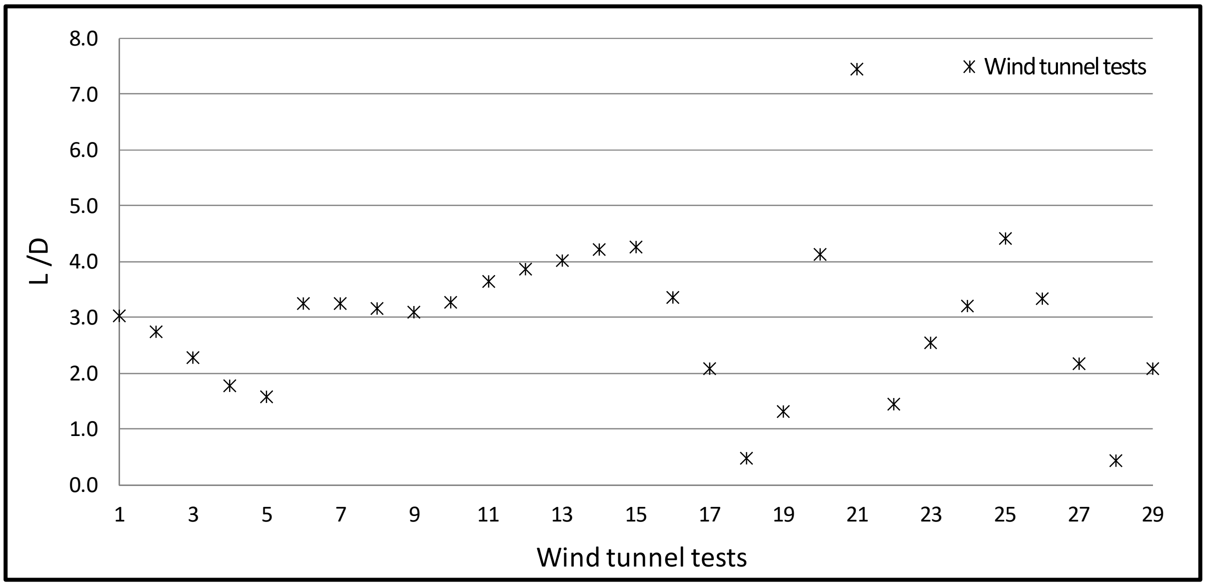

Figure 4. 27 Lift-to-drag wind tunnel results of the adaptive wing prototype at cruising speed of 30.1 m/s

Acknowledgments: The authors would like to express their thanks to Michael Païdoussis and Stuart Price for the donation of the Price–Païdoussis Open Return Subsonic Wind Tunnel at the LARCASE research laboratory at École de technologie supérieure. The authors gratefully acknowledge the financial support by the Natural Sciences and Engineering Research Council of Canada (NSERC).

CHAPITRE 5

EXPERIMENTAL WIND-TUNNEL STUDY OF THE DYNAMICS OF INVERTED FOILS FOR ENERGY HARVESTING

Manuel Flores Salinas[a], Ruxandra Mihaela Botez[b] Mohammad Tavallaeinejad[c] and Michael P. Païdoussis[d]

[a,b] Department of Systems Engineering, École de Technologie Supérieure,
1100 rue Notre-Dame West, Montreal, Québec, Canada H3C 1K3
[c,d] Department of Mechanical Engineering, McGill University,
845 Sherbrooke St West, Montreal, Québec, Canada H3A 0G4

Paper published in Aeronautical Journal, May 2023

Résumé

Cet article décrit la méthodologie utilisée pour analyser les oscillations des plaques flexibles ayant leur rapport de dimensions (Aspect Ratio AR) $0.5 \leq AR \leq 4.0$, et les nombres de Reynolds, $10^4 \leq Re \leq 10^5$, à des fins de production d'énergie renouvelable. Ces plaques flexibles ont été fixées uniquement d'un bord, et des oscillations grandissantes ont été observées au fur et à mesure que la vitesse de l'écoulement augmentait. Les oscillations ont été ensuite analysées en fonction de la vitesse de l'écoulement, du nombre de Reynolds, de l'amplitude des oscillations et de leurs fréquences. De plus, les forces produites par les plaques flexibles ont été mesurées à l'aide d'une balance aérodynamique, conçue spécialement pour cette recherche. La production d'énergie de chaque plaque flexible a été établie par une équation empirique. Les conclusions de l'étude montrent qu'une plaque flexible de dimensions AR=3 produit des oscillations périodiques de large amplitude sur une grande plage de vitesse et des grandes forces d'oscillations, ce qui rend cette plaque très efficace pour la production d'énergie renouvelable.

Abstract

This paper describes the methodology used to analyze oscillations of foils of a wide range of aspect ratios, $0.5 \leq \mathrm{AR} \leq 4$, and Reynolds numbers, $10^4 \leq \mathrm{Re} \leq 10^5$, for energy harvesting purposes. The foils were fixed at their trailing edge, and their dynamical behavior was captured as the wind speed was varied. The foil response was then analyzed as a function of velocity, Reynolds number, oscillation amplitude and frequency. Additionally, the forces and moments acting on the foils were measured, utilizing an aerodynamic scale, designed and built in-house. An empirical power generation equation was derived to determine the foil characteristics for maximum energy harvesting production. The results show that a flexible foil with AR=3 with oscillations in the large-amplitude regime is the most effective for energy harvesting.

Nomenclature

A	Oscillation amplitude	P_t	Fluid total pressure
AR	Foil aspect ratio	P_s	Fluid static pressure
B	Deflection rigidity	q_c	Fluid dynamic pressure
d	Dimensionless amplitude	PDF	Probability density function
E	Young's modulus	PSD	Power spectral density
f	Vortex shedding frequency	Re	Reynolds number
F_x , F_y	Foil force components	St	Strouhal number
H, L, h	Foil height, length, thickness	U	Flow velocity
Kb	Bending stiffness ratio	μ	Mass ratio
LE	Foil leading edge	ν	Kinematic viscosity
l/L	Foil dimensionless deflection	ν_p	Poisson's ratio
$\Delta l/L$	Dimensionless tip deflection	ρ_s	Foil density
M_x , M_y	Foil moment components	ρ_f	Fluid density, air density
TE	Foil trailing edge	w(L, t)	Foil displacement
$\overline{P}$	Power extracted	$\dot{w}(L, t)$	Foil velocity

5.1 Introduction

Renewable energy production that can function for extended periods of time and reduce the need for batteries is of major concern in the modern world (Matlock et al., 2019), (Stockbridge, Ceruti & Marzocca, 2012), (Afonso et al., 2021). A great deal of effort has been expended towards developing self-powered devices that can capture energy from oscillating foils and convert it into energy (Alam et al., 2021), (Allen & Smits, 2001), (Dunnmon et al., 2011). A flexible foil immersed in a fluid flow can experience self-induced periodic oscillations at various flow velocities. The oscillation of foils is of interest not only because of its occurrence in nature, but also because it can generate great amounts of clean renewable energy, even with relatively small-sized foils (Rostami & Armandei, 2017), (Nabavi & Zhang, 2016), (Machado, Matlock & Suleman, 2019).

In this research, we consider cantilevered foils exclusively, with a clamped trailing edge (TE), a free leading edge (LE), and no other support elsewhere. This configuration is referred to as the "inverted foil configuration". The flow direction is parallel to the rest position of the foil, and is presumed to be uniform and steady, as shown in Figure 5.1. The 2D representation shows the length (*L*) and height (*H*) of the foil and the mean flow speed *U* direction.

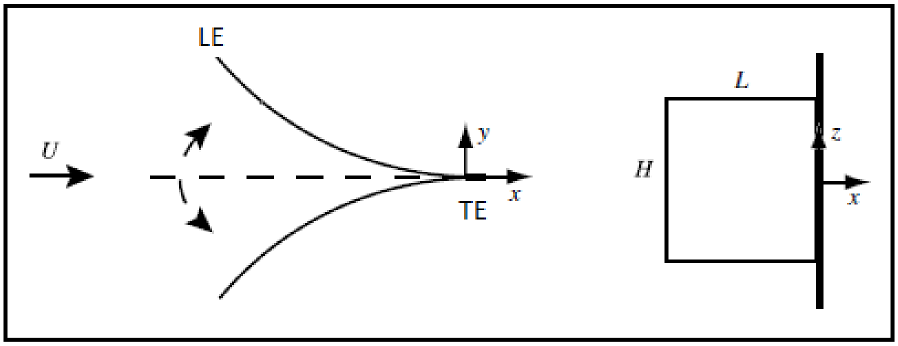

Figure 5. 1 Physical parameters of an inverted foil configuration

Analytical and experimental studies on conventional plates in axial flow were performed by Guo & Païdoussis (2000) who employed inviscid potential flow theory to predict the onset of oscillatory instability. They were the first to conclude that the plates oscillate at critical velocities inversely proportional to their mass ratio.

In 2013, the first experimental investigation on inverted foil flapping was conducted by Kim et al. (2013) who identified three flow regimes, namely, with the foil straight, undergoing large-amplitude flapping, and fully deflected. Additionally, they reported that the foil mass ratio has little effect on the onset of large-amplitude flapping.

In a 2016 study by Sader, Huertas-Cerdeira & Gharib, (2016) it was found that two key parameters of the dynamics of inverted foils are the foil's length (*L*) and height (*H*). For foils, where *L* is at least 10 times *H*, they found that foils do not flap, but they go from the straight mode (a) to the fully-deflected mode (f) shown in Figure 5.2. Additional dynamical states have been identified in that and subsequent studies (Sader, Huertas-Cerdeira & Gharib, 2016), (Tavallaeinejad et al., 2020), (Tavallaeinejad, Païdoussis & Legrand, 2020) (Tavallaeinejad et al., 2020) as a function of flow velocity and foil aspect ratio. For sufficiently large aspect ratio, as shown in Figure 5.2, the foil (a) is straight, (b) is buckled, undergoes (c) small-amplitude asymmetric flapping, (d) large-amplitude flapping, (e) aperiodic or chaotic flapping, and (f) becomes fully deflected.

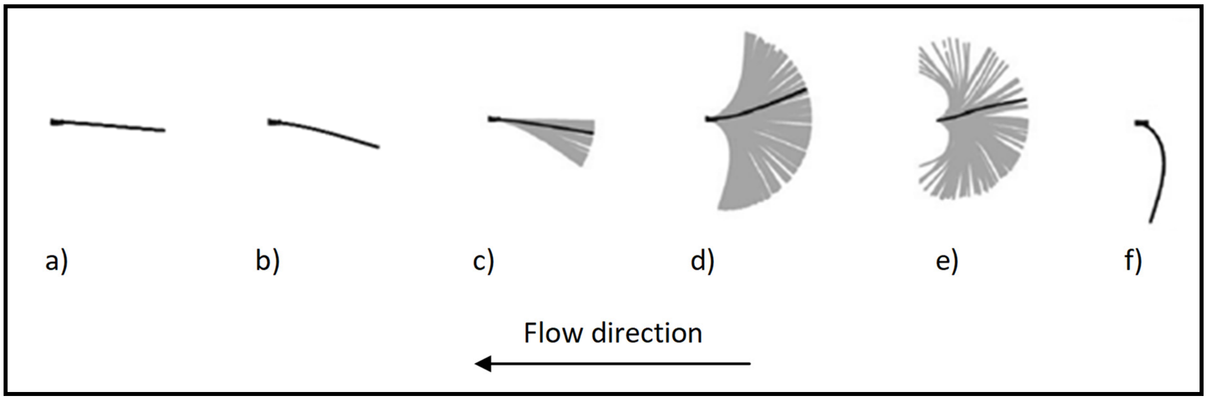

Figure 5. 2 Experimental measurement of a foil clamped at the trailing edge (inverted foil configuration) in axial flow. The direction of the flow is from right to left, as shown by the arrow. The foil is in black color and its recorded path is in gray color. The foil dynamics shows the followings modes: (a) straight, (b) buckled, (c) small-amplitude asymmetric flapping, (d) large-amplitude flapping, (e) aperiodic or chaotic flapping and (f) fully deflected state. Data collected and image produced in Matlab software version 9.0 (R2016a)

In this paper, we analyze the dynamics of inverted foils over a wide range of foil aspect ratios, $0.5 \leq \mathrm{AR} \leq 4$, in the Reynolds number regime of $10^4 \leq \mathrm{Re} \leq 10^5$, in well-defined and controlled experimental tests. The inverted foil configuration was chosen in this research because: (i) inverted-foils are more susceptible to instabilities at various flow conditions and can exhibit more flapping modes; (ii) an inverted foil configuration can produce energy several times larger than a conventional-foil configuration for the same foil size (Yu, Liu & Chen, 2017), (Zhao et al., 2012), (Chen et al., 2021), (Hu et al., 2018).

As stated earlier, the overall motivation for this research is to investigate the dynamics of inverted foils as an efficient energy harvesting system. This method of renewable energy production requires fluid kinetic energy to be transferred to the foil (as strain energy), and then the strain energy to be converted into energy with an "energy generator mechanism" that will rotate a motor shaft. The "energy generator mechanism" design and validation is part of a future study by the present authors. The Power $\overline{P}$ extracted from the "energy generator mechanism" is equivalent to the extracted energy from foil oscillations. As there is no actuation system, the input energy is null, and thus the net energy extracted is always guaranteed to be positive. The extracted energy from an oscillating foil can be determined using the empirical equation of Mitcheson et al. (2008),

$$\overline{P} \approx A\,\mathrm{St}^3. \tag{5.1}$$

where $\overline{P}$ is the extracted power, A is the oscillation amplitude, and St is the Strouhal number.

The research objectives in this paper are the following.

(1) Investigate the effects of foil length and height (aspect ratio), flapping frequency, flapping regime, Strouhal number, Reynolds number and foil peak-to-peak amplitude.

(2) Analyze the characteristics of inverted foils for power generation.

(3) Analyze the forces acting on inverted foils for a better understanding of foil dynamics and power generation.

5.2 Definitions of dimensionless parameters

We consider a foil of length *L*, height *H*, density ρ_s, thickness h, in fluid flow of density ρ_f and flow velocity *U*. The aspect ratio AR, mass ratio μ, and Reynolds number are defined by Kim et al., (2013),

$$\mathrm{AR} = \frac{H}{L},\ \mu = \frac{\rho_f\, L}{\rho_s\, h},\ Re = \frac{U\, L}{\nu}, \tag{5.2}$$

where ν is the fluid kinematic viscosity.

A dimensionless amplitude of oscillation is defined by Kim et al., (2013),

$$d = \frac{A}{L}, \tag{5.3}$$

where *A* is the maximum peak-to-peak amplitude.

We also define a parameter *Kb* as defined by Kim et al., (2013).

Bending stiffness *Kb* is the ratio of the deflection rigidity *B* of the foil and the fluid inertia, as shown by equation (5.4). The fluid inertia is defined by the product between fluid density ρf, flow velocity *U* and foil length *L*, as shown in equation (5.5). The deflection rigidity *B*, which is the force required to bend a flexible foil, depend on the Young's modulus *E*, the foil thickness h, and the Poisson' ratio of the foil material defined by the variable ν, as shown in equation (5.6).

$$Kb = \frac{\text{Deflection rigidity}}{\text{Fluid inertia}}, \tag{5.4}$$

$$Kb = \frac{B}{\rho_f\, U^2\, L^3}, \tag{5.5}$$

$$B = \frac{E\,h^3}{12(1-\nu^2)}, \tag{5.6}$$

Also, presuming that vortex shedding from the deformed upstream end of the foil occurs, we define the Strouhal number as shown in equation (5.7) from the work of Mitcheson et al., (2008).

$$\mathrm{St} = \frac{fA}{U}, \tag{5.7}$$

where f is the vortex shedding frequency in Hz.

5.3 Apparatus and Instrumentation

The experimental tests were performed in the Price-Païdoussis subsonic wind tunnel of the Research Laboratory in Active Controls, Avionics and Aeroservoelasticity (LARCASE). New methodologies in the aeronautical field have been developed at the LARCASE, including Computational Fluid Dynamics model validations with experimental results from subsonic wind tunnel tests (Grigorie, Botez & Popov, 2015), (Koreanschi, Gabor & Botez, 2016), (Tchatchueng et al., 2016), (Gabor, Koreanschi & Botez, 2016), (Botez, 2018), (Gabor, Koreanschi & Botez, 2016), (Koreanschi, Gabor & Botez, 2016), (Salinas, Botez & Gauthier, 2021), (Mosbah et al., 2013), (Communier et al., 2015).

The properties of the inverted foils, the novel design of the aerodynamics scale, the P-M wind tunnel, as well as the real-time data acquisition system and instrumentation used in this research are described in this section.

5.3.1 Foil properties

Foils made of various metal and plastic materials were tested in the wind tunnel. Brass foils were found to give asymmetric oscillation and undergo permanent deformation. Zinc foils were found to have a high material damping and could not flap at all. Stainless steel and Propylene foils had other problems (Tavallaeinejad et al., 2020). Polycarbonate foils were found to behave best, and they were chosen for the experiments to be described. Table 5.1 lists the properties and dimensions of the foils used.

Table 5. 1 Material and geometric properties of the foils tested in the wind tunnel

Foil properties	
Material	Polycarbonate
Young's Modulus E	2.38 GPa
Poisson ratio v	0.38
Foil density ρ_s	1200 Kg m^{-3}
Foil properties (continued)	
Foil aspect ratio (Length x Height x Thickness)	AR=0.50 (150 x 75 x 1.02) 10^{-3} m
Foil aspect ratio (Length x Height x Thickness)	AR=0.75 (150 x 112.5 x 1.02) 10^{-3} m
Foil aspect ratio (Length x Height x Thickness)	AR=1 (150 x 150 x 1.02) 10^{-3} m
Foil aspect ratio (Length x Height x Thickness)	AR=2 (150 x 300 x 1.02) 10^{-3} m
Foil aspect ratio (Length x Height x Thickness)	AR=3 (150 x 450 x 1.02) 10^{-3} m
Foil aspect ratio (Length x Height x Thickness)	AR=4 (150 x 600 x 1.02) 10^{-3} m
Air density ρ_f	1.225 Kg m^{-3}
Mass ratio μ ρ_f x Length / (ρ_s x Thickness)	μ = 0.15 1.225 x 150 / (1200 x 1.02)

5.3.2 Experimental setup

For the study and analysis of foil dynamics in the inverted foil configuration, a novel design was developed in-house of an aerodynamic scale for measuring forces and moments, along the three axes oriented parallel and perpendicular to the foil's surface and parallel to the foil's height. The parts of this aerodynamic scale are illustrated in Figure 5.3. The novel clamping screw mechanism uses 27 flat-head screws and two symmetrical NACA 0012 airfoils to support the inverted foil at the trailing edge, without obstructing the flow. An important characteristic of this design is that the clamping screw mechanism and the strain gauge sensors are mechanically aligned and joined together with a coupling mechanism which allows all forces and moments on the foil's surface to be transmitted to the aerodynamic scale. This unique clamping and coupling mechanism makes it possible to measure and record the foil's displacement (by a high-speed camera), and to simultaneously measure and record the forces and moments acting on the foil. The aerodynamic scale has a measured drag coefficient of only C_d=0.008 for an angle of attack AoA= 0˚.

For each flow speed, the foil displacement, forces and moments were recorded simultaneously. The interface plate allows positioning the aerodynamic scale inside the test-section without interfering with the incoming flow. The foil's clamping and the coupling mechanism were machined from high strength aluminum alloy 606. This aerodynamic scale can measure Fx, Fy and Fz forces of up to 290 N and moments Mx, My and Mz of up to 10 Nm, with a full-scale accuracy of 1/8 N and 1/19 N m, respectively. The output signals, of the measured forces and moments on all three axes, were amplified, filtered, and sent to the data acquisition system for recording and treatment.

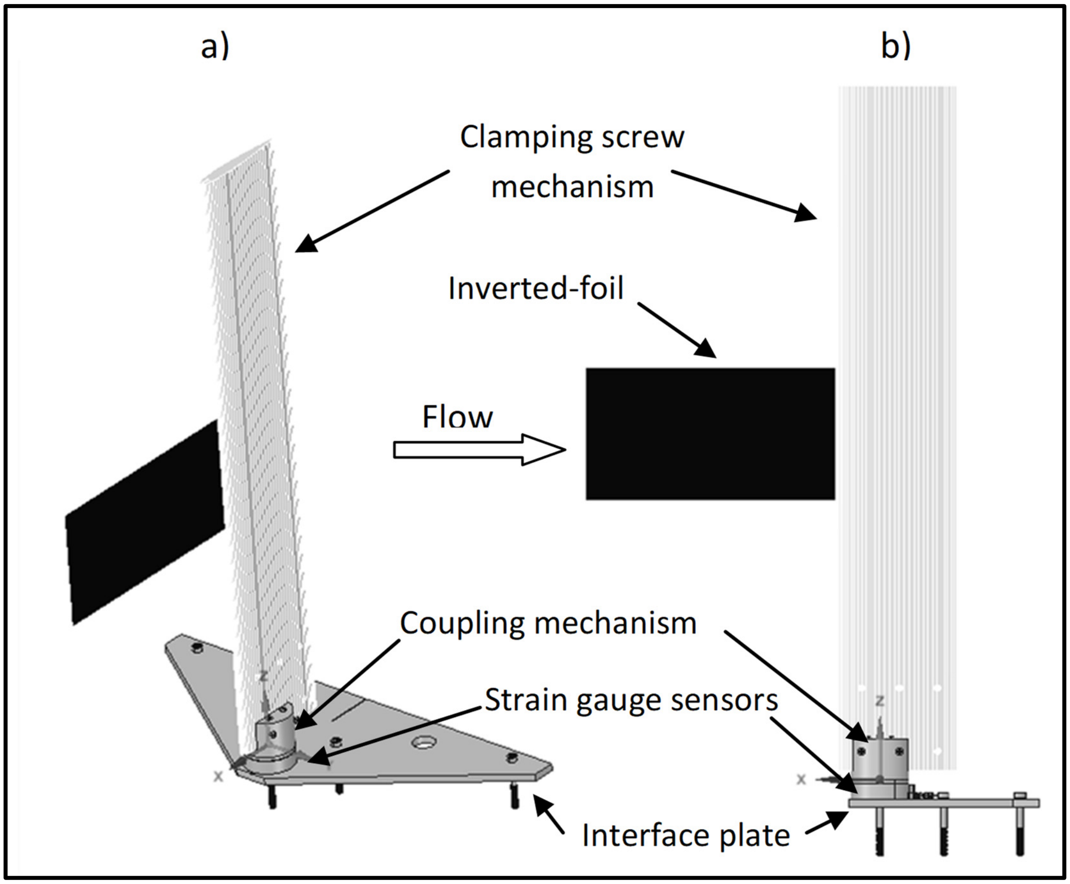

Figure 5. 3 Inverted foil aerodynamic scale for forces and moments measurements (a) side view; (b) left view

5.3.3 Wind tunnel

The Price-Païdoussis open-return subsonic wind tunnel consists of a centrifugal fan, a diffusing and settling chamber, a contraction section, and a test-chamber or test section, as shown in Figure 5.4. The air enters the wind tunnel by two inlets located on opposite sides of the centrifugal fan. The engine and the centrifugal fan are located in the mechanical room, and they are protected from dust particles by filters in an enclosed area. The main parameters to characterize the flow during wind tunnel tests are: (i) the total, static and dynamic pressures; (ii) the temperature variation during the test; (iii) the controlled flow speed, and (iv) the Reynolds number. The turbulence reduction air filters with honeycomb cell shape and squared cell shape (black dashed lines) can be seen in the settling chamber in Figure 5.4; their main function is dissipating and reducing the flow turbulence to a value below 1% (Barlow, Rae & Pope, 1999). The experiments took place in the test-section with height x width x length of 0.62 x 0.91 x 1.83 meters.

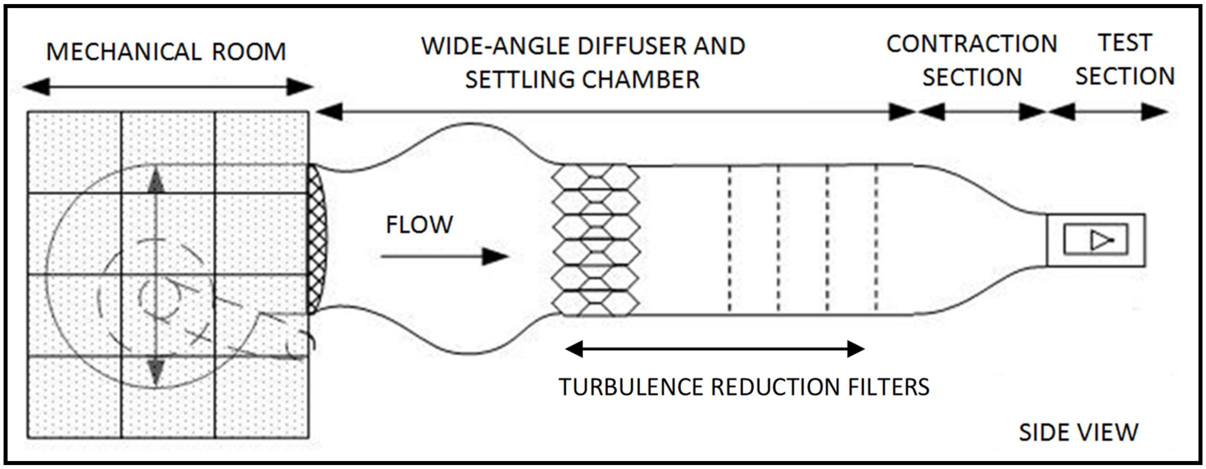

Figure 5. 4 Price-Païdoussis Wind Tunnel schematic

The flow velocity in the test-section was determined by a Pitot tube. The mean flow speed U was determined for a temperature of 22°C and using the air density ρ_f and the difference between the total pressure P_t and the static pressure P_s, as stated in equation (5.8) (Barlow, Rae & Pope, 1999),

$$P_t - P_s = q_c = \frac{1}{2}\rho_f U^2 . \tag{5.8}$$

Figure 5.5 shows an inverted foil in the wind tunnel setup for the experiments. The foil trailing edge TE was fixed and the leading-edge LE was free.

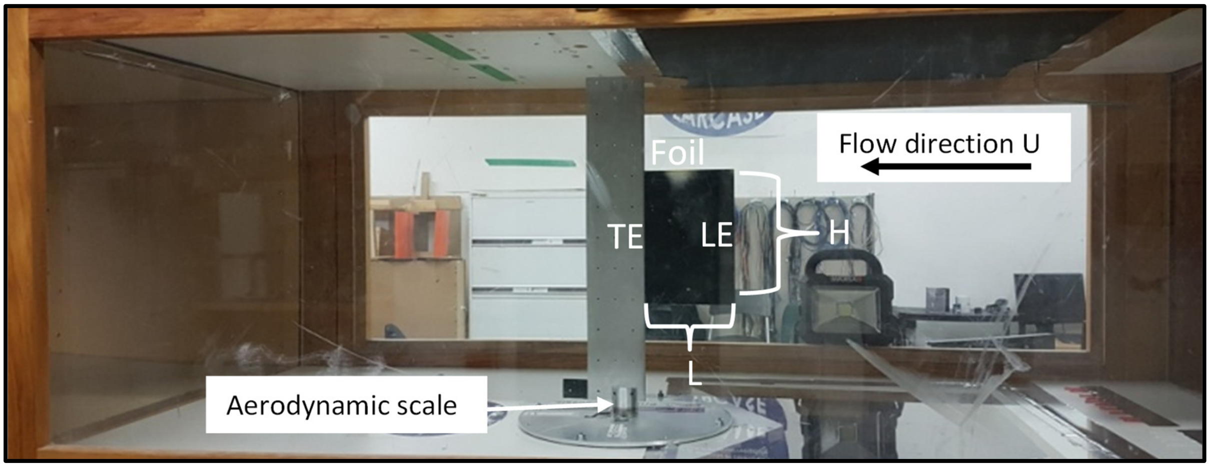

Figure 5. 5 Side view of an inverted foil configuration mounted in a wind tunnel

5.3.4 High-speed camera

Measurements were made using a FLIR Systems high-speed camera. This camera has a global shutter, minimizing “blur effects” on moving objects. It operates at 163 fps at a maximum resolution of 1920x1200 pixels; the exposure time range can vary between 0.005 ms to 31.98 seconds (FLIR, 2023). This exposure time range is sufficient to capture approximately 16 frames for a typical cycle of foil flapping. A fixed focal length lens was set on the image sensor. The camera system enables multiple points painted at the leading edge of the foils to be traced. These points help to determine the foil's displacement in real-time. A MATLAB image-processing script was developed in-house for extracting the displacements of the foils from the video images. The leading edge slope of the foil was determined, using a linear fit. A point at the leading edge of the foil was used to determine the foil’s transverse and longitudinal deflections. The length of each foil at rest was used as the reference image for calibration.

5.3.5 Data acquisition system

A multifunction data acquisition system (DAS) from National Instruments (NI), USB-6210, was chosen to convert the analog signals of the aerodynamic scale into digital data, and to save the post-processed data. The USB-6210 allows measurements of up to 16 analog inputs and does not require external power for its functioning. A video was recorded for each flow speed, from 5.0 m/s to 18.4 m/s with an increment of 0.2 m/s, to capture the foil's displacement. The high resolution and high frequency video signals were also sent to the data acquisition system for data treatment and post-processing. This data acquisition system made it possible to record the signal from the aerodynamic scale and the video signal simultaneously and in real-time. The sampling rate was 300 Hz for the foil's displacement videos and 1,000 Hz for the forces and moments.

The data collected from the videos, as well as the forces and moments, were imported with a hardware timing resolution of 50 ns (National Instruments, 2021) using an in-house MATLAB script (version 9.0-2016b), for the analysis in the post-processing phase.

5.4 Results

In this section, a combination of empirical analysis and wind tunnel measurements is used to establish the relation between foil dynamics and energy production (Poirel & Mendez, 2014), (Poirel, Harris & Benaissa, 2006). The time history of tip displacement recorded during the wind tunnel tests, the displacement at a specific flow speed (probability density function), the dominant frequencies (power spectral density) and the phase-plane portrait are used to analyze the foil dynamics.

There are three regimes of dynamic behavior for a foil with $AR < 0.1$: (i) stretched-straight, (ii) flapping and (iii) fully deflected, as observed by Sader et al., (2016). For foils with $AR \geq 0.2$, the recent work of Tavallaeinejad et al., (2021) has identified three other regimes, for a total of six possible foil dynamical states.

In this paper, we use the regimes identified in (Tavallaeinejad et al., 2021) to classify foil deflection at different flow speeds.

1. The stretched-straight regime with small vibrations superimposed.
2. The buckled regime, involving a small mean deflection with small-amplitude random-like vibrations superimposed.
3. The small-amplitude regime with coherent, periodic oscillations around the deflected equilibrium.
4. The large-amplitude flapping regime.
5. The aperiodic (chaotic) regime with intermittent flapping around the origin and to one side.
6. The fully deflected regime.

The next sub-sections present the experimental data, analyze the inverted foil deflections, describe the inverted foil's dynamics regimes and analyze the forces produced by the inverted foils.

5.4.1 Oscillations of the AR=1 inverted foil

The first experimental data presented are those of the square-shaped foil (AR=1), with $H=L=150$ mm. This foil will be the reference foil, utilized to assess if a more slender or a wider foil is better suited for energy harvesting.

At very low airflow speeds, between 5.0 m/s and 7.0 m/s, the foil stays in a stable undeformed equilibrium, parallel to the incoming flow without any oscillation, as shown in Figures 5.6(a) and 5.7(a). The quasi-Gaussian form of the probability density function (PDF) plots suggests small random oscillations, induced by turbulence and unsteadiness of the incoming flow, as shown in Figures 5.6(b) and 5.7(b).

Increasing the flow speed in the wind tunnel test chamber to 7.5 m/s and 7.9 m/s causes the AR=1 foil to buckle slightly and exhibit random oscillations with small amplitudes. As shown in Figure 5.8(a), the tip displacement time history is very small, and the probability density function shows a small oscillation between 0.055*L* and 0.065*L* for *U*=7.9 m/s in Figure 5.8(b).

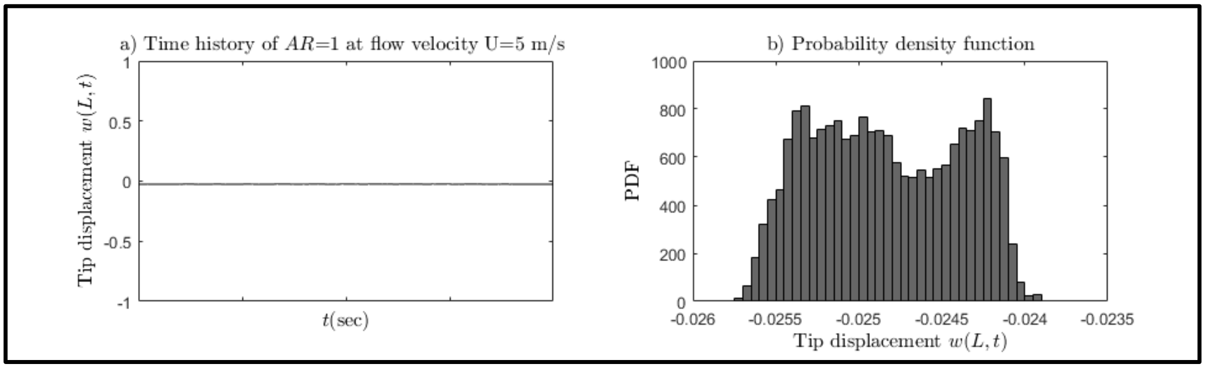

Figure 5. 6 Time history (a) and PDF (b) of the tip displacement of AR=1 foil for *U*=5.0 m/s

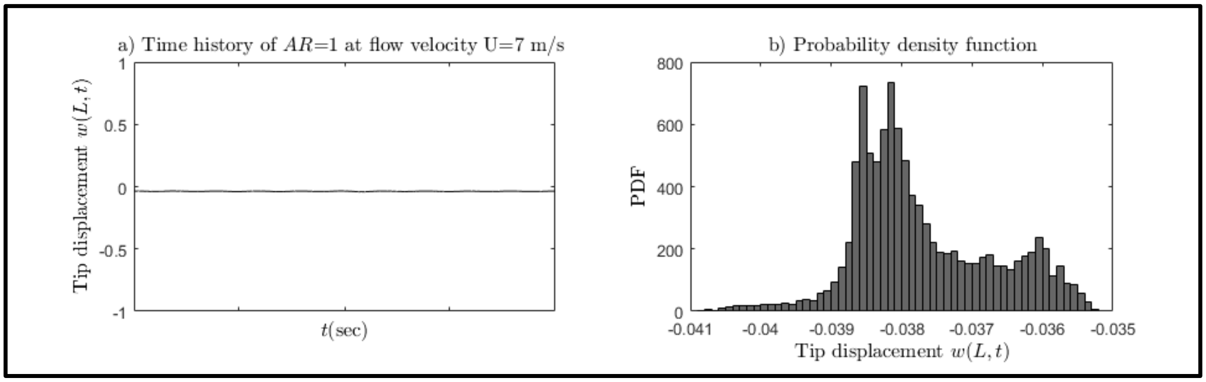

Figure 5. 7 Time history (a) and PDF (b) of the tip displacement of AR=1 foil for *U*=7.0 m/s

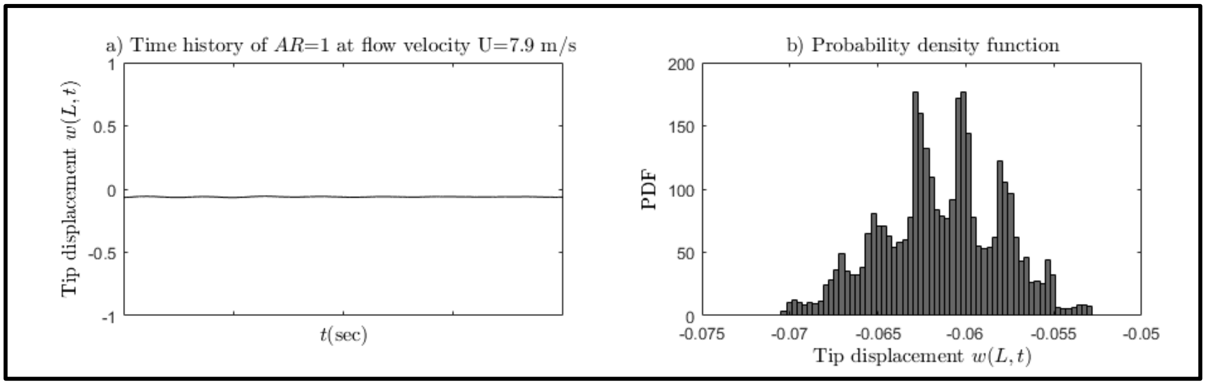

Figure 5. 8 Time history (a) and PDF (b) of the tip displacement of AR=1 foil for *U*=7.9 m/s

Increasing the wind speed to 8.1 m/s, the foil started flapping abruptly, with an amplitude of 0.8*L* and a frequency of 4.75 Hz, as seen in Figures 5.9 (a) and (d). The double mast and convex shape of the probability density function and the single-loop response of the phase-plane portrait indicate a periodic oscillation of the foil, as shown in Figures 5.9 (b) and (c), respectively.

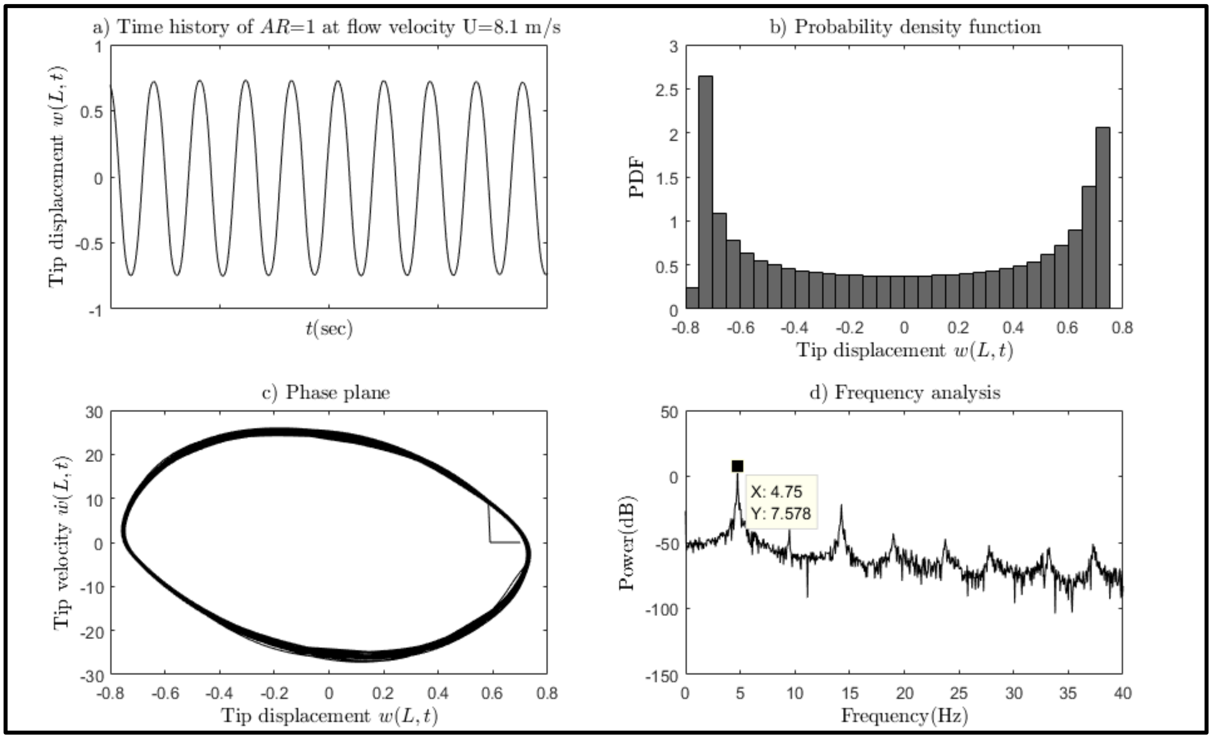

Figure 5. 9 Time history (a), PDF (b), phase-plane (c) and frequency (d) of the tip displacement of AR=1 foil for *U*=8.1 m/s

For flow speeds ranging from 8.5 m/s to 10.5 m/s, the flapping transverse amplitude reached 0.8*L*, with a flapping frequency decreasing from 4.85 Hz to 4.6 Hz (refer to Figures 5.10 and 5.11). The phase-plane plots show that the large-amplitude flapping is predominantly periodic, as does the classical double-masted shape of the PDFs, with a transition to a damped behavior of the foil deflections, as the flow speed increases.

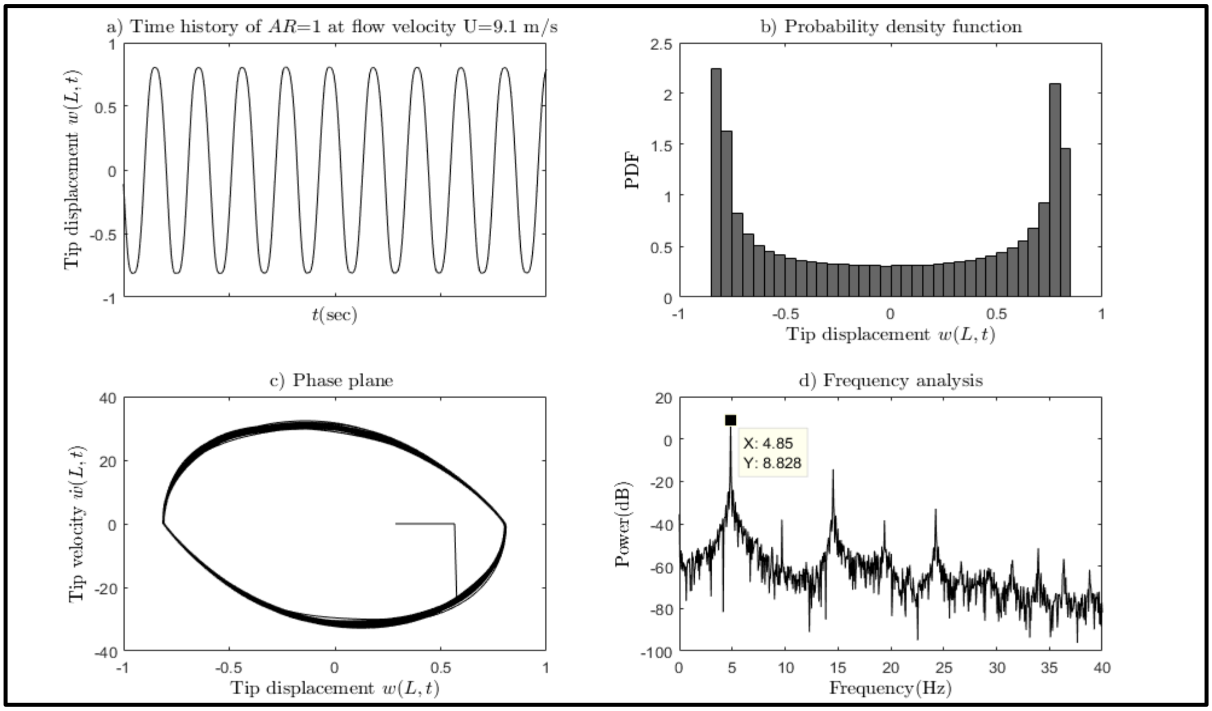

Figure 5. 10 Time history (a), PDF (b), phase-plane (c) and frequency (d) of the tip displacement of AR=1 foil for *U*=9.1 m/s

As the air flow speed is increased to 11.0 m/s, the transverse deflection response of the inverted foil shows an interesting feature with double peaks, marked by a dotted circle in Figure 5.11. The double peaks can be detected in the time history and probability density function of Figures 5.11 (a) and (b). These double peak responses indicate that the foil undergoes extremely large-amplitude bending with the tip slope going beyond 90 degrees. As a result, the transverse deflection displays local minima. This indicates that the flapping amplitude continues to increase as the wind speed increases as shown in Figure 5.11(c). In Figure 5.11(d), the frequency domain (power spectral density plot) shows higher harmonics contributing to the system response.

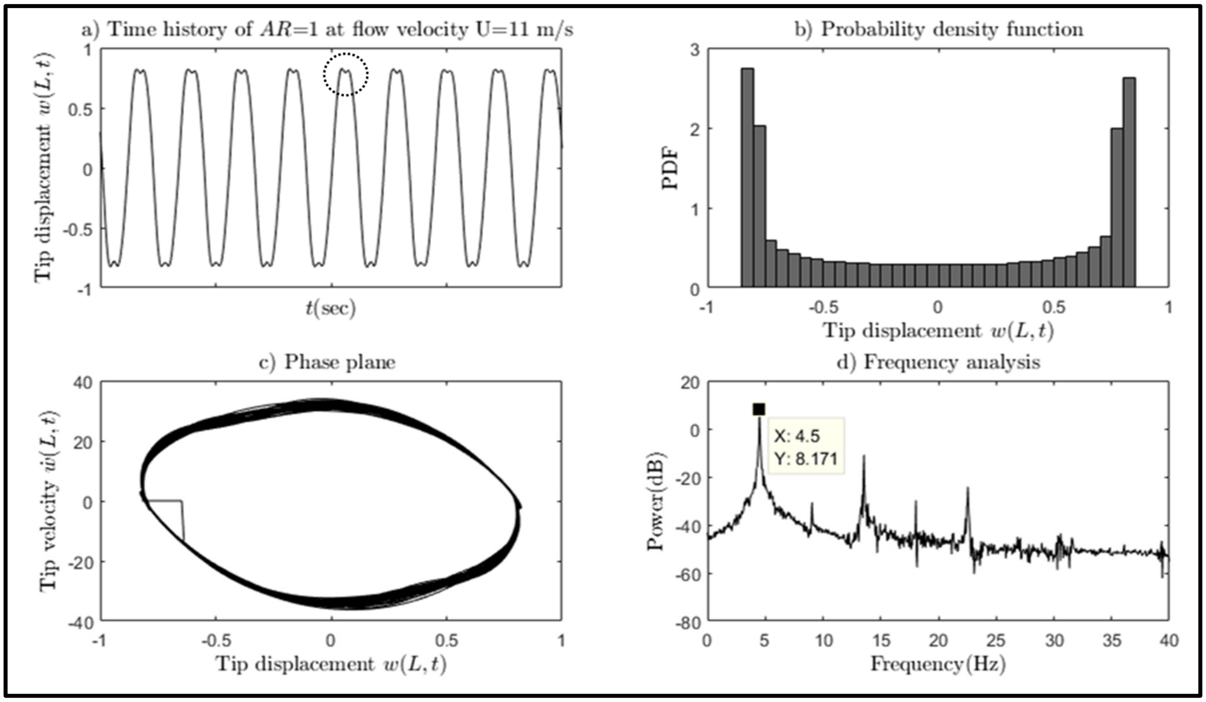

Figure 5. 11 Time history (a), PDF (b), phase-plane (c) and frequency (d) of the tip displacement of AR=1 foil for U = 11.0 m/s

For the flow speed range of 12.0≤U≤13.5 m/s, the oscillation frequency is reduced from 4.25 Hz to 3.8 Hz. Figure 5.12 shows the chaotic regime characteristics (tip displacement, PDF, phase-plane and power spectral density) of the AR=1 foil for U = 13 m/s.

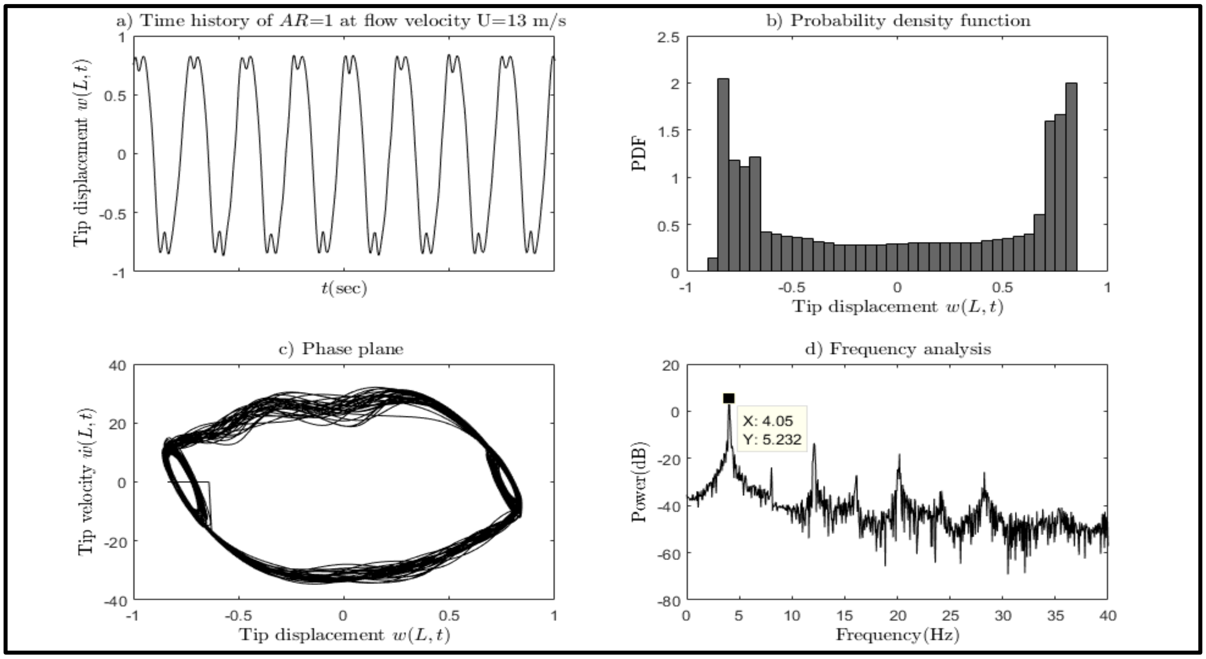

Figure 5. 12 Time history (a), PDF (b), phase-plane (c) and frequency (d) of the tip displacement of AR=1 foil for U = 13.0 m/s

For flow speed higher than 13 m/s (as seen on Figure 5.13, for 14 m/s), the two peaks at the edge of the foil oscillation have increased in size and the oscillation is no longer periodic; the inverted foil is considered in a chaotic regime. Sader et al., (2016) were among the first to identify the chaotic regime of an inverted foil. The definition given was "*when the foil transitions from a periodic, large-amplitude flapping regime to an aperiodic flapping regime, it is considered a chaotic regime*".

It can be noted in Figure 5.13 (a)-(d) for U=14 m/s, while the flapping amplitude is still ~0.8L, the dominant frequency of the inverted foil's oscillation decreases to 3.575 Hz and the phase-plane no longer shows a periodic shape. At the flow speed critical value higher than 14.0 m/s, the foil displays a one-sided deflected shape, showing the fully-deflected regime identified by Kim et al., (2013) and any oscillation will cease suddenly.

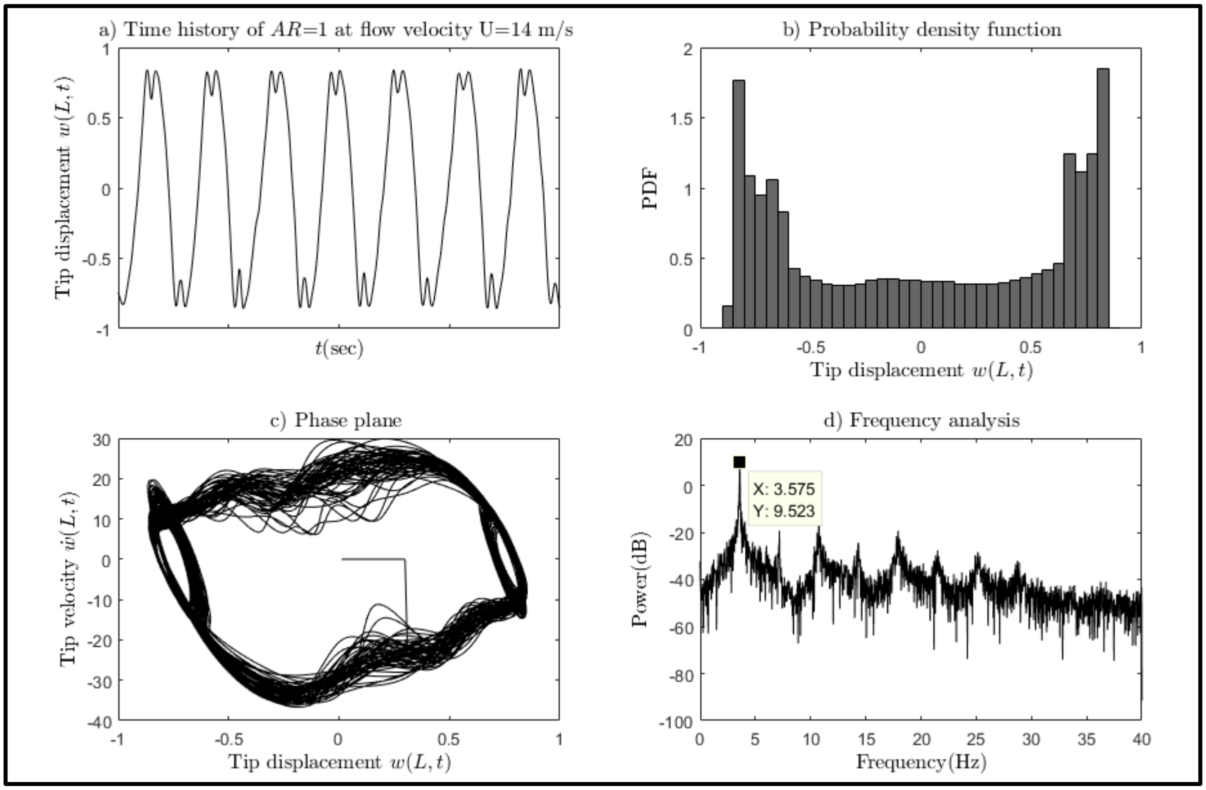

Figure 5. 13 Time history (a), PDF (b), phase-plane (c) and frequency (d) of the tip displacement of AR=1 foil for *U* = 14.0 m/s

5.4.2 Dynamic regimes of AR=1 inverted foil

Figure 5.14 shows the various transitions in dynamical state that the AR=1 inverted foil undergoes are: (a) quasi-static state with very low amplitude oscillation (less than 0.1*L*, where *L* is the foil length) for *U*<8.0 m/s corresponding to Re<8x10^4 ;(b) flapping, with amplitude 0.85*L* for *U*>8.0 m/s; (iii) cessation of flapping at *U*≈14.0 m/s.

A more refined classification of these dynamical states is given as follows: (i) totally static, (ii)-(iii) quasi-static with small oscillations; (iii)-(iv) asymmetric flapping; (iv)-(v) large amplitude flapping; beyond (v) cessation of flapping. In the range 13.0 m/s <*U*< 14.0 m/s, the oscillation is aperiodic (chaotic), with the flapping occurring more often on one side than on the other.

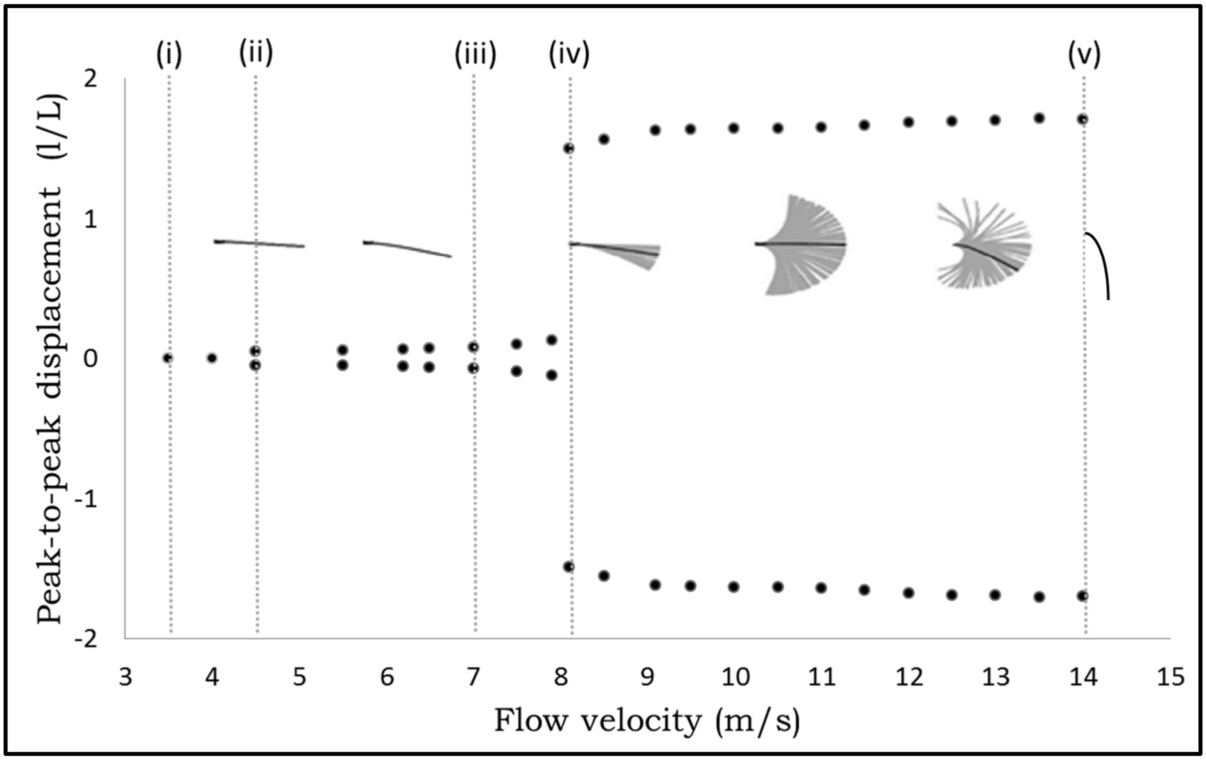

Figure 5. 14 Bifurcation of Poincaré points for the AR=1 foil

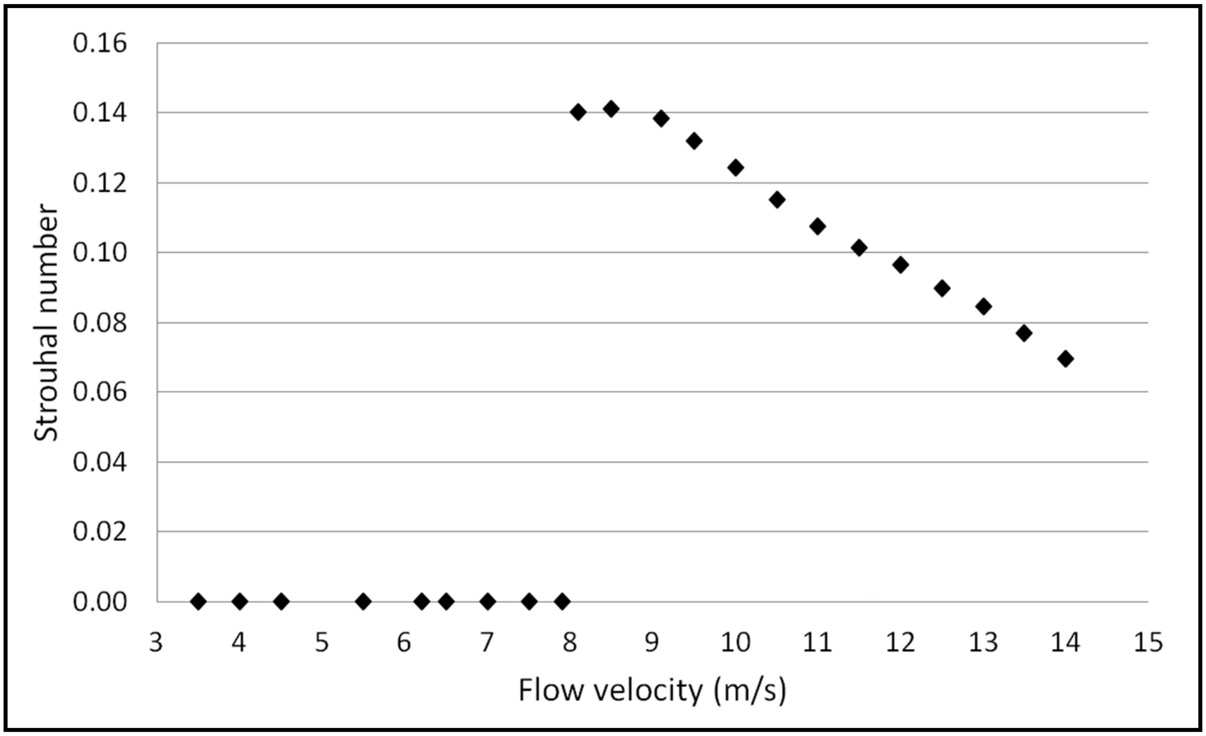

Figure 5. 15 Strouhal number of function of flow velocity for the AR=1 foil

The Strouhal number (St) variation with the *U* for the inverted AR=1 foil is provided in Figure 5.15. A non-zero St occurs once oscillation (flapping) takes place. With increasing flow velocity, St decreases from St=0.140 to St= 0.063.

5.4.3 Oscillations of the AR<1 inverted foils

The phase-plane and PSD diagrams of a foil of AR=0.5 are shown in Figure 5.16.

For *U*=9.8 m/s, the foil undergoes small oscillations as seen in Figure 5.16(a),(b), then it exhibits large-amplitude oscillations for *U*=10.0 m/s in Figure 5.16 (c),(d), aperiodic oscillations for *U*=16.7 m/s in Figure 5.16 (e),(f) and chaotic oscillations for *U*=18.5 m/s in Figure 5.16 (g),(h).

The corresponding results for a foil of AR=0.75 are shown in Figure 5.17.

For *U*=9.8 m/s, as seen in Figure 5.17 (a),(b), the foil undergoes small oscillations. At *U*=11.6 m/s, as seen in Figure 5.17 (c),(d), the large-amplitude regime is observed with a single-loop in the phase-plane diagram and a dominant frequency of 5.2 Hz in the power spectral density (PSD) diagram. At *U*=17.1 m/s, as seen in Figure 5.17 (e),(f), the foil oscillations are irregular with a reduced and not well defined (not prominent) flapping frequency of ≈2 Hz. At *U*=18.8 m/s, as seen in Figure 5.17 (g),(h), the foil fully deflects to one side and ceases oscillating.

a) Phase-plane of AR=0.5 foil at flow velocity U=9.8 m/s

b) Frequency analysis of AR=0.5 foil at flow velocity U=9.8 m/s

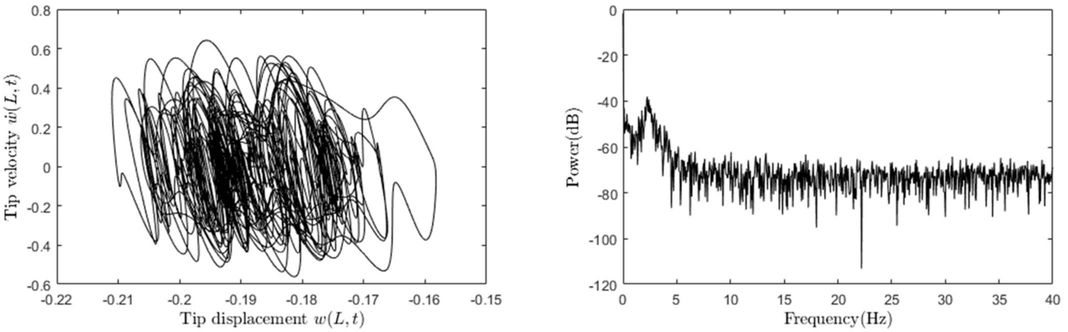

c) Phase-plane of AR=0.5 foil at flow velocity U=10.0 m/s

d) Frequency analysis of AR=0.5 foil at flow velocity U=10.0 m/s

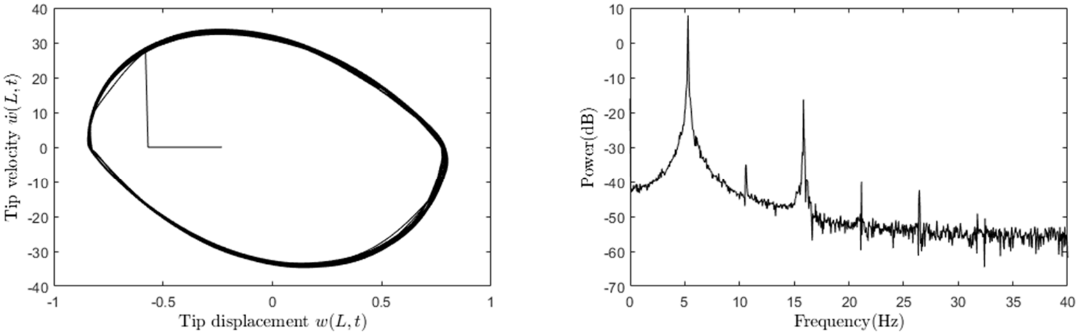

e) Phase-plane of AR=0.5 foil at flow velocity U=16.7 m/s

f) Frequency analysis of AR=0.5 foil at flow velocity U=16.7 m/s

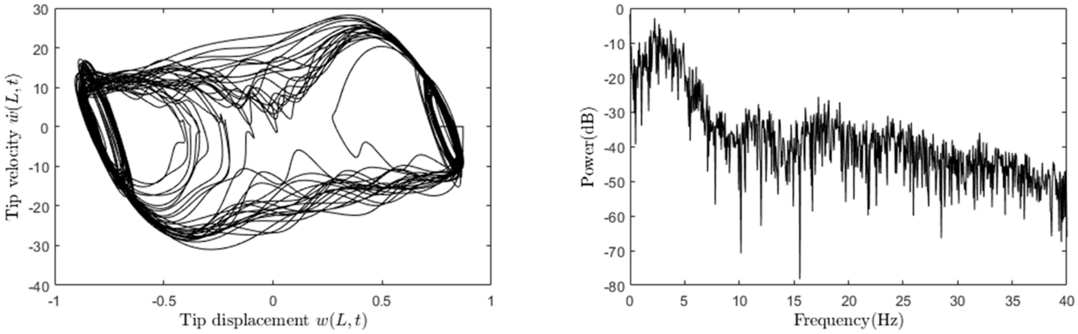

g) Phase-plane of AR=0.5 foil at flow velocity U=18.5 m/s

h) Frequency analysis of AR=0.5 foil at flow velocity U=18.5 m/s

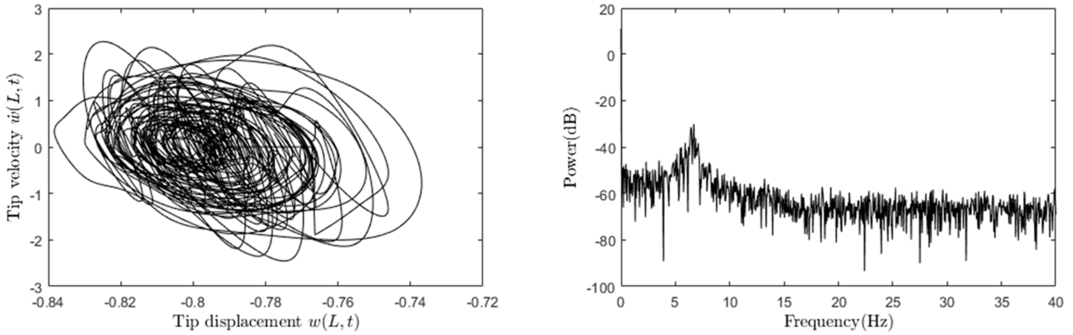

Figure 5. 16 (a,b) Phase-plane and frequency of AR=0.50 foil for U=9.8 m/s; (c,d) for U=10.0 m/s; (e,f) for U=16.7 m/s; and (g,h) for U=18.5 m/s

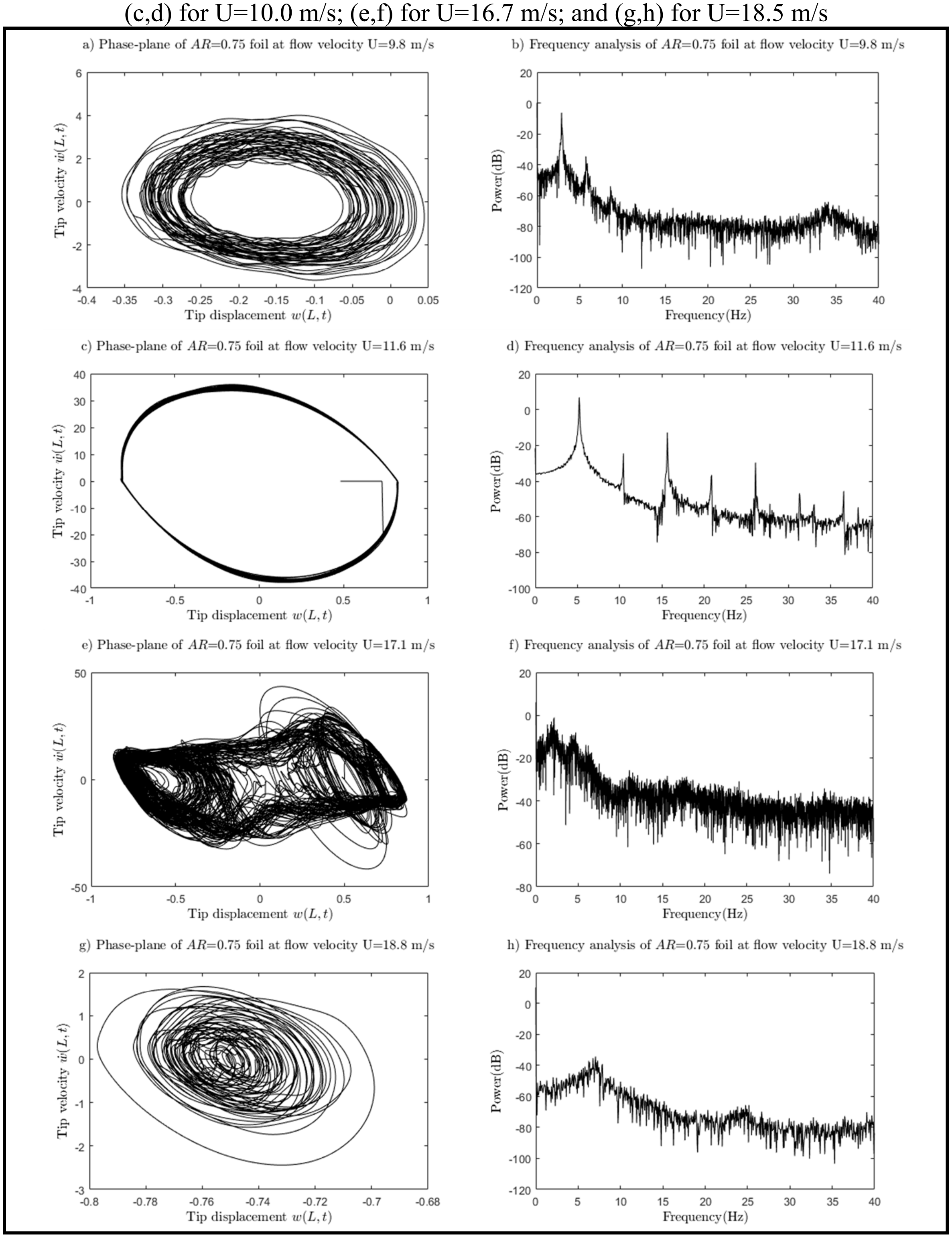

a) Phase-plane of AR=0.75 foil at flow velocity U=9.8 m/s

b) Frequency analysis of AR=0.75 foil at flow velocity U=9.8 m/s

c) Phase-plane of AR=0.75 foil at flow velocity U=11.6 m/s

d) Frequency analysis of AR=0.75 foil at flow velocity U=11.6 m/s

e) Phase-plane of AR=0.75 foil at flow velocity U=17.1 m/s

f) Frequency analysis of AR=0.75 foil at flow velocity U=17.1 m/s

g) Phase-plane of AR=0.75 foil at flow velocity U=18.8 m/s

h) Frequency analysis of AR=0.75 foil at flow velocity U=18.8 m/s

Figure 5. 17 (a,b) Phase-plane and frequency of AR=0.75 foil for U=9.8 m/s; (c,d) for U=11.6 m/s; (e,f) for U=17.1 m/s; and (g,h) for U=18.8 m/s

5.5 Oscillations of the AR>1 inverted-foils

In this section, we explore the dynamic regimes of foils whose heights are two, three and four times their lengths, AR=2, AR=3 and AR=4, respectively.

Figure 5.18 shows the experimental data and different oscillation regimes obtained for the AR=2 foil for three flow speeds U = 8.0 m/s, 8.78 m/s and 16.6 m/s. Small-amplitude oscillations around the zero (neutral) position can be seen in Figure 5.18 (a),(b) for U = 8.0 m/s. Large-amplitude oscillations, with a well-defined "single-loop" phase–plane shape and a dominant frequency of 5.3 Hz are seen in Figure 5.18 (c),(d) for U = 8.78 m/s. The ill-defined shapes on the phase-plane and the absence of a dominant frequency are signs of a chaotic regime, as observed in Figure 5.18 (e),(f) for U = 16.6 m/s.

At a flow speed U of 7.1 m/s, the AR=3 foil starts showing small-amplitude oscillations behavior, as seen in Figure 5.19(a),(b). As soon as the flow speed reaches 7.6 m/s, the large-amplitude oscillations start showing a very well-defined phase-plane shape and a dominant frequency of 5.2 Hz, as seen in Figure 5.19(c),(d). Then, a chaotic regime follows at U = 16.2 m/s, as seen in Figure 5.19 (e),(f).

The last foil tested had an aspect ratio AR=4. The small-amplitude oscillations and the phase-plane shapes are not periodic with a dominant frequency of 2.7 Hz for U=7.0 m/s is not well-defined, as observed in Figure 5.20 (a),(b). At a flow speed of 9.0 m/s, the single-loop phase-plane shape and the dominant frequency of 5.7 Hz are signs of a periodic oscillation, as seen in Figures 5.20 (c),(d). At and above U=15.9 m/s, the signs of chaotic oscillations are clearly seen: the phase-plane is no longer defined by a single loop, and a dominant frequency is absent, as seen in Figures 5.20 (e), (f). Therefore, the AR=4 foil periodic regime ranges from 9.0 m/s to 15.9 m/s, which is a wide range of flow speeds and it is promising for energy harvesting.

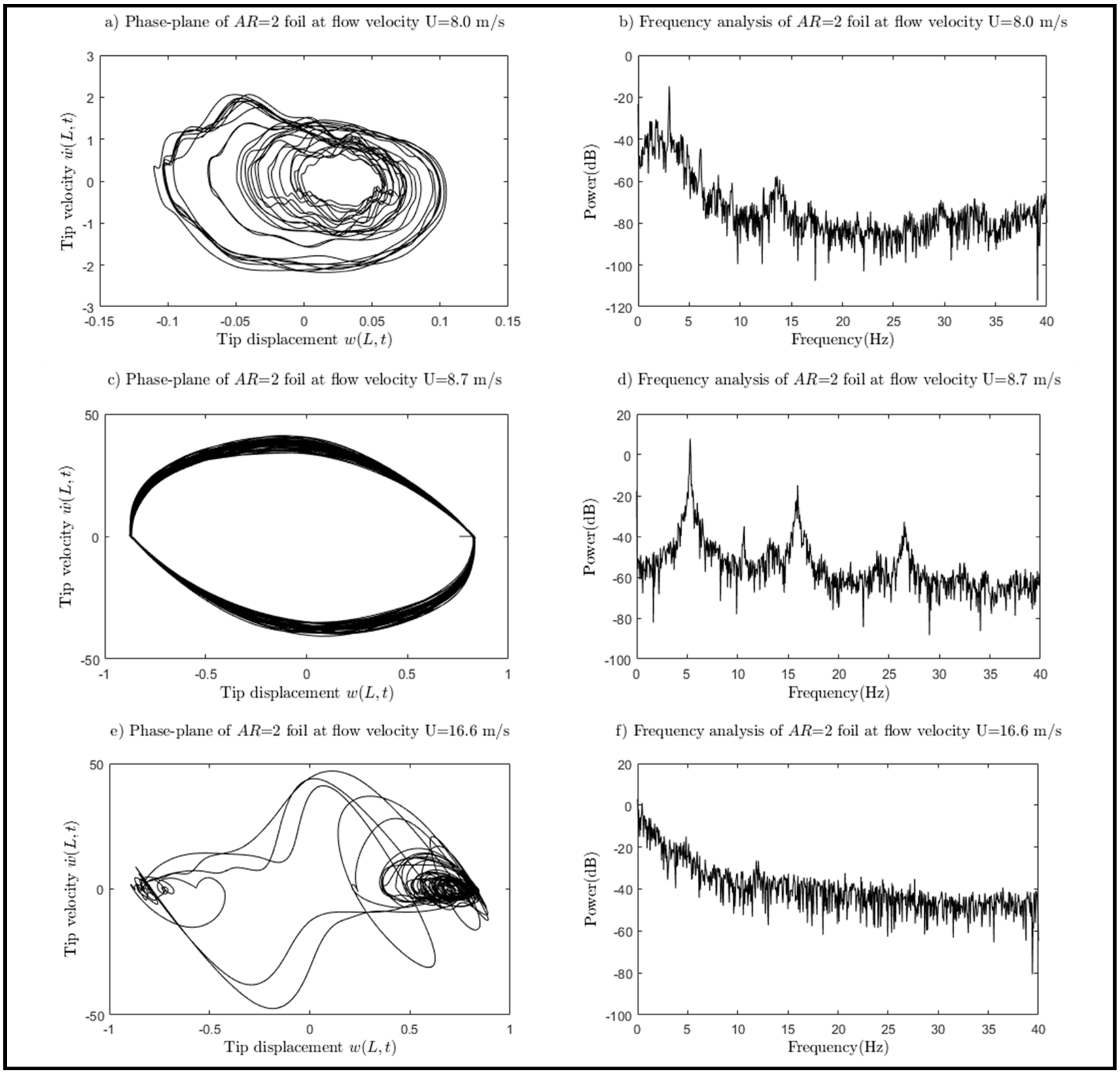

a) Phase-plane of AR=2 foil at flow velocity U=8.0 m/s

b) Frequency analysis of AR=2 foil at flow velocity U=8.0 m/s

c) Phase-plane of AR=2 foil at flow velocity U=8.7 m/s

d) Frequency analysis of AR=2 foil at flow velocity U=8.7 m/s

e) Phase-plane of AR=2 foil at flow velocity U=16.6 m/s

f) Frequency analysis of AR=2 foil at flow velocity U=16.6 m/s

Figure 5. 18 (a,b) Phase-plane and frequency of AR=2 foil for U=8.0 m/s; (c,d) for U=8.7 m/s; and (e,f) for U=16.6 m/s

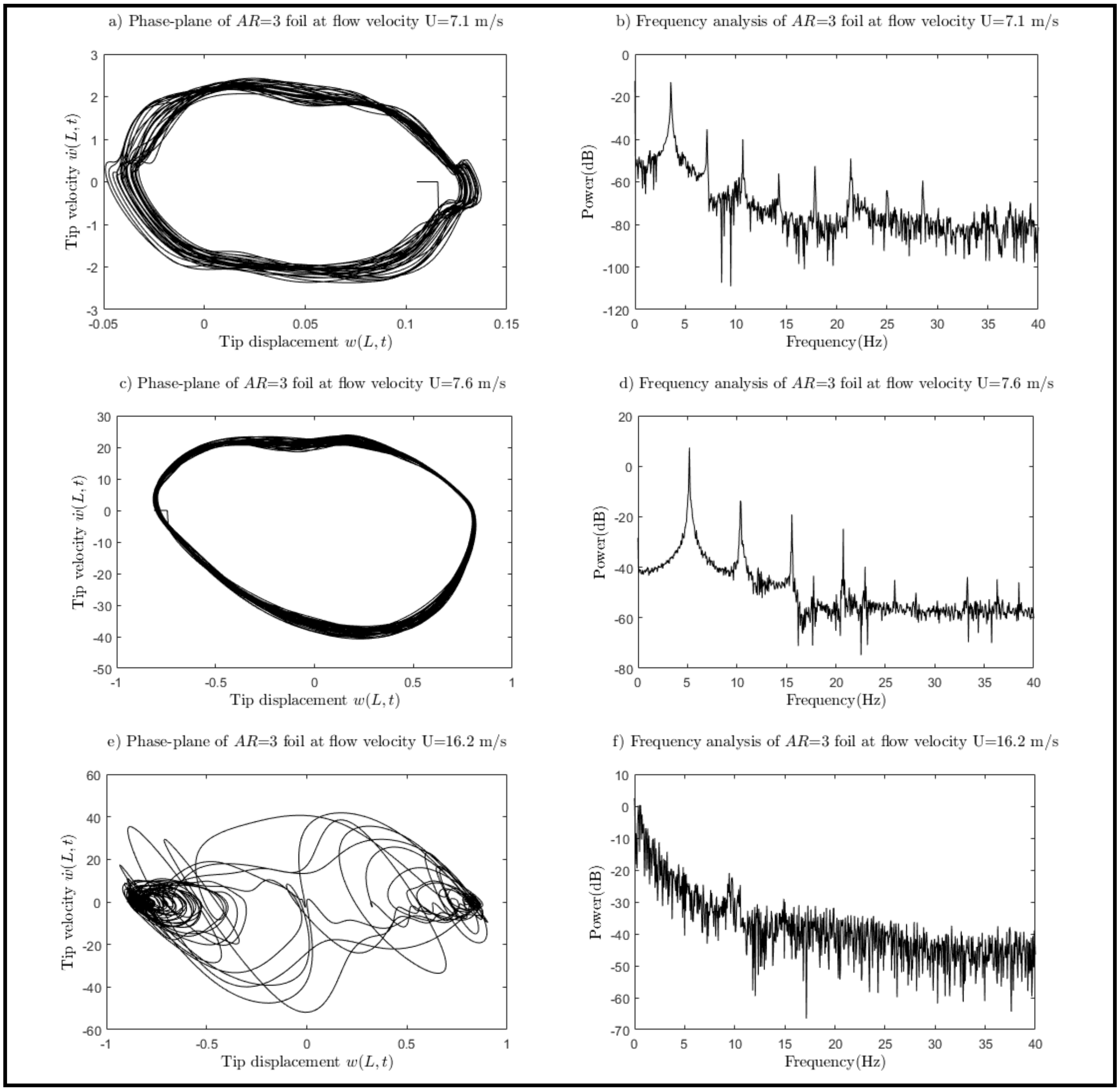

a) Phase-plane of AR=3 foil at flow velocity U=7.1 m/s

b) Frequency analysis of AR=3 foil at flow velocity U=7.1 m/s

c) Phase-plane of AR=3 foil at flow velocity U=7.6 m/s

d) Frequency analysis of AR=3 foil at flow velocity U=7.6 m/s

e) Phase-plane of AR=3 foil at flow velocity U=16.2 m/s

f) Frequency analysis of AR=3 foil at flow velocity U=16.2 m/s

Figure 5. 19 (a,b) Phase-plane and frequency of AR=3 foil for U=7.1 m/s; (c,d) for U=7.6 m/s; and (e,f) for U=16.2 m/s

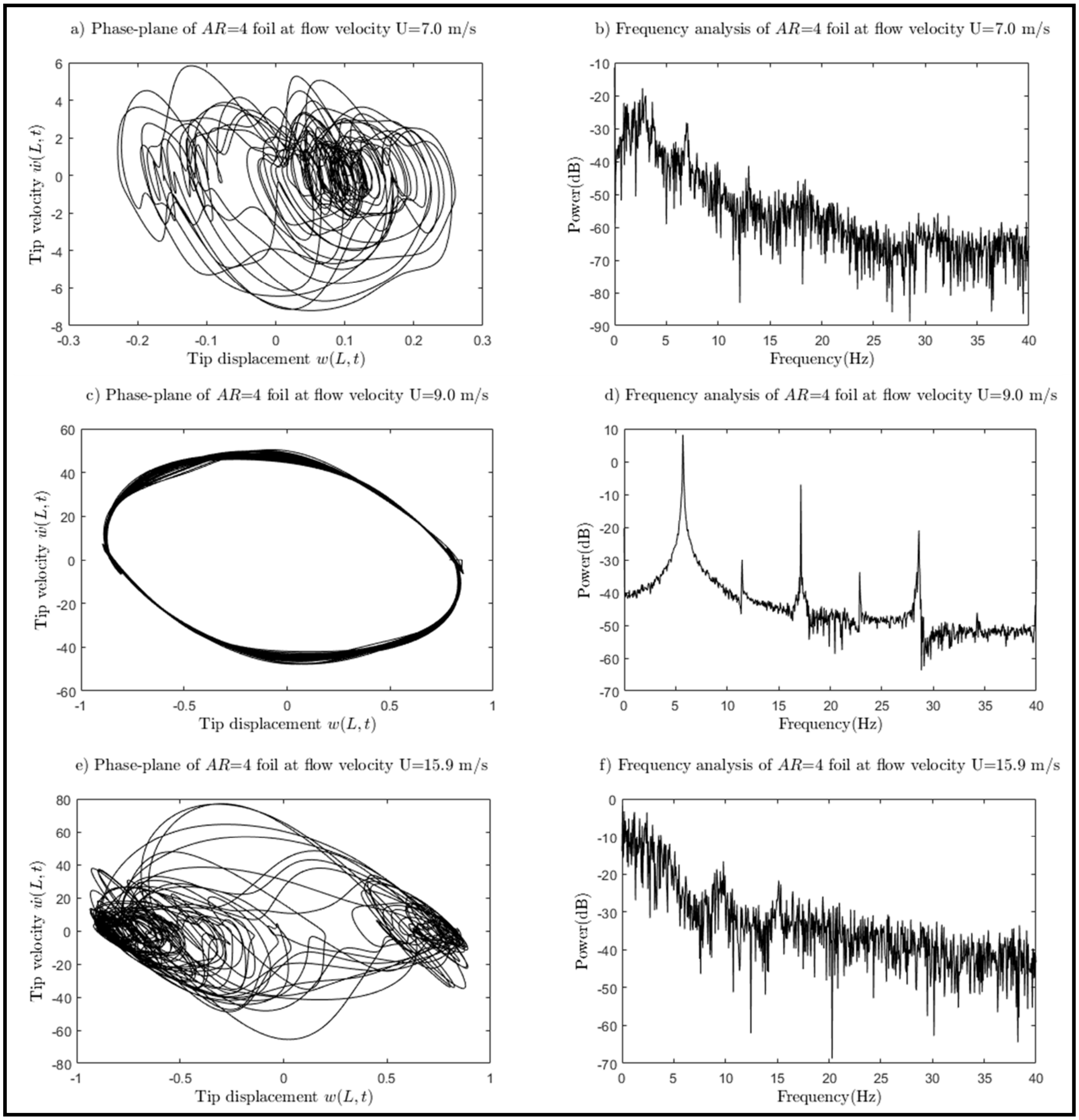

a) Phase-plane of *AR*=4 foil at flow velocity U=7.0 m/s

b) Frequency analysis of *AR*=4 foil at flow velocity U=7.0 m/s

c) Phase-plane of *AR*=4 foil at flow velocity U=9.0 m/s

d) Frequency analysis of *AR*=4 foil at flow velocity U=9.0 m/s

e) Phase-plane of *AR*=4 foil at flow velocity U=15.9 m/s

f) Frequency analysis of *AR*=4 foil at flow velocity U=15.9 m/s

Figure 5. 20 (a,b) Phase-plane and frequency of AR=4 foil for U=7.0 m/s; (c,d) for U=9.0 m/s; and (e,f) for U=15.9 m/s

5.5.1 Dynamic regimes of the 0.5≤AR≤4 inverted-foils

The bifurcations of Poincaré maps allow the six regimes identified previously to be observed in a single graph for each foil size (Poirel & Price, 2007). Figure 5.21 shows the six possible regimes encountered by the AR=0.50 foil as a function of the flow speed. The large-amplitude regime is wide before the foil's surface fully deflects.

The bifurcation diagram for the AR=0.75 foil, shown in Figure 5.22, presents well-defined regimes, with a fully deflected foil after a flow value of 18 m/s.

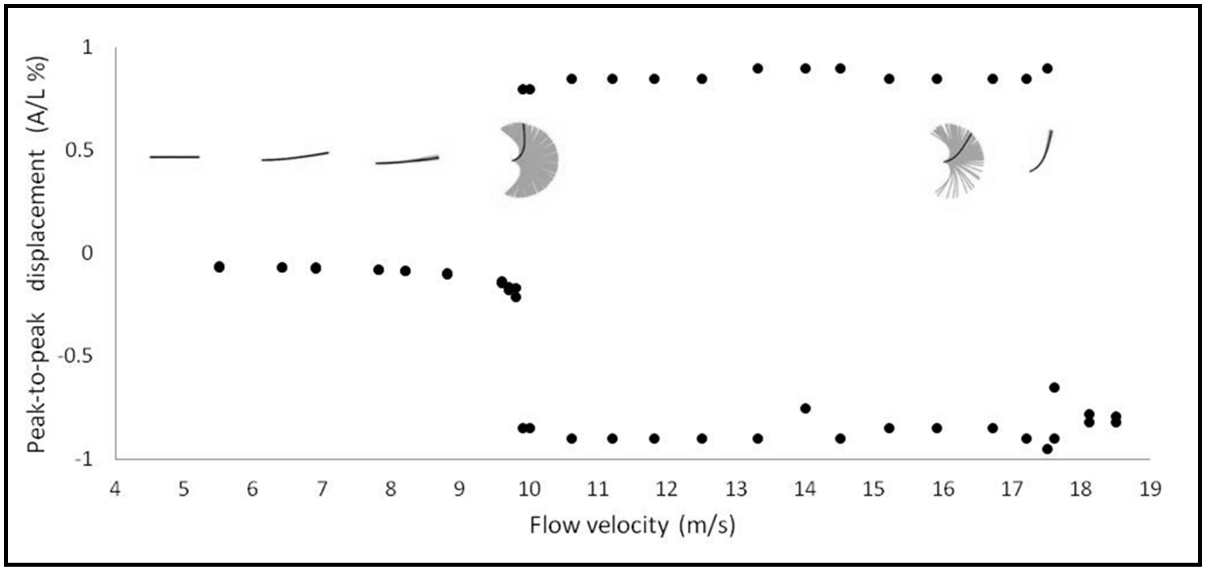

Figure 5. 21 Bifurcations of Poincaré points for AR=0.50 foil

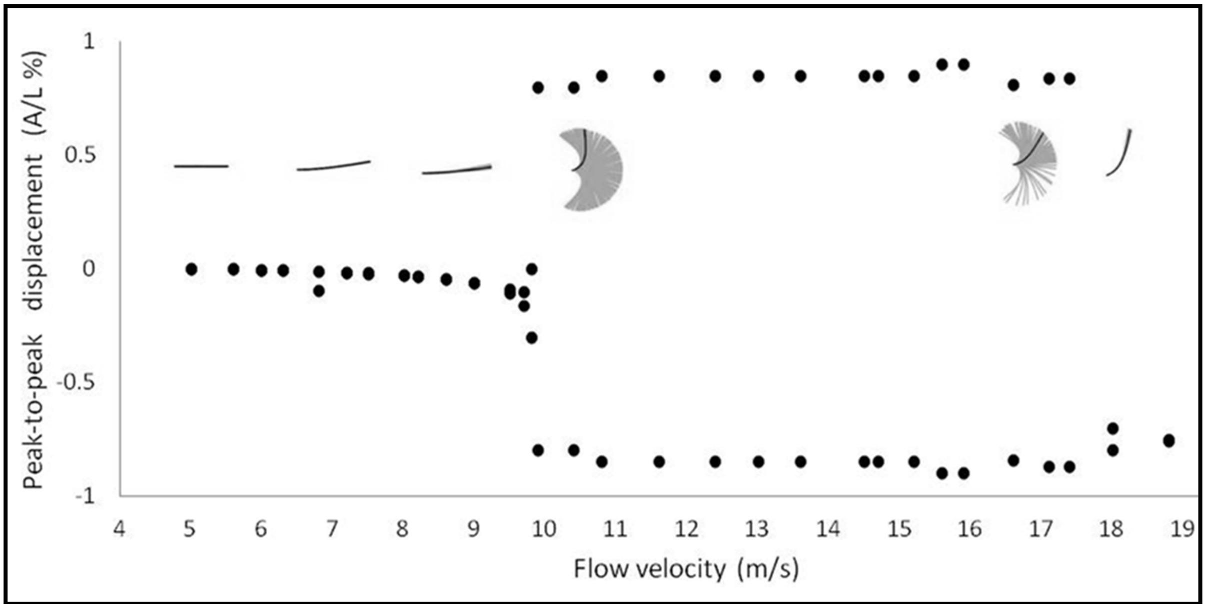

Figure 5. 22 Bifurcation of Poincaré points for AR=0.75 foil

For the two foils with AR=0.5 and AR=0.75, the small-amplitude regime was around ≈10.0 m/s, but for AR=1, the foil passes suddenly from a straight position to full-amplitude oscillations, as shown in Figure 5.14.

The regimes for AR=2, AR=3 and AR=4 foils are presented in the bifurcations shown in Figures 5.23, 5.24 and 5.25, respectively. We can observe that, with increasing AR, the critical wind speed at which the large amplitude regime initiates, is diminished. The critical flow speed for foils with AR>1 is smaller than ~8 m/s, which is significantly different from that for AR=0.5 and AR=0.75 (that is larger than 10 m/s). Another interesting feature observed is that for the foils with AR=0.5 and 0.75 the chaotic regime lasts longer. Thus, for larger foils (AR>1), the foil transitions fairly quickly from a large-amplitude regime to a fully deflected regime.

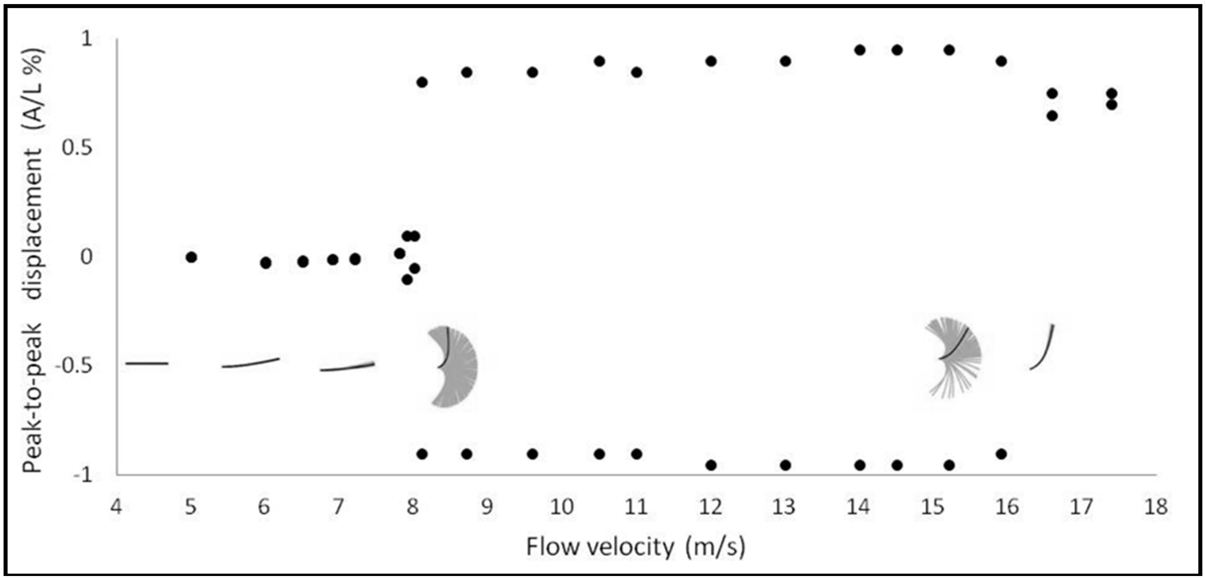

Figure 5. 23 Bifurcation of Poincaré points for AR=2 foil

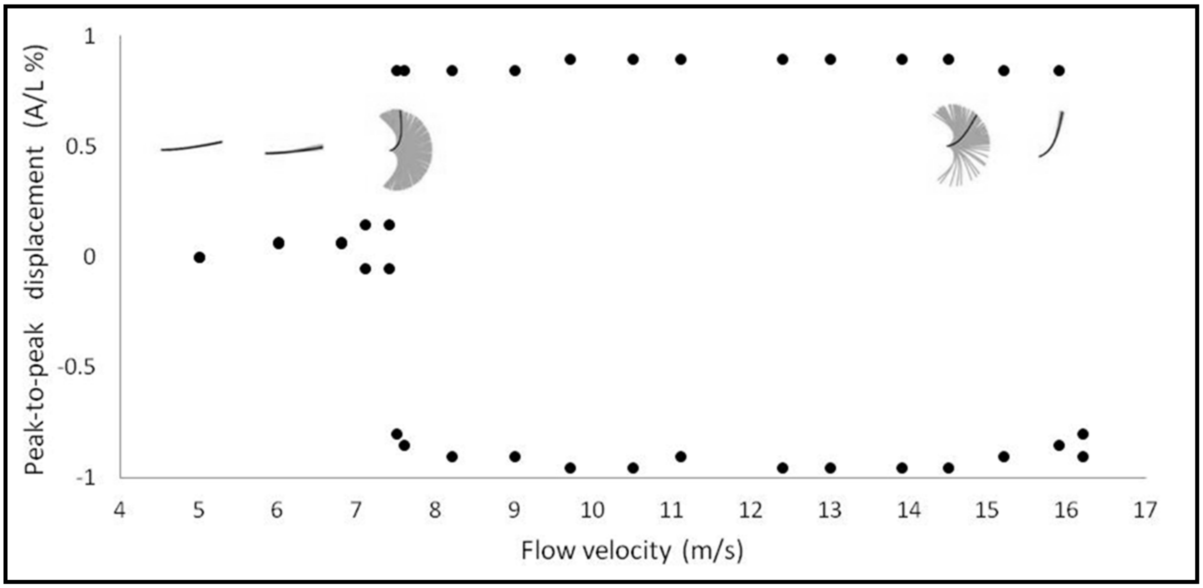

Figure 5. 24 Bifurcation of Poincaré points for AR=3 foil

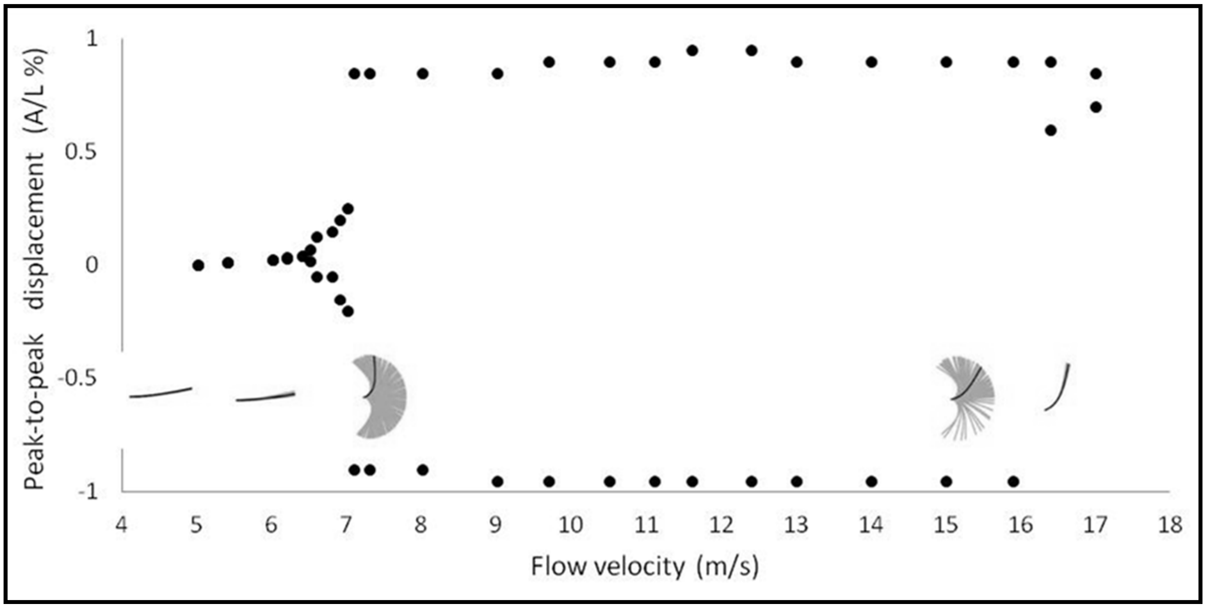

Figure 5. 25 Bifurcation of Poincaré points for AR=4 foil

5.6 Forces and moments for 0.5≤AR≤4 inverted foils

The aerodynamic scale designed for the experiments enabled us to measure the forces and moments of six polycarbonate foils with aspect ratios in the range 0.50≤AR≤4 and with a mass ratio μ=0.15. The foil with aspect ratio AR=0.5 can produce forces up to 8 Newtons during the large-amplitude regime in the flow regime Re = 1.1×10^5.

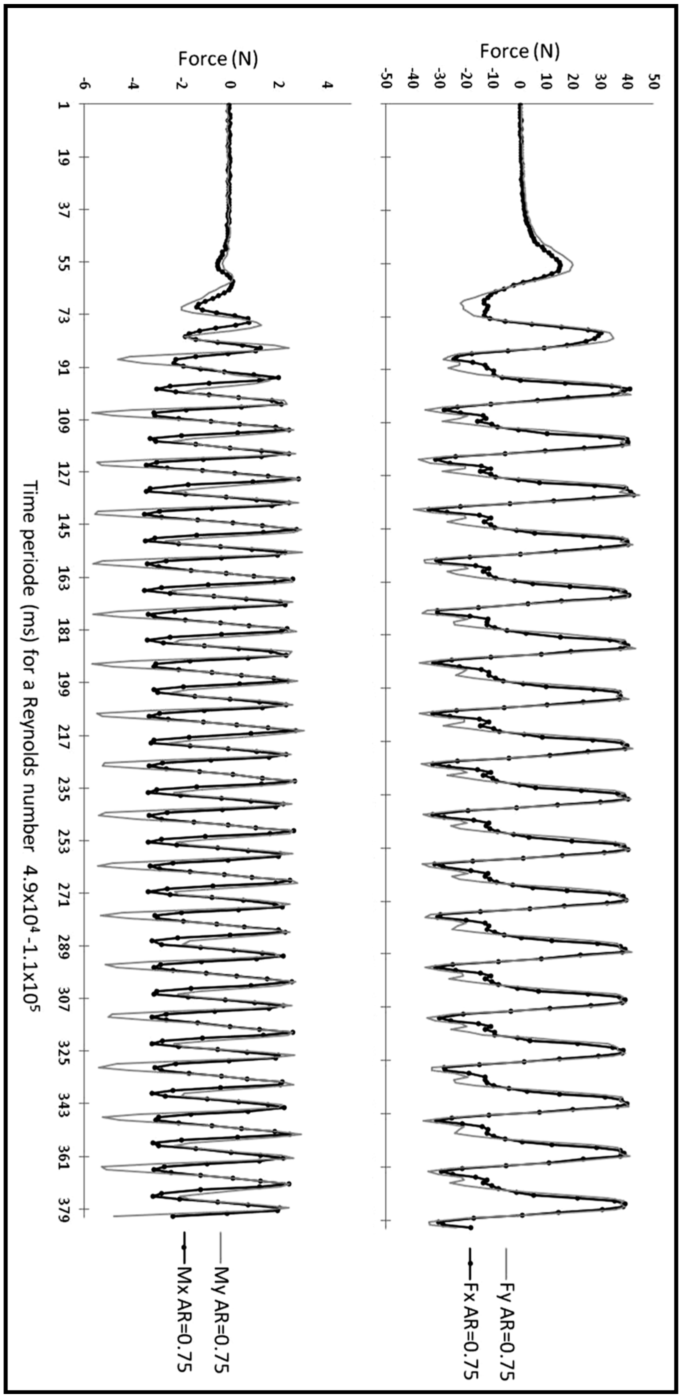

Figure 5. 26 Forces *Fx* and *Fy* and moments
Mx and *My* for the AR=0.75 foil for a
Reynolds flow range $4.9x10^4 \leq Re \leq 1.1x10^5$

The force and moment measurements for the transition between the straight regime and the large-amplitude regime can be observed in Figures 5.26-5.29. For the AR=0.75 foil, the force produced was much higher, as it increased to *Fx* = 35 N and *Fy* = 38.5 N in the large-amplitude regime range. Figure 5.26 shows how the forces and moments increase fairly quickly as soon as the foil starts flapping.

For a foil with an AR of 1, the forces *Fx* and *Fy* produced are close to 60 N for the whole large-amplitude regime, and seem to be synchronized. The forces and moments develop gradually as the foil transitions from the stretched-straight regime to the large-amplitude regime.

The transition from the straight regime to the large-amplitude regime observed in Figure 5.23 for an AR=2 foil can be also observed in the graph of forces *Fx* and *Fy* shown in Figure 5.27. For this foil, the forces and moments did not increase considerably, but remained very close to those of the AR=1 foil, 40 N for *Fx* and 3.5 Nm and 3.0 Nm for the moments *Mx* and *My*, respectively. The force *Fy* for AR=2 foil was lower than that of the AR=1 foil.

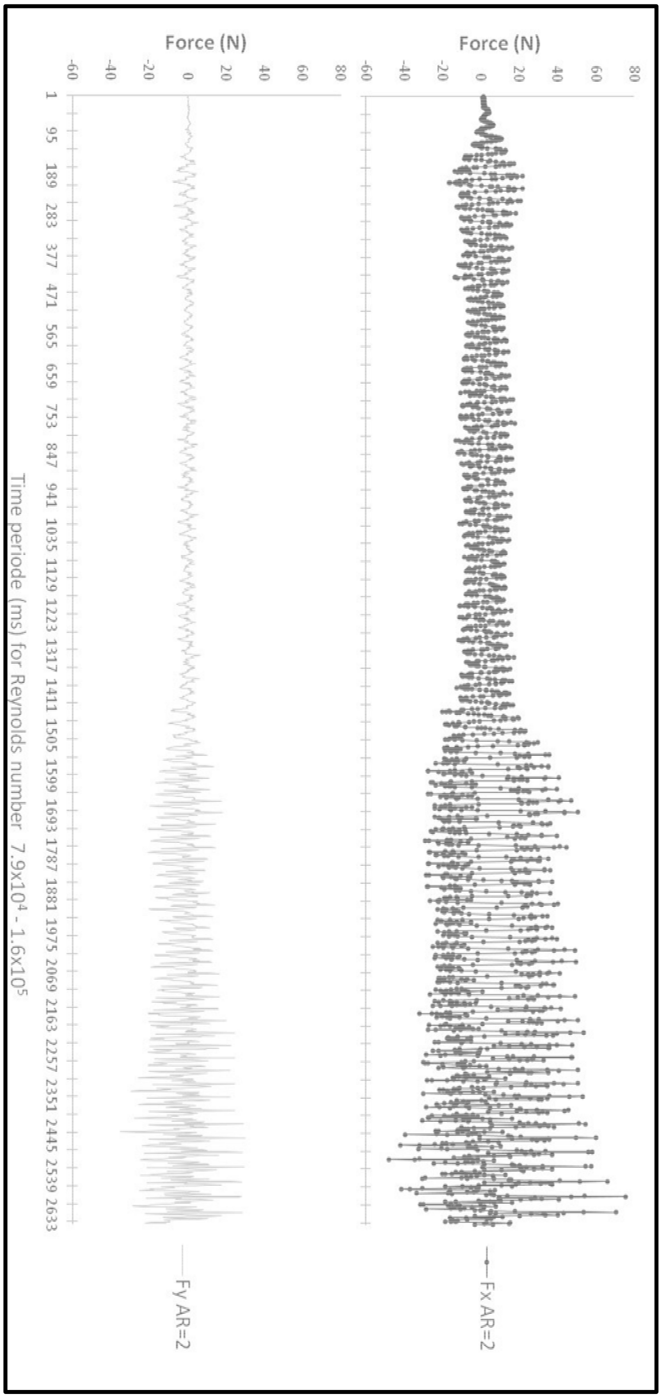

Figure 5. 27 Forces *Fx* and *Fy* for the AR=2 foil for a Reynolds flow range 7.9x10^4≤Re≤1.6x10^5

The AR=3 foil developed the largest forces and moments among all six foils; as the foil reached the large-amplitude regime, the forces measured were $Fx \approx 125$N and $Fy \approx 65$N and the moments were $Mx \approx 9$Nm and $My \approx 8$Nm. This foil produced the largest forces during the large-amplitude regime, until it reached the fully-deflected regime. Figure 5.28 shows the high forces produced by the oscillation of this flexible foil.

The last foil with AR=4, exhibits smaller forces *Fx* and *Fy* and moments compared to the AR=3 foil in the large-amplitude regime. Figure 5.29 shows that the AR=4 foil does not produce constant forces. For the large-magnitude regimes of AR=3 and AR=4 foils, even if the foil deflection displays a full amplitude of $0.8L$, the maximum numerical values forces *Fx* produced by the AR=4 foil are 56% less than the *Fx* forces produced by the smaller AR=3 foil. (Calculation: Table 5.3: AR=3 foil, *Fx*=125N and AR=4 foil, *Fx*=70N; 125N x 56% is equal to 70 N. For the AR=4 foil, *Fx* is 56% of *Fx* of the AR=3 foil).

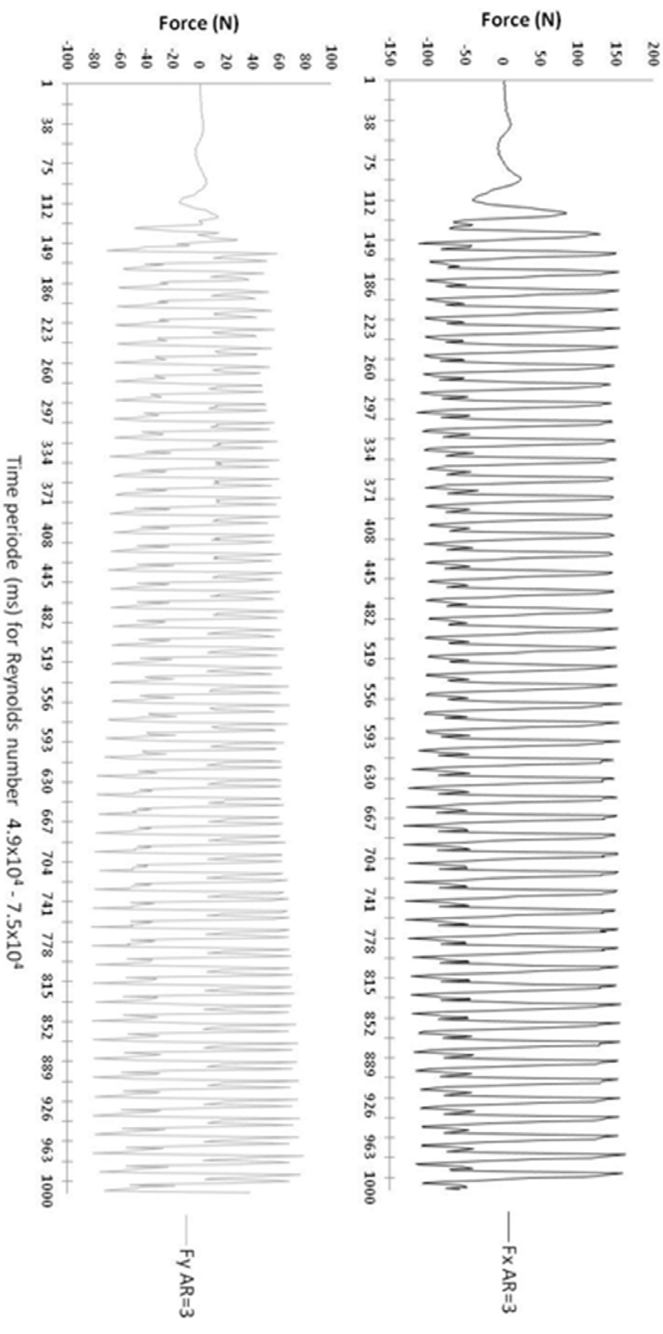

Figure 5. 28 Forces *Fx* and *Fy* for the AR=3 foil for a Reynolds flow range $4.9\text{x}10^4 \leq \text{Re} \leq 7.5\text{x}10^4$

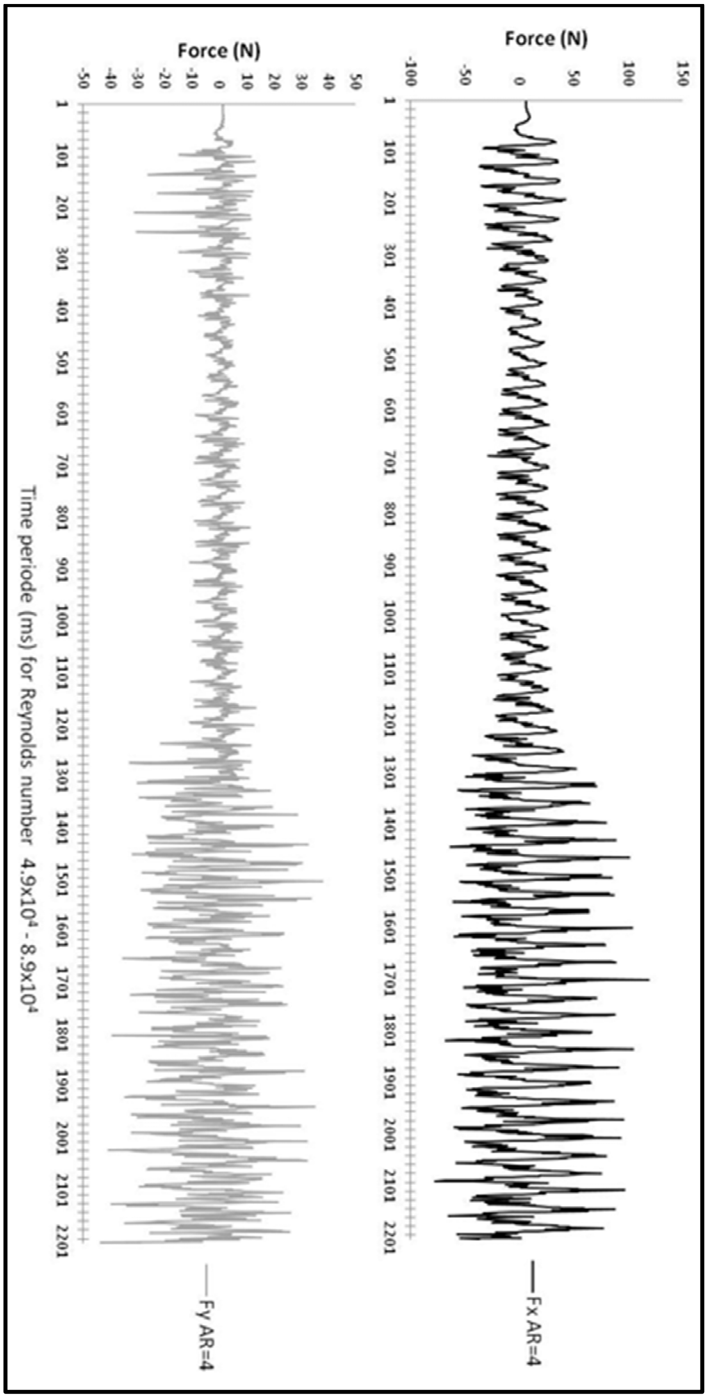

Figure 5. 29 Forces *Fx* and *Fy* for the AR=4 foil for a Reynolds flow range 4.9x10^4≤Re≤8.9x10^4

5.7 Power and force generation

We examined the effects of Re and AR on the flapping regimes, and particularly on the *Fx* and *Fy* force generation, as these forces are very important to maximize energy harvesting. It was observed, when calculating the power output $\overline{P}$, that a large-amplitude regime, high oscillation frequency and a Strouhal number of 0.14 maximized the energy production of the foil.

The work on harvested energy performed by Mitcheson (2008) applied to inverted foils shows that the harvested power $\overline{P}$ is proportional to the amplitude times the cube of the frequency, as shown in equation (5.1). The amplitude corresponds to the tip displacement of the foil, and the frequency of vibration of a blunt body is given by the Strouhal number. Thus, large amplitude with a high Strouhal number would increase the output power. The output power calculated for each foil is presented in Table 5.2.

Table 5. 2 Power generation as function of inverted-foil aspect ratio

Aspect Ratio	0.50	0.75	1	2	3	4
Output Power (mW)	0.494	0.299	0.650	0.956	1.06	1.07

The energy harvesting performance of six foils in the inverted foil configuration was analyzed. The inverted foil with AR=3 is best for maximizing energy harvesting production, because: (i) the inverted foil configuration oscillates over a relatively large range of flow speeds, providing sustained power generation over a large wind speed range, as seen in Table 5.2; (ii) it can produce up to 1.06 mW of output power, which is the second-highest amount of power generated by the six foils tested. The AR=4 foil displays spanwise motion which can lead to a deterioration of the energy generation capability of the foil.

Table 5.3 shows the forces (*Fx*, *Fy*) and moments (*Mx*, *My*) generated by the six inverted-foils during the large-amplitude regime. Large-amplitude flapping with a constant frequency is the most effective condition to produce large quantities of force from flexible foils in the inverted foil configuration. The AR=3 foil is optimal for force and moment generation, as obtained experimentally and shown in Table 5.3.

Table 5. 3 Frequencies, forces *Fx*, *Fy* and moments *Mx*, *My* generation in terms of foil AR and fluid velocity during large-amplitude regime

AR	*U* (m/s)	*f* (Hz)	*Fx* (N)	*Fy* (N)	*Mx*(Nm)	*My*(Nm)
0.5	10.0	5.3	4.5	6	0.25	0.4
0.75	11.6	5.2	35	38.5	0.25	0.4
1	9.1	4.85	60	60	3.0	7.0
2	8.78	5.3	40	25	3.5	3.0
3	7.6	5.2	125	65	9.0	8.0
4	9.0	5.7	70	22.5	4.0	5.0

The results discussed in this section, show that the inverted-foil is capable of power generation over a wide range of flow regimes under realistic wind environments. The main characteristics of flapping of an inverted foil are: (i) the flapping regimes occur over a wide range of flow velocities, which makes them suitable for wind energy harvesting in realistic wind conditions with fluctuating flow speeds, as shown in Table 5.3; (ii) the peak-to-peak amplitude is large, leading to a high magnitude of stress on the surface of the foil, and therefore to a high output of energy production, as shown in Table 5.2.

It should be mentioned that using a foil configuration and a clamping mechanism different from the one presented in this study (Figure 5.3), could affect greatly the foil's energy generation performance.

5.8 Conclusions

In this article, we presented experimental results for flexible foils of different aspect ratio for the purpose of optimizing energy harvesting. We presented the foils' experimental data in Poincaré bifurcation diagrams, in which the variation of the foil's displacement was shown as a function of increased flow speeds. In addition, the forces and moments at the foil's surface, the time-histories, probability density functions (PDF), phase-plane portraits and power spectral density (PSD) plots were presented for different Reynolds numbers to help understanding the foil's dynamics for energy harvesting purposes. This paper also investigated the evolution of the flapping instability as a function of some pertinent parameters, including flow speed, flapping frequency, Reynolds number, aspect ratio, bending rigidity and force production.

We investigated the energy harvesting capabilities of flexible foils in the inverted-foil configuration. More specifically, we focused on a wide range of foil sizes, $0.5 \leq AR \leq 4$, at high Reynolds number regimes of $10^4 \leq Re \leq 10^5$ in well-defined and controlled experimental tests. Through a series of wind tunnel tests, we studied the range of wind speed in which the flapping instability occurs. Additionally, we showed that the power generation capability of inverted foils increases with AR, and tends to converge to a certain value. Then, we identified the optimum AR foil for sufficient power generation with predominantly chordwise motion. Moreover, the present study allowed us to characterize the foil regimes, detect the critical flow speed to maximize energy harvesting performance, and measure, in real-time, the generated flapping forces and moments. The measurements suggest that foils with aspect ratio equal to 3, in the inverted-foil configuration, seem to be viable candidates for producing clean and renewable energy via small remote devices.

Acknowledgements

The authors would like to express their thanks to Dr Michael Païdoussis and Dr Stuart Price for the donation of the Price-Païdoussis Open Return Subsonic Wind Tunnel at the LARCASE research laboratory at École de technologie supérieure. The authors gratefully acknowledge the financial support by the Natural Sciences and Engineering Research Council of Canada (NSERC).

DISCUSSIONS AND CONCLUSION

Summary of original findings

The methodologies and results obtained in this thesis have been independently presented in the aforementioned chapters, while the present section presents a summary and analysis of the results. Chapters 3 and 4 presented numerical and experimental results obtained for the surveillance system FLIR and the UAS-S45 drone adaptive wing. Chapter 5 presented an experimental study and analysis of foils for energy production (harvesting).

Discussion of Chapter 3 Results

Chapter 3 proposed a new methodology allowing the experimental investigation of the wake region of a ground surveillance system (radar), modelled as a blunt body. It is known that a blunt body produces turbulent wake regions with periodic vortex shedding, boundary layer separation and high levels of turbulent flows. Experimental analysis using parameters such as Strouhal number, Reynolds number, drag coefficients, and spectral analysis were performed on the FLIR ground surveillance system (radar). The flow pattern at the wake region was identified in the absence of distorting effects of direct measurements using probes and other visualization methods, such as “white smoke” and “tufts”. It was demonstrated that a “turbulence-reduction” system mounted on the radar surface has improved the flow behavior; the turbulent flow intensity was reduced by 50%, the transition point has been delayed by 7.6 times from its original location, and the drag coefficient has decreased by a percentage of 9.67% from the original radar, without a turbulence reduction system.

The CFD model was an important tool to understand and analyze the flow around the radar because it predicted accurately regions where flow separated and then reattached; regions of stagnation and recirculation, eddies and vortices formation. Based on the CFD model results, it was concluded that the turbulence flow intensity and drag coefficient have significantly decreased by 50% and 9.67% respectively, with the proposed “turbulence-reduction” system.

Also, this system reduced vortex shedding in the wake region of the radar, and helped the boundary layer to reattach and kept attached to the radar's surface.

Discussion of Chapter 4 Results

Chapter 4 presents methods and algorithms developed and applied for the study of aerodynamic improvements obtained through the application of an adaptive wing prototype for the UAS-S45 drone. The adaptive wing consisted of a flexible upper surface; its shape could be changed using an actuation system placed inside the wing prototype. The leading edge, trailing edge and upper surface of the adaptive wing were considered for their shape optimization. The initial calculations were performed in two-dimensions plane using the XFOIL solver. Delay of the laminar-to-turbulent transition region towards the trailing edge, and drag reductions were obtained for airfoils. The modifications implemented on the airfoil shapes allowed for local modification of their shapes by respecting the constraints limitations. The genetic algorithm is a powerful global optimization tool, suitable for solving constrained and non-linear problems, such as aerodynamic optimizations. Airfoil optimizations were performed for the cruise flight phase of the UAS-S45 drone. These optimized shapes proved to be very efficient in delaying the laminar-to-turbulent transition region, thus the boundary layer separation and in reducing the drag coefficient.

Three dimensional plane Computational Fluid Dynamics (CFD) model was designed and validated for this study. High-fidelity simulations of the adaptive wing prototype equipped with an adaptive leading and trailing edge and a deformable upper surface were performed for each of the 29 flight cases presented in Table 4.9. The reference geometry design was based on UAS-S45 wing design. The CFD model was simulated for cruising flight conditions of the UAS-S45, expressed in terms of a Mach number value of 0.09 (correspoinding to the speed 30.1 m/s), a Reynolds number value $9.0\text{x}10^5$, and an angle of attack range between 0 to 5 degrees.

A grid convergence study of the numerical three-dimensional model was performed for the cruising flight conditions. This study showed a refined meshing requirements of a number of $2.258\text{x}10^5$ cells, with a near wall mesh refinement value of $y^+<1$ in order to obtain grid-independent. Very good numerical versus experimental agreements were obtained for the lift Fx, drag Fy forces, moments (*Mx,My*) and lift-to-drag ratio, as function of all 29 flight cases. The experimental results of the adaptive wing system were observed in Figure 4.27, where the lift-to-drag ratios have increased up to $L/D = 7.5$ (flight case #21), compared to the S45 original wing shape value of $L/D = 3.0$. The prototype wing can produce high lift-to-drag ratio $3.0 \leq L/D \leq 7.5$ in 59% of the flight cases tested (17/29 = 59%),without using extra fuel consumption from the UAS's engine. The low drag production and high lift-to-drag ratio (efficiency factor) of the adaptive wing translate into a reduction in fuel consumption and an increase in the S45 effective range. Adaptive wing systems for UAS are a promising technology and an effective solution for fuel efficiency.

Discussion of Chapter 5 Results

In Chapter 5, dynamics instabilities of flexible foils of sizes 0.5≤AR≤4.0, in a cantilevered configuration, subjected to a subsonic axial airflow were analyzed. A spectrum of nonlinear dynamic behaviors was observed, as the flow speed was increased. Foil sizes AR<1.0 develop initials transverse instabilities and then a deflected equilibrium regime for higher flow speeds. Large foil sizes AR≥1.0 develops symmetric oscillations, with large-amplitude oscillations as the flow speed is increased; a critical high-speed flow, will bring the inverted-foil to a fully deflected regime. It was observed that inverted-foils AR≥1.0 exhibit a wide range of dynamics regimes, with "onset" and "cessation" flapping motion; which make them more prone to oscillation at lower flow speed that conventional-foil configuration.

Section 5.4 results, for foils sizes 0.5≤AR≤4.0, suggests that the dynamic characteristics of inverted foils were independent of vortex shedding from the leading and trailing edges. In other words, the periodic vortex shedding was not the cause, but an effect of large-amplitude flapping. It was concluded that the mechanism for large-amplitude flapping, for foil AR≥1.0 can be a vibration excitation mechanism, known as "fluid-elastic instability", which generally occurs at very high flow velocities. This means that flapping of foils AR≥1.0, can be described as a self-excited or self-induced vibration, similar to aircraft wings flutter.

Experimental measurements on the dynamics of inverted-foils were conducted and the results were reported in Section 5.5. Bifurcations of Poincaré maps, time histories of the foils motion, phase-plane portraits and dominant frequency response were obtained for different aspect ratios 0.5≤AR≤4.0. Experimental tests were performed in ours Price-Païdoussis Subsonic Wind Tunnel. The experimental measurements were compared to the numerical results obtained from theoretical models prior to this research. The validation shows reasonably good agreement for the different AR foils observed.

The energy harvesting performances of six foils were analyzed in Section 5.6 and 5.7. AR=3.0 foil produced the highest flapping force (*Fx*=125N, *Fy*=65N) which is 56% higher than the forces produced by the AR=4 foil. It is important to notice that the surface of the AR=4.0 foil is 25% larger that the AR=3.0. The empirical power generation equation by Mitcheson (2008) states a power output value of 1.06mW and 1.07mW for AR=3 and AR=4 respectively.

It is hoped that the findings of the article presented in Chapter 5 will motivate further research into inverted-foils. Such studies should provide deeper insight into the underlying mechanisms for the various instabilities involved, and the impact of different parameters on the foils dynamics. The experimental results presented in Chapter 5 could potentially contribute in the design and development of energy harvesting systems for small electronic devices.

RECOMMENDATIONS

The research presented in the thesis could further be improved using the following recommendations:

In Chapter 3 new contributions can be done in the:

1. Design of an adaptive turbulence reduction system that would use a brushless actuation system to change the wing upper surface, and to vary the angular position of its trailing edge. A CFD analysis could be done to measure the reduction of the drag coefficient.

In Chapter 4 new research can be performed to:

1. Analyze the effects of the adaptive wing prototype on the S45, on high-maneuvers flight phases preceding (climb) and succeeding (descent) cruising-phase and on high-to-low lift configurations during take-off and landing.
2. Obtain the in-flight data, therefore the adaptive wing should be incorporated on an UAS-S45 and perform long range flight. The on-board instrumentation can record and send the pressure values p_s, p_t, flow speed U, angle of incidence α (provided by a gyroscope) and wing oscillations (provided by accelerometers).

Chapter 5 aimed to study the foil dynamics and stability for energy harvesting purposes. Although a lot of work has been presented, there is still a lot of room for expanding this research in order to:

1. Conduct further experimental investigations on the role of vortex shedding in the large-amplitude flapping of inverted-foils. A more systematic test on foils with larger surface (AR>4) and different masses would draw more comprehensive conclusions on the underlying mechanism understanding the flapping motions. A flow visualization technique should be

implemented to prove that the splitter plate and the serrations do suppress the formation of vortices at trailing and leading edges, or at least inhibit vortex-vortex interactions.

2. Investigate the effect of different types of imperfections on the stability. Imperfections related to clamping support or fixation device (of the inverted-foil inside the wind tunnel) can be investigated. Also, the effect of foil manufacturing defects, such as small curvature along the length or in the span direction of the foil

3. The large-amplitude self-sustained flapping of inverted-foils with AR=3 in a steady flow is particularly interesting for energy harvesting. A piezoelectric material, attached at the surface of the foil, would convert bending motion into energy, in terms of direct current (DC) to be stored or recharge an small electronic device operating remotely.

ANNEX A

VORTEX SHEDDING INTERFERENCE

A I Vortex shedding interference at the wake region

The experiments described in Annex A try to explore the impact of periodic vortex shedding from the leading edge and trailing edges of inverted-foils with 0.5≤AR≤4.0. The effect of vortex shedding from both leading and trailing edges was investigated. The experimental observations detailed in this Annex A show that production alteration (variation) of the leading and trailing edge vortices has resulted in very small quantitative changes in the critical flow velocity, amplitude and frequency; but the most important fact of altering the vortex shedding production is that it did not change the foils dynamics regimes while large-amplitude flapping persisted for the foils tested in the experiments. Inverted-foils are known to exhibit large-amplitude periodic flapping around their undeflected original equilibrium. A number of studies on the dynamics of inverted-foils (Sader et al. 2016, Pazhani & Acharya, 2019, Goza et al. 2018, Gurugubelli and Jaiman, 2019) suggest that the mechanism for large-amplitude flapping may be Vortex-Induced Vibration (VIV). In these studies, the flapping phenomenon is attributed to the periodic formation and synchronized shedding of vortices from the inverted-foil surface. These vortices are characteristic of VIV dynamics.

Figure-A I-1 shows the experimental setup for the splitter plate wind tunnel tests. A splitter plate placed after the trailing edge of the inverted-foil and dividing symmetrically the test section interfered and altered the vortices interaction in the wake region. The splitter plate divides the wind tunnel test section in two symmetrical sections, in the wake region, thus interfering and altering the vortex-to-foil interaction. It is believed by Gurugubelli and Jaiman (2019) that vortices at the wake region affect the bending moment and curvature of the foil, in addition, a reduction in local pressure results in a fast foil deflection (from one side to the other side), which leads to a higher frequency of the foil motion, and then to a transition of the inverted-foil in the flapping regimes as shown in Figures 2.3 (page 23).

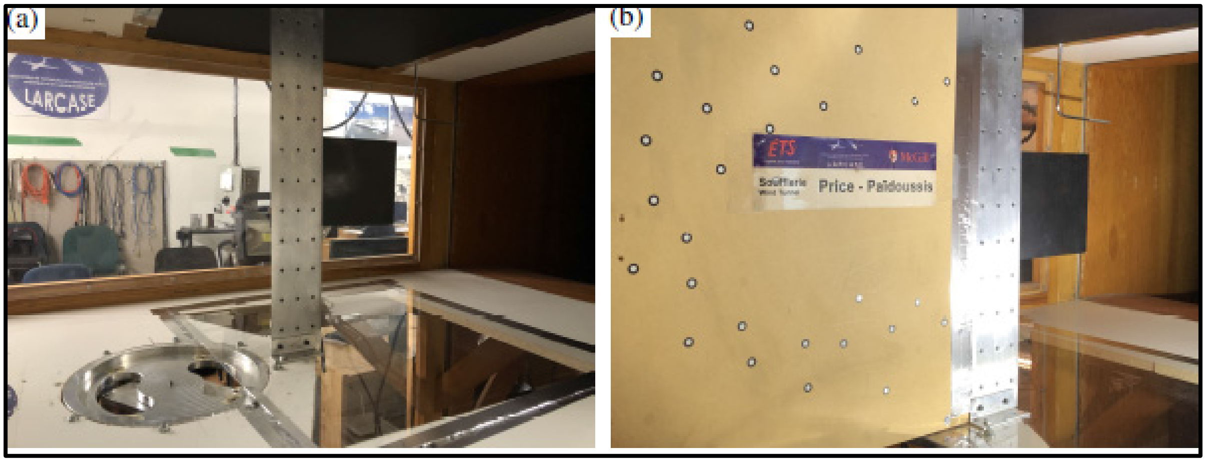

Figure-A I-1 Wind tunnel test a) without splitter plate b)with splitter plate

Figure-A I-2 shows the Poincaré bifurcation for the wind tunnel tests with (“red” circles) and without a splitter plate (“black” squares). A very small variation of the amplitude ratio *l/L* can be seen when the splitter plate is installed inside the test section. In the beginning of the oscillations and at the end of large-amplitude flapping, very small variations can be observed between “red” circles and “black” squares, as seen in Figure-A I-2. These results can be explained by the numerical simulations of Gurugubelli and Jaiman (2019), which state that in the interference-formation of the trailing edge vortices at the wake region of the foil there is a small bending moment and small foil curvature, which result in a small reduction of the flapping amplitude.

The near-identical dynamic behavior observed experimentally between non-modified inverted-foils and modified inverted-foils (vortex-generator patterns) with and without a splitter plate at the wake region shows that the dynamics of inverted-foils with their sizes $0.5 \leq AR \leq 4.0$ are independent of vortex shedding.

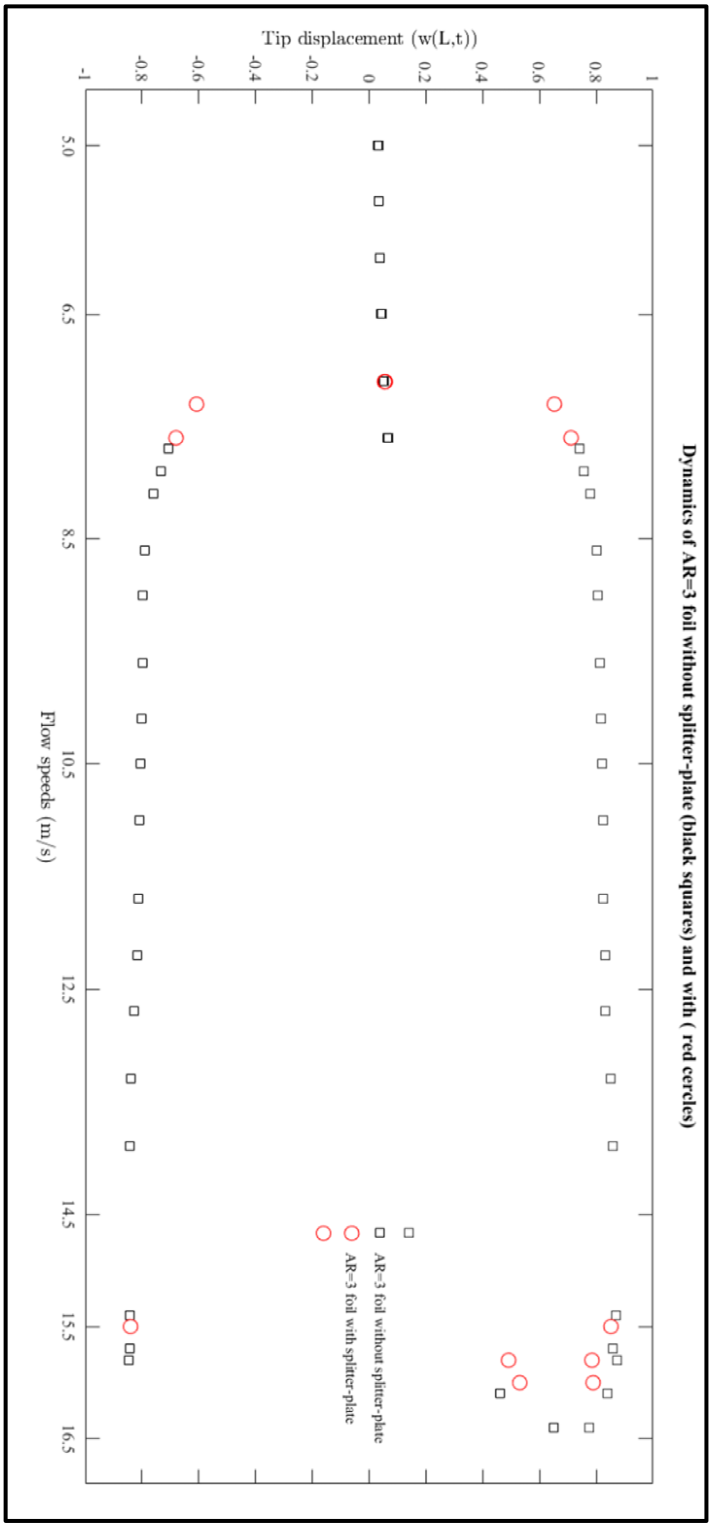

Figure-A I-2 Poincaré bifurcations for the wind tunnel tests with spliter plate (red circle) and without spliter plate (black squares)

A II Vortex shedding interference at the leading edge with vortex-generator patterns

Vortex-generators patterns are often used to reduce the separation of the boundary layer and to delay flow separation at the surface of aeronautical vehicules flying at subsonic speeds. The authors believe that the serrations and peak patterns of the vortex-generators reduce the eddies and vortex formation, thus alter the dynamics of the inverted-foils.

An inverted-foil composed of a series of vortex-generator patterns at the leading edge was designed and manufactured for the inverted-foils with sizes 0.5≤AR ≤4. The authors will describe the results of the foil with AR=3, as the observations, finding and conclusion are applied to all inverted-foil sizes.

A II-1 Vortex-generator patterns

This section presents the observations of the original inverted-foil and an inverted-foil with a modified leading edge (LE) of size AR=3, as shown in Figure-A II-1. The modified AR=3 foil has at it leading edge, a series of sharp protrusions patterns, that act as vortex-generators. Vortex-generators are not new to engineering, as they are an important study of modern aircraft design. Wings use Vortex-generators devices to improve their efficiency by creating more efficient shapes during specific fight phases, such as cruise and high maneuvering flight modes. These devices are attached to wings to reduce flow separation and increase lift at low angles or speeds, also, they can reduce drag by preventing boundary layer separation. The successful application of vortex-generator patterns at the leading edge of an inverted-foil could delay boundary layer separation and reduce the forces produced by the flapping foil. Additionally, these vortex-generation patterns should give us more information regarding the flapping mechanisms of inverted-foil; It should be analyzed if Vortex Induced Vibration (VIV) or another mechanism produces the foils flapping.

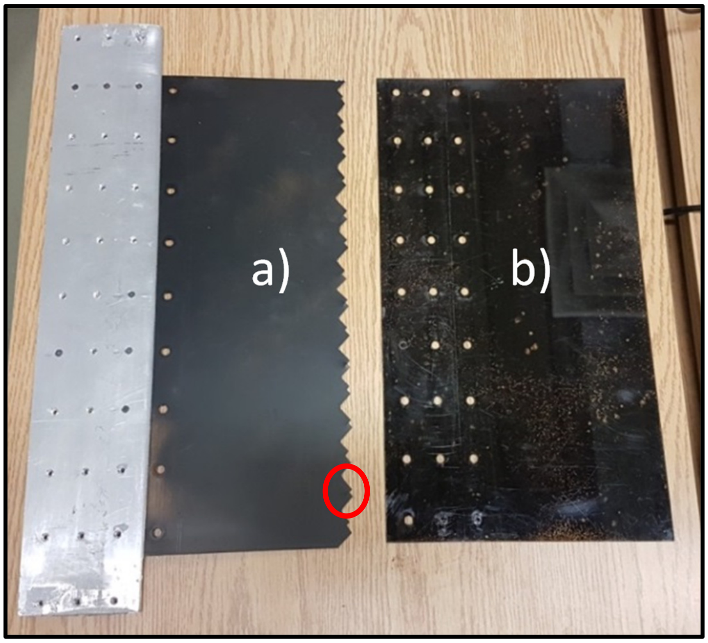

Figure-A II-1 Side views of a foil with AR=3
a) modified edge with vortex-generation patterns.
b) original edge

The foil AR=3 with the vortex-generator patterns (Figure-A II-1 a) data will be compared with the results presented for the foil AR=3 with an unmodified edge (Figure-A II-1 b) to understand the effects of vortex shedding. The unconventional leading edge shapes should produce a smaller counter-rotating pair of vortices, which should interfere with the periodic vortex shedding production by the foil's flapping motion. The shape and non-negligible size of the peaks (red circle) patterns should suppress the foil small-amplitude regime oscillation. Reducing the vortex shedding at the leading edge of the foil should affect/alter the foil flapping regimes.

A.II.2 Forces measurement

A vortex-generation leading edge, composed of sixteen "double peaks", was designed and fabricated. This leading edge (LE) shape should reduce the vortex shedding formation and alter the flapping amplitude and forces produced by the foil. The modified inverted-foil (vortex reduction patterns) experimental data is compared with the experimental results presented for its original AR=3 foil in Chapter 5. The experimental forces *Fx* and *Fy* measured by the in-house aerodynamic scale were recorded, in time (ms), continuously. The authors wanted to observe all differences produced by the modified leading edge (LE), in the AR=3 foils motion, in terms of force (N) production. From the beginning of the foils motions (low oscillations) until the foil stopped all motion (deflected to one side), the forces were measured and recorded. The wind tunnel test started at a flow regime with a $4.9x10^4$ Reynolds number, a flow speed of 4.5 m/s until the foil stopped flapping and deflected to one side at a $Re=1.7x10^5$ (16.0 m/s).

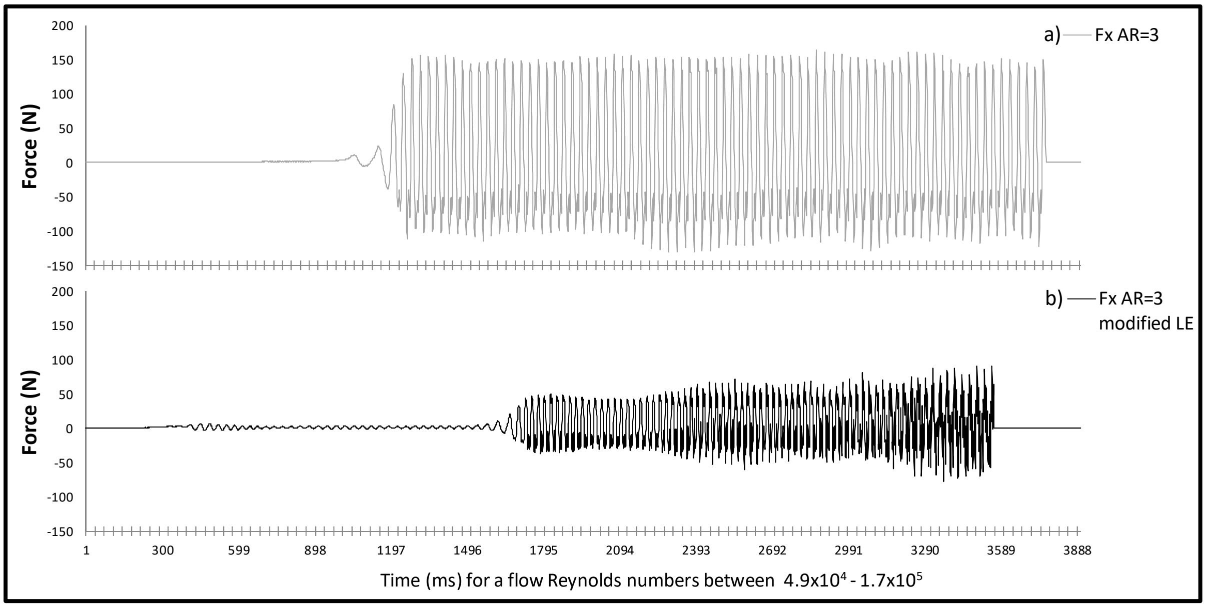

Figure-A II-2.1 Comparison of an inverted-foil forces *Fx* a) with an unmodified leading edge (LE) and b) with a modified (vortex-generation patterns) leading edge (LE)

The foil with a modified leading edge presents very small force values, and it seems that the large forces expected for an AR=3 foil (≈150N) were damped to a value ≈60N and shifted or pushed back at higher flow velocities. It can be observed in Figure- A II-2.1, that a foil with a modified LE "retard" and setback in time the apparition of full-amplitude flapping. For the AR=3 foil, the full-amplitude flapping was observed at a time of ≈1000 ms. The AR=3 foil with a modified LE started its full-amplitude flapping at a time of ≈1650 ms. In the same matter, the *Fy* forces were damped for the foil with a modified LE, as observed in the Figure-

A II-2.1. The original foil could produce forces up to *Fy*≈70N, but a foil with a modified LE could only produce forces *Fy*≈25N. The *Fy* forces were reduced by almost 3 times from their original values of the AR=3 foil.

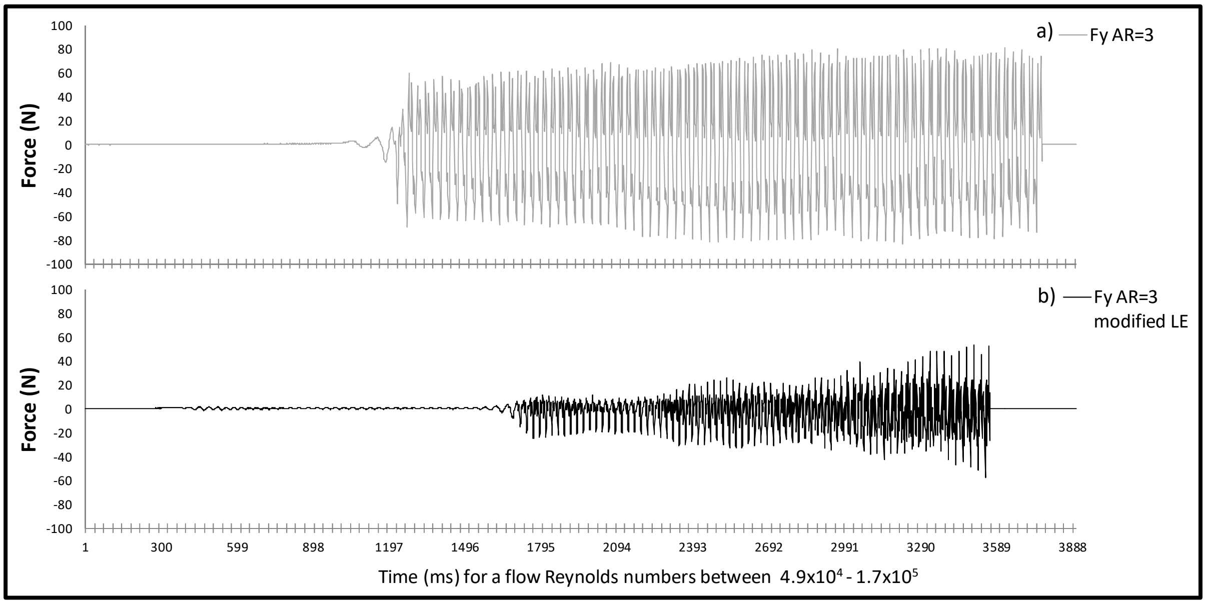

Figure-A II-2.2 Comparison of an inverted-foil forces *Fy* a) with an unmodified leading edge (LE) and b) with a modified (vortex-generation patterns) leading edge (LE)

The modified leading edge has indeed significantly reduced the foil's force production. The foil with modified leading edge had the same full-amplitude length and flapping frequency as the unmodified AR=3 foil, but the forces *Fx* and *Fy* produced by the modified foil were reduced significantly. The forces *Fx* and *Fy* for both foils are observed in Figure-A II-2.1 and Figure-A II-2.2.

From the data presented in this section, we can conclude that a reduction in vortex shedding at the leading edge can reduce the flapping force in a significant way as the forces were much lower on the modified LE foil. The observed behavior suggests that the foil's dynamics, particulary, its large-amplitude regime, is not very sensitive to the vortex shedding at the leading edge, but the forces produced by the flapping inverted-foil are very sensitive to vortex shedding. The leading edge (LE) pattern plays an important role in the force produced by the foil, as shown by the experimental observation, in this section. Vortex shedding was reduced, with a leading edge vortex-generation pattern, resulting in a reduction of 50% in the magnitudes of the *Fx* and *Fy* forces.

ANNEX B

INVERTED-FOILS RESEARCH PREPARATION

B II Foils Initial Options

At the beginning of the inverted-foil research, there was an interrogation of which foil would oscillate when subjected to an axial flow. We decided to test foils with AR sizes, from very large (AR=4) to very small (AR=0.01). Figure-B II-1 shows all the analyzed foils.

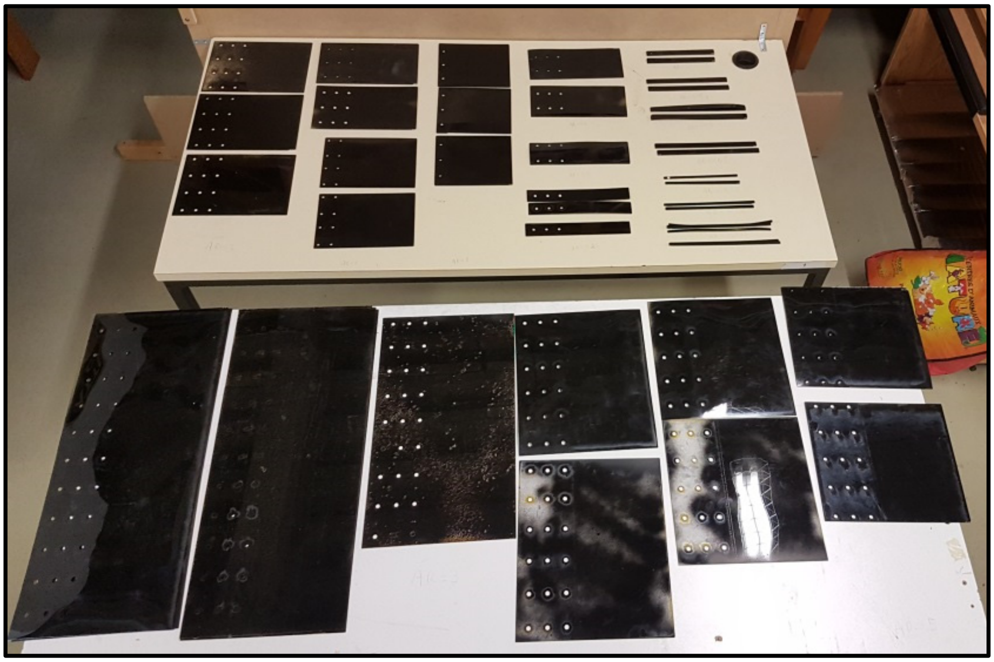

Figure-B II-1 Foils tested experimentally at the beginning of the research.
From AR=4.0 to AR=0.01

We have observed that foils with an aspect ratio (AR) smaller than 0.5 cannot oscillate or flap when they are subjected to an axial speed flow *U* ranging from 5.0 m/s to 18.0 m/s. This experimental observation is the same as the one found by other researchers.

The first experiments which gave information on the effect of foil geometry can be attributed to Cossé et al. (2014), whose measurements with foils of different aspect ratios ($0.08 < AR < 2.08$) revealed that the aspect ratio of a foil can dramatically alter its dynamics. Later, Wind Tunnel measurements performed by Kim et al. (2013) and Sader et al. (2016b) have revealed that, the aspect ratio (AR) of foils is the one of the key parameters for quantifying their dynamics. They found a threshold below which the dynamics of the inverted-foil changes dramatically. More specifically, Sader et al. (2016b) showed that the inverted-foils with AR below 0.1 do not undergo the sequence of regimes shown in Figure 2.3 (page 23), but they transition directly from the undeflected to fully deflected mode, without encountering other regimes.

Our experimental observations confirm the observations of Cossé et al. (2014), and the experimental measurements of Kim et al. (2013) and Sader et al. (2016b), that flapping motions do not exist for foils with their AR below 0.1, and the foil goes from stretched-straight regime to fully deflected regime, without any other regimes in between them. We have observed and presented in Chapter 5 that foils with $AR \geq 0.5$ can undergo the following states: small oscillations, large-amplitude, aperiodic and chaotic regimes, when subjected to an axial flow.

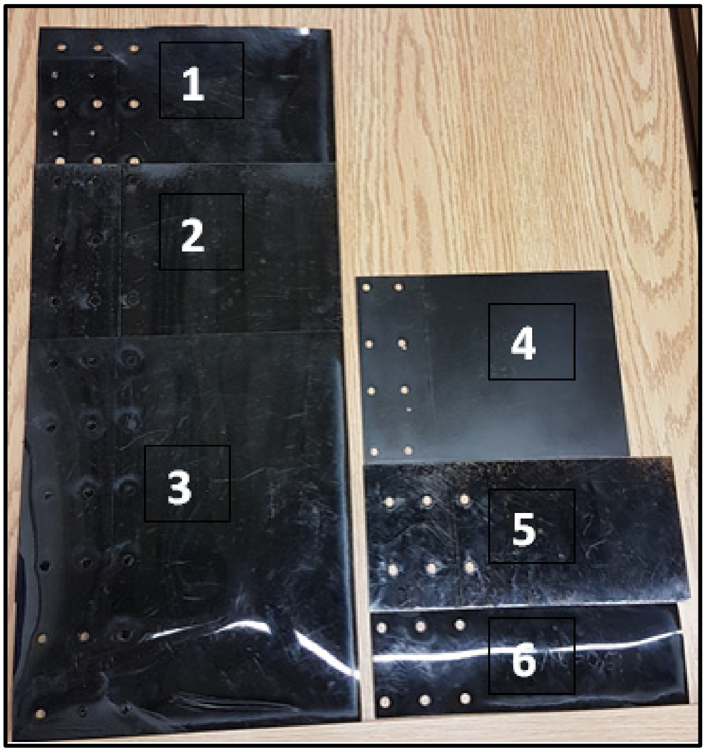

Figure-B II-2 Foils tested for this thesis. Aspect ratios are: 1)AR=4, 2)AR=3, 3)AR=2, 4)AR=1, 5)AR=0.75, 6)AR=0.5

II.2 Force and Moment Scale Design and Manufacturing

The force and moment aerodynamic scale design CAD drawing is shown in Figure-B II-2.1 (page 190). The foils are clamped to the NACA 0012 support by 27 flat-head screws. The locations of the holes and the sizes of the screws are represented in the CAD file. The "streamlined interface" connecting the inverted-foils to the aerodynamic scale is shown on green color, in Figure-B II-2.2 (page 191).

The piece, shown in green color, is fixed to the F/T sensor by a 35mm and 10mm screw length, which are:

i) Six screws M3, 35mm long. The precise description of these screws is Button Head Hex Drive Screw Black-Oxide Alloy Steel, M3x0.50 mm thread, 35 mm long (91239A128).

ii) Two screws (M3 x5 10 mm long). The precise description of these screws is Black-Oxide Alloy Steel Hex Drive Flat Head Screw M3 x 0.5 mm Thread, 10 mm Long (91294A130).

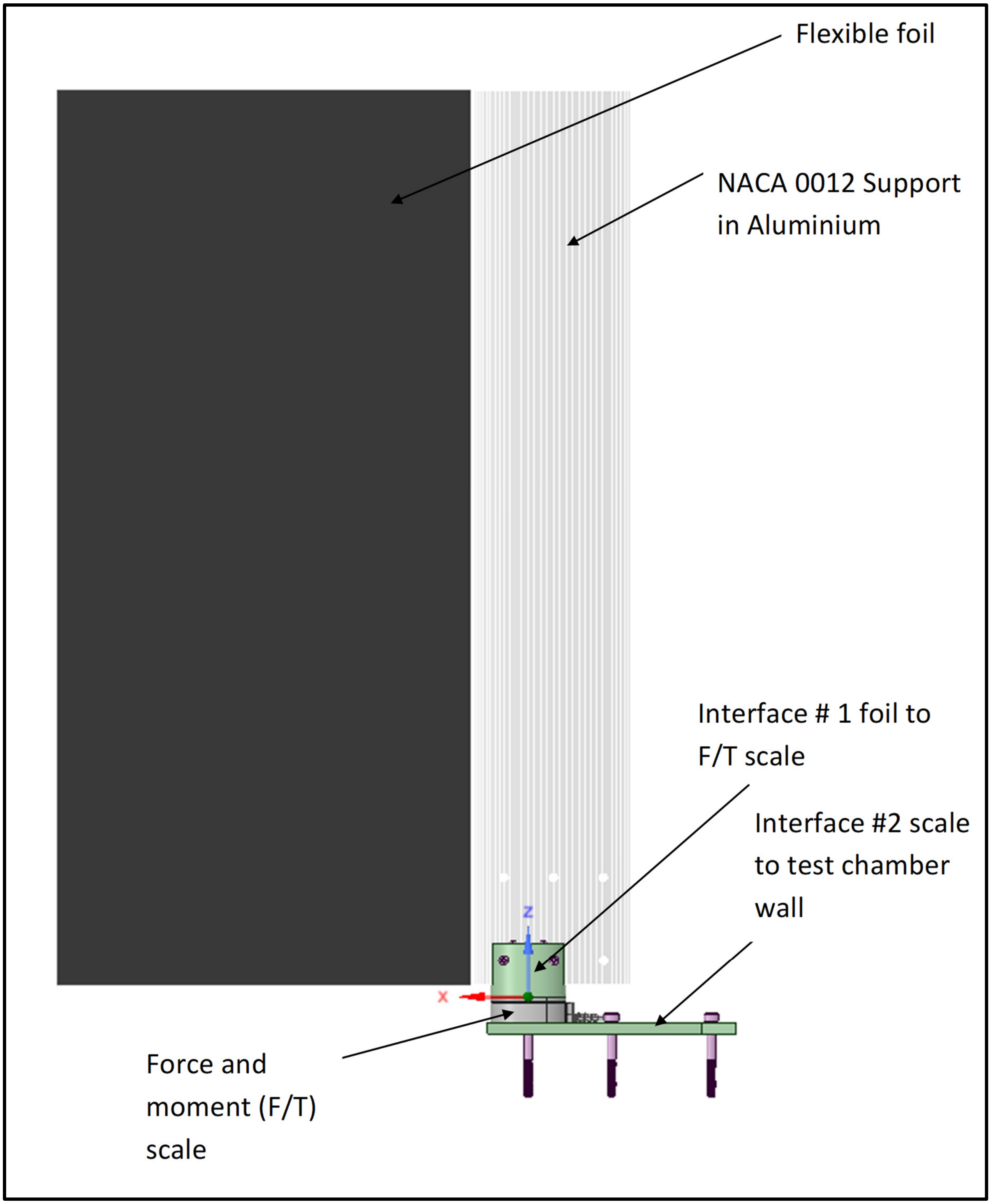

Figure-B II-2.1 Force and moment aerodynamic scale design CAD drawing

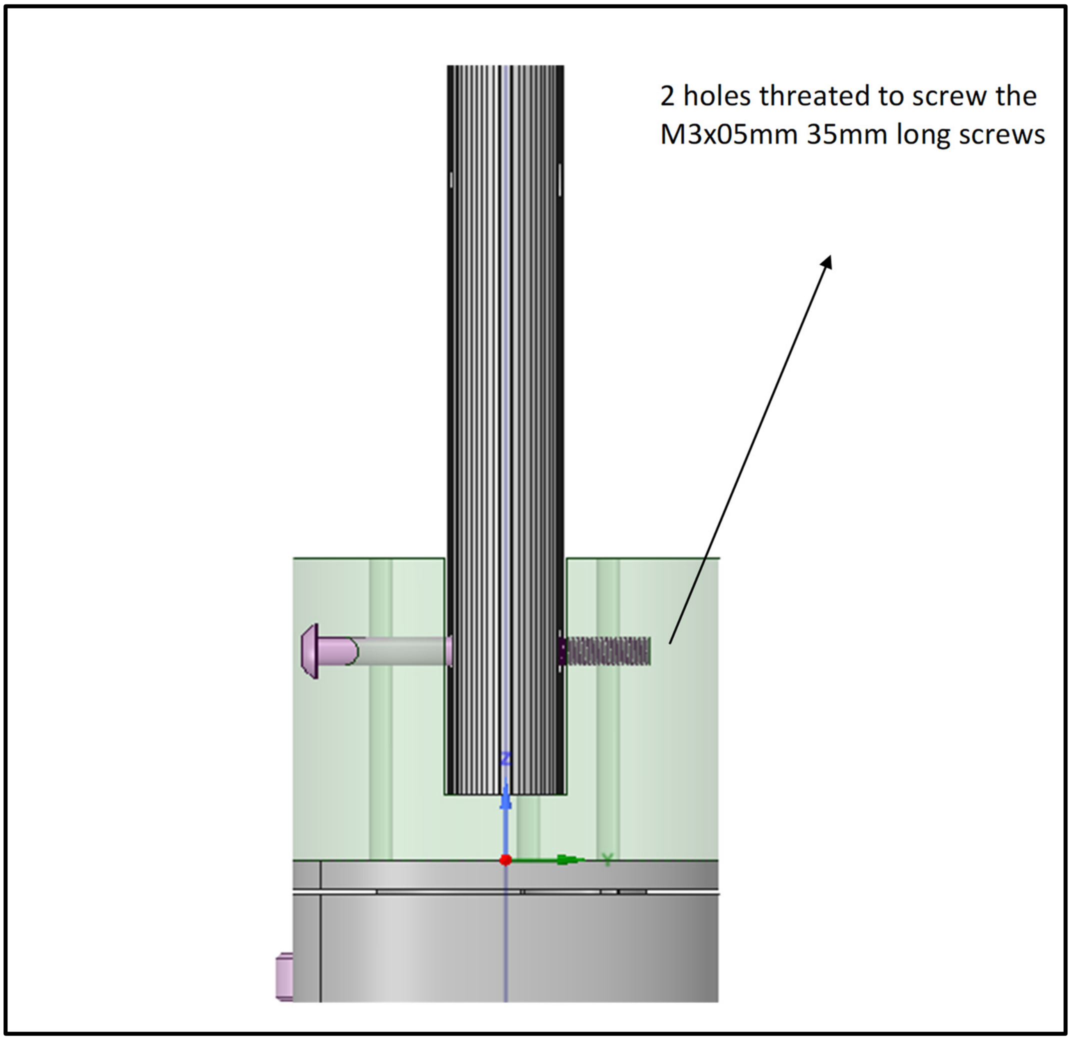

2 holes threated to screw the M3x05mm 35mm long screws

Figure-B II-2.2 Streamlined coupling interface (green color)

The aerodynamic scale system needs a second coupling interface, as shown in Figure-B II-2.3, to be installed in the test section. This coupling interface must resist high forces and moments, thus a high stiffness is required for this coupling interface to resist foils deformation during wind tunnel tests. The thickness of this piece is ¼ inch (6.35mm).

This piece uses two different (M3 and M5) set of screws; a set of six screws M3x5 12mm long (Flat Head) to connect the sensor. The precise description of these screws is:

i)Black-Oxide Alloy Steel Hex Drive Flat Head Screw. M3 x 0.5 mm Thread, 12 mm Long

(91294A132).

And a set of five screws M5 x 8 45mm long to connect to the Wind Tunnel. The precise description of these screws is:
ii)Button Head Hex Drive Screw. Black-Oxide Alloy Steel. M5 x 0.80 mm Thread, 45 mm Long (91239A244).

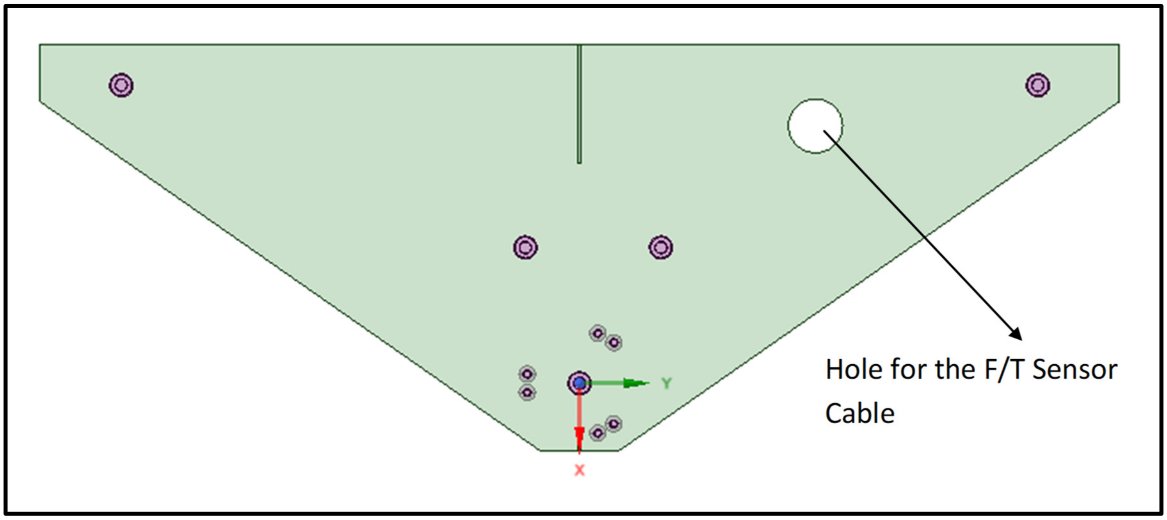

Figure-B II-2.3 Scale to wind tunnel coupling interface

II.3 Camera Set-Up

An opening was designed at the lower wall of the test section (Figure-B II-3.1). The size of the opening was large enough to be able to capture the dynamics of the inverted-foil motion for the large size foil AR=4.0. The opening was covered with a transparent window, with a high degree of light transmission. A Plexiglas window on the test-section allowed for camera-based motion capture as the main form of data acquisition. The camera was installed on a tripod, secured to the ground with bolts, for maximum stability during the wind tunnel running (in operation). To capture high resolution frames, LED lights were installed at each side of the test section, as shown in Figure-B II-3.1. These LED lights created a high contrast in white (foil edge painted white) and black (test section upper wall) colors allowed for a high pixel resolution (enhanced images quality), and rate frames, up to 100 FPS.

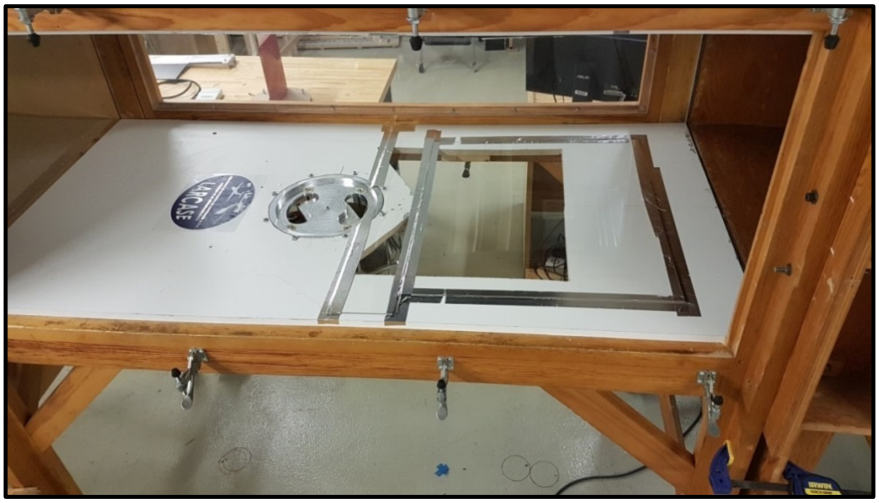

Figure-B II-3.1 Plexiglas window in the test-section

Figure-B II-3.2 Video recording installation and wind tunnel setup. The camera position is shown by the white arrow

II.4 Images Process Method

First, a video of the wind tunnel test is recorded in a format .CSV, as shown in Figure-B II-4 (page 194). A video per flow speed is recorded for each of the foil analyzed in this research. The images are cropped to reduce the field of view to the area where the foil motion occurs.

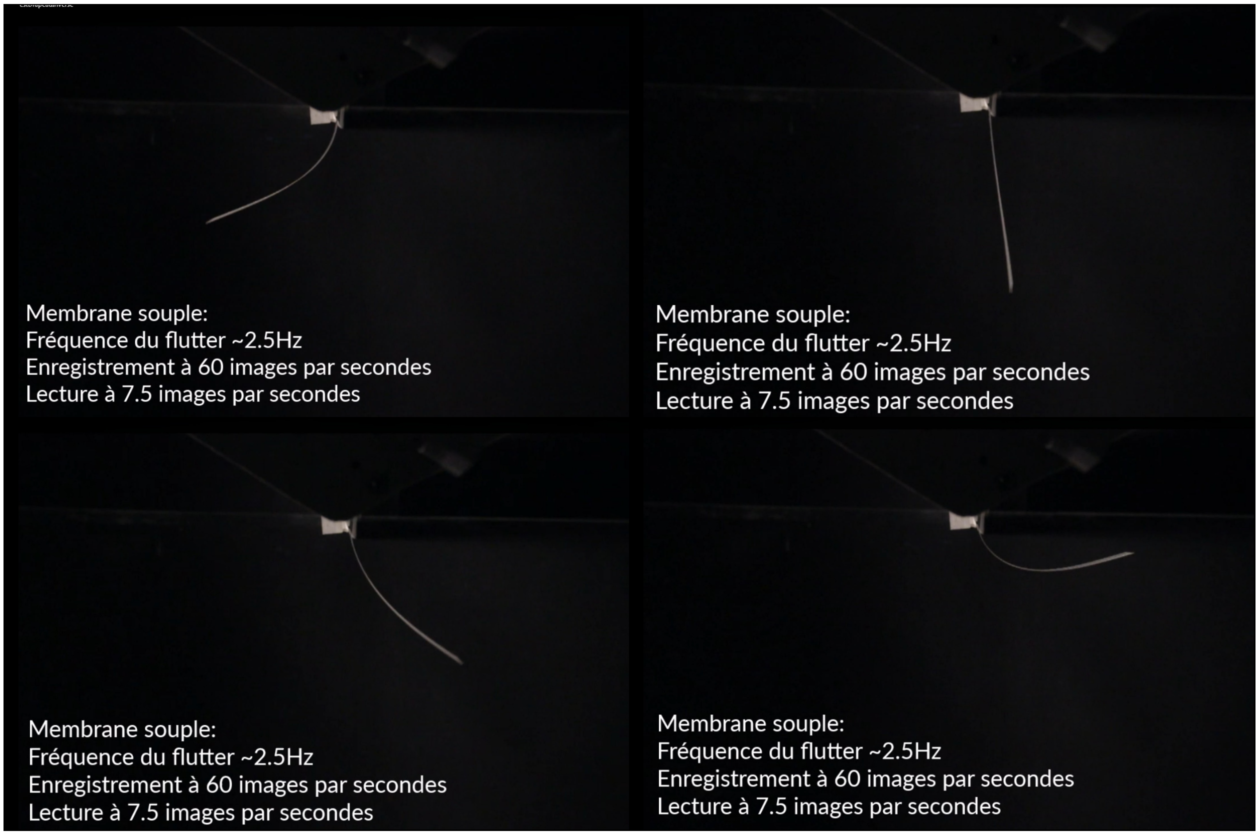

Figure-B II-4 Images showing 4 frames of the motions of a foil AR=0.5. These images are taken from a post-processing video prepared by the author

II.5 Image process Matlab Scripts (Core program)

Matlab program developed for the inverted-foil project.

```
%% Initialization
%  This code reads .csv file to plot ...
%  It captures the Velocity and FPS from the file name
%% Import data from csv files.
myFolder = pwd;   % Define the working folder
filePattern = fullfile(myFolder, '*.csv');
csvFiles = dir(filePattern);
%% Specify the file name and velocity here
%input 1
FileName = '079-PC-762-160-160-B_2019-07-16-124412-000080.csv'
%input 2
Vel=7.9
%%
%Sampling frequency of the video recorded
FPS=80
```

```
foil_length = 160 %mm
x0=400;
y0=400;
width=550;
height=400;
  raw_data=csvread(FileName);
  Theta_tip=raw_data(1:end,1);
  u_tip=raw_data(1:end,5)/foil_length;
  w_tip=raw_data(1:end,4)/foil_length;
   numFrames=length(Theta_tip);
  time(:,1)=(0:numFrames-1)*(1/FPS); %The time variable

  %Data extracted traitement
  tol=0.0000005;
  [sp_theta,Theta_smooth(:,1)]=spaps(time,Theta_tip,tol);
  [sp_u,u_smooth(:,1)]=spaps(time,u_tip,tol);
  [sp_w,w_smooth(:,1)]=spaps(time,w_tip,tol);

  %High Resolution
  Time_HiRes =  [0:0.0005:time(end)];
  Theta_HiRes = fnval( sp_theta,Time_HiRes );
  u_HiRes = fnval( sp_u,Time_HiRes );
  w_HiRes = fnval( sp_w,Time_HiRes );

  %Time derivatives
  ThetaDot(:,1)=diff(Theta_tip,1)*FPS; % theta dot
  [sp_thetaDot,ThetaDot_smooth(:,1)]=spaps(time(1:end-
1),diff(Theta_smooth,1*FPS,0.000001);
  Theta_Dot_HiRes = fnval(sp_thetaDot,Time_HiRes) ;

  WDot(:,1)=diff(w_tip,1)*FPS; % theta dot
  [sp_WDot,WDot_smooth(:,1)]=spaps(time(1:end-1),diff(w_smooth,1)*FPS,0.000001);
  w_Dot_HiRes = fnval(sp_WDot,Time_HiRes) ;
```

BIBLIOGRAPHY

Afonso, F., Ferreira, A., Ribeiro, I., Lau, F., & Suleman, A. (2021). On the design of environmentally sustainable aircraft for urban air mobility. *Transportation Research Part D: Transport and Environment*, *91*, 102688.

Alam, M. M., Chao, L. M., Rehman, S., Ji, C., & Wang, H. (2021). Energy harvesting from passive oscillation of inverted foil. *Physics of Fluids*, *33*(7), 075111.

Allen, J. J., & Smits, A. J. (2001). Energy harvesting eel. *Journal of fluids and structures*, *15*(3-4), 629-640.

Ameduri, S., & Concilio, A. (2020). Morphing wings review: aims, challenges, and current open issues of a technology. *Proceedings of the Institution of Mechanical Engineers, Part C: Journal of Mechanical Engineering Science*, 0954406220944423.

Arena, M., Concilio, A., & Pecora, R. (2019). Aero-servo-elastic design of a morphing wing trailing edge system for enhanced cruise performance. *Aerospace Science and Technology*, *86*, 215-235.

ASME. (2016), *Guide for Verification and Validation in Computational Solid Mechanics*; Release 10; The American Society of Mechanical Engineers: New York, NY, USA.

Baals, D. D. (1981). Wind tunnels of NASA (Vol. 440). Scientific and Technical Information Branch, National Aeronautics and Space Administration.

Barlow, J. B., Rae, W. H., & Pope, A. (1999). *Low-speed wind tunnel testing*. John wiley & sons.

Bendler, J. T. (Ed.). (1999). *Handbook of polycarbonate science and technology*. CRC press.

Botez, R. M. (2018). Morphing wing, UAV and aircraft multidisciplinary studies at the Laboratory of Applied Research in Active Controls, Avionics and AeroServoElasticity LARCASE. *Aerospace Lab*, (14), 1-11.

Botez, R. M., Grigorie, T. L., Khan, S., Mamou, M., & Mebarki, Y. (2021). A smart controlled morphing wing experimental model with the structure based on a full-scaled portion of a real wing. In *AIAA Scitech 2021 Forum* (p. 1836).

Bowman, J., Sanders, B., Cannon, B., Kudva, J., Joshi, S., & Weisshaar, T. (2007, April). Development of next generation morphing aircraft structures. In *48th AIAA/ASME/ASCE/AHS/ASC Structures, Structural Dynamics, and Materials Conference* (p. 1730).

Bradshaw, P. (1997). Understanding and prediction of turbulent flow. 1996. *International journal of heat and fluid flow*, *18*(1), 45-54.

Brahimi, M. T., Allet, A., & Paraschivoiu, I. (1995). Aerodynamic analysis models for vertical-axis wind turbines. *International Journal of Rotating Machinery*, *2*(1), 15-21.

Brahimi, M. T., & Paraschivoiu, I. (1995). Darrieus rotor aerodynamics in turbulent wind. *Journal of Solar Energy Engineering*, *117*(2).

Cestino, E., Frulla, G., Spina, M., Catelani, D., & Linari, M. (2019). Numerical simulation and experimental validation of slender wings flutter behaviour. *Proceedings of the Institution of Mechanical Engineers, Part G: Journal of Aerospace Engineering*, *233*(16), 5913-5928.

Chang, E., Matloff, L. Y., Stowers, A. K., & Lentink, D. (2020). Soft biohybrid morphing wings with feathers underactuated by wrist and finger motion. *Science Robotics*, *5*(38),1246.

Chatenet, Q., Tahan, A., Gagnon, M., & Chamberland-Lauzon, J. (2016, November). Numerical model validation using experimental data: Application of the area metric on a Francis runner. In *IOP Conference Series: Earth and Environmental Science* (Vol. 49, No. 6, p. 062015). IOP Publishing.

Chen, D., Gu, C., Zhang, R., Liu, J., Guo, D., & Marzocca, P. (2021). Vortex-induced vibrations of two degrees-of-freedom sprung cylinder with a rotational nonlinear energy sink: A numerical investigation. *Journal of Computational and Nonlinear Dynamics*, *16*(7).

Cheng, Y. T., & Cheng, C. M. (2004). Scaling, dimensional analysis, and indentation measurements. *Materials Science and Engineering: R: Reports*, *44*(4-5), 91-149.

Communier, D., Salinas, M. F., Carranza Moyao, O., & Botez, R. M. (2015). Aero structural modeling of a wing using CATIA V5 and XFLR5 software and experimental validation using the Price-Païdoussis wing tunnel. In *AIAA atmospheric flight mechanics conference* (p. 2558).

Concilio, A., Ciminello, M., Galasso, B., Pellone, L., Mercurio, U., Apuleo, G. & Bardenstein, D. (2022). De-Bonding Numerical Characterization and Detection in Aeronautic Multi-Element Spars. *Sensors*, *22*(11), 4152.

Correa, G., Santarelli, M., Borello, F., Cestino, E., & Romeo, G. (2015). Flight test validation of the dynamic model of a fuel cell system for ultra-light aircraft. *Proceedings of the Institution of Mechanical Engineers, Part G: Journal of Aerospace Engineering*, *229*(5), 917-932.

Degani, A. T., Walker, J. D. A., & Smith, F. T. (1998). Unsteady separation past moving surfaces. *Journal of Fluid Mechanics*, *375*, 1-38.

Devore, J. L. (2008). Probability and Statistics for Engineering and the Sciences.

Dimino, I., Lecce, L., & Pecora, R. (2017). *Morphing wing technologies: Large commercial aircraft and civil helicopters*. Butterworth-Heinemann.

Dubief, Y., & Delcayre, F. (2000). On coherent-vortex identification in turbulence. *Journal of turbulence*, *1*(1), 011.

Duell, E. G., & George, A. R. (1993). *Measurements in the unsteady near wakes of ground vehicle bodies* (No. 930298). SAE Technical Paper.

Dunnmon, J. A., Stanton, S. C., Mann, B. P., & Dowell, E. H. (2011). Power extraction from aeroelastic limit cycle oscillations. *Journal of fluids and structures*, *27*(8), 1182-1198.

Durbin, P. A. (1995). Separated flow computations with the k-epsilon-v-squared model. *AIAA journal*, *33*(4), 659-664.

Eisenlohr, H., & Eckelmann, H. (1989). Vortex splitting and its consequences in the vortex street wake of cylinders at low Reynolds number. *Physics of Fluids A: Fluid Dynamics*, *1*(2), 189-192.

Elelwi, M., Kuitche, M. A., Botez, R. M., & Dao, T. M. (2020). Comparison and analyses of a variable span-morphing of the tapered wing with a varying sweep angle. *The Aeronautical Journal*, *124*(1278), 1146-1169.

Elelwi, M., Calvet, T., Botez, R. M., & Dao, T. M. (2021). Wing component allocation for a morphing variable span of tapered wing using finite element method and topology optimisation–application to the UAS-S4. *The Aeronautical Journal*, *125*(1290), 1313-1336.

Elelwi, M., Pinto, F. S., Botez, R. M., & Dao, T. M. (2022, April). Multidisciplinary optimization for weight saving in a variable tapered span-morphing wing using composite materials—application to the UAS-S4. In *Actuators* (Vol. 11, No. 5, p. 121). MDPI.

Fasel, U., Keidel, D., Molinari, G., & Ermanni, P. (2019). Aeroservoelastic optimization of morphing airborne wind energy wings. In *AIAA Scitech 2019 Forum* (p. 1217).

Ferson, S., Oberkampf, W. L., & Ginzburg, L. (2008). Model validation and predictive capability for the thermal challenge problem. *Computer Methods in Applied Mechanics and Engineering*, *197*(29-32), 2408-2430.

FLIR Inc. Available online: https://www.flir.ca/support/products/ranger-r20ss/ (accessed on January 11, 2021).

FLIR camera. Technical information of the FLIR camera. Available online: https://www.flir.ca/products/grasshopper3-gige/ (accessed on March 18, 2023).

Fluent User's Manual. Available online: https://www.sharcnet.ca/Software/Ansys/17.0/en-us/help/flu_ug/flu_ug.html (accessed on 9 February 2021).

Fröhlich, J., & Von Terzi, D. (2008). Hybrid LES/RANS methods for the simulation of turbulent flows. *Progress in Aerospace Sciences*, *44*(5), 349-377.

Frunzulica, F., Dumitrescu, H., & Dumitrache, A. (2013). A numerical investigation on the dynamic stall of a vertical axis wind turbine. *PAMM*, *13*(1), 295-296.

Gabor, O. Ş., Koreanschi, A., & Botez, R. M. (2016). Analysis of UAS-S4 Éhecatl aerodynamic performance improvement using several configurations of a morphing wing technology. *The Aeronautical Journal*, *120*(1231), 1337-1364.

Gabor, O. S., Koreanschi, A., & Botez, R. M. (2013). Optimization of an Unmanned Aerial System'wing using a flexible skin morphing wing. *SAE International Journal of Aerospace*, *6*(2013-01-2095), 115-121.

Gabor, O. Ş., Koreanschi, A., Botez, R. M., Mamou, M., & Mebarki, Y. (2016). Numerical simulation and wind tunnel tests investigation and validation of a morphing wing-tip demonstrator aerodynamic performance. *Aerospace Science and Technology*, *53*, 136-153.

Gabor, O. Ş., Simon, A., Koreanschi, A., & Botez, R. (2014, November). Application of a morphing wing technology on hydra technologies unmanned aerial system UAS-S4. In *ASME International Mechanical Engineering Congress and Exposition* (Vol. 46421, p. V001T01A037). American Society of Mechanical Engineers.

Gabor, O. Ş., Simon, A., Koreanschi, A., & Botez, R. M. (2016). Improving the UAS-S4 Éhecal airfoil high angles-of-attack performance characteristics using a morphing wing approach. *Proceedings of the institution of mechanical engineers, Part G: Journal of Aerospace Engineering*, *230*(1), 118-131.

Garner, H. C., Rogers, E. W. E., Acum, W. E. A., Maskell, E. C., & Garner, H. C. (1966). Subsonic wind tunnel wall corrections. National Physical Laboratory. UK.

Garner, H. C., Rogers, E. W., Acum, W. E., & Maskell, E. C. (1966). *Subsonic wind tunnel wall corrections*. AGARD, NATO.

Giuliani, M., Dimino, I., Ameduri, S., & Pecora, R. (2022). Status and Perspectives of Commercial Aircraft Morphing. *Biomimetics*, *7*(1), 11.

Grigorie, T. L., Popov, A. V., Botez, R. M., Mamou, M., & Mébarki, Y. (2012). On–off and proportional–integral controller for a morphing wing. Part 1: Actuation mechanism and control design. Proceedings of the Institution of Mechanical Engineers, Part G: Journal of Aerospace Engineering, 226(2), 131-145.

Grigorie, T. L., Botez, R. M., Popov, A. V., Mamou, M., & Mébarki, Y. (2012). A hybrid fuzzy logic proportional-integral-derivative and conventional on-off controller for morphing wing actuation using shape memory alloy Part 1: Morphing system mechanisms and controller architecture design. The Aeronautical Journal, 116(1179), 433-449.

Grigorie, T. L., Botez, R. M., & Popov, A. V. (2015). How the airfoil shape of a morphing wing is actuated and controlled in a smart way. *Journal of Aerospace Engineering*, *28*(1), 04014043.

Grisval, J. P., & Liauzun, C. (1999). Application of the finite element method to aeroelasticity. *Revue européenne des éléments finis*, *8*(5-6), 553-579.

Gundlach, J. (2014). *Designing unmanned aircraft systems*. American Institute of Aeronautics & Astronautics.

Guo, C. Q., & Païdoussis, M. P. (2000). Stability of rectangular plates with free side-edges in two-dimensional inviscid channel flow. *J. Appl. Mech.*, *67*(1), 171-176.

Haghighat, S., Martins, J. R., & Liu, H. H. (2012). Aeroservoelastic design optimization of a flexible wing. *Journal of Aircraft*, *49*(2), 432-443.

Dette, H., & Munk, A. (1998). Validation of linear regression models. *Annals of Statistics*, 778-800.

Hu, G., Tang, L., Das, R., & Marzocca, P. (2018). A two-degree-of-freedom piezoelectric energy harvester with stoppers for achieving enhanced performance. *International Journal of Mechanical Sciences*, *149*, 500-507.

Hunt, J. C., Wray, A. A., & Moin, P. (1988). Eddies, streams, and convergence zones in turbulent flows. *Studying turbulence using numerical simulation databases, 2. Proceedings of the 1988 summer program*.

Huvelin, F., Dequand, S., Lepage, A., & Liauzun, C. (2018). On the validation and use of high-fidelity numerical simulations for gust response analysis. *Aerospace Lab*, (14), 1-16.

Jameson, A., Martinelli, L., & Pierce, N. A. (1998). Optimum aerodynamic design using the Navier–Stokes equations. *Theoretical and computational fluid dynamics*, *10*(1), 213-237.

Jeong, J., & Hussain, F. (1995). On the identification of a vortex. *Journal of fluid mechanics*, *285*, 69-94.

Johnson-Laird, P. N. (2005). Flying bicycles: How the Wright brothers invented the airplane. *Mind & Society*, *4*, 27-48.

Kalitzin, G., Medic, G., Iaccarino, G., & Durbin, P. (2005). Near-wall behavior of RANS turbulence models and implications for wall functions. *Journal of Computational Physics*, *204*(1), 265-291.

Kammegne, M. J. T., Botez, M. R., Mamou, M., Mebarki, Y., Koreanschi, A., Gabor, O. S., & Grigorie, T. L. (2016, April). Experimental wind tunnel testing of a new multidisciplinary morphing wing model. In *Proceedings of the 18th International Conference on Mathematical Methods, Computational Techniques and Intelligent Systems (MAMECTIS 2016)*.

Katoch, S., Chauhan, S. S., & Kumar, V. (2021). A review on genetic algorithm: past, present, and future. *Multimedia Tools and Applications*, *80*, 8091-8126.

Katz, A., & Sankaran, V. (2011). Mesh quality effects on the accuracy of CFD solutions on unstructured meshes. *Journal of Computational Physics*, *230*(20), 7670-7686.

Kim, D., Cossé, J., Cerdeira, C. H., & Gharib, M. (2013). Flapping dynamics of an inverted flag. *Journal of Fluid Mechanics*, *736*, R1.

Koreanschi, A., Gabor, O. S., Acotto, J., Brianchon, G., Portier, G., Botez, R. M. & Mebarki, Y. (2017). Optimization and design of an aircraft's morphing wing-tip demonstrator for drag reduction at low speeds, Part II-Experimental validation using Infra-Red transition measurement from Wind Tunnel tests. *Chinese Journal of Aeronautics*, *30*(1), 164-174.

Koreanschi, A., Sugar-Gabor, O., & Botez, R. M. (2016). Numerical and experimental validation of a morphed wing geometry using Price-Païdoussis wind-tunnel testing. *The Aeronautical Journal*, *120*(1227), 757-795.

Koreanschi, A., Sugar-Gabor, O., & Botez, R. M. (2016). Drag optimization of a wing equipped with a morphing upper surface. *The Aeronautical Journal*, *120*(1225), 473-493.

Koreanschi, A., Gabor, O. S., Acotto, J., Brianchon, G., Portier, G., Botez, R. M., & Mebarki, Y. (2017). Optimization and design of an aircraft's morphing wing-tip demonstrator for drag reduction at low speed, Part I–Aerodynamic optimization using genetic, bee colony and gradient descent algorithms. *Chinese Journal of Aeronautics*, *30*(1), 149-163.

Kroll, N., Gauger, N. R., Brezillon, J., Dwight, R., Fazzolari, A., Vollmer, D. & Hazra, S. (2007). Flow simulation and shape optimization for aircraft design. *Journal of Computational and applied mathematics*, *203*(2), 397-411.

Kudva, J. N., Appa, K., Van Way, C. B., & Lockyer, A. J. (1995, May). Adaptive smart wing design for military aircraft: requirements, concepts, and payoffs. In *Smart Structures and Materials 1995: Industrial and Commercial Applications of Smart Structures Technologies* (Vol. 2447, pp. 35-44).

Launder, B. (1995). Turbulence modelling for CFD. DC Wilcox. *Journal of FluidMechanics, 289*, 406-407.

Lee, H., Sengupta, B., Araghizadeh, M. S., & Myong, R. S. (2022). Review of vortex methods for rotor aerodynamics and wake dynamics. *Advances in Aerodynamics*, *4*(1), 20.

Lee, J. L. (2001). *Into the wind: A history of the American wind tunnel, 1896–1941*. Auburn University.

Lee, Y., Rho, J., Kim, K. H., & Lee, D. H. (2011). Fundamental studies on free stream acceleration effect on drag force in bluff bodies. *Journal of mechanical science and technology*, *25*, 695-701.

Liauzun, C. D. (2010, January). Aeroelastic response to gust using CFD techniques. In *Fluids Engineering Division Summer Meeting* (Vol. 54518, pp. 269-276).

Liebeck, R. H. (2004). Design of the blended wing body subsonic transport. *Journal of aircraft*, *41*(1), 10-25.

Liu, Y., Chen, W., Arendt, P., & Huang, H. Z. (2011). Toward a better understanding of model validation metrics. *Journal of Mechanical Design*, *133*(7).

Lo, S. H., & Lee, C. K. (1992). On using meshes of mixed element types in adaptive finite element analysis. *Finite Elements in Analysis and Design*, *11*(4), 307-336.

Machado, L., Matlock, J., & Suleman, A. (2020). Experimental evaluation of a hybrid electric propulsion system for small UAVs. *Aircraft Engineering and Aerospace Technology*, *92*(5), 727-736.

Mariotti, A., Buresti, G., & Salvetti, M. V. (2019). Separation delay through contoured transverse grooves on a 2D boat-tailed bluff body: Effects on drag reduction and wake flow features. *European Journal of Mechanics-B/Fluids*, *74*, 351-362.

Martin, S. (1990, January). PC-based data acquisition in an industrial environment. In *IEE Colloquium on PC-Based instrumentation* (pp. 2-1).

Maskell, E. C. (1963). *A theory of the blockage effects on bluff bodies and stalled wings in a closed wind tunnel*. Aeronautical Research Council London (United Kingdom).

Mason, W., Robertshaw, H., & Inman, D. (2004). Recent experiments in aerospace and design engineering education. In *42nd AIAA Aerospace Sciences Meeting and Exhibit* (p. 415).

Mason Jr, W. T., & Beebe, P. S. (1978). The drag related flow field characteristics of trucks and buses. In *Aerodynamic drag mechanisms of bluff bodies and road vehicles* (pp. 45-93). Boston, MA: Springer US.

Matlock, J., Warwick, S., Sharikov, P., Richards, J., & Suleman, A. (2019). Evaluation of energy efficient propulsion technologies for unmanned aerial vehicles. *Transactions of the Canadian Society for Mechanical Engineering*, *43*(4), 481-489.

Mehta, R. D., & Bradshaw, P. (1979). Design rules for small low speed wind tunnels. *The Aeronautical Journal*, *83*(827), 443-453.

Mendez, P. F., & Ordonez, F. (2005). Scaling laws from statistical data and dimensional analysis.

Menter, F. R. (2009). Review of the shear-stress transport turbulence model experience from an industrial perspective. *International journal of computational fluid dynamics*, *23*(4), 305-316.

Menter, F. R., & Kuntz, M. (2004). Adaptation of eddy-viscosity turbulence models to unsteady separated flow behind vehicles. In *The aerodynamics of heavy vehicles: trucks, buses, and trains* (pp. 339-352). Springer Berlin Heidelberg.

Min, Z., Kien, V. K., & Richard, L. J. (2010). Aircraft morphing wing concepts with radical geometry change. *The IES Journal Part A: Civil & Structural Engineering*, *3*(3), 188-195.

Mitcheson, P. D., Yeatman, E. M., Rao, G. K., Holmes, A. S., & Green, T. C. (2008). Energy harvesting from human and machine motion for wireless electronic devices. *Proceedings of the IEEE*, *96*(9), 1457-1486.

Monner, H. P., Breitbach, E., Bein, T., & Hanselka, H. (2000). Design aspects of the adaptive wing—the elastic trailing edge and the local spoiler bump. *The Aeronautical Journal*, *104*(1032), 89-95.

Mosbah, A. B., Salinas, M. F., Botez, R., & Dao, T. M. (2013). New methodology for wind tunnel calibration using neural networks-EGD approach. *SAE International Journal of Aerospace*, *6*(2013-01-2285), 761-766.

Nabavi, S., & Zhang, L. (2016). Portable wind energy harvesters for low-power applications: A survey. *Sensors*, *16*(7), 1101.

Oberkampf, W. L., & Trucano, T. G. (2002). Verification and validation in computational fluid dynamics. *Progress in aerospace sciences*, *38*(3), 209-272.

Pankonien, A. M., & Inman, D. J. (2015, April). Spanwise morphing trailing edge on a finite wing. In *Active and Passive Smart Structures and Integrated Systems 2015* (Vol. 9431, pp. 248-262). SPIE.

Pecora, R. (2021). Morphing wing flaps for large civil aircraft: Evolution of a smart technology across the Clean Sky program. *Chinese Journal of Aeronautics*, *34*(7), 13-28.

Poirel, D., Harris, Y., & Benaissa, A. M. (2006, January). Aeroelastic dynamics of a NACA 0012 airfoil in the transitional Reynolds number regime. In *ASME Pressure Vessels and Piping Conference* (Vol. 47888, pp. 847-854).

Poirel, D., & Mendes, F. (2014). Experimental small-amplitude self-sustained pitch–heave oscillations at transitional Reynolds numbers. *AIAA journal*, *52*(8), 1581-1590.

Poirel, D., & Price, S. J. (2007). Bifurcation characteristics of a two-dimensional structurally non-linear airfoil in turbulent flow. *Nonlinear dynamics*, *48*, 423-435.

Popov, A. V., Grigorie, L. T., Botez, R., Mamou, M., & Mebarki, Y. (2010). Closed-loop control validation of a morphing wing using wind tunnel tests. *Journal of Aircraft*, *47*(4), 1309-1317.

Popov, A. V., Grigorie, T. L., Botez, R. M., Mébarki, Y., & Mamou, M. (2010). Modeling and testing of a morphing wing in open-loop architecture. Journal of Aircraft, 47(3), 917-923.

Popov, A. V., Botez, R. M., & Labib, M. (2008). Transition point detection from the surface pressure distribution for controller design. *Journal of Aircraft*, *45*(1), 23-28.

Rawlings, J. O., Pantula, S. G., & Dickey, D. A. (Eds.). (1998). *Applied regression analysis: a research tool*. New York, NY: Springer New York.

Raymer, D. (2012). *Aircraft design: a conceptual approach*. American Institute of Aeronautics and Astronautics.

Rebuffet, P.(1996). *Aérodynamique Expérimentale*, 1st ed.; Paris Dunod: Paris, France, pp. 566.

Rocchio, B., Mariotti, A., & Salvetti, M. V. (2020). Flow around a 5: 1 rectangular cylinder: Effects of upstream-edge rounding. *Journal of Wind Engineering and Industrial Aerodynamics*, *204*, 104237.

Romeo, G., Cestino, E., Pacino, M., Borello, F., & Correa, G. (2012). Design and testing of a propeller for a two-seater aircraft powered by fuel cells. *Proceedings of the Institution of Mechanical Engineers, Part G: Journal of Aerospace Engineering*, *226*(7), 804-816.

Roshko, A. (1954). *On the drag and shedding frequency of two-dimensional bluff bodies* (No. NACA-TN-3169).

Roskam, J. (2005). Airplane design, Part I: Preliminary sizing of aircraft. DARCorporation: Lawrence, KS, USA.

Rostami, A. B., & Armandei, M. (2017). Renewable energy harvesting by vortex-induced motions: Review and benchmarking of technologies. *Renewable and Sustainable Energy Reviews*, *70*, 193-214.

Sader, J. E., Huertas-Cerdeira, C., & Gharib, M. (2016). Stability of slender inverted flags and rods in uniform steady flow. *Journal of Fluid Mechanics*, *809*, 873-894.

Sadraey, M. H. (2012). *Aircraft design: A systems engineering approach*. John Wiley & Sons.

Salinas, M. F., Botez, R. M., & Gauthier, G. (2023). New validation methodology of an adaptive wing for UAV S45 for fuel reduction and climate improvement. *Applied Sciences*, *13*(3), 1799.

Salinas, M. F., Botez, R. M., & Gauthier, G. (2021). New numerical and measurements flow analyses near radars. *Applied Mechanics*, *2*(2), 303-330.

Simpson, A., Coulombe, N., Jacob, J., & Smith, S. (2005). Morphing of inflatable wings. In *46th AIAA/ASME/ASCE/AHS/ASC Structures, Structural Dynamics and Materials Conference* (p. 2110).

Sofla, A. Y. N., Meguid, S. A., Tan, K. T., & Yeo, W. K. (2010). Shape morphing of aircraft wing: Status and challenges. *Materials & Design*, *31*(3), 1284-1292.

Spalart, P. R. (2000). Strategies for turbulence modelling and simulations. *International journal of heat and fluid flow*, *21*(3), 252-263.

Stockbridge, C., Ceruti, A., & Marzocca, P. (2012). Airship research and development in the areas of design, structures, dynamics and energy systems. *International Journal of Aeronautical and Space Sciences*, *13*(2), 170-187.

Strelec, J. K., Lagoudas, D. C., Khan, M. A., & Yen, J. (2003). Design and implementation of a shape memory alloy actuated reconfigurable airfoil. *Journal of Intelligent Material Systems and Structures*, *14*(4-5), 257-273.

Suzuki, S., & Yonezawa, S. (1993). Simultaneous structure/control design optimization of a wing structure with a gust load alleviation system. *Journal of Aircraft*, *30*(2), 268-274.

Tavallaeinejad, M., Païdoussis, M. P., Legrand, M., & Kheiri, M. (2020). Instability and the post-critical behaviour of two-dimensional inverted flags in axial flow. *Journal of Fluid Mechanics*, *890*, A14.

Tavallaeinejad, M., Païdoussis, M. P., Salinas, M. F., Legrand, M., Kheiri, M., & Botez, R. M. (2020). Flapping of heavy inverted flags: a fluid-elastic instability. *Journal of Fluid Mechanics*, *904*, R5.

Tavallaeinejad, M., Païdoussis, M., Salinas, M. F., Legrand, M., Kheiri, M., & Botez, R. M. (2020, May). Why inverted flags flap: An experimental study. In *Second International Symposium on Flutter and its Application (ISFA2020)*.

Tavallaeinejad, M., Salinas, M. F., Païdoussis, M. P., Legrand, M., Kheiri, M., & Botez, R. M. (2021). Dynamics of inverted flags: Experiments and comparison with theory. *Journal of Fluids and Structures*, *101*, 103199.

Kammegne, M. J. T., Grigorie, L. T., Botez, R. M., & Koreanschi, A. (2016). Design and wind tunnel experimental validation of a controlled new rotary actuation system for a morphing wing application. *Proceedings of the Institution of Mechanical Engineers, Part G: Journal of Aerospace Engineering*, *230*(1), 132-145.

Tong, X., Ge, W., Sun, C., & Liu, X. (2014). Topology optimization of compliant adaptive wing leading edge with composite materials. *Chinese Journal of Aeronautics*, *27*(6), 1488-1494.

USB6210 Data Acquisition Card Module manual. Available online: https://www.ni.com/

pdf/manuals/375194d.pdf (accessed on Monday, October 18, 2021).

Valasek, J. (Ed.). (2012). *Morphing aerospace vehicles and structures*. John Wiley & Sons.

Vasista, S., Tong, L., & Wong, K. C. (2012). Realization of morphing wings: a multidisciplinary challenge. *Journal of aircraft*, *49*(1), 11-28.

Wang, I., Gibbs, S. C., & Dowell, E. H. (2012). Aeroelastic model of multisegmented folding wings: theory and experiment. *Journal of aircraft*, *49*(3), 911-921.

Wang, N., Yao, W., Zhao, Y., Chen, X., Zhang, X., & Li, L. (2018). A new interval area metric for model validation with limited experimental data. *Journal of Mechanical Design*, *140*(6).

Woods, B. K., & Friswell, M. I. (2015). The Adaptive Aspect Ratio morphing wing: Design concept and low fidelity skin optimization. *Aerospace Science and Technology*, *42*, 209-217.

Yu, Y., Liu, Y., & Chen, Y. (2017). Vortex dynamics behind a self-oscillating inverted flag placed in a channel flow: Time-resolved particle image velocimetry measurements. *Physics of Fluids*, *29*(12), 125104.

Zhao, W., Païdoussis, M. P., Tang, L., Liu, M., & Jiang, J. (2012). Theoretical and experimental investigations of the dynamics of cantilevered flexible plates subjected to axial flow. *Journal of Sound and Vibration*, *331*(3), 575-587.